



POLITECNICO DI TORINO  
Repository ISTITUZIONALE

Bioactive Membranes and Nanocoatings for Guided Tissue Regeneration in Periodontal Diseases

*Original*

Bioactive Membranes and Nanocoatings for Guided Tissue Regeneration in Periodontal Diseases / Nardo, Tiziana. - (2015).

*Availability:*

This version is available at: 11583/2614171 since:

*Publisher:*

Politecnico di Torino

*Published*

DOI:10.6092/polito/porto/2614171

*Terms of use:*

openAccess

This article is made available under terms and conditions as specified in the corresponding bibliographic description in the repository

*Publisher copyright*

(Article begins on next page)

POLITECNICO DI TORINO

SCUOLA INTERPOLITECNICA DI DOTTORATO

Doctoral Program in Biomedical Engineering

Final Dissertation

**Bioactive Membranes and Nanocoatings for Guided  
Tissue Regeneration in Periodontal Diseases**



Tiziana Nardo

Tutor  
prof. Gianluca Ciardelli

Co-ordinator of the Research Doctorate Course  
prof. Cristina Bignardi

March 2015



# Table of Contents

Acknowledgements .....	XI
Short Curriculum Vitae .....	XII
List of Publications .....	XIV
Abstract .....	XVI
Introduction to the Thesis Format .....	XX
List of Abbreviations .....	XXII

## SECTION I

### Chapter 1 - Guided Tissue Regeneration membranes for periodontal applications:

#### State of the Art and future trends

1.1 Introduction .....	3
1.2 Anatomy of the periodontium .....	4
1.2.1 Dentogingival junction .....	5
1.2.2 Cementum .....	6
1.2.3 Periodontal ligament .....	7
1.2.4 Alveolar bone .....	7
1.3 Periodontal diseases .....	8
1.4 Prevention and treatment of periodontal diseases .....	12
1.5 Biology of periodontal healing and regeneration .....	13
1.5.1 Gingival wound healing process .....	14
1.5.2 Bone regeneration process .....	15
1.6 Current treatments for clinical periodontal regeneration .....	16
1.6.1 Bone replacement grafts .....	17
1.6.2 Biomodification of the tooth-root surface .....	18
1.6.3 Guided Tissue/Bone Regeneration .....	18
1.6.4 Delivery of growth factors .....	19
1.6.5 Gene therapies .....	20
1.7 Commercially available membranes for GTR and GBR applications .....	21
1.7.1 Non-resorbable membranes .....	22
1.7.1.1 PTFE-based membranes .....	23
1.7.1.2 Titanium mesh .....	24
1.7.2 Resorbable membranes .....	25

1.7.2.1 Synthetic resorbable membranes .....	26
1.7.2.2 Membranes based on natural materials .....	28
1.8 Current trends in the development of membranes for GTR/GBR.....	33
1.9 Layer-by-Layer deposition technique (LbL).....	40
1.9.1 Film growth and influencing factors .....	41
1.9.2 Monitoring multilayer build up.....	44
1.9.3 State of the art of LbL technique for gingival wound healing applications .....	45
1.10 Mussel-inspired coatings: definition and state of the art .....	49
1.11 Factors influencing the success of GTR/GBR .....	57
1.12 Thesis goal .....	57
References.....	61

## SECTION II

### **Chapter 2 - PolyDOPA mussel-inspired coating as a means for hydroxyapatite entrapment on polytetrafluoroethylene surface for application in Periodontal diseases**

Abstract .....	73
2.1 Introduction.....	75
2.2 Materials and methods .....	77
2.2.1 Materials .....	77
2.2.2 Methods .....	77
2.2.2.1 Surface treatment.....	77
2.2.2.2 Surface analyses .....	77
2.2.2.3 Cell culture .....	78
2.2.2.4 SEM analyses .....	79
2.2.3 Statistical analyses .....	79
2.3 Results and discussion .....	79
2.3.1 Chemical composition .....	79
2.3.2 Morphology .....	83
2.3.3 Surface roughness and wettability properties .....	84
2.3.4 Cell proliferation and adhesion .....	85
2.3.5 Coating dissolution .....	87
2.4 Conclusions .....	90
References.....	91

### **Chapter 3 - Self-polymerizing DOPA as a functional layer for the development of antimicrobial coating on PTFE barrier membranes for GTR procedures**

Abstract .....	93
3.1 Introduction .....	94
3.2 Materials and methods .....	96
3.2.1 Materials .....	96
3.2.2 Methods .....	96
3.2.2.1 Surface functionalization.....	96
3.2.2.2 Water contact angle measurements .....	97
3.2.2.3 Morphological and compositional analysis .....	97
3.2.2.4 Atomic force microscopy .....	97
3.2.2.5 X-ray photoelectron spectroscopy .....	97
3.2.2.6 Stability test.....	98
3.2.2.7 Antibacterial assay .....	98
3.2.2.8 Cell culture .....	98
3.2.2.9 Cell adhesion.....	99
3.2.3 Statistical analyses .....	99
3.3 Results and discussion .....	99
3.3.1 Chemical composition .....	99
3.3.2 Morphological analysis.....	102
3.3.3 Surface roughness and wettability properties .....	103
3.3.4 Cell proliferation and adhesion.....	105
3.3.5 Antibacterial efficiency.....	107
3.3.6 Dissolution feature of coating .....	108
3.4 Conclusions .....	110
References.....	112

## **SECTION III**

### **Chapter 4 - Investigation of PLCL/PLGA blends physical properties and biocompatibility for Tissue Engineering applications**

Abstract .....	117
4.1 Introduction .....	118
4.2 Materials and methods .....	119
4.2.1 Materials .....	119
4.2.1.1 Poly(DL-lactide-co-glycolide) .....	120

4.2.1.2 Poly(DL-lactide-co- $\epsilon$ -caprolactone) .....	121
4.2.2 Methods .....	121
4.2.2.1 Blend preparation .....	121
4.2.2.2 Scanning electron microscopy.....	122
4.2.2.3 Differential scanning calorimetry.....	122
4.2.2.4 Tensile testing .....	122
4.2.2.5 <i>In vitro</i> testing .....	122
4.2.2.6 <i>In vitro</i> degradation .....	123
4.2.3 Statistical analyses .....	124
4.3 Results and discussion .....	124
4.3.1 Morphological analysis.....	124
4.3.2 Thermal analysis .....	125
4.3.3 Mechanical characterization .....	126
4.3.4 Cell proliferation and adhesion .....	128
4.3.5 <i>In vitro</i> degradation test .....	130
4.3.5.1 Weight loss and pH variations.....	131
4.3.5.2 Molecular weight measurements .....	132
4.3.5.3 Thermal properties .....	133
4.3.5.4 FTIR-ATR analysis .....	135
4.3.2.5 Morphological analysis .....	136
4.4 Conclusions .....	138
References.....	139

**Chapter 5 - Improving fibroblast response and antimicrobial efficiency via polyelectrolytes multilayer assembly for Tissue Engineering applications**

Abstract .....	141
5.1 Introduction.....	142
5.2 Materials and methods .....	144
5.2.1 Materials .....	144
5.2.1.1 Chitosan.....	144
5.2.1.2 Chondroitin sulfate.....	145
5.2.2 Sample preparation .....	145
5.2.2.1 Preparation of PLCL/PLGA 25/75 samples via solvent casting .....	145
5.2.2.2 Surface activation through aminolysis treatment .....	146
5.2.2.3 Preparation of multilayer coating .....	146

5.2.3 Sample characterization .....	147
5.2.3.1 Water contact angle measurement.....	147
5.2.3.2 Infrared analysis in ATR modality .....	147
5.2.3.3 Colorimetric method to quantify amino groups .....	147
5.2.3.4 Morphological analysis .....	148
5.2.3.5 Quartz crystal microbalance analyses .....	148
5.2.3.6 Fluorescence microscopy .....	149
5.2.3.7 Cell proliferation and adhesion .....	149
5.2.3.8 X-ray photoelectron spectroscopy.....	150
5.2.3.9 Stability test.....	150
5.2.3.10 Antibacterial assay .....	150
5.2.4 Statistical analyses .....	151
5.3 Results and discussion .....	151
5.3.1 Characterization of aminolysis treatment .....	151
5.3.2 Characterization of multilayer coating.....	154
5.3.2.1 CHS/CH film build up.....	154
5.3.2.2 Contact angle measurement.....	156
5.3.2.3 Fluorescence microscopy .....	157
5.3.2.4 Morphological analysis .....	159
5.3.2.5 FTIR-ATR analysis .....	159
5.3.2.6 Cell proliferation and adhesion .....	160
5.3.2.7 XPS analysis and CH quantification .....	163
5.3.2.8 Antibacterial efficiency .....	165
5.3.2.9 Dissolution feature of coating .....	166
5.4 Conclusions .....	167
References.....	169

## **Chapter 6 - Composite porous membranes for bone tissue regeneration**

Abstract .....	171
6.1 Introduction.....	172
6.2 Materials and methods .....	174
6.2.1 Materials .....	174
6.2.1.1 Gelatin.....	174
6.2.1.2 $\beta$ -tricalcium phosphate .....	175
6.2.1.3 Genipin.....	175

6.2.1.4 Dibasic sodium phosphate.....	177
6.2.2 Sample preparation .....	177
6.2.3 Sample characterization.....	178
6.2.3.1 Cross-linking degree determination .....	178
6.2.3.2 Morphological analysis .....	179
6.2.3.3 Infrared analysis in ATR modality.....	179
6.2.3.4 Thermogravimetric analysis .....	179
6.2.3.5 Tensile test .....	180
6.2.3.6 Water absorption and dissolution tests .....	180
6.2.3.7 Cell viability and adhesion .....	181
6.2.4 Statistical analyses .....	182
6.3 Results and discussion .....	182
6.3.1 Cross-linking degree .....	182
6.3.2 Porosity and morphological analysis .....	183
6.3.3 FTIR-ATR analysis.....	186
6.3.4 TGA analysis .....	187
6.3.5 Mechanical characterization .....	188
6.3.6 Water absorption and dissolution tests.....	190
6.3.7 <i>In vitro</i> cell tests.....	192
6.4 Conclusions.....	193
References.....	195

## **Chapter 7 - Bi-layered absorbable membrane for Guided Tissue Regeneration**

Abstract.....	197
7.1 Introduction.....	199
7.2 Materials and methods .....	201
7.2.1 Materials .....	201
7.2.1.1 Polyvinylpyrrolidone.....	201
7.2.1.2 Polyethylene glycol.....	202
7.2.2 Sample preparation .....	203
7.2.2.1 Preparation of blend PVP/PEG .....	203
7.2.2.2 Preparation of bi-layered absorbable membrane .....	203
7.2.3 Sample characterization.....	204
7.2.3.1 Water contact angle measurement.....	204
7.2.3.2 Infrared analysis in ATR modality.....	204

7.2.3.3 Thermogravimetric analysis .....	204
7.2.3.4 Differential scanning calorimetry .....	204
7.2.3.5 Lap shear strength test .....	204
7.2.3.6 Morphological analysis .....	205
7.2.3.7 Tensile test .....	205
7.2.3.8 Bi-layered membrane manageability .....	206
7.2.4 Statistical analyses .....	206
7.3 Results and discussion .....	206
7.3.1 Characterization of PVP/PEG blend .....	206
7.3.2 Preliminary characterization of absorbable bi-layered membrane .....	214
7.4 Conclusions .....	216
References .....	218

## SECTION IV

### Chapter 8 - Final discussion and conclusions

8.1 General discussion .....	221
8.2 Conclusions and future developments .....	226
References .....	228



# Acknowledgements

During the course of the last three years I had the fortune of working and being in contact with several people and institutions that marked my work and, at the same time, thought me a lot about science and life itself.

I would like to acknowledge Prof. Gianluca Ciardelli and Dr. Valeria Chiono. Over these years they guided me through my research work, providing revealing and constructive suggestions and giving me the chance to collaborate on several events and projects, and in this sense to become a more complete and independent researcher.

I am also completely thankful to Prof. Maryam Tabrizian for giving me the opportunity to spend seven months in her group at McGill University. She accepted me in her group without knowing me and received me as I was one of her students. The thoughtful discussions that we had were a valuable input for my research work and allowed me to grow as a researcher.

During my stay at Tabrizian's research group, I came in contact with students and technicians from different countries. Mina, Amir, Kaushar, Khalil, Kristen, Lamees, Rafael, Rosey, Ryan, Samira, Sandrine, Tim. All of you, in your own way, helped me in several stages of my research work and my life outside the lab.

Then I wish to thank all my friends that enrich every moment of my life. The friends in the Bioengineering Industrial Group at Politecnico di Torino: Andres, Chiara, Clara, Diana, Diego, Emilia, Fra, Gianpaolo, Gioseffino, Gioseffo, Giuseppe, Irene, Mara, Monica, Sadegh, Silvia, Susanna, Tianran, Umberto. The friends from my little town: Cla and John, Daffu, Davidino, Fla, Michi. My volley team's friends: Ale, Chia, Cri, Fra, Manu, Mari e Marti. The friends of the university years: Ale, Cami, Cle, Giulia, Kri, Simo.

Finally, thanks to my family!

# Short Curriculum Vitae

Tiziana Nardo was born in 1986 in Torino, Italy. She lives in Fiano (TO), Italy, and works in the Industrial Bioengineering Group at Department of Mechanical and Aerospace Engineering, Politecnico di Torino.

She received a BS degree (October 2008) and a MS degree (December 2010) in Biomedical Engineering from Politecnico di Torino. During her MS degree, she worked within the NANOSTENT Regional Project for the development of polymeric materials for biodegradable stents and nanocoatings for metal stents with antithrombogenic and antiinflammatory properties, and able to promote stent endothelialization.

In 2011 she was qualified to practice the profession of Industrial Engineer. From September to December 2011 she worked at Sorin CRM in the Clinical Development Department. There, she supported the organization, coordination, monitoring and analyses of the international clinical studies managed by the department, in compliance with the ICH-GCP guidelines and laws.

From January 2012 to December 2014, she was a PhD student in Biomedical Engineering at the Department of Mechanical and Aerospace Engineering, Politecnico di Torino. Her research activity was part of BIO-PATH (“Bioengineered barrier membranes for the treatment of dental bone pathologies”) MANUNET ERA-NET project, which aimed at the development of advanced bioabsorbable and non-bioabsorbable innovative barrier devices (membranes) for guided tissue/bone regeneration.

In 2014 she worked 7 months in the Biomat’X Research Laboratories (Department of Biomedical Engineering, McGill University, Montreal, Canada) to develop bioactive nanocoatings.

As a PhD student of Industrial Bioengineering group, she has been involved for scientific research in HERNAX (“Auto-adhesive prosthesis for abdominal wall repair”) Regional Project, MES-STAR (“Morphologically engineered scaffold for soft tissue application and regeneration”) MANUNET ERA-NET project and B<sup>3</sup>-BARRIER (“Bioartificial and bioabsorbable barrier devices with biomimetic properties for oral regenerative surgery”) M.I.S.E.-ICE-CRUI project.

As a result of her research work she has attended 6 important national and international meetings in the tissue engineering and biomaterial fields. Presently, she is the author of 3

papers in international refereed journal (1 published, 2 submitted), 1 book chapters and 7 abstracts in international conference proceedings.

# List of Publications

## International Journal with referee

1. **Poly(lactic acid)-based blends with tailored physicochemical properties for tissue engineering applications: a case study**

Irene Carmagnola, Valeria Chiono, Tiziana Nardo, Clara Mattu, Sara Cabodi, Paola Defilippi, Gianluca Ciardelli

International Journal of Polymeric Materials and Polymeric Biomaterials 64: 2, 90-98, DOI: 10.1080/00914037.2014.886247

## International Journals: submitted

1. **Layer-by-layer assembly for biomedical applications in the last decade**

Piergiorgio Gentile, Irene Carmagnola, Tiziana Nardo, Valeria Chiono, Paul V Hatton, Gianluca Ciardelli

Acta Biomaterialia

2. **PolyDOPA mussel-inspired coating as a means for hydroxyapatite entrapment on polytetrafluoroethylene surface for application in Periodontal diseases**

Tiziana Nardo, Valeria Chiono, Gianluca Ciardelli, Maryam Tabrizian

Acta Biomaterialia

## Book chapter

1. **Bioartificial biomaterials for regenerative medicine applications**

Chiono V, Nardo T, Ciardelli G

Regenerative Medicine Applications in Organ Transplantation, 1<sup>st</sup> Edition (Orlando G, Ed). Academic Press (ISBN: 978-0-12-398523-1)

## Communications in National/International Conferences

1. **Self-polymerizing DOPA as a functional layer for the development of antimicrobial coating on PTFE barrier membranes for GTR procedures**

Nardo T, Chiono V, Fracchia L, Ceresa C, Tabrizian M, Ciardelli G

ISSIB2015, April 7<sup>th</sup>-10<sup>th</sup> 2015, Sydney, Australia (Oral Presentation)

- 2. Surface modification of polyester blend films via aminolysis and Layer-by-Layer assembly of chondroitin sulfate and chitosan for gingival wound healing**  
Tiziana Nardo, Valeria Chiono, Maryam Tabrizian, Gianluca Ciardelli  
2<sup>nd</sup> International Conference on Bioinspired and Biobased Chemistry & Materials, October 15<sup>th</sup>-17<sup>th</sup> 2014, Nice, France (Oral Presentation)
- 3. Biomimetic fibrous mats for wound healing**  
Irene Carmagnola, Valeria Chiono, Piergiorgio Gentile, Tiziana Nardo, Rosario Patamia, Paul Hatton, Gianluca Ciardelli  
TERMIS2014, June 10<sup>th</sup>-13<sup>th</sup> 2014, Genova, Italy (Oral Presentation)
- 4. Blending as a tool to tailor physicochemical properties of polymeric materials for Tissue Engineering applications**  
Tiziana Nardo, Valeria Chiono, Piergiorgio Gentile, Francesca Boccafoschi, Gianluca Ciardelli  
ESB2013, September 8<sup>th</sup>-12<sup>th</sup> 2013, Madrid, Spain
- 5. Surface modification of Poly(DL-lactide-co-ε-caprolactone) and Poly(DL-lactide-co-glycolide) blend films for tissue engineering applications**  
Tiziana Nardo, Valeria Chiono, Francesca Boccafoschi, Gianluca Ciardelli  
SIB2013, June 3<sup>rd</sup>-5<sup>th</sup> 2013, Baveno, Italy
- 6. Layer-by-layer as a tool to tailor the surface properties of biomedical devices**  
Chiono V, Carmagnola I, Ferreira AM, Nardo T, Gentile P, Tonda-Turo C, Ruini F, Abrigo M, Boccafoschi F, Ciardelli G  
GNB2012, June 26<sup>th</sup>-29<sup>th</sup> 2012, Rome, Italy
- 7. Degradable polyester blends in biomedical applications**  
Chiono V, Carmagnola I, Nardo T, Boccafoschi F, Morello V, Defilippi P, Tarone G, Ciardelli G  
XX Convegno Italiano di Scienza e Tecnologia delle Macromolecole, 4-8 Settembre 2011, Terni, Italia

# Abstract

Periodontal diseases are highly prevalent in population of all ages. They are initiated by bacterial accumulation at the interface of bone and soft tissue leading to the loss of gingival tissue attachment to the root surface, that may eventually lead to tooth loss. Regenerative approaches to treat periodontitis lesions offer exciting possibilities; in particular, guided tissue/bone regeneration (GTR/GBR) approaches are promising for periodontal tissues regeneration in periodontal loss because, through the insertion of a physical barrier, they can exclude unwanted epithelial and gingival connective tissue cells from the healing area and allow bone tissue cells to repopulate the bony defect.

In the past few decades, different resorbable and non-resorbable membranes have been developed. Expanded polytetrafluoroethylene (ePTFE) membranes are the “gold standard” for GTR/GBR applications. However, they are non-resorbable and they need a second surgical operation to repair dehiscence. Although membranes based on biodegradable synthetic polymers avoid a second surgical operation, they show drawbacks concerning their capacity of space maintenance, early/late absorption, mechanical properties and bacterial infection during degradation. On the other hand, collagen membranes have advantages related to biological properties of collagen itself but are characterized by low mechanical strength. Thus, the “ideal” membrane for use in periodontal regenerative therapy has yet to be developed.

The main purpose of this thesis was the design of biologically active products, with improved osteoconductive and antimicrobial properties, for GTR/GBR applications in periodontal diseases.

In a more traditional approach, a commercially available membrane (based on PTFE) was surface modified by environmentally friendly technique to tailor the surface properties, allowing rapid bone re-growth and exerting antimicrobial action. Binding ability of 3,4-dihydroxy-DL-phenylalanine (DOPA) to samples of any type, size and shape was exploited to improve PTFE film surface properties. In particular, a hydroxyapatite nanoparticles (HAp) coating was applied by DOPA polymerization on PTFE membrane surface in the presence of HAp nanoparticles, with the aim to promote the bone re-growth properties of PTFE membranes. Chemical composition analysis by XPS and FTIR-ATR analyses demonstrated the successful deposition of polyDOPA and HAp on PTFE coated with a combination of DOPA and HAp. Morphological and topographical characterizations further

confirmed the total surface coverage of the substrates by the coatings causing an increase in surface roughness ( $39.8 \pm 5.2$  nm for PTFE films vs  $236.5 \pm 12.0$  nm for polyDOPA/HAp coated films) and wettability ( $110.8 \pm 2.8^\circ$  for PTFE films vs  $46.1 \pm 12.4^\circ$  for polyDOPA/HAp coated samples). The coating stability was also studied by incubating coated PTFE films in PBS: the HAp coating was still present after 14 days of incubation, with a reduced surface roughness and an unchanged hydrophilicity. Finally, MC3T3-E1 pre-osteoblastic cells cultured on polyDOPA/HAp coated films showed a pronounced increase of cell proliferation and cellular adhesion.

Regarding the antimicrobial action, silver nanoparticles (AgNPs) have been selected as antimicrobial agents due to their good antimicrobial efficacy against bacteria, viruses and other eukaryotic micro-organisms. The successful deposition of AgNPs on PTFE film surface, through the functional groups of DOPA, has been demonstrated by physico-chemical and morphological analyses. Nanoparticles exhibited a diameter around 68 nm and were homogeneously distributed on the surface, with only some agglomerates. *In vitro* cell tests with fibroblast NIH 3T3 cells showed an inhibition of cells proliferation on PTFE films functionalized with AgNPs after 3 days of culture, while good cell adhesion was observed with cells randomly distributed on sample surface and extensively spread. Finally, the antimicrobial efficiency was demonstrated against *Staphylococcus aureus* (*S. aureus*) and Ag release was sustained for at least 14 days. These findings suggested that the mussel-inspired coated PTFE membrane could find potential application as GTR/GBR strategy for the treatment of periodontal diseases.

In a highly innovative approach, a bi-layered bioabsorbable membrane was developed, by the assembly of a compact and a porous layer. The rationale of having a periodontal membrane with a multi-component structure relies on the idea that GTR/GBR membranes can be considered an interface-implant between gingival connective tissue/epithelium and alveolar bone tissue. Thus, developing a multi-component structure membrane with compositional and structural gradients that meet the local functional requirements could represent a challenge. The multifunctional membranes represent the next generation of GTR/GBR membranes for periodontal tissue engineering.

Binary blends of poly(DL-lactide-co- $\epsilon$ -caprolactone) (PLCL) and poly(DL-lactide-co-glycolide) (PLGA) with various compositions (100/0, 75/25, 50/50, 25/75, 0/100 wt/wt) were prepared by solvent casting technique as compact layer of the bi-layered membrane. Morphological analysis of fractured sections of PLCL/PLGA blend films did not evidence phase separation between blend components and the behavior of blend glass transition

temperatures as a function of composition suggested some degree of blend compatibility. On the other hand, the elastic modulus of PLCL/PLGA blends showed a negative deviation from the additive law of mixture. *In vitro* cell tests with fibroblast NIH 3T3 cells showed improved cell adhesion and growth on PLCL/PLGA 25/75 blend. Thus, due to its biocompatibility, its superior mechanical properties ( $E = 10.2 \pm 0.6$  MPa,  $\sigma_{\max} = 0.8 \pm 0.0$  MPa, and  $\epsilon_{\max} = 548.8 \pm 57.9\%$ ) and compatibility between the components, PLCL/PLGA 25/75 blend was selected for this application. Compact films were then surface modified via layer-by-layer (LbL) technique to enhance fibroblast cell response and confer antibacterial efficacy. A surface priming treatment was applied and optimized before depositing LbL coating. PLCL/PLGA 25/75 films were pre-functionalized through aminolysis by using the following parameters:  $C = 0.08$  g/mL,  $t = 8$  min and  $T = 37$  °C. Then, multilayered chondroitin sulfate/chitosan (CHS/CH) coatings were deposited on the aminolysed films. The feasibility of multilayer coating was confirmed by QCM-D analysis. Further confirmations of LbL build up on blend films derived from water contact angle measurements, which showed that the contact angle jumped alternatively between 45° and 65° depending on the outmost layer component. FTIR-ATR analysis evidenced the appearance of absorbance peaks characteristics of CHS and CH, namely a broad peak between 3600  $\text{cm}^{-1}$  and 3200  $\text{cm}^{-1}$  attributed to the stretching vibrations of the N-H/O-H, a wide band in the 1650-1600  $\text{cm}^{-1}$  region associated to amide I stretching vibration, and a peak at around 1550  $\text{cm}^{-1}$  arised from amide II bending vibration. FTIC-labelled CH was also employed to follow LbL built up by fluorescence microscopy analysis. *In vitro* cell tests demonstrated the ability of coated samples to improve NIH 3T3 fibroblast adhesion and proliferation. Biocompatibility properties increased with increasing the layer number and were superior in the case of CH-terminating layers. However, no antibacterial activity was observed for films coated with 16 layers.

Three dimensional sponge-like composite membranes fabricated by freeze-drying, with a similar composition to that of natural bone, and based on  $\beta$ -tricalcium phosphate (TCP) dispersed in a chitosan/gelatin (CH/G) network cross-linked with genipin (GP) and disodium phosphate salt (DSP) were developed as porous layer of the bi-layered device. Three kinds of membranes were developed (CH/G, CH/G+GP-DSP and CH/G/TCP+GP-DSP) and characterized in terms of their cross-linking degree (Kaiser test), morphology (SEM analysis), chemical structure (EDS and FTIR-ATR analyses), thermal stability (TGA analysis), tensile mechanical behavior, stability in water (water absorption and dissolution tests), and biological response by *in vitro* cell tests using MG-63 human osteoblast-like

cells. Successful double cross-linking of CH/G network was confirmed by the performed characterizations. All membranes showed a typical foam-like morphology with interconnected pores having an average diameter of 100-200  $\mu\text{m}$ . Both cross-linking and TCP presence caused a marked increase of membrane stability in water solution, as well as of tensile modulus and maximum tensile strength (respectively,  $14.9 \pm 5.1$  MPa and  $0.6 \pm 0.0$  MPa for CH/G, and  $29.4 \pm 2.7$  MPa and  $0.8 \pm 0.1$  MPa for CH/G/TCP+GP-DSP.). In addition, compared to uncross-linked samples, CH/G+GP-DSP and CH/G/TCP+GP-DSP membranes showed improved cell response, in terms of cell viability and morphology. Finally, the assembly process of the compact and porous layer was developed based on the insertion of an intermediate adhesive layer composed by a polyvinylpyrrolidone/polyethylene glycol (PVP/PEG) 70/30 (wt/wt) blend. Preliminary characterizations of the bi-layered membrane were carried out. Morphological analysis did not show changes in compact and porous layer structure due to the presence of PVP/PEG 70/30 adhesive. The final device showed an elastic modulus of about 61 MPa in dry condition that markedly decreased in wet state (to about 5 MPa). Finally, qualitative analysis of membrane manageability revealed its ability to adapt to mandible conformation after immersion in physiological solution. Despite the need for additional tests, the bi-layered membrane appeared promising for GTR/GBR applications.

# Introduction to the Thesis Format

This thesis is divided in **IV sections**, containing globally 8 chapters (six of them describing the experimental work performed): the content of each section is summarized below.

**Section I** (Chapter 1) gives an overview of the current state of the art on guided tissue/bone regeneration membranes for periodontal applications, focusing on all the scientific and technological aspects which have been demonstrated to be crucial for a successful approach within this field, as well as some brief insights on future trends.

**Section II** describes the preparation and characterization of non-absorbable polytetrafluoroethylene membranes, surface modified with hydroxyapatite (Chapter 2) and silver nanoparticles (Chapter 3). The main aim of this part of the work was to prepare membranes with enhanced bioactivity, by the addition of inorganic phase, and antimicrobial activity, by the addition of silver.

Chapter 2 is focused on the development and characterizations of non-degradable polytetrafluoroethylene membranes coated with bioactive hydroxyapatite by an environmentally friendly technique, with the aim to tailor the surface properties, allowing rapid bone re-growth.

Chapter 3 is focused on the preparation and characterization of an antimicrobial coating on polytetrafluoroethylene membrane, in order to eliminate pathogens in the treated site. Silver nanoparticles have been selected as antimicrobial agents due to their good antimicrobial efficacy against bacteria, viruses and other eukaryotic micro-organisms.

**Section III** describes the preparation and characterization of an innovative bi-layered absorbable membrane (Chapter 7), based on a compact (Chapter 4 and 5) and a porous layer (Chapter 6).

Chapter 4 is focused on the preparation and characterization of different compositions of poly(DL-lactide-co- $\epsilon$ -caprolactone)/poly(DL-lactide-co-glycolide) blends with the aim to select the one with the best mechanical behavior and biocompatibility for the perspective application.

Chapter 5 is focused on the preparation and characterization of nanostructured coating via the Layer-by-Layer technique on the previously blend substrate selected, with the aim to improve cell response and antimicrobial activity. A surface priming functionalization method was also studied.

Chapter 6 is focused on the preparation and characterization of sponge-like membranes by the freeze-drying method, having a similar composition to that of natural bone and containing bioactive  $\beta$ -tricalcium phosphate, able to stimulate biomineralisation. The organic phase is based on gelatin and chitosan. The scaffolds are fully characterized in their physiochemical, structural, mechanical and biological properties.

Chapter 7 is focused on the development of the assembly method for the compact and porous layers, previously developed. A biomedical glue based on polyvinylpyrrolidone and polyethylene glycol blend was selected and preliminary characterizations were performed on the final bi-layered membrane.

**Section IV** (Chapter 8) presents the main achievements of the experimental work developed within the scope of the present thesis drawing the general conclusions and indication for future work.

# List of Abbreviations

## A

**AFM** Atomic Force Microscopy

**Ag** Silver

**AgNPs** Silver nanoparticles

**AgNO<sub>3</sub>** Silver Nitrate

**ALP** Alkaline Phosphatase

**ATR-FTIR** Attenuated Total Reflection Fourier Transform Infrared Spectroscopy

## B

**Blend PLCL/PLGA 25/75 (wt/wt)** blend

**Blend-*n*L** Blend film coated with *n* layers

**Blend-NH<sub>2</sub>** Aminolyzed Blend film

**BMP** Bone Morphogenetic Protein

## C

**CAL** Clinical Attachment Level

**CaP** Calcium Phosphate

**CH** Chitosan

**CH/G** Uncross-linked polymeric blend based on CH and G

**CH/G+GP-DSP** Polymeric blend based on CH and G, cross-linked with GP and DSP

**CH/G/TCP+GP-DSP** Composite blend of CH, G and TCP, cross-linked with GP and DSP

**CHS** Chondroitin sulfate A sodium salt

**COL** Collagen

**CX** Chlorhexidine

## D

**DFDBA** Demineralized Freeze-Dried Bone Allografts

**DOPA** 3,4-dihydroxy-DL-phenylalanine

**Dopamine** 3,4-dihydroxyphenethylamine

**dPTFE** High-density Polytetrafluoroethylene

**DS** Dextran Sulfate

**DSC** Differential Scanning Calorimetry

**DSP** Dibasic sodium phosphate

## **E**

**E** Young's modulus

**ECM** Extracellular Matrix

**E. coli** Escherichia coli

**EDC** 1-ethyl-3-(3-dimethylaminopropyl) carbodiimide

**EDTA** Ethylenediaminetetraacetic Acid

**ePTFE** Expanded Polytetrafluoroethylene

## **F**

**FDBA** Freeze-Dried Bone Allografts

**FFB** Fresh Frozen Bone

**FGF** Fibroblast Growth Factor

**FITC-CH** Fluorescein isothiocyanate conjugated-CH

**FTIR-ATR** Fourier Transform Infrared Spectroscopy

## **G**

**G** Gelatin

**GAG** Glycosaminoglycan

**GBR** Guided Bone Regeneration

**GNP** Gold Nanoparticles

**GP** Genipin

**GPC** Gel Permeation Chromatography

**GS** Gentamicin Sulfate

**GTR** Guided Tissue Regeneration

## **H**

**HAp** Hydroxyapatite

**HE** Heparin

**HIV-1** Human Immunodeficiency Virus type 1

**hMSC** Human Mesenchymal Stem Cell

**HYA** Hyaluronic Acid

## **I**

**IGF** Insulin-like Growth Factor

## **L**

**LbL** Layer-by-layer

**Lys** Lysozyme

## **M**

**MAP** Mussel Adhesive Protein

**Mefp** *Mytilus edulis* foot protein

**MET** Metronidazole benzoate

**M<sub>w</sub>** Molecular weight

## **N**

**NaBH<sub>4</sub>** Sodium Borohydride

**nBGC** Nano Bioactive Glass Ceramic

**nCHAC** Nano-carbonated Hydroxyapatite/Collagen

**n-HAp** Nano-hydroxyapatite

**NMR** Nuclear Magnetic Resonance

## **P**

**PAA** Poly(acrylic acid)

**PAH** Poly(allylamine hydrochloride)

**PBS** Phosphate Buffer Salin

**PCL** Poly( $\epsilon$ -caprolactone)

**PDDA** Poly(diallyldimethylammonium chloride)

**PDGF** Platelet-Derived Growth Factor

**PDLLA** Poly(DL-lactic acid)

**PE** Polyelectrolyte

**PEG** Poly(ethylene glycol)

**PEI** Polyethylenimine

**PEM** Polyelectrolyte Multilayers

**PES** Polyethersulfone

**PGA** Polyglycolic Acid

**P. gingivalis** Porphyromonas gingivalis

**PHMB** Polyhexamethylene Biguanide

**PHGH** Polyhexamethylene Guanidine Hydrochloride

**PI** Polydispersity index

**PLA** Polylactic Acid

**PLCL** Poly(D,L-lactide-co- $\epsilon$ -caprolactone)  
**PLCL/PLGA 25/75** Binary blend formed by 25% of PLCL and 75% of PLGA  
**PLCL/PLGA 50/50** Binary blend formed by 50% of PLCL and 50% of PLGA  
**PLCL/PLGA 75/25** Binary blend formed by 75% of PLCL and 25% of PLGA  
**PLGA** Poly(D,L-lactide-co-glycolide)  
**PLGC** Poly(L-lactide-co-glycolide-co- $\epsilon$ -caprolactone)  
**PLL** Poly(lysine)  
**PLLA** Poly(L-lactic acid)  
**PolyDOPA** Self-polymerized DOPA  
**PolyDopamine** Self-polymerized Dopamine  
**PSS** Poly(4-sodium styrene sulfonate)  
**PTFE** Polytetrafluoroethylene  
**PTFE-Ag** Polytetrafluoroethylene coated with Ag nanoparticles  
**PTFE-DOPA** Polytetrafluoroethylene coated with DOPA  
**PTFE-DOPA-Ag** Polytetrafluoroethylene coated with DOPA and Ag nanoparticles  
**PTFE-DOPA-HAp** Polytetrafluoroethylene coated with DOPA and HAp  
**PTFE-HAp** Polytetrafluoroethylene coated with HAp  
**PVDF** Poly(vinylidene fluoride)  
**PVP** Poly(vinyl pyrrolidone)  
**PVP/PEG 80/20** Binary blend formed by 80% of PVP and 20% of PEG  
**PVP/PEG 70/30** Binary blend formed by 70% of PVP and 30% of PEG  
**PVP/PEG 60/40** Binary blend formed by 60% of PVP and 40% of PEG  
**PVPh** Poly(4-vinylphenol)

## Q

**QCM-D** Quartz Crystal Microbalance, relate vibration Dissipation

## S

**S. aureus** Staphylococcus aureus

**SBF** Simulated Body Fluid

**SEM** Scanning Electron Microscope

## T

**TA** Terephthalaldehyde

**TCP**  $\beta$ -Tricalcium Phosphate

**TE** Tissue Engineering

**T<sub>g</sub>** Glass transition temperature

**TGA** Thermogravimetric analysis

**TGF-β** Transforming Growth Factor-β

**THF** Tetrahydrofuran

**Ti** Titanium

**Ti-ePTFE** Titanium-reinforced polytetrafluoroethylene

**Ti-mesh** Titanium mesh

**W**

**WA** Water absorption

**X**

**XPS** X-ray Photoelectron Spectroscopy

# SECTION I



# Guided Tissue Regeneration membranes for periodontal applications: State of the Art and future trends

---

## 1.1 Introduction

The aging population is one of the main reasons we need to advance the understanding of dental biomaterials. The progressive aging of population will cause an increase in the number of surgical and restorative procedures related to either oral rehabilitation, with the placement of dental implants and ceramic crowns, or to periodontal regeneration, which often requires the use of membranes for guided tissue regeneration (GTR) and grafting materials.

Periodontitis is one of the most destructive pathologies that affect the integrity of the periodontal system and lead to damage of the periodontal tissues and, ultimately, tooth loss [1]. The development of periodontal disease is affected by individual conditions, such as life-style and genetics. It often starts in middle age and its incidence increases with age and is accelerated by systemic disorders such as diabetes, osteoporosis, cardiovascular and respiratory disease, and metabolic deficiencies. Data from the National Institute of Dental and Craniofacial Research (NIDCR, National Institutes of Health, United States) have revealed that nearly 90% of the adult population more than 70 years old present at least a moderate level of periodontal-related diseases [1, 2].

Clinical and/or surgical intervention is needed to reestablish healthy periodontal tissues. During the last decade, various regenerative surgical procedures have been proposed and examined for the regeneration of those part of the tooth-supporting apparatus which have been lost due to periodontitis, including alveolar bone, cementum, periodontal ligament and gingival. These

treatments have encompassed the utilization of a wide variety of surgical approaches, barrier membranes, a series of bone grafts and other osteoconductive/inductive materials or protein mixtures, exogenous growth factors, cell-based technologies and genes from recombinant technology. Among these approaches, periodontal tissues regeneration has achieved a significant success following the use of GTR strategies. Nonetheless, results are variable and reliant on patient age, defect size, and other demographic and lifestyle effects [3, 4].

GTR was first developed in the early 1980s by Nyman and Karring with the aim to regenerate lost periodontal tissues [5]. GTR is based on the concept that specific cells contribute to the formation of the different specific tissues. Melcher described selective cell repopulation of defects as a tool to enhance healing [6]. Exclusion of fast-growing epithelium and connective tissue from a periodontal wound for 6-8 weeks allows cells of the slower growing tissues, including osteoblasts, cementoblasts, and periodontal ligament cells, to fill the space adjacent to the tooth.

Soon, GTR found applications in other areas, including the regeneration of bone tissue. The term guided bone regeneration (GBR) was introduced as a corollary of GTR by Nyman and Gottlow, who applied occlusive barriers in periodontal healing studies to stop the cell migration from gingival connective tissue and epithelium to the periodontal defect, which can interfere with tissue regeneration. Subsequently, Buser et al. [7] introduced the principle of GBR, applied in clinical dentistry to promote bone regeneration using a barrier membrane allowing the repopulation of the osseous wound space. Since then, membrane barriers and bone grafting materials in GBR technique have been extensively investigated in periodontal regenerative medicine and dental implant therapies to enhance new bone formation for the placement of implants [8, 9].

## **1.2 Anatomy of the periodontium**

The periodontium (pert = around, odontos = tooth) is an intricate system comprising the following tissues (Fig. 1.1): (1) the dentogingival junction (part of the gingival facing the tooth), (2) the periodontal ligament, (3) the root cementum, and (4) the alveolar bone (bone lining the tooth socket).

The main function of the periodontium is to attach the tooth to the bone tissue of both mandible and maxilla and preserve their position, and to maintain the integrity of the surface of the masticatory mucosa of the oral cavity [10]. Additionally, it assures proper function and dissipation forces, preventing injury to teeth, mandible, and maxilla [11].

The periodontium, also called “the attachment apparatus” or “the supporting tissue of the teeth”, constitutes a development, biologic, and functional unit which undergoes certain changes with age and is, in addition, subjected to morphologic changes related to functional alterations and modifications in the oral environment. It is important to understand that each of the periodontal components has its highly specialized structure which directly defines its function. Indeed, proper functioning of the periodontium is only achieved through structural integrity and interaction between its components [12].

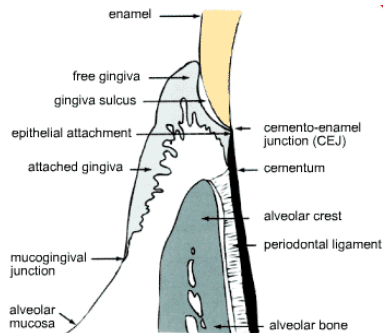


**Fig. 1.1** Schematic illustration showing a longitudinal section through dento-gingival part of a tooth and its periodontal tissue apparatus.

### 1.2.1 Dentogingival junction

The dentogingival junction is an adaptation of the oral mucosa that consists of an epithelial layer and an underlying connective tissue layer. The epithelium may be differentiated as follows:

- oral epithelium, which faces the oral cavity;
- oral sulcular epithelium, which faces the tooth without being in contact with the tooth surface;
- junctional epithelium, which provides the contact between the gingiva and the tooth.

The connective tissue, called lamina propria, is the predominant tissue component of the dentogingival junction and is divided into superficial and deep compartments. The major components of the connective tissue are collagen fibers (around 60% of connective tissue volume), fibroblasts (around 5%), vessels and nerves (around 35%) which are embedded in an amorphous ground substance (matrix).

The junctional epithelium plays a crucial role since it essentially seals off periodontal tissues from the oral environment. Its integrity is thus essential for maintaining a healthy periodontium. Periodontal disease sets in when the structure of the junctional epithelium starts to fail, an excellent example of how structure determines function [10, 12].

### 1.2.2 Cementum

The cementum is a specialized mineralized tissue covering the root of teeth. It has many features in common with bone tissue. However, the cementum contains no blood or lymph vessels, has no innervations, does not undergo physiologic resorption or remodeling, but is characterized by continuing deposition throughout life. Like other mineralized tissues, it contains collagen fibers embedded in an organic matrix. Its mineral content, mainly consisting of hydroxyapatite (HAp), is about 65% by weight, slightly higher than that of bone (60%).

Cementum has different functions: it attaches the periodontal ligament fibers to the root and it contributes to the process of repair after damage to the root surface [10]. Three types of cementum exist, distinguished on the basis of the presence or absence of cells and the origin of the collagen fibers of the matrix. Acellular extrinsic fiber cementum (primary cementum or acellular cementum) is found in the coronal and middle portions of the root; its thickness is around 10  $\mu\text{m}$ . It develops very slowly and is defined acellular because cells are only found on its surface. The presence of an elevated number of main periodontal ligament fibers attached to the acellular cementum (where they are called Sharpey's fibers) underlines its important role in tooth attachment to the alveolar bone. The overall degree of mineralization of acellular cementum is about 45–60%: the innermost layer is the less mineralized while the outer layers are characterized by the presence of alternating bands with high and low mineral content that run parallel to the root surface.

Cellular intrinsic fiber cementum (secondary cementum or cellular cementum) is distributed along the apical third or half of the root and in furcation areas; it can grow up to 100  $\mu\text{m}$  or more. As cellular intrinsic fiber cementum is also produced as a repair tissue that fills resorptive defects and root fractures, it may also be found further coronally. Collagen produced by cementoblasts (intrinsic collagen fibers) and the presence of cementoblasts entrapped in lacunae within the matrix they produce (cementocytes) are the characteristic features of cellular intrinsic fiber cementum. The heterogeneous collagen organization, its rapid speed of formation, and the presence of cells and lacunae may be the reason why this cementum variety is less mineralized than acellular extrinsic fiber cementum.

Cellular intrinsic fiber cementum constitutes the intrinsic component of cellular mixed stratified cementum, which possesses a stratification that is derived from consecutively deposited, alternating layers of acellular extrinsic fiber cementum and cellular intrinsic fiber cementum. Cellular mixed stratified cementum is always present in human teeth and it may serve as a means to adjust the tooth position to new requirements [12].

### **1.2.3 Periodontal ligament**

The periodontal ligament is the soft, richly vascular and cellular connective tissue situated between the cementum covering the root of the tooth and the bone forming the socket wall. Similar to all other connective tissues, the periodontal ligament consists of cells and an extracellular compartment comprising collagenous and non-collagenous matrix constituents. The cells include osteoblasts and osteoclasts, fibroblasts, epithelial cells, monocytes and macrophages, undifferentiated mesenchymal cells, and cementoblasts and odontoclasts. The extracellular compartment consists mainly of well-defined collagen fiber bundles embedded in an amorphous background material, known as ground substance. The width of the periodontal ligament is approximately 0.25 mm and it maintains its width more or less over time.

The presence of a periodontal ligament permits forces, elicited during masticatory function and other tooth contacts, to be distributed to and resorbed by the alveolar bone. The periodontal ligament is also essential for the mobility of the teeth, which is determined to a large extent by the width, height, and quality of the periodontal ligament. Importantly, it is a cell reservoir for tissue homeostasis and repair/regeneration.

Finally, the periodontal ligament has the capacity to adapt to functional changes. When the functional demand increases, the width of the periodontal ligament can increase by as much as 50%, and the fiber bundles also increase markedly in thickness. Conversely, a reduction in function leads to narrowing of the ligament and a decrease in number and thickness of the fiber bundles. These functional modifications of the periodontal ligament also implicate corresponding adaptive changes in the bordering cementum and alveolar bone [12].

### **1.2.4 Alveolar bone**

The alveolar process is defined as the parts of the maxilla and mandible that form and support the sockets of the teeth. It consists of outer cortical plates (buccal, lingual, and palatal) of compact bone, a central spongiosa, and bone lining the alveolus (alveolar bone). The cortical plate and bone lining the alveolus meet at the alveolar crest.

The cortical plates consist of surface layers (lamellae) of fine-fibered bone supported by Haversian systems. They are generally thinner in the maxilla and thickest on the buccal aspect of mandibular premolars and molars. The trabecular (or spongy) bone occupying the central part of the alveolar process also consists of bone disposed in lamellae, with Haversian systems present in the larger trabeculae. Yellow marrow, rich in adipose cells, generally fills the intertrabecular spaces, although sometimes there can also be some red or hematopoietic

marrow. Trabecular bone is absent in the region of the anterior teeth and, in this case, the cortical plate and alveolar bone are fused together [12].

Together with the root cementum and the periodontal membrane, the alveolar bone constitutes the attachment apparatus of the teeth, the main function of which is to distribute and resorb forces generated by mastication and tooth contacts [10]. Because the tooth is constantly making minor movements and alveolar bone must respond to the functional demand placed on it by the forces of mastication, the bone of the socket wall is constantly remodeled and its structural organization varies along the wall [13]. The organization of the alveolar process is yet another example of structure-function relationship in the periodontium.

Whereas the overall formation and regulatory events in alveolar bone are the same as at other anatomical sites, alveolar bone is distinctive because it turns over very rapidly and it is lost in the absence of a tooth. These two characteristics suggest that local regulatory mechanisms are particularly important in the case of alveolar bone. They also clearly demonstrate the interdependence of the periodontal tissues and underlines the important fact that the periodontal tissues function together as a unit [12].

The remodeling process of alveolar bone is essentially similar to that of bone in general [13]. However, resorption is asynchronous, so that periodontal ligament attachment is lost only focally and for short periods of time. During tooth migration, the distribution of force is such that bone lost by resorption on one surface of the tooth socket is balanced by bone formation along the opposite surface. This bone balance together with the continued deposition of cementum throughout life act to maintain a more or less constant relationship between the root surface and that of the alveolar socket.

### **1.3 Periodontal diseases**

The performance of the periodontium depends upon its structural integrity and interactions among its components [12]. Periodontal disease can progressively destroy the periodontium, ultimately resulting in tooth loss.

The term periodontal disease usually refers to the common inflammatory disorders of gingivitis and periodontitis that are caused by pathogenic microflora in the biofilm or dental plaque that forms adjacent to the teeth on a daily basis [14]. In 1999, the International Workshop for a Classification of Periodontal Diseases and Conditions classified the periodontal diseases in eight main categories [15]:

- I. Gingival diseases
- II. Chronic periodontitis

- III. Aggressive periodontitis
- IV. Periodontitis as a manifestation of systemic diseases
- V. Necrotizing periodontal diseases
- VI. Abscesses of the periodontium
- VII. Periodontitis associated with endodontic lesions
- VIII. Developmental or acquired deformities and conditions.

Gingivitis, the mildest form of periodontal disease, is caused by the bacterial biofilm (dental plaque) that accumulates on teeth adjacent to the gingival (gums). However, gingivitis does not affect the underlying supporting structures of the teeth and is reversible [14]. On the contrary, inflammation that extends deeper into the tissue and causes loss of supporting connective tissue and alveolar bone is known as periodontitis. It results in the formation of soft tissue pockets or deepened crevices between the gingival and tooth root, and, with time, in tooth mobility, drifting, and ultimately tooth loss. Severe periodontitis can result in considerable loss of function of the dentition, occasional pain and discomfort, and in aesthetic problems [1, 16].

Gingivitis and periodontitis are infectious diseases that afflict a high percentage of the population, even at younger ages. In its FY2003 Fact Sheet, the American Association for Dental Research reports that 48% of adults aged 35–44 years have inflammation of the gingiva (gingivitis), and 22% destructive periodontal disease, a major cause of tooth loss. In addition, evidence has been mounting that chronic periodontal diseases are linked with major systemic diseases, such as cardiovascular and pulmonary diseases [17, 18]. Although bacteria are essential for periodontitis to develop, the fact that it develops to variable degrees in different individuals suggests a multifactorial etiology. All forms of periodontitis, however, appear to have a common series of underlying events leading to tissue breakdown and tooth attachment loss.

Bacteria are necessary for periodontal disease to take place but a susceptible host is also needed. The immune-inflammatory response that develops in the gingival and periodontal tissues in response to the chronic presence of plaque bacteria results in destruction of structural components of the periodontium leading, ultimately, to clinical signs of periodontitis. An individual's risk for periodontal disease could be linked to gingival inflammation in response to plaque accumulation [19]. The host response is essentially protective, but both hypo-responsiveness and hyper-responsiveness of certain pathways can result in enhanced tissue destruction [20].

Both the host and bacteria in the periodontal biofilm release proteolytic enzymes that damage tissue. They release chemotactic factors that recruit polymorphonuclear leucocytes into the

tissues; if sustained, these cells release various enzymes that break down tissues. Hundreds or even thousands of microbial antigens evoke both humoral antibody-mediated and cell-mediated immune responses. These responses are usually protective, but a sustained microbial challenge in the presence of the risk factors (i.e., smoking, genetic polymorphisms, diabetes) results in the breakdown of both soft and hard tissues, mediated by cytokine and prostanoid cascades [1]. Once a periodontal pocket forms and becomes filled with bacteria, the situation becomes largely irreversible. Gingival epithelium proliferates to line the pocket and even if treatment resolves the inflammation and some bone and connective tissue are regenerated, complete restoration of the lost tooth support is impossible. Without adequate treatment, active periodontitis leads to tooth loss.

As mentioned before, different factors contribute to the cause of periodontal diseases.

#### 1) Oral microorganisms

The mouth, like all external surfaces of the body and the gut, has a substantial microflora living in symbiosis with a healthy host. The microflora of the mouth contains over 500 different species of aerobic and anaerobic bacteria and the junctional epithelium provides a very efficient barrier against periodontal pathogens and their products. These organisms grow on tooth surfaces as complex, mixed, interdependent colonies in biofilms, and are attached and densely packed against the tooth [21]. As dental plaque matures to a state that is associated with periodontal disease, the number of gram-negative and anaerobic bacteria increases [22]. Bacterial counts above the gums (supragingival) on one tooth surface can exceed  $1 \cdot 10^9$  bacteria. Below the gum, the number of bacteria ranges from  $1 \cdot 10^3$  in a healthy shallow crevice to more than  $1 \cdot 10^8$  in a periodontal pocket [23]. Certain clusters of bacterial species commonly cohabit subgingival sites and are reproducibly associated with disease. These putative pathogens include *Porphyromonas gingivalis*, *Tannerella forsythensis*, and the spirochaete *Treponema denticola*. Infection of periodontal tissues with these and other organisms is accompanied by the release of bacterial leucotoxins, collagenases, fibrinolysins, and other proteases [24]. *Actinobacillus actinomycetemcomitans* is another species commonly associated with disease, especially in young adults [25].

#### 2) Genetics

Rare syndromes affecting phagocytes, the structure of the epithelia, connective tissue, or teeth, could have severe periodontal manifestations. Haim-Munk and Papillon-Lefèvre syndromes are rare autosomal recessive disorders associated with periodontitis onset at childhood and early loss of both deciduous and permanent teeth. Other disorders that have severe periodontal

manifestations include Chédiak-Higashi, Ehlers-Danlos (types 4 and 8), Kindlers, and Cohen syndromes [1].

### 3) Tobacco and alcohol use

Oral smokeless tobacco can lead to gingivitis, loss of tooth support, and precancerous gingival leucoplakia at the site of quid placement [26]. The risk of periodontal disease in long-term smokers is equal to that of lung cancer, and smoking has a strong negative effect in response to periodontal treatment and other oral surgical interventions [27]. By contrast with tobacco use, a small but significant association exists between alcohol consumption and loss of periodontal support [28].

### 4) Nutrition

Historically, specific, overt nutritional deficiencies have been associated with periodontal disease. Vitamin C deficiency leads to scurvy with decreased formation and maintenance of collagen, increased periodontal inflammation, hemorrhage, and tooth loss [29].

### 5) Diabetes

People with type 1 diabetes at all ages and adults with type 2 diabetes have more widespread or severe periodontal disease than individuals without diabetes. Although people with well-controlled diabetes do not seem to be at increased risk of periodontal disease respect to people without diabetes, those with poorly controlled diabetes are at raised risk for periodontitis and progressive bone loss [30]. Diabetes is associated with impaired wound healing, exaggerated monocyte response to dental plaque antigens, and impaired neutrophil chemotactic responses, all of which can lead to increased local tissue destruction [31, 32].

### 6) Impaired host response

As an inflammatory disease, severe periodontal disease and loss of tooth-supporting tissues often occur if the individual's host response or immune function is impaired. Various systemic diseases such as leukaemia, thrombocytopenia, and leucocyte disorders such as agranulocytosis, cyclic neutropenia, and leucocyte adhesion deficiency could be associated with increased severity of periodontal disease [1].

Gingival recession is another periodontal problem that affects millions of people worldwide [33]. It is a multifactorial condition (i.e., periodontal disease, trauma, gender, and tobacco consumption) found primarily in adult patients regardless of oral hygiene [34, 35]. It is a result of apical migration of the gingival margin that leads to root surface exposure [35].

## 1.4 Prevention and treatment of periodontal diseases

Prevention of gingivitis and periodontitis is based on the control of their causal and risk factors. The most widely accepted risk factor is the periodontal biofilm that forms on the teeth in the absence of effective oral hygiene [1].

Tooth brushing and the use of dental floss and other devices to remove plaque from the teeth are the most common ways of disrupting or removing the periodontal biofilm from teeth. Although these methods are effective if used every day, they require motivation and dexterity. Mouthwashes and dentifrices containing antibacterial drugs have been used as adjuncts for controlling the biofilm. These combinations contain various biocides, surfactants, polymers, or other components that can reduce the biofilm and are generally not associated with the emergence of a resistant microbiota [36].

After all oral hygiene procedures are ceased, the biofilm begins to develop on the teeth within 24 h and causes gingivitis in 10–21 days. Thorough tooth cleaning returns the gingiva to a healthy condition in about 1 week [37]. Control of the periodontal biofilm with professionally administered oral hygiene can slow or stop periodontitis and tooth loss for many years [38].

Treatment for gingivitis and periodontitis should establish periodontal health, arrest the progression of disease, prevent recurrence of disease, and preserve the dentition in a state of health, comfort, and function. This goal can be accomplished by various non-surgical and surgical therapies, depending on the specific treatment objective [1]: for patients with early or moderate disease, non-surgical treatment is often sufficient; for patients with advanced disease, a variety of types of periodontal surgery can be used.

The different strategies of periodontal therapy aim to (1) reduce and/or eliminate inflamed tissues caused by bacterial plaque, (2) correct defects or anatomical problems due to the disease, and (3) regenerate new periodontal tissues [39, 40].

The cornerstone of periodontal therapy is anti-infective non-surgical treatment aimed at controlling the biofilm and other prominent risk factors. Dental plaque and calculus deposits adherent to the tooth both supra- and subgingivally can be removed by use of various manual or powered instruments [41]. In some cases this non-surgical therapy may also be combined with adjunctive antimicrobial therapy. In addition, long-term outcomes of treatment are dependent on the patient's commitment to maintaining a high standard of regular oral hygiene in order to prevent bacterial recolonization of the affected lesions [16, 42].

This non-surgical therapy can reduce tissue inflammation and pocket depths and improve clinical periodontal attachment. The tissues typically heal by repair, being characterized by

tissue shrinkage, fibrosis, and limited bone remodelling, but without any appreciable coronal regeneration of the lost tissues present [1, 16].

While this treatment may be very effective in preventing future progression of disease and therefore any ultimate tooth loss, there are a number of limitations of this treatment outcome [16].

- 1) The treatment may have very limited impact on the existing mobility of teeth in view of the lack of regeneration of lost tissues.
- 2) The treatment results typically in large amounts of gingival recession, which is both unsightly and may result in increased tooth sensitivity and susceptibility to root caries.
- 3) It is postulated that, without restitution of the original anatomy, the site may be more susceptible to recurrence of disease in the future.

An important long-standing aim of periodontal treatment has been to devise therapeutic interventions that would allow the clinician to regenerate the lost periodontal tissues.

Periodontal regeneration requires the coordinated formation of new alveolar bone, dental cementum, and functionally oriented periodontal ligament interposed between these two tissues.

In this contest, four particular issues are posed [16]:

- 1) the requirement for the coordinated formation of the three tissues of the periodontal ligament;
- 2) the potential role of bacterial contamination during healing;
- 3) the specific requirement for dental cementum formation, a tissue that is not seen in other parts of the body;
- 4) the requirement for coronal regeneration of tissues towards the overlying superficial tissues.

The achievement of predictable periodontal regeneration has proved to be a remarkably elusive goal for clinical periodontists in most clinical circumstances.

## **1.5 Biology of periodontal healing and regeneration**

Previous research on periodontal healing has provided a basic understanding of the mechanisms favoring periodontal tissue regeneration. A number of valuable findings at both the cellular and molecular levels was revealed and subsequently used to engineer the regenerative biomaterials currently available in periodontal medicine [43]. The rationale to consider when developing biomaterials and devices for periodontal healing and regeneration relies on the fact that, on one side, they will face the bone defect while, on the other side, they will face the gingival connective tissue/epithelium. Therefore, the implants should be designed to meet the local

functional requirements [44]: rapid wound healing and antimicrobial action on the side in contact with gingival tissue and rapid bone re-growth and osteointegration on the side in contact with bone tissue.

### **1.5.1 Gingival wound healing process**

The biology and principles of wound healing in non oral sites, also apply to the healing process that take place following periodontal surgery. The sequence of healing after blood-clot formation is commonly divided into three phases: (1) inflammation, (2) granulation tissue formation, and (3) intercellular matrix formation and remodeling. These stages may overlap considerably and the time needed for completion of each stage may vary, depending on local and systemic factors [45, 46].

Traumatic injury causes capillary damage and hemorrhage and, as a result, a blood clot is formed. It has two functions: it temporarily protects the denuded tissues and it serves as a provisional matrix for cell migration [47]. The blood clot consists of all cellular components of blood (including red and white blood cells and platelets) in a matrix of fibrin, plasma fibronectin, vitronectin, and thrombondin [48].

Within hours of injury, the inflammatory phase of healing initiates with polymorphonuclear leukocytes infiltration into the fibrin clot from the wound margins, followed shortly afterwards by macrophages [49]. The major function of the polymorphonuclear leukocytes is to debride the wound by removing bacterial cells and injured tissue particles through phagocytosis. The macrophages, in addition, have an important role in the initiation of tissue repair. Within 3 days, the inflammatory reaction moves into its late stage as the amount of polymorphonuclear leukocyte infiltrate gradually decreases while the macrophage influx continues. These macrophages contribute to the cleaning process through the phagocytosis of used polymorphonuclear leukocytes and erythrocytes. They release also a number of biologically active molecules, such as inflammatory cytokines and tissue growth factors, which recruit further inflammatory cells as well as fibroblastic and endothelial cells, thus playing an essential role in the transition of the wound from the inflammatory stage to the granulation tissue-formation phase.

The influx of fibroblasts and budding capillaries from the gingival connective tissue and the periodontal ligament connective tissue initiate the phase of granulation-tissue formation in the periodontal wound approximately 2 days after incision. The cell-rich granulation tissue next undergoes maturation and remodeling. Fibroblasts responsible for the replacement of the provisional extracellular matrix produce a new collagen-rich matrix. Approximately 1 week

following wounding, and once the collagen matrix has been synthesized, some fibroblasts undergo transformation into myofibroblasts and express  $\alpha$ -smooth muscle actin. This transformation and synthesis is responsible for wound contraction. Endothelial cells, responsible for angiogenesis, migrate into the provisional wound matrix to form vascular tubes and loops, and as the provisional matrix matures, the endothelial cells undergo programmed cell death (apoptosis) and the number of vascular units is reduced [48, 50].

Maturation of the granulation tissue will lead to the final phase of healing where the reformed, more cell-rich tissue, undergoes maturation and sequenced remodeling to meet functional needs [45, 46].

There has been general observations that wounds in oral sites heal faster and with less scarring than extraoral wounds. It is probable that oral wound healing is enhanced partly because of factors present in the saliva and by the specific microflora of the oral cavity [51]. Generally, the healing of gingival epithelia and their underlying connective tissues concludes in a number of weeks.

### **1.5.2 Bone regeneration process**

Bone possesses the intrinsic capacity for regeneration as part of the repair process in response to injury, as well as during skeletal development or continuous remodeling throughout adult life [52, 53]. Bone regeneration is comprised of a well-orchestrated series of biological events of bone induction and conduction, involving a number of cell types and intracellular and extracellular molecular-signaling pathways, with a definable temporal and spatial sequence, in an effort to optimize repair and restore function [53, 54]. Unlike in other tissues, the majority of bony injuries heal without the formation of scar tissue, and bone is regenerated with its pre-existing properties largely restored, and with the newly formed bone being eventually indistinguishable from the adjacent uninjured bone [53].

Improved knowledge about the biological mechanisms and the temporal dynamics of new bone formation under the conditions of guided regeneration is critical. However, scientists and clinicians considered this knowledge a prerequisite to better understand the healing steps leading to regenerated and fully mature bone in order to be able to beneficially influence healing for further developments in the field and for increased predictability of the clinical outcomes [55].

Bone contains three main bone-specific cell types: osteocytes are mature cells that reside in bone lacunae, communicate with other osteocytes through long cellular processes, sense mechanical stress in bone, and send signals for bone remodeling as a result of mechanical

stress. The responding cells are osteoblasts, cells specialized to secrete the unique collagen-rich extracellular matrix in bone that enables mineralization; and osteoclasts, macrophage-like cells that degrade the bone structure through a combination of localized acidification (removes the minerals) and protease secretion (breaks down matrix). Osteoclasts tunnel through bone and are usually followed close behind by osteoblasts [56].

The type of bone being formed by applying the principle of GTR has been investigated in both animals [57-59] and human studies [60]. In all these experiments, a similar basic pattern of bone formation was observed. Initially, trabeculae of woven bone proliferated into the defect. Then, the bone volume increased with time and the primary intramembraneous trabecular scaffold underwent intense remodeling: numerous osteoclasts arose and began to eliminate the primitive woven bone, whereas a new generation of osteoblasts deposited mature lamellar bone layers on the woven bone remnants. As a consequence of the continuous remodeling of the primary bony network, most of the trabeculae contained only a small, intensely stained core of woven bone surrounded by thick bone layers of regular lamellar texture and thus comprised the secondary spongiosa. The continuous growth of the bone trabeculae resulted in the narrowing of the intertrabecular connective tissue and in the formation of primary osteons containing vascular channels. The presence of osteoid seams with overlying osteoblasts indicated continuation of the osteogenic process. At the defect borders facing the membranes, cortical bone was formed by continuous lamellar bone deposition. Finally, secondary osteons were formed replacing the previously formed cortical bone.

The mechanism of bone healing depends on the size of the defect [55]. In cortical bone, circular defects of less than 200  $\mu\text{m}$  had the potential to heal with concentric formation of lamellar bone [57]. In larger defects of 200 to 500  $\mu\text{m}$ , bone healing was characterized by formation of a trabecular network of woven bone bridging the defect. Subsequently, the spaces between the trabeculae were filled with lamellar bone. In defects of 500  $\mu\text{m}$  and larger, bridging by direct formation of bone did not occur. Following 3 weeks of healing, such defects exhibited a central area characterized by the presence of connective tissue.

## **1.6 Current treatments for clinical periodontal regeneration**

Periodontal regeneration is defined as the regeneration of the tooth-supporting tissues including cementum, periodontal ligament and alveolar bone [61]. A number of different treatments have been developed to promote periodontal regeneration since the mid-1980s; they include bone replacement grafts, root surface biomodifications, cell-occlusive barrier membranes used in GTR/GBR procedures, and delivery of growth factors or gene therapies [62]. All of these

strategies aim to correct defects due to disease, and regenerate new periodontal tissues. In general, however, the clinical outcome of periodontal regenerative techniques depends on (i) patient-associated factors (i.e. plaque control, smoking habits, residual periodontal infection), (ii) effects of occlusal forces that deliver intermittent loads in axial and transverse directions, and (iii) factors associated with the clinical skills of the operator [63]. Consequently, both clinical and preclinical research continues to evaluate advanced regenerative approaches using new barrier membranes [64], cell-growth-stimulating proteins [65, 66] or gene delivery applications [67] in order to simplify and enhance the rebuilding of missing periodontal support.

### **1.6.1 Bone replacement grafts**

Bone replacement grafts remain the most widely used therapeutic strategies for the correction of periodontal osseous defects; they provide demonstrable clinical improvements in periodontal osseous defects compared to surgical debridement alone [68].

Grafts can play a part in the correction of the osseous aspects of periodontal defects either by the process of osteoinduction or by osteoconduction [68, 69]. An osteoinductive material can induce bone formation by recruiting undifferentiated mesenchymal cells and causing them to differentiate into osteoblastic cells. An osteoconductive material acts principally as a scaffolding material for new bone formation to occur.

Four major graft materials commonly used in clinics are autologous grafts, allografts, xenografts, and synthetic grafts or alloplasts. Autogenous bone grafts obtained either from intraoral sites or extraoral sites are thought of as “gold standard” with the ideal properties of grafts. They are a source of autogenous osteogenic cells as well as osteoinductive scaffolds. However, the volume of bone may be limited and the resorption may be unpredictable [70]. The autogenous bone collected during the surgery may also be contaminated by the microorganisms in the oral cavity [71].

To overcome these problems, a range of other bone graft materials have been utilized. Allografts are graft materials derived from a donor of the same species, which may be a fresh frozen bone (FFB), freeze-dried bone allografts (FDBA) or demineralized freeze-dried bone allografts (DFDBA). They can act as osteoconductive scaffolds and osteoinductive materials, due to the remaining proteins [72]. Xenografts are graft materials derived from another species, particularly bovine inorganic freeze-dried bone, widely used as osteoconductive scaffold materials [73]. However, a theoretical risk of disease transmission, such as prion disease in allografts and viral transmission in xenografts, remains.

Alloplastic bone substitute materials eliminate the problem of limited supply of autografts bone and risk of disease transmission from allografts and xenografts. Presently, six basic type of alloplastic materials are commercially available: porous and non-porous HAp, HAp cement,  $\beta$ -tricalcium phosphate (TCP), polymers, and bioactive glasses. While clinical results of using alloplast grafts to treat periodontal disease appear promising, histologically the grafts remain in situ for long time and they are encapsulated by fibrous tissue rather than resulting in true bone formation and periodontal regeneration [74, 75]. Moreover, in clinical use, these materials appear to act largely as biocompatible space.

### **1.6.2 Biomodification of the tooth-root surface**

A number of studies have focused on the modification of the periodontitis-involved root surface in order to advance the formation of a new connective tissue attachment. Root surface demineralization with citric acid has been used as a part of regenerative procedure. Citric acid is able to modify the root surface by “detoxifying” the surface and exposing collagen fibrils within the cementum or dentin matrix [76, 77]. Despite histological evidence of regeneration following root-surface biomodification with citric acid, the outcomes of controlled clinical trials have failed to show any improvements in clinical conditions compared with nonacid-treated controls [78, 79].

More recent studies [80, 81] indicate that the use of materials with less acidic pH, such as ethylenediaminetetracetic acid (EDTA), may also expose collagen fibers, thus promoting cell attachment without having damaging effect on the surrounding tissues. In recent years, biomodification of the root surface with enamel matrix proteins during periodontal surgery and following demineralization with EDTA has been introduced to promote periodontal regeneration. The application of enamel matrix proteins seems to promote periodontal regeneration as it initiates events that occur during the growth of periodontal tissues [82]. Moreover, enamel matrix derivatives have a key role also in periodontal wound healing [83], as reported in histological results from both animal and human studies [84].

Thus far, enamel matrix derivatives, either alone or in combination with grafts, have demonstrated their potential to effectively treat intraosseous defects and the clinical results appear to be stable long term [85].

### **1.6.3 Guided Tissue/Bone Regeneration**

The strategy of using barrier membranes with or without bone grafts has received great attention for restoring the function of a damaged or pathologically affected periodontium [4, 86-

88]. In this context, two surgical techniques have been developed to restore/regenerate the different periodontal tissues, namely GTR and GBR.

The use of an occlusive membrane interfacing with gingival connective tissue/epithelium and a PDL/alveolar bone tissue to promote periodontal tissue regeneration is called GTR while the restoration of deficient alveolar sites for posterior implant placement has been named GBR. Both techniques involve the placement of a membrane over a contained bony defect during surgery, based on the principles of space maintenance of the wound, excluding the gingival tissues from the healing area, allowing wound repopulation by appropriate progenitor cells, and clot stabilization to act as a scaffold for repopulating cells [89].

The types of barrier membranes evaluated in clinical studies vary in design, configuration and composition. A variety of membrane materials have been utilized. Originally GTR/GBR made use of expanded polytetrafluoroethylene (ePTFE) membranes. These membranes are highly biocompatible but are non-resorbable and require re-entry surgery a few weeks after treatment for their removal. Because of this limitation, a number of resorbable membrane types have been introduced [4, 87, 88]. These include membranes of polylactic acid (PLA), polyglycolic acid (PGA), bovine collagen membranes, and human cadaverous duramater-derived membranes. Clinical studies do not suggest any consistent difference in outcomes with any of these materials [90].

A deep analysis of GTR/GBR membranes in terms of required properties, materials employed in commercial products and research trends will be carried out in the next sections.

#### **1.6.4 Delivery of growth factors**

Wound-healing approaches using growth factors and bone morphogenetic proteins (BMPs) to target restoration of tooth-supporting bone, periodontal ligament and cementum have been shown to significantly advance the field of periodontal-regenerative medicine. Much of the research in growth factor application for periodontal regeneration has been focused on the use of BMPs. BMP-2 and BMP-7 have been shown to possess unique properties for inducing ectopic bone formation and new cementum formation [91, 92]. Other growth factors, mainly acting as a mitogen or differential factor on regenerating periodontal tissues, include: transforming growth factor- $\beta$  (TGF- $\beta$ ), platelet-derived growth factor (PDGF), insulin-like growth factor (IGF), and fibroblast growth factor (FGF) [41].

Doses and delivery system for growth factors may play an important role in regenerative response. To achieve a therapeutic effect by the local release of exogenous growth factors, supraphysiological doses are required, together with a method for sustained growth factor

release [16]. Various delivery systems have been developed based on collagen sponges, membranes or gels, gelatin matrices with varying degrees of cross-linking [93-95], alloplastic calcium phosphate materials such as TCP and HAp [96], and resorbable polymers such as PLA [97]. Surface area, surface properties for cell-surface interactions, inflammatory and immune reactions, and degradation kinetics are of particular interest in growth factor systems.

Bone and cementum formation occur in different time spans in animal models. This factor has to be considered during the growth factors delivery. The degradation kinetics of bioabsorbable carriers seem to influence the type of new tissue formation: a fast degradation and fast release of BMP induced bone formation to a greater extent, whereas cementum formation was significantly greater with the slow degrading and slow releasing BMP gelatin carrier [95]. Whether these findings apply to humans in an inflamed environment is unknown. Since limited human clinical data are available, more studies are still needed to fully evaluate the potential of growth factors for enhancing periodontal regeneration.

### **1.6.5 Gene therapies**

Given the relative difficulty of producing sustained release of growth factors from a suitable carrier, and the large pharmaceutical doses of factors required, one alternative approach to growth factor delivery is the use of gene therapy for periodontal regeneration. The aim is to maximize the therapeutic outcome of periodontal-regenerative procedures [62]. Genetic approaches in periodontal tissue engineering show early progress in achieving delivery of growth-factor genes to periodontal lesions and gene-transfer methods may circumvent many of the limitations with protein delivery to soft-tissue wounds [98]. It has been shown that the expression of growth factors [99, 100] or soluble forms of cytokine receptors [101] by gene transfer provides greater sustainability than the application of a single protein. As a consequence, gene therapy may achieve greater bioavailability of growth factors within periodontal wounds and hence provide greater regenerative potential.

Various gene-delivery methods are available to administer growth factors to periodontal defects. The delivery method can be tailored to the specific characteristics of the wound site. In order to overcome the short half-lives of growth factors *in vivo*, gene therapy using a vector encoding the growth factor is preferred to stimulate tissue regeneration.

Two main strategies of gene vector delivery have been applied to periodontal tissue engineering: gene vectors can be introduced directly to the target site (*in vivo* technique) [99] or selected cells can be harvested, expanded, genetically transduced and then re-implanted (*ex vivo* technique) [100]. *In vivo* gene transfer involves the insertion of the gene of interest directly into

the body, anticipating the genetic modification of the target cell. *Ex vivo* gene transfer includes the incorporation of genetic material into cells exposed from a tissue biopsy with subsequent re-implantation into the recipient.

In proof of principle studies, cells have been transduced to express PDGF, BMP-7, BMP-2, and FGF-2 *in vitro* using adenovirus vectors, and transfected cells have been subsequently reimplanted into surgically created periodontal defects. These studies have demonstrated the potential of this technology to stimulate regeneration of the periodontal tissues [102, 103]. While this approach may offer promising prospects for the future, there are a number of critical issues, particularly related to safety of adenovirus vectors, that will need to be demonstrated prior to considering this type of approach in human studies.

## **1.7 Commercially available membranes for GTR and GBR applications**

The rationale of GTR is to impede apical migration of the epithelium and gingival cells by placing a barrier membrane (resorbable or non-resorbable), which forms a space that allows the repopulation of PDL and alveolar bone cells onto the dental root surface [104].

The development of GTR was created in order to selectively guide tissue regeneration in the periodontium following periodontal disease. Following flap surgery in monkeys exposed to plaque for 6 months, a cellulose acetate laboratory filter or ePTFE was used by Gottlow et al. to successfully prevent gingival connective tissue from contacting the root surface during healing and to produce a space for tissue in-growth of the periodontal ligament [105]. After 3 months from implantation, histological analysis of explants evidenced that membranes exhibited improved bone re-growth. The results from this study confirmed the hypothesis that by selectively controlling the proliferation of the periodontal ligament cells and preventing contact from epithelium and connective tissues, the space-maintaining capability allowed improved regeneration of the attachment apparatus of the tooth.

Subsequently, Buser et al. [7] introduced the basic principles of GBR, which is aimed at bone regeneration through a membrane avoiding connective tissue collapse into bone defect. The work from the above mentioned authors has been confirmed and reproduced in a number of animal and clinical studies on various periodontal defects including intrabony, furcation recession and supra-alveolar defects [106, 107].

As a medical application in dental implantology and to achieve better clinical outcomes, barrier membranes should fulfill some fundamental requirements [108-110].

- 1) **Biocompatibility:** the interaction between membrane and host tissue should not induce adverse effects.

- 2) Non-immunogenic and non-toxic
- 3) Cell exclusion: the barrier membrane is used to prevent gingival fibroblasts and/or epithelial cells from gaining access to the wound site and forming fibrous connective tissue, that delay bone formation.
- 4) Space-making: the ability to maintain a space for cells from surrounding bone tissue to migrate for stable time duration.
- 5) Mechanical strength: proper physical properties to allow and protect the healing process, including protection of the underlying blood clot, avoiding the membrane collapse.
- 6) Tenting: the membrane is carefully fitted and applied in such a manner that a space is created beneath the membrane, completely isolating the defect to be regenerated from the overlying soft tissue. It is important that the membrane be trimmed so that it extends 2 to 3 mm beyond the margins of the defect in all directions. The corners of the membrane should be also rounded to prevent inadvertent flap perforation.
- 7) Scaffolding: this tented space initially becomes occupied by a fibrin clot, which serves as a scaffold for the in-growth of progenitor cells.
- 8) Stabilization: the membrane must also protect the clot from being disturbed by movement of the overlying flap during healing. It is therefore often, but not always, fixed into position with sutures, mini bone screws, or bone tacks. Sometimes, the edges of the membrane are simply tucked beneath the margins of the flaps at the time of closure, providing stabilization.
- 9) Biodegradability: adequate degradation time matching the regeneration rate of new tissue to avoid a secondary surgical procedure to remove the membrane.

Various types of materials have been developed, which can be grouped together as either non-resorbable or resorbable membranes. The properties of commercially available membranes are discussed in the following paragraphs and summarized in Table 1.1.

### **1.7.1 Non-resorbable membranes**

Non-resorbable membranes include expanded, high-density and Titanium-reinforced PTFE, and titanium mesh (Ti-mesh) [111] (Fig. 1.2). Although a number of animal studies involving a variety of defect configurations and human histological data after treatment of intrabony lesions with ePTFE membranes demonstrate high clinical attachment level (CAL) gain and residual probing depth [112], the requirement of a second surgical intervention to remove the barrier 4 to 6 weeks after implantation is a significant drawback [113]. The need for a second surgery may injure and/or compromise the obtained regenerated tissue, since it is known that flap elevation

results in a certain amount of crestal resorption of the alveolar bone. Furthermore, the use of non-resorbable membranes involves extra surgical times, which leads to increased costs, patient discomfort and duration of the therapy.

These undesirable characteristics are often weighed with the positive effects of using non-resorbable membrane, which include effective biocompatibility and ability to maintain sufficient space in the membrane for longer periods compared to resorbable membranes, due to their ability to retain shape and structure in the tissues. They have a more predictable profile during the healing process for their adequate mechanical strength and they are easy to handle in clinics [110].



**Fig. 1.2** Commercially available non-resorbable membranes: (a) Cytoflex® Tefguard®, (b) Cytoplast™, (c) Cytoplast™ Ti-250, (d) Cytoflex® Mesh, (e) Cytoplast™ Osteo-Mesh TM-300.

### 1.7.2.1 PTFE-based membranes

PTFE (Teflon®) is a synthetic fluoropolymer that relies on an extremely strong bond between carbon and fluorine for its non degradable, biologically inert properties. There is no known enzyme in the body capable of cleaving carbonfluorine bonds. Added rigidity of PTFE material can be achieved by reinforcement with fluorinated ethylene propylene, resulting in ePTFE (Gore-Tex®) [114]. Study by Buser et al. [7] was one of the first to report successful ridge augmentation with GBR in humans using an ePTFE membrane and tenting pins.

The first commercial membrane was first introduced in dentistry in 1984 and it was produced from ePTFE. However, the membrane had been used clinically for some previous years as a vascular graft material for hernia repair [115]. This membrane (Cytoflex<sup>®</sup> Tefguard<sup>®</sup>, Fig. 1.3 a) is the gold standard of GTR and GBR treatments.

The microstructure of ePTFE consists of solid nodes interconnected by fine, highly oriented fibrils, providing an unique porous structure. Both sides of the porous structure of ePTFE membrane have their own features [116]: on one side, an open microstructure collar of 1 mm thick and 90% porosity inhibits or retards the epithelium migration during the early phase of wound healing and promotes connective tissue in-growth [117]; on the other side, a 0.15 mm thick and 30% porous membrane provides the structural stability and the space for new bone growth, and acts to prevent fibrous in-growth. Effectiveness of ePTFE membranes was investigated in numerous clinical studies, that confirmed their excellent biocompatibility, leading to an average healing period after *in vivo* implantation of about 3–6 months [118, 119]. Drawbacks of ePTFE membranes are (i) the need for a second surgical procedure and (ii) membrane stiffness that may result in soft tissue dehiscence, allowing the exposure of the membrane to bacterial infection [120]. For these reasons, a membrane made of high-density PTFE (dPTFE) can be used alternatively.

The dPTFE membrane (Cytoplast<sup>™</sup> TXT-200 and GBR-200, Fig. 1.3 b; TefGen-FD) was introduced by Bartee in 1993; it is a non-resorbable membrane having submicron (0.2  $\mu\text{m}$ ) pores [121]. The advantages of dPTFE membranes is that they do not require primary closure and preserve the full width of keratinized mucosa. Compared with the conventional ePTFE, the density of dPTFE membranes (i) prevents the infections and (ii) does not require second-stage surgery for retrieval because the membrane can be removed with a gentle tug, in a manner similar to that used for the removal of a suture. The successful use of this membrane was shown in animal and clinical studies. Marouf et al. [122] compared the patterns of bone healing obtained with Gore-Tex and TefGen-FD membranes. Clinically, they found that TefGen membrane was much easier to detach from the underlying bone than was the Gore-Tex membrane, which showed strict adherence to bone surface on removal. Macroscopically, a relatively greater speed and quantity of bone regeneration were observed in the defective cavities covered with Gore-Tex membrane than in those covered with TefGen membrane.

#### 1.7.2.2 Titanium mesh

Creation and maintenance of a sufficient space underneath the barrier is an important factor for successful result. Titanium-reinforced PTFE (Ti-ePTFE; Cytoplast<sup>™</sup> Ti-250, Fig. 1.3 c) and

titanium barrier membranes (Cytoflex<sup>®</sup> Mesh and Cytoplast<sup>™</sup> Osteo-Mesh TM-300, Fig. 1.3 d and e) were introduced as an option for GBR, because they provide advanced mechanical support which allows a larger space for bone and tissue re-growth. The exceptional properties of rigidity, elasticity, stability and plasticity make Ti-mesh an ideal alternative for ePTFE products as non-resorbable membranes [111].

Titanium-reinforced barrier membranes were first introduced by Jovanovic and Nevins who reported the superior regenerative ability of these membranes in respect to the conventional ePTFE ones [123]. The titanium reinforcement provides mechanical support to the overlying soft tissue preventing its collapse into the defect. Moreover, during the surgical procedure, titanium struts permit the surgeon to easily place the membrane under flaps with minimal dissection and flap reflection [124]. Since 1995, titanium membranes with microperforations (FRIOS BoneShield) have been used for GBR. The membranes are either triangular or oval. The mechanical properties of the membrane prevent its collapse providing the maintenance of a constant volume for regeneration. The membrane has a suitable microporosity preventing soft tissue penetration through the membrane and permitting diffusion of interstitial fluid [125].

Rakhmatia et al. [111] demonstrated that there are four main advantages of Ti-mesh membranes over their alternative PTFE membranes: (1) rigidity provides extensive space maintenance and prevents contour collapse, (2) elasticity prevents mucosal compression, (3) stability prevents graft displacement, and (4) plasticity permits bending, contouring and adaptation to any unique bony defect. The main disadvantage of Ti-mesh membranes is increased exposure due to their stiffness and also a more complex secondary surgery to remove them.

### **1.7.2 Resorbable membranes**

A variety of resorbable membranes are currently available (Fig. 1.3). Their advantages are: 1) they allow a single-step procedure reducing patient discomfort and costs, 2) the shape and volume of the regenerated bone can be predefined-prefabricated, 3) they are radiolucent allowing imaging, and 4) their bioresorption eliminates potential surgical complications [126, 127]. The main limitation of resorbable membranes is related to the resorption time, the degree of degradation and the effect of their degradation on tissue formation. The ideal membrane should be capable of being degraded or resorbed over time at the same rate that bone formation occurs. It is reported that an optimal persistence and stability of membranes *in vivo* should be guaranteed for at least 4-6 weeks until several months, to allow successful regeneration of periodontal system [128].

There are two broad categories of bioresorbable membranes: the natural and the synthetic membranes. Natural membranes are made of collagen, whereas synthetic products are made of aliphatic polyesters [69].

The polyester-based membranes are biodegradable, allow tissue integration and are easier to handle surgically compared with non-resorbable membranes. However, their poor cell response is a drawback [86]. In contrast, collagen membranes have shown favorable regenerative results due to their excellent cell affinity and biocompatibility. Nevertheless, collagen based membranes show relatively poor mechanical and dimensional stability due to their rapid degradation and early collapse [129].

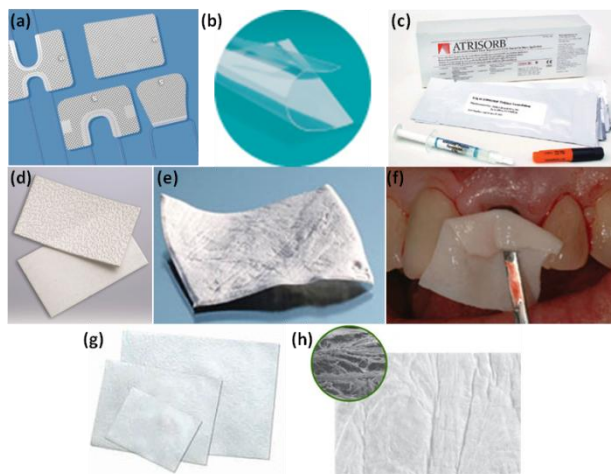


**Fig. 1.3** Commercially available resorbable membranes: (a) Guidor<sup>®</sup> Matrix Barrier, (b) Vivosorb<sup>®</sup>, (c) Atrisorb<sup>®</sup>, (d) Epi-Guide<sup>®</sup> Bioresorbable Barrier Matrix, (e) Bio-Gide<sup>®</sup>, (f) Alloderm<sup>®</sup>, (g) BioMend<sup>®</sup>, and (h) Cytoplast<sup>®</sup> RTM Collagen.

### 1.7.2.1 Synthetic resorbable membranes

Synthetic resorbable membranes mainly consist of polyesters such as PGA, PLA, poly( $\epsilon$ -caprolactone) (PCL) and their co-polymers. Aliphatic polyesters can be prepared reproducibly under strictly controlled conditions. The wide range of available polyester materials allows for the fabrication of a wide spectrum of membranes with different physical, chemical and mechanical properties. Another advantage is the ability of these polymers to completely degrade through hydrolysis and the degradation products are metabolized through the citric acid cycle [109].

The Guidor<sup>®</sup> Matrix Barrier (Fig. 1.3 a) was the first resorbable membrane to be approved by the Food and Drug Administration for membrane techniques and it was the first used membrane for the regeneration of tissues in periodontology. It consists of PLA treated with

acetyltributylcitrate to achieve flexibility to guarantee close barrier adaptation to the bone defect. It has a matrix with two differently perforated layers (Fig. 1.4). The external layer, aimed at the integration of the overlying gingival flap, presents larger sized pores (with rectangular shape) to promote tissue integration and to allow gingival connective tissue penetration into the matrix. The inner layer presents lower sized pores (circular shape), able to retard tissue penetration but allowing nutrient permeation. The two layers are separated by many inner spacers forming an interspace into which tissue can grow.

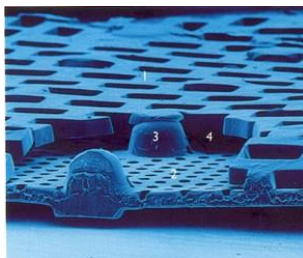


**Fig. 1.4** Guidor<sup>®</sup> Matrix design: (1) external layer facing the gingival, (2) internal layer facing the tooth and (3) inner spacers to form an interspace (4) into which tissue can grow.

According to the manufacturer, the barrier structure is not affected by the material degradation for at least the first 6 weeks, after which it slowly resorbs. A complete resorption occurs at approximately 12 months [130].

Poly(L-lactic acid) (PLLA) is one of two stereoisomers of PLA; it is used for the preparation of different bioabsorbable membranes, characterized by thermal plasticity, suitable mechanical properties and biocompatibility [131, 132]. PLLA presents the disadvantage to be absorbed completely after at least 4 years, while an ideal membrane should be absorbed within 1 year. To overcome this problem, copolymers of lactide and  $\epsilon$ -caprolactone, glycolide, trimethylene carbonate, have been produced to reduce the resorption rate.

Resolut<sup>®</sup> is a commercially available product consisting of two layers: a poly(D,L-lactide-co-glycolide) (PLGA) compact layer, that prevents epithelial cell penetration, and a porous network of PGA fibers, promoting tissue integration. Histological studies showed a similar effectiveness to non-resorbable membranes and complete resorption 5–6 months after placement [133, 134]. Fibers of polyglactin 910, a copolymer of glycolide and L-lactide (9:1 wt/wt), were used to produce a woven mesh (Vicryl Periodontal Mesh<sup>®</sup>). The polyglactin 910 is inert (no reactions in the surrounding tissue during its adsorption were observed), not antigenic and preserves its physico-mechanical properties during the first 3–4 weeks [135]. Although animal studies indicated a lack of tissue integration and recession formation, clinical evaluation suggested a similar effectiveness as compared to that of other GBR membranes [133-136].

Membranes based on copolymers of lactic acid and  $\epsilon$ -caprolactone have been produced, showing a lower degradation time as compared to pure PLA membranes. PCL is characterized by higher hydrophobicity and lower water-solubility than PLA, PGA and their copolymers. A commercial product (Vivosorb<sup>®</sup>, Fig. 1.3 b), consisting of poly(DL-lactide-co- $\epsilon$ -caprolactone) (PLCL), was found to be biocompatible, non-cytotoxic, occlusive and space maintaining. It retains its mechanical properties up to 8 weeks, providing support and protection to the healing tissue; its period of resorption may take approximately 24 months [137].

Atrisorb<sup>®</sup> membrane is the first liquid product adapted directly at the surgical site (Fig. 1.3 c): it consists of poly-DL-lactide acid dissolved in N-methyl-2-pyrrolidone. An irregular membrane is produced after polymer exposure to 0.9% saline solution for 4–6 min in a special cassette, in which it is possible to cut it into the desired shape. Membrane thickness is 600–750  $\mu$ m, and it is positioned into the defect site by applying a moderate pressure. A histological complete resorption was observed 6–12 months after implantation. Clinical studies reported its efficacy in the treatment of periodontal defects [138, 139].

The Epi-Guide<sup>®</sup> Bioresorbable Barrier Matrix is another membrane consisting of D-L polylactic acid (Fig. 1.3 d). It is a porous membrane with a unique three-layer technology, used as an adjunct to periodontal restorative surgery. The layer in contact with the gingival tissue is porous to promote fibroblast infiltration and attachment. On the contrary, the layer in contact with bone defects has a limited porosity that supports fluid uptake, helps adherence to the tooth surface, and inhibits fibroblast movement. Finally, the inner labyrinth layer creates pathways, while internal chambers enable collateral circulation and flow of interstitial fluid in the membrane. The Epi-Guide maintains its structure and functions for 5 months after implantation with a complete bioresorption between 6-12 months [140].

#### *1.7.2.2 Membranes based on natural materials*

Natural polymers are characterized by their intrinsic biocompatibility, non-antigenicity, and bioresorption tuned by cross-linking treatment [141]. Membranes consisting of non-mineralized collagen have been shown in animal and human clinical trials to be as effective as other GTR membranes in inhibiting epithelial migration and in promoting new connective tissue attachment and new bone re-growth [142-144]. Drawbacks of collagen membranes are (i) loss of space maintenance in physiological condition, (ii) high cost, and (iii) risks of disease transmission to humans for animal-derived collagen [145].

Collagen is the predominant protein in alveolar bone and periodontal connective tissues. Some of the positive properties of collagen when used for GTR procedures include its hemostatic

function through its ability to aggregate platelets. This feature may facilitate early clot formation and wound stabilization, both of which are considered essential for successful regeneration [146]. In addition, collagen possesses a chemostatic function for fibroblasts, which may aid in cell migration to promote primary wound closure, an essential component for successful GTR outcomes [147]. Collagen is also well tolerated and easily manipulated and adapted [108].

Membranes based on natural materials are typically derived from human skin (Alloderm<sup>®</sup>), bovine achilles tendon (BioMend<sup>®</sup> and Cytoplast<sup>®</sup> RTM Collagen) or porcine skin (Bio-Gide<sup>®</sup>). The most important commercial collagen membrane is Bio-Gide<sup>®</sup> (Fig. 1.3 e), which is based on Xenogenic collagen Type I from porcine skin and is characterized by a bi-layered structure with a dense and a porous layer (Fig. 1.5). The dense layer has a smooth surface able to avoid epithelial cell infiltration into bone defects, while the porous layer allows tissue integration.

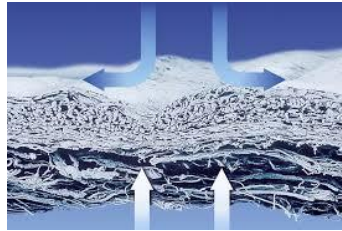


**Fig. 1.5** Bio-Gide<sup>®</sup> membrane design.

Taguchi et al. [8] have described a clinical study in which Bio-Gide<sup>®</sup> membranes were inserted into artificial bone defects formed by drilling 20 4-week-old male Wistar rats. Alkaline phosphatase-positive cells and osteocalcin and osteopontin-immunopositive sialoproteins were observed after 14 days post-implantation, suggesting osteoblastic differentiation in the porous layer. Moreover, membrane was well integrated into the surrounding tissue. In addition, the compact layer of Bio-Gide<sup>®</sup> membrane avoided invasion of epithelial and connective tissue, and maintained a free space where cells from the surrounding tissues could migrate.

Alloderm<sup>®</sup> (Fig. 1.3 f) is an acellular freeze-dried dermal matrix graft composed mainly of type-I collagen derived from human cadaveric skin. It has been used in periodontal, plastic and reconstructive surgery since 1994. Borges et al. compared the effectiveness of the acellular dermal matrix as a membrane for GBR, with a bioabsorbable membrane. In seven dogs, the mandibular premolars were extracted; after 8 weeks, one bone defect was surgically created bilaterally and the GBR was performed. Each side was randomly assigned to the control group (bioabsorbable membrane made of glycolide and lactide copolymer) or the test group (Alloderm<sup>®</sup> membrane). No statistically significant differences between the groups were

observed for any histomorphometric measurement. Clinically, both groups showed an increase in the thickness of keratinized tissue and a reduction in the width of keratinized tissue. Radiographically, an image suggestive of new bone formation could be observed in both groups at 8 and 16 weeks following GBR [148].

The use of Alloderm<sup>®</sup> has several advantages because it does not contain cellular material, which eliminates the possibility of rejection because of the presence of major histocompatibility complex class I and II antigens. In addition, the unlimited supply, color match, and thickness, as well as no degradation if primary closure is not achieved, and formation of additional attached gingival tissue makes this material a good choice for membrane barrier techniques.

Type I collagen membranes are also manufactured from bovine Achilles tendon. BioMend<sup>®</sup> membrane (Fig. 1.3 g) is semi-occlusive with nano-sized pores and resorbable within 8 weeks. Cytoplast<sup>®</sup> RTM Collagen membrane (Fig. 1.3 h) is characterized by (i) a multi-layer construction that allows tissue integration into outer layer, while preventing direct passage of bacteria and epithelial cells, and (ii) a longer and predictable resorption time (26–38 weeks) [110].

Oh et al. [149] compared two collagen membranes, Bio-Gide<sup>®</sup> and BioMend<sup>®</sup>, for the treatment of implant dehiscence defects in eight mongrel dogs. The results of this study indicated that: (1) GBR treatment with collagen membranes may significantly enhance bone regeneration, manifested at late stage (16 weeks) of healing, and (2) space maintenance and membrane coverage were the two most important factors affecting GBR using bioabsorbable collagen membranes.

**Table 1.1** Available commercial non-resorbable and resorbable membranes.

	<b>Commercial Name</b>	<b>Material</b>	<b>Properties</b>	<b>Reference</b>
<b>Non-Resorbable Membranes</b>	Cytoflex Tefguard	ePTFE	Excellent biocompatibility Healing period of about 3-6 months	118, 119
	Cytoplast TXT-200	dPTFE	0.2 $\mu\text{m}$ pores $E \sim 16 \text{ MPa}$ ; $\sigma_{\text{max}} \sim 2 \text{ MPa}$ ; $\epsilon_{\text{max}} \sim 545\%$ No second-stage surgery	121
	Cytoplast Ti-250	Ti-ePTFE	Easy to place 250 $\mu\text{m}$ thick	124
	Cytoplast Osteo-Mesh TM-300	Ti	300 $\mu\text{m}$ pores	125
<b>Resorbable Membranes</b>	Guidor	PLA treated with acetyltributylcitrate	Bi-layer membrane Resorption: 6 weeks-12 months Easy to use	130
	Resolut	PLGA and PGA	Bi-layer membrane Resorption: 10 weeks Good space maintainer $\sigma_{\text{max}} \sim 11.7 \text{ MPa}$	133, 134
	Vicryl	Polyglactin 910	Resorption 4-12 weeks Inert and no antigenic	135
	Vivosorb	PLCL	Resorption: 24 months Up to 8 weeks' mechanical properties Anti-adhesive barrier	137
	Atrisorb	Poly-DL-lactide and solvent	Resorption: 6-12 months Liquid product 600-750 $\mu\text{m}$ thick	138, 139
	Epi-Guide	Poly-DL-lactic acid	Three-layer membrane Resorption: 6-12 months	140
	Bio-Gide	Xenogenic collagen Type I from porcine skin	Bi-layer membrane Resorption: 24 weeks At least 6 weeks bioactive $\sigma_{\text{max}} \sim 7.5 \text{ MPa}$	8

	Alloderm	Type-I collagen from human skin	Eliminates the possibility of rejection $\sigma_{\max} = 9.4-21.5 \text{ MPa}$	148
	BioMend	Type-I collagen from bovine Achille	Resorption: 4-8 weeks $\sigma_{\max} = 3.5-22.5 \text{ MPa}$	110
	Cytoplast RTM	Type-I collagen from bovine Achille	Multi-layer construct Resorption: 26-38 weeks $E \sim 170 \text{ MPa}$ ; $\sigma_{\max} \sim 8 \text{ MPa}$ ; $\epsilon_{\max} \sim 12\%$	110

## 1.8 Current trends in the development of membranes for GTR/GBR

Although a number of barrier membranes are already being used in clinical practice, novel membranes have been developed in an effort to overcome the limitations of the currently used membranes. The polymeric commercial products described previously are characterized by weak mechanical and osteoconductive/osteoinductive properties. The researchers are looking for different approaches to meet the demands of degradable GTR/GBR membranes in terms of mechanical properties and biocompatibility:

- 1) the incorporation of bioactive inorganic fillers
- 2) the production of multi-component structure
- 3) the surface modification of synthetic polymers/copolymers to graft bioactive proteins or biomolecules.

The use of polymers in combination with a bioactive inorganic filler is considered a suitable strategy for producing bone regenerative materials with physicochemical properties approaching those of bone and with good tissue compatibility, such as cell affinity, osteoconductivity and enhanced bone formation [150, 151]. Bioactive inorganic components, including calcium phosphates (i.e. HAp, TCP) and bioactive glasses/glass ceramics, are the most widely used inorganic fillers, while the polymeric components are natural and/or synthetic polymers. For example, Xianmiao et al. [152] prepared nano-hydroxyapatite and chitosan (n-HAp/CH) composite membranes by solvent casting and evaporation methods. CH is a biocompatible, antimicrobial, and biodegradable natural polymer with outstanding biological properties for promoting osteogenesis. The surface of the composite membranes was rough and microporous, suitable for adhesion, crawl and growth of cells. The hydroxyapatite holds nano size in the composite membranes and its Ca ions and –OH groups could interact with –NH<sub>2</sub> or –OH groups of CH. Cell culture and MTT assays showed that n-HAp/CH composite membranes had no cytotoxic effect on cells and possessed good biocompatibility. Therefore, the n-HAp/CH composite membranes showed promising properties for GBR membrane applications. Synthesis of a new flexible and thermoplastic copolymer, such as poly(L-lactide-co-glycolide-co-ε-caprolactone) (PLGC), and its conjugation with TCP has been carried out by Kikuchi et al. [12]. The bioactive composite films have been prepared by a heat-kneading method. The composites formed an electrostatic interaction between the TCP surface and ester C=O bond of the polymer, and the interaction maintained mechanical strength of the composites to the same or greater degree as the pure polymers. The composites had a pH maintenance effect and decomposed in 24 weeks after soaking in both physiological saline and phosphate buffered

saline (PBS). The GBR application of the membrane, in animal tests in beagle model, indicated good regeneration of mandibular bones.

In several works, bioactive glass addition into PGA or PLA membranes has been shown to stimulate different biological processes, such as the enhancement of osteoblastic activity and new collagen production [153, 154]. In addition, differentiation of mesenchymal stem cells into bone-forming cells was observed by Blaker et al. [155] in composite porous membranes consisting of Bioglass<sup>®</sup> and PLA. Bioactive glass increased significantly the bioactivity, in terms of formation of a bone-like mineral layer on the surface of membranes, which is an essential requirement for an implant to exhibit a bone-bonding behavior. The addition of nano bioactive glass ceramic (nBGC) particles into scaffold material has also been studied by Srinivasan and co-workers [156]. The scaffold has been developed from alginate, a natural polysaccharide with high hydrophilicity and biocompatibility, relatively economic and widely used in the food and pharmaceutical industry. The alginate/nBGC composite scaffolds were found to have suitable physico-chemical and biological properties to facilitate periodontal regeneration. They had a pore size of about 100-300  $\mu\text{m}$ , controlled porosity and swelling ability, limited degradation and enhanced biomineralization, ideally controlled due to the presence of bioglass in the scaffold. Incorporation of nBGC helped to attain good protein adsorption, human periodontal ligament fibroblast and osteosarcoma cells attachment and proliferation onto the scaffolds. The periodontal ligament fibroblast also showed distinct osteoblast-like behavior with enhanced alkaline phosphatase activity.

Advances in the science and technology of nanomaterials have led to increased enthusiasm for approaches such as electrospinning of biomimetic multifunctional growth-enhancing regenerative membranes for periodontal tissue engineering. Electrospun nanofibrous scaffolds/membranes mimic more closely the scales and morphologies of the extracellular matrix (ECM) proteins (fibers with diameters ranging from 50 to 500 nm). The thin fibers are characterized by large surface areas, possibility of functionalization for various applications, superior physico-chemical properties. Sui et al. [157] developed an electrospun PLLA/HAp hybrid membrane for bone tissue regeneration. Synthesized HAp nanoparticles were carefully dispersed in PLLA solution and nanosized PLLA/HAp hybrid fibers were electrospun to obtain hybrid membranes. The introduction of HAp nanoparticles increased the specific surface area and mechanical properties, slowed down the degradation rate of PLLA/HAp membrane, and maintained constant the pH value of the incubation solution during degradation, which facilitated osteoblast cell adhesion and growth on the hybrid membrane. HAp nanoparticles were also dispersed in PCL matrix [158]. The coupling agent  $\gamma$ -glycidoxypropyltrimethoxysilane

known as A-187 was utilized to treat HAp nanoparticles to improve their dispersion in PCL matrix. To fabricate fibrous scaffolds mimicking the natural bone structure, electrospinning was adopted and two scaffolds were developed (HAp/PCL and A187-HAp/PCL). The good dispersion of HAp in PCL enhanced tensile strength and modulus of the scaffold. Furthermore, the surface modification of HAp using A-187 did not affect its bioactivity. Both scaffolds were *in vitro* bioactive, in fact HAp coating was observed on the scaffolds surface when they were soaked in 1.5 SBF, while no HAp formation was found on net PCL scaffold. Finally, the *in vitro* cellular assays suggested the electrospun fibrous scaffolds of A187-HAp/PCL and HAp/PCL were non-toxic to fibroblasts and osteoblasts.

Lee et al. used the electrospinning technique to produce nanofibrous bioactive glass; then, the researchers introduced the bioglass nanofibers into a degradable polymer, PCL, to form a nanocomposite with a thin membrane form (Fig. 1.6) [159]. The nanocomposite membrane induced the rapid formation of apatite-like minerals on the surface when immersed in a simulated body fluid. Murine-derived osteoblastic cells grew actively over the nanocomposite membrane with cell viability significantly improved compared to those on the pure PCL membrane. Moreover, the osteoblastic activity, as assessed by the expression of alkaline phosphatase, was significantly higher on the nanocomposite membrane than on the pure PCL membrane.

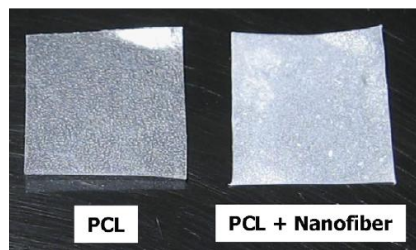


**Fig. 1.6** Optical views of the pristine PCL and PCL-glass nanofiber nanocomposite prepared in membrane form [159].

Electrospinning could be also used for the production of barrier membranes with a multi-component structure to obtain tuned mechanical and degradation characteristics. The rationale of having a periodontal membrane with a multi-component structure relies on the principle that one can tailor the properties of the different layers to meet the local functional requirements, enhancing bone re-growth while preventing the gingival tissue down-growth. A novel multi-component membrane was designed and fabricated via multilayering electrospinning by Bottino et al. [126]. Researchers have proposed a multilayered membrane consisting of three layers (Fig. 1.7): a core layer (CL) and two functional surface layers (SL), interfacing bone and epithelial tissues. The CL comprised a neat PLCL layer surrounded by two composite layers

based on a gelatin/polymer ternary blend (PLCL:PLA/G). To obtain this membrane, a sequential multilayer electrospinning process was carried out in the order: PLA:G (type-B gelatin)+10 wt% n-HAp, followed by the core layers (namely PLCL:PLA:G, pure PLCL and PLCL:PLA:G), and finally PLA:GEL+25 wt% MET (metronidazole benzoate). n-HAp was loaded on the outer layer in contact with bone tissue to enhance bone formation, while the layer in contact with epithelial and gingival tissues was functionalized with MET, a common antibiotic used in periodontitis treatment preventing bacterial colonization [160].

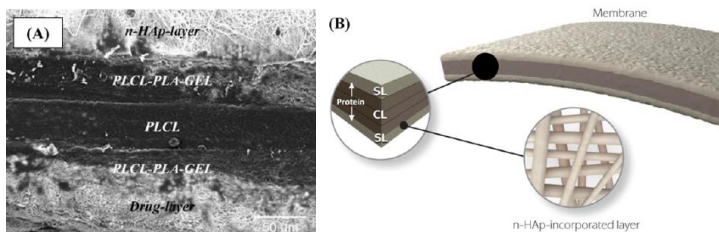


**Fig. 1.7** (A) Cross-section SEM micrographs of the FGM processed via multilayering electrospinning (B) Schematic illustration of the FGM [126].

The multi-component device exhibited an open porosity and interconnected structures formed by randomly oriented non-woven fibers. The majority of fibers had submicron diameters and displayed a topography that closely resembled the native ECM structure. In GBR, the mechanical properties of the membranes are of the utmost importance for the clinical success of the therapy. The mechanical properties of the CL were a major contributor to, and, therefore, predictor of, the *in vivo* mechanical performance of the FGM. Under hydrated conditions, the CL presented a high tensile strength (8.7 MPa) and tensile modulus (156 MPa) with a strain at failure of 375%. No delamination was observed in the CL membrane, indicating that the compositionally graded layers remained intact under physiological conditions. The multi-component membrane exhibited a tensile strength of 3.5 MPa and a tensile modulus of 80 MPa with a strain at break equal to 297%. These results were comparable with those recently reported in the literature [4, 9] and suggested that addition of two SLs rich in protein decreased the tensile properties in both the dry and hydrated conditions.

Other multi-component structures have been developed by Reis et al. [161] and Liao et al. [162]. In the first study, a semi-rigid PLGA/CaP (calcium phosphate) bilayered construct has been developed to promote periodontal regeneration. The device was characterized by a continuous outer barrier membrane and an inner topographically complex component (Fig. 1.8).

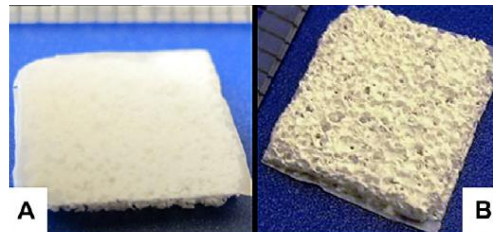


**Fig. 1.8** Optical views of the membrane (A) and the macroporous (B) surfaces of the bilayered construct [160].

Researchers compared periodontal prophylaxis alone with prophylaxis and biomaterial implantation in the treatment of class II furcation defects in dogs. Healing occurred uneventfully and bone volumetric values, trabecular number and trabecular thickness were all significantly greater in the treated group; while trabecular separation was significantly greater in the control group. New cementum, bone, and periodontal ligament with Sharpey fibre insertions were only seen in the treated group. Although periodontal regeneration has been reported elsewhere, the advantages of employing bilayered PLGA+CaP construct are twofold: (1) it did not collapse into the defect and (2) its inner side was able to retain the blood clot throughout the buccal defect.

Liao and co-workers selected nano-carbonated hydroxyapatite/collagen (nCHAC) as bioactive component and PLGA as barrier to prepare a novel three-layered membrane (Fig. 1.9). The nCHAC material facilitated reliable bone regeneration by inducing undifferentiated cells in the graft recipient site to become osteoblasts and form new bone. The composite also supplied a ready source of calcium for rapid mineralization.

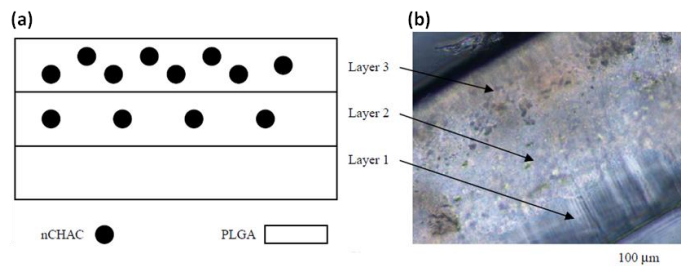


**Fig. 1.9** (a) Schematic representation of three-layered membrane (b) The optical microscopy result of the section of the nCHAC/PLGA membrane [161].

This new mineralized collagen/PLGA membrane was considered to have many medical applications because of its flexibility, strong mechanical strength, easy manipulation character, excellent biocompatibility and controllable bioresorption. It could be used in medical applications such as for repairing periodontal defects, membranes for covering bone defect surgery and for bone substitutes, skin wound repair and healing, skin sealing, and as a carrier

for antibiotic, bone growth factors, skin growth factors, and so forth. Osteoblast cells were cultured on the three-layered composite membrane; primary results showed a positive response compared with pure PLGA membrane.

The third strategy adopted by researchers to obtain membranes for GTR/GBR with improved biocompatibility properties, makes use of different surface engineering techniques to graft bioactive molecules accelerating ECM secretion and tissue regeneration. Biomacromolecules, such as proteins, polysaccharides, proteoglycans and their derivatives are known to act as biological cues for adherent cells. Therefore, if biomaterial surfaces are functionalized with these bioactive macromolecules, the biocompatibility can be significantly improved.

Several approaches can be adopted to modify the surface properties of biocompatible polymers with biomacromolecules, such as covalent attachment, physical adsorption, and affinity bonding (Table 1.2).

The surface modification techniques, as briefly summarized in Table 1.2, have been described in many reviews and book chapters (163- 165). In particular, an exhaustive list of cross-linkers for the immobilization of bioactive molecules to a functionalized substrate has been reported by Goddard et al. (166).

**Table 1.2** Surface modification approaches.

<b>Modifications</b>	<b>Mechanisms</b>	<b>Methods</b>
Chemical grafting	Covalent grafting of bioactive peptides, proteins and polysaccharides to improve cell adhesion and biocompatibility.	Carbodiimide (87, 167-169), glutaraldehyde (170, 171), hydroxyethylmethacrylate (172, 173)
Physical adsorption	Non-covalent immobilization of bioactive macromolecules and growth factors (by hydrogen bonding, van der Waals interactions or electrostatic forces) to promote cell interaction and response, respectively. Layer-by-layer (LbL) self assembly and mussel inspired techniques belong to physical adsorption techniques.	Physical adsorption (174- 177)
Affinity bonding	Streptavidin (avidin)/biotin non covalent interaction	Surface functionalization with a biotin containing molecule, able to interact with streptavidin(avidin), then binding to a biotin-functionalized bioactive molecule (178).

Surface coating by the three above mentioned approaches is often preceded by a surface pre-functionalization step via surface chemical etching (in acidic or basic solution [179]), chemical functionalization (i.e. by aminolysis [173, 180]) or plasma treatment [181, 182].

Chemical etching involves the partial degradation of the surface material by the corrosive action of a liquid or gaseous acid or an alkali. Etching treatment of aliphatic polyesters results in the hydrolysis of exposed macromolecules, leading to the formation of carboxylic and hydroxylic moieties [166]. Aminolysis is another widely applied technique for surface functionalization of polyesters with amino groups, which allows the grafting of biomolecules. During the aminolysis reaction, a diamine reagent reacts with exposed ester groups of polyesters, reducing the molecular weight of surface macromolecules and forming amide bonds. As a result, amino and hydroxyl groups form on the material surface (183, 184). Plasma treatment can introduce hydroxyl, carboxyl and amino groups on polymer surfaces using different carrier reactive gases such as argon, oxygen, nitrogen, hydrogen, and ammonia. When these gases are exposed to plasma, they dissociate and react with the surface, creating different chemical functional groups on the surface. The plasma process results in a physical and/or chemical modification of the first few molecular layers of the polymer surface. The effectiveness of the treatment is determined by the plasma source gases, the configuration of the plasma system and the plasma operating parameters [163].

Some examples of successful surface modification strategies for GTR/GBR application are reported below, based on a pre-modification step, followed by surface functionalization.

Park et al. have recently proposed a novel biocompatible and degradation-controlled membrane formed by two layers: a PLGA grafted hyaluronic acid (HYA) layer and a PLGA layer [87]. As a natural linear polysaccharide, HYA is biodegradable, biocompatible and non-immunogenic [185]. It is also known to be osteoconductive, to promote angiogenesis, and moderate immune responses. In this work, HYA was chemically modified with adipic acid dihydrazide (ADH) in the mixed solvent of water and ethanol, and grafted to PLGA, previously activated by N,n'-dicyclohexyl carbodiimide and N-hydroxysuccinimide. According to *in vitro* degradation tests in PBS, HYA-PLGA/PLGA (weight ratio of 1/2) film degraded relatively slowly compared to PLGA film and HYA coated PLGA film. The innovative membrane was also used to cover up bone defects in rats to study *in vivo* bone regeneration. Histological and histomorphometric analyses revealed that HYA-PLGA/PLGA film resulted in the most effective bone regeneration compared to other samples (control and PLGA films) with a regenerated bone area of 63.1% covering the bone defect area.

Chen and co-workers [171] developed a PLLA electrospun membrane aminolyzed with CH (PLLA-CH) to enhance both the biocompatibility and the degradation. To graft CH, the membrane was first aminolyzed in a 1,6-hexanediamine/isopropanol solution and then immersed in a glutaraldehyde solution to obtain the aldehyde PLLA electrospun membrane. The modification of CH promoted the hydrophilicity, enhanced the bioactivity, and accelerated the degradation rate of PLLA electrospun membrane. Moreover, the grafting process did not change membrane morphology: statistical analysis showed no significant difference in fiber diameter and pore sizes between PLLA and PLLA-CH membranes. *In vitro* cell culture showed that the modified membrane had a better biocompatibility and promoted osteoblast proliferation compared with pure PLLA. Besides, it could also prevent fibroblasts invasion. CH was also used as substrate for covalent immobilization of BMP-2, a prominent cytokine in osteogenesis, to develop a potential membrane for GBR. For the covalent grafting, 1-ethyl-3-(3-dimethylaminopropyl) carbodiimide (EDC) was used to form covalent bonds between carboxyl groups of the growth factor and amine groups of CH. The films with covalently immobilized BMP-2 stimulated osteoblast attachment, proliferation, and differentiation in a dose-dependent manner. After 3 weeks of immersion in PBS, about 80% of the immobilized growth factor was retained on the films, and enabled its stimulation effect to persist for a longer period of time [167].

Nanocoatings can be also fabricated using (i) the layer-by-layer (LbL) self-assembly technique [186], one of the most rapidly growing strategies of generating thin films in the field of materials science, and (ii) the mussel-inspired technique [187], an innovative versatile and attractive method for surface modification of solid materials. A detailed discussion of this techniques in terms of assembly mechanism, advantages and applications in GTR/GBR will be carried out in the next sections.

## **1.9 Layer-by-Layer deposition technique (LbL)**

Employed in a variety of biomedical applications, LbL deposition is a simple and versatile technique used for the fabrication of thin films and coatings. This method, proposed firstly by Decher et al. in 1991 [188, 189], is mainly driven by the electrostatic attraction between oppositely charged polyelectrolytes (PEs) [190]. Generally, LbL self-assembly proceeds as schematically reported in Fig. 1.10. A charged substrate is immersed in a solution of an oppositely-charged PE to electrostatically attract a first monolayer. A washing step follows to remove unbound material and to avoid contamination of the subsequent oppositely-charged PE solution, in which the substrate is then submerged to deposit the second PE layer. A washing

step is then performed again. These four steps are repeated several times to obtain a multilayered coating. LbL films can not only be developed using the dipping method described above, but can also be produced via spin-coating [191] or spray-coating [192] of alternating species.

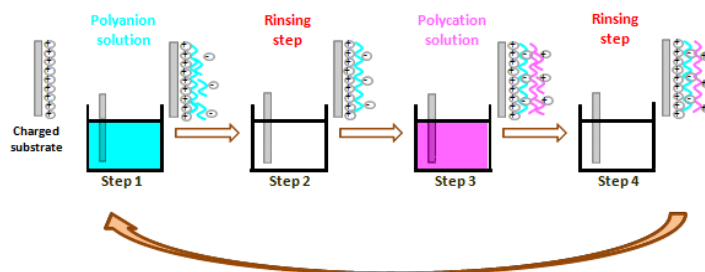


**Fig. 1.10** A schematic illustration of the LbL film-deposition process, based on the alternating exposure of a charged substrate to solutions of positively and negatively charged PEs. A rinsing step is included between the two previously described adsorption processes, to remove excess as well as to prevent cross-contamination of the PE solutions.

LbL film can be formed on nearly any 2D or 3D substrates and a wide range of charged species can be incorporated within LbL multilayers, including natural and synthetic polymers, proteins, DNA, drugs, dyes, inorganic nanoparticles, and carbon nanotubes [193 - 200]. At the beginning, only electrostatic interactions were utilised for LbL assembly. Subsequently, other interactions such as covalent bonding, hydrogen bonding, charge transfer, hydrophobic interactions, and coordination bonding [201 - 205] have been investigated to facilitate polymer association for ultrathin film deposition.

Film properties such as thickness, mechanical stability, permeability, and surface roughness, chemistry and wettability can be fine tuned by altering the PEs, layer numbers, architecture and fabrication conditions employed (i.e. pH, ionic strength and PEs concentration) [206]. This flexibility makes LbL deposition an attractive method for a diversity of applications; it is also environmentally friendly and it allows room temperature processing and low-cost manufacturing [207].

### 1.9.1 Film growth and influencing factors

The mass and thickness of multilayer films can grow either linearly or “exponentially” with the number of deposited bilayers, depending upon a number of factors. Linearly growing films are generally formed from strong PEs with a high charge density, such as poly(4-sodium styrene sulfonate) (PSS) and poly(allylamine) (PAH), which lead to films consisting of relatively immobile polymer chains. These linear films thus tend to be thinner, more mechanically rigid, and less permeable [208]. Exponential multilayers, by contrast, tend to be formed from weaker

PEs, especially biopolymers such as proteins and polysaccharides, and tend to be significantly thicker, more visco-elastic, and somewhat more permeable [209].

“Exponential” multilayer growth, as proposed by the model developed by Lavallo et al. [210], appears to be due to diffusion of one or more of the PEs into and out of the film system. An example, is represented by the poly(lysine) (PLL)/HYA system, where PLL is the freely diffusing PE and HYA can only interact with the outermost layers during a deposition step [211]. When a negatively charged HYA outer layer is brought into contact with a positively charged PLL solution, the PLL chains not only interact with this layer to adsorb and form PLL-HYA complexes, but also diffuse down throughout the film. This free PLL interacts weakly with the film matrix and may even exchange with some of the bound PLL within the film. PLL diffusion into the film stops as the PLL-HYA complexes that form at the film surface invert the surface charge, thus creating an electrostatic barrier. When a buffer solution is introduced in the rinsing step, some of the free PLL diffuses back out. However, as this diffusion lowers the chemical potential inside the film, which in turn increases the height of the electrostatic barrier to be overcome by the remaining PLL chains, not all the free PLL leaves the film. As the oppositely charged HYA solution is brought into contact with the film for the next deposition step, the electrostatic barrier is removed, and some of the free PLL left within the film diffuses out to interact with the HYA at the film/solution interface. Thus the HYA that adsorbs in this step is not only proportional to the amount of PLL adsorbed in the last step, but is additionally dependant upon the amount of free PLL that diffuses to the film surface (Fig. 1.11). This, in turn, is related to the total thickness of the film. The mass increase of the film thus increases with total film thickness, becoming “exponential”.

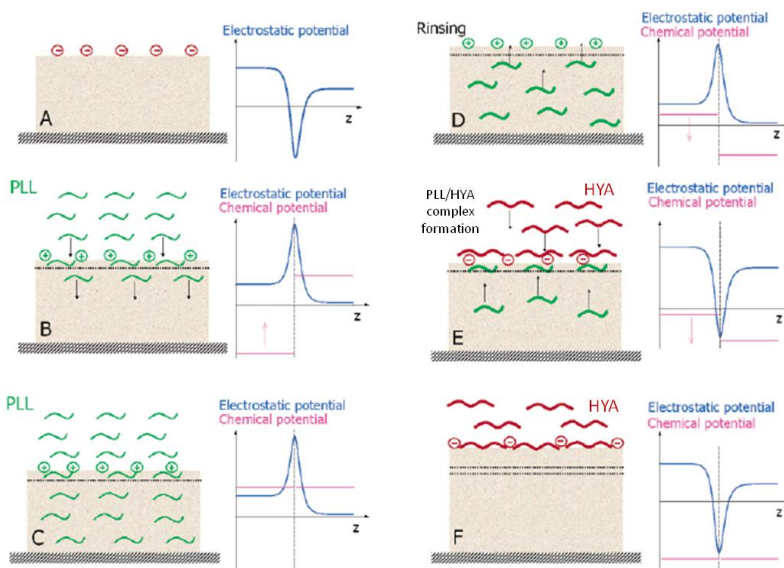


**Fig. 1.11** Drawing of the build up mechanism of PLL/HYA film. (A) At the end of a HYA deposition step with a negative electrostatic potential at the top of the film. (B) PLL interaction with the surface renders it positive; PLL chains can cross the energy barrier and diffuse down throughout the film. As they diffuse into the film, the chemical potential of free PLL chains increases and (C) diffusion stops as the PLL-HYA complexes that form at the film surface invert the surface charge, thus creating an electrostatic barrier. (D) During the rinsing phase with pure buffer, the free PLL chains can cross the electrostatic energy barrier in the reverse direction and diffuse back out. During this process, the chemical potential of these chains diminishes as well. (E) When this film is further brought in contact with a HYA solution, HYA chains interact with the outer PLL layer to form PLL/HYA complexes which form the new outer layer of the film. The positive electrostatic barrier totally disappears. The remaining free PLL chains can thus diffuse out of the film. (F) The diffusion process stops when all the free PLL chains inside of the film have diffused out of it [211].

While it is difficult to predict which growth regime will characterize a given PE pair, in general, linear film growth is associated with strongly interacting PEs which are highly exothermic, while exponential growth is linked to more weakly interacting PEs which are endothermic or weakly exothermic [212]. However, most PE systems can be made to transition from linear to exponential growth, or vice versa, given the right conditions. For example, linear films can be made to grow exponentially with an increase in solution salt concentration and many exponentially growing films transition to linear growth once a certain critical number of deposited bilayers is reached [213, 214].

Many factors influence the strength of PE interactions and thus whether a film system grows linearly or exponentially, including polymer charge density, the concentration and type of counter ions present in the depositing and rinsing solutions, the deposition time and temperature, solvent quantity, and solution pH [215].

The presence of salt ions in LbL deposition and rinsing solutions strongly influences the formation and resulting properties of multilayer films. The addition of salt in the deposition solution screens charges on the PE chains, minimizing repulsion interactions within chains and

thus leading to chain coiling. These coiled chains adsorb in extended “loopy” conformations which allow for greater PE surface density and thus thicker and rougher films [216]. Film thickness tends to increase proportionally to salt concentration, reaching a maximum at an optimal concentration which depends upon the given PE system [217]. The type of salt ions used also affects LbL film formation, with multilayer thickness generally varying as  $\text{Li}^+ < \text{Na}^+ < \text{K}^+$  and  $\text{F}^- > \text{Cl}^- > \text{Br}^-$  [218, 219]. Generally, ions characterized by smaller and weaker hydration shells interact more strongly with PEs, promoting chain coiling and thicker and smoother surface.

PE structure, molecular weight and charge density also play important roles in determining multilayer properties. For most PE system there is a minimum charge density required for LbL film formation [217]. Charge density in strong PEs is determined by chemical structure alone, while for weak PEs it is also highly dependant upon the solution pH. Generally, fully charged PE chains adsorb in a flat, spread out conformation due to intra-chain repulsion and increased chain-surface interactions, thus leading to thinner films. In this fully charged state, molecular weight appears to have little effect on film thickness for many PE system. Meanwhile, less charged PEs tend to coil and adsorb as thicker layer, with increased molecular weight, in this case, leading to thicker films [216, 220, 221].

While the broad range of factors influencing the formation and properties of LbL films may seem daunting, it also provides a great flexibility for multilayer design, enabling fine, nano-scale tuning of film features. By carefully selecting the PE used, and the layer architecture and preparation conditions employed, multilayer films can be designed for a wide variety of biomedical applications, including modifying cellular and protein adhesion, and tunable drug, protein and gene delivery.

### **1.9.2 Monitoring multilayer build up**

The combination of several techniques can be used to study the construction, disassembly or release of captured content from LbL polyelectrolyte multilayers (PEM). These methods can be divided into two groups.

#### 1) *Ex-situ* characterization

The easiest way to follow multilayer build up is probably by UV/Vis spectroscopy that determines cumulative absorption attributed to stepwise deposition of UV-active colloids [222]. However it works only for materials having UV/Vis absorbance. Equivalent to measuring the optical absorbance, one can also determine the film thickness by ellipsometry or X-ray reflectometry. The first determines the distance-dependent change in polarization of a light

source as a function of reflection or transmission through a substance [223]. X-ray reflectometry measures the intensity of x-rays reflected and compares it with the value predicted by the law of Fresnel reflectivity; the deviations from the law can then be analyzed to obtain the density profile of the interface normal to the surface [224]. Very recently, nuclear magnetic resonance (NMR) was added to the “toolbox” of multilayer research [225, 226] and this deserves special attention as it gives access to important new data. In order to monitor the correct growth of the multilayer films, measure of static contact angle can be performed. The change of the surface wettability of multilayer films after each step of adsorption of polycations and polyanions layers can be evaluated. Usually contact angle analysis shows a “zig-zag” trend due to the alternate deposition of polycations and polyanions [227].

## 2) *In situ* characterization

The characterization methods described above are straightforward and widely available, but they require the interruption of the deposition process to analyze samples. Moreover, analysis has to be performed in the dry state. It has been observed that films deposited from identical solutions under the same adsorption times and temperature show different film thickness for the same number of layers, depending on whether layers have intermittently been dried or not. *In-situ* methods allow to follow the kinetics of adsorption and/or multilayer reorganization. Typical analysis *in-situ* methods are the zeta potential measurements, quartz crystal microbalance, surface plasmon spectroscopy, optical waveguide lightmode spectroscopy, scanning angle reflectometry, *in situ* atomic force microscopy (AFM) and attenuated total reflection fourier transform infrared spectroscopy (ATR-FTIR). Quartz crystal microbalance studies relate vibration dissipation (QCM-D) as a function of the step-wise amount of colloid adsorbed to a quartz crystal surface in real time. The dissipation values are then converted to the amount of material that was adsorbed per layer [228]. Electrophoretic particle mobility enables zeta potential measurements of charged, therefore efficiently coated, surfaces to study charge reversal and colloidal stability [229]. The surface texture and roughness of PEMs can be elucidated by AFM [230]. AFM can also aid studying the changes in wettability, contact angle and subsequently surface energy [228].

### **1.9.3 State of the art of LbL technique for gingival wound healing applications**

Beside the need to improve biocompatibility of GTR membranes, in recent years, the focus of many laboratories has been the design of membranes with antibacterial properties [11]. To this purpose, surface functionalizations of membranes with (a) controlled release system of biocides

[231, 232], (b) antibacterial polymer or peptides [233, 234], and (c) microbe-repelling or anti-adhesive polymer [235, 236] have been developed to ensure the safety of implanted materials. The most common biocidal leaching materials used in PEMs are silver (Ag) and Ag ions [237-239]. Although the mechanism of Ag effects is not completely clear, its multilevel antimicrobial mode has been well known [240], which ensures that Ag are proven biocides against a broad spectrum of bacterial strains, fungi, and viruses even at low concentrations [241].

One strategy for incorporating Ag into PEMs has involved treating the PEM film as a nanoreactor within which Ag ions can be incorporated directly during the assembly process and subsequently reduced to form Ag nanoparticles. By utilizing the excess charged groups naturally present in all PEMs, the ion-exchange/reduction approach can be extended to incorporate nanoparticles into PEMs fabricated from any polyelectrolyte. For example, Zan and Su [242] developed a facile approach for the fabrication of transparent antimicrobial coatings based on poly(diallyldimethylammonium chloride)/poly(styrene sulfonate) (PDDA/PSS) PEMs. In brief, a PDDA/PSS multilayer film was immersed in a silver nitrate ( $\text{AgNO}_3$ ) solution to introduce Ag ions into the PEM, which were converted into Ag nanoparticles *in situ* by treating with a freshly prepared sodium borohydride ( $\text{NaBH}_4$ ). The antibacterial efficacy of the films against *Escherichia coli* (*E. coli*) was assessed by the Kirby–Bauer method. The PEMs containing Ag in the ionic form exhibited high activities in short terms while the PEMs loaded with Ag nanoparticles showed lower initial bactericidal effects, but remained active after long periods of time. Combining the two Ag form, it could be possible to develop PEMs with high initial antimicrobial efficacy as well as long-term performance. A similar approach was also adopted by Agarwal and co-workers [243], who loaded Ag nanoparticles in PEM films of PAH and poly(acrylic acid) (PAA).

Preformed silver nanoparticles have also been assembled into multilayers during the dipping-assembly process [244].

In the context of metallic materials with antimicrobial properties, Zhou and co-workers [245] developed a potential long-term antibacterial coating through the alternate deposition of negatively charged gold nanoparticles (GNP) and positively charged lysozyme (Lys) on highly porous electrospun cellulose nanofibrous mats. Lys is a natural enzyme and, as part of the innate immune system, one of its major functions *in vivo* is against infection [246]. GNP have been extensively used in biological applications due to their biocompatibility, low size (<50 nm) and ease of characterization [247], and they have been shown to exhibit good antimicrobial effects [248]. The antibacterial bioactivity against *E. coli* and *Staphylococcus aureus* (*S.*

*aureus*) of uncoated and LbL coated cellulose nanofibrous mats was determined. Uncoated cellulose mats hardly showed inhibitory effect while functionalized mats revealed significant antibacterial activity, which was enhanced with increasing the numbers of bilayers.

In addition to Ag and GNP, releasable antibiotics have been incorporated into PEMs. Chlorhexidine (CX) is a promising candidate antimicrobial agent for incorporation into wound dressings. It is considered the “gold standard” antiseptic that is active against gram-positive/gram-negative bacteria, facultative anaerobes/aerobes, molds, yeasts and viruses [249]. It exhibits both immediate bactericidal effect and excellent residual effect, which prevents reestablishment of microorganisms on the skin [250]. Agarwal et al. [251] functionalized the wound-contact surface of a synthetic biologic dressing with antibacterial nanofilms containing CX. The PEMs was composed of PAH and PAA, and cationic chlorhexidine acetate. In a full-thickness ‘splinted’ dermal wound-model in normal wild-type mice, the CX-functionalized dressing showed no decrease in either its adherence to the wound-bed or wound closure rate over 14 days. Significantly, CX/PEMs reduced viable counts of *S. aureus* by 3 log<sub>10</sub> within 3 days in murine wounds incubated with bacteria, compared to persistent bacterial colonization observed in wound treated with unmodified dressing.

Another antibiotic commonly used to treat infections is gentamicin, an aminoglycoside antibiotic most effective against gram-negative bacteria, but also efficacious against certain gram-positive species such as *S. aureus* [252]. Chuang and co-workers [253] tried to develop an antimicrobial coating that can both discourage bacteria attachment to the implant surface and be able to release gentamicin into the surrounding tissues at a tunable dosage and rate. The researchers studied the possibility to construct a hydrolytically degradable thin film via the LbL deposition of poly( $\beta$ -amino ester)s, HYA and gentamicin. The PME film demonstrated to have *in vitro* efficacy against *S. aureus* proliferation, comparable to those of positive controls of direct gentamicin administration.

An alternative strategy that could be adopted to ensure the safety of wound healing dressing is the surface functionalizations of biomaterial with antibacterial polymer or peptides. Over many years, the cytotoxic properties of polycations in solution have been documented [254]; as a result, antibacterial strategies based on surface immobilized polycations have been widely explored [255, 256].

Among common synthetic polyelectrolytes, polyethylenimine (PEI) has intrinsic antibacterial property, as demonstrated in different studies [257, 258]. He and Chan [259] developed a stable PEM films by covalent LbL assembly of PEI, followed by *in situ* reduction of Ag ions. The covalent build up of PEI layers has been carried out through the use of a chemical cross-linker,

terephthalaldehyde (TA), while Ag nanoparticles were incorporated into PEI multilayers through *in situ* reduction of  $\text{Ag}^+$  by the pre-absorption of  $\text{NaBH}_4$ . The antibacterial properties of PEI multilayer in the presence or absence of embedded Ag nanoparticles were measured by several standard assays. The live/dead bacterial assay showed that PEI multilayer film possessed considerable antimicrobial property against *S. aureus* and *E. coli* upon contact formation. The inclusion of Ag nanoparticles in PEI film not only increased to over 99% its contact killing efficiency but also led to the inhibition of the bacteria growth in suspended culture via the long-term release of  $\text{Ag}^+$  into the liquid medium.

Another synthetic polyelectrolyte with antibacterial property is the polyhexamethylene biguanide (PHMB), a positively charged polymer with a broad-spectrum of antimicrobial effects toward gram-positive and gram-negative bacteria, fungi, yeast, and human immunodeficiency virus type 1 (HIV-1) [260]. For biomedical applications, PHMB has been assessed as one of the most suitable antiseptic agents for clinical practice, due to its non- or low-toxicity to human cells [261, 262]. Tang and co-workers [263] developed a LbL nanocoating on PCL fiber surface composed of PHMB and PAA. The uniform coating showed excellent antibacterial ability, but had no toxicity on mammalian cells. PCL fibrous matrix with electrostatically self-assembled PHMB coating may provide a new anti-infective tissue scaffold for various biomedical applications.

CH is a natural biocompatible cationic polysaccharide and a weak polyelectrolyte, whose antibacterial activity has received considerable attention in recent years. Although many mechanisms of action have been proposed, CH and its derivatives have been shown to bind to the negatively charged bacterial cell membrane and cause leakage, both when used in solution and when immobilized on surfaces [264]. Yu et al. [265] combined the widely described antimicrobial properties of Ag nanoparticles and CH to improve the antibacterial activity of a PLLA membrane. The polysaccharide PEMs included CH and dextran sulfate (DS)-stabilized silver nanosized colloid (DSS). The non-cytotoxic DS and dextrose served as stabilizer and reducing agent, respectively to form well-distributed Ag nanosized colloid (DSS). Bactericidal activity against Methicilin-resistant *S. aureus* was evidenced by PLLA-PEM membranes.

Finally, Pinto et al. [266] explored the use of a negatively charged antibacterial agent as a possible surface active agent. The researchers have been able to incorporate the pseudo-polyelectrolyte, poly(4-vinylphenol) (PVPh) onto multilayered systems with both weak and strong polycation, respectively PAH and PDDA. Phenol is a strong disinfectant that is used as the standard to which other antimicrobials are compared [267]. The study showed that the antimicrobial nature of PEM films was pH dependant. Both PAH/PVPh and PDDA/PVPh

systems were able to inhibit the growth of the Gram (+) bacteria, *S. epidermidis*, by 60–70%, respectively, when assembled at a pH of 10.5; however they both showed very little activity towards the Gram (–) *E. coli* bacteria.

Designing a multifunctional surface by composition of anti-adhesion and contact killing polyelectrolytes may represent a viable chance to ensure the safety of wound healing dressing. For example, Wang et al. [268] developed a stable PEMs coating that combines the anti-adhesion property of poly(vinyl pyrrolidone) (PVP) and contact killing ability of CH. Adherences of *S. aureus* and *E. coli* on substrate with CH/PVP coating were significantly reduced. Bactericidal activity of CH/PVP coatings was good against *E. coli* and *S. aureus* and the addition of PVP increased its anti-adhesion property. *In vitro* cytotoxicity tests, cell morphology and activity evaluation of human umbilical vein endothelial cells showed that CH/PVP coatings had also good biocompatibility. Mei et al. [269] developed antibacterial polyacrylonitrile nanofibrous membranes by combining the anti-adhesive property of heparin (HE) with the antibacterial property of polyhexamethylene guanidine hydrochloride (PHGH). It was found that these LbL-modified nanofibrous membranes possessed high antibacterial activities against Gram-positive bacterium *S. aureus* and Gram-negative *E. coli*.

In conclusion, PEMs can be tailored to leverage the key advantages of bacterial adhesion resistance, contact killing, and biocide leaching strategies. Moreover, the addition of biocide leaching to contact killing PEMs can significantly improve antibacterial efficacy.

## **1.10 Mussel-inspired coatings: definition and state of the art**

In recent years, mussel adhesive proteins (MAPs) excreted by marine mussels have attracted much attention for their ability to form strong adhesive interaction with various substrates in wet environment [270].

Mussels are promiscuous fouling organisms and have been shown to attach to virtually all types of inorganic and organic surfaces [271], including classically adhesion-resistant materials such as PTFE. Clues to mussels' adhesive versatility may lie in the amino acid composition of proteins found near the plaque-substrate interface, which are rich in 3,4-dihydroxy-DL-phenylalanine (DOPA) and lysine amino acids (Fig. 1.12) [272]. Proteins found in the mussel adhesive plaque, *Mytilus edulis* foot protein (Mefp), were largely characterized and six of them were identified to present a DOPA content ranging from 3 mol% (Mefp-2) to 30 mol% (Mefp-5).

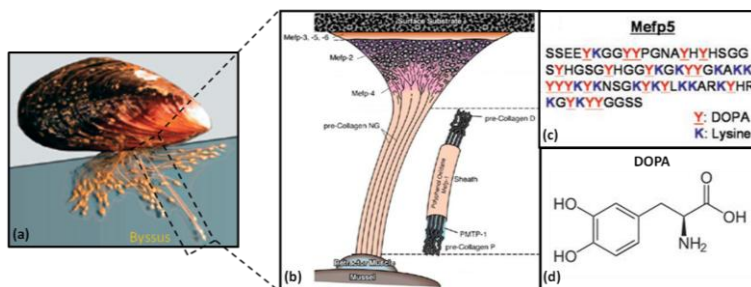


**Fig. 1.12** (a) Photograph of a mussel attached to a mica surface, (b) schematic illustrations of the interfacial location of adhesive related proteins identified in the byssus of *M. edulis* [273], (c) amino acid sequence of Mefp-5 [274], (d) DOPA contains both amine and catechol functional groups found in Mefp-5 and was used as a molecular building block for polymer coatings.

Specific adhesion mechanism of these small molecules to a large panel of surfaces is still not completely understood. It has been studied for many years and several proposals of interaction modes can be found in the literature [275]. However in all cases, covalent or strong non-covalent interactions (hydrogen bonds or  $\pi$ - $\pi$  stacking interactions for instances) can be found between catechol groups and inorganic substrates [276]. Inspired by the adhesive proteins secreted by mussels for attachment to wet surfaces, the interest for an attachment strategy based on catecholic chemistry [275] has increased, opening the door to the design of new (multi)functional platforms based on catechols.

Lee et al. [277] proposed a convenient and versatile method for the surface modification of various solid materials by just immersing the substrate in a DOPA solution for a few hours, resulting in spontaneous deposition of a thin adherent polymer film (polyDOPA) whose thickness was a function of the immersion time and the polymerization temperature. Moreover, to avoid non-specific microparticle deposition on surfaces, stirring and/or vertical sample orientation was necessary.

Although the exact polymerization mechanism is unknown at this time, it is likely to involve oxidation of the catechol to a quinone group which further participate in the functionalization process. In general, the polymerization process should include oxidation, intramolecular cyclisation and rearrangement of the DOPA structure as reported in Fig. 1.13. The reaction with other catechol/quinone and amine functions results then in a cross-linking polymer film [278, 279].

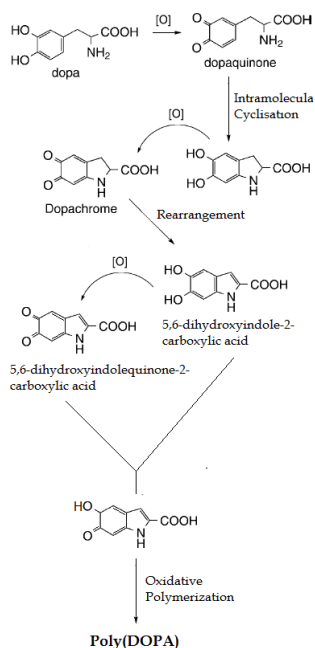


**Fig. 1.13** The scheme of DOPA polymerization process.

The polyDOPA coating is able to form on virtually all types of material surfaces: metals such as gold [280], platinum [281], stainless steel [282], nitinol [283] and titanium [284]; ceramics such as zirconia [285] and TCP [286]; synthetic polymers such as polyethersulfone (PES) [287], poly(vinylidene fluoride) (PVDF) [288], PLLA [289], PLGA [178]; natural polymers such as CH [290]. Then, the polyDOPA coating can further support a variety of secondary reactions, leading to tailoring of the coating for diverse functional uses. For example, the metal-binding ability of catechols [283, 291] present in the polyDOPA coating was exploited to deposit adherent and uniform metal coatings onto substrates by electroless metallization. This was demonstrated through deposition of silver metal nanoparticles via dip-coating of polyDOPA coated objects into silver nitrate solutions (Fig. 1.15 A). Based on these remarkable binding properties toward metal ions, different research groups have also used polyDOPA coatings as templates for the formation of HAp by co-precipitation of calcium and phosphate ions [282, 292].

PolyDOPA coatings were also exploited to graft various (bio)macromolecules (Fig. 1.14 B, C) for the creation of functional ad-layers. Under oxidizing conditions, catechols react with thiols and amines via Michael addition or Schiff base reactions. These can either favor cell adhesion and improve blood compatibility by grafting heparin or bovine serum albumin (BSA) [293-295] or avoid protein adhesion with poly(ethylene glycol) (PEG) [296].

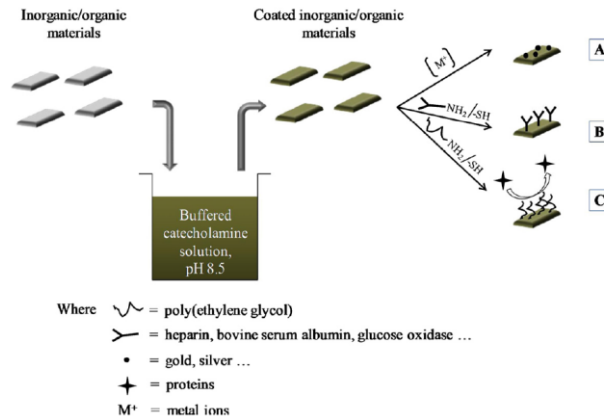


**Fig. 1.14** PolyDOPA coating and further derivatizations.

In this context, mussel-inspired coatings can be used to improve biocompatibility and/or osteoinductive/osteoconductive properties of GTR/GBR membranes by grafting bioactive compounds. Rim et al. [289] developed functionalized PLLA electrospun fibers using a mussel-inspired surface coating (PD-PLLA) to regulate adhesion, proliferation and differentiation of human mesenchymal stem cells (hMSCs). They also examined the effect of the modified surface on the osteogenic differentiation of hMSCs. The homogeneous coating modulated hMSC responses in several aspects. Firstly, adhesion and proliferation of hMSCs cultured on PD-PLLA were significantly enhanced relative to those on PLLA. In addition, it enhanced osteogenic differentiation and calcium mineral deposition for up to 14 days of culture. These results suggested that the bio-inspired coating synthetic degradable polymer is a very promising tool to regulate stem cell function, which may serve as an effective osteoinductive material for engineering bone tissue in GBR applications.

Insufficient osteoconductive ability and bacterial infections may lead to the failure of membranes for periodontal regeneration. Lee and co-workers [284] studied a functionalization method able to enhance osteoblast functions, while simultaneously decreasing bacterial infections. The coating has been developed on titanium (Ti) discs as schematically reported on Fig. 1.15. Substrates were first functionalized with heparin-dopamine by mimicking a mussel adhesion mechanism and, then, gentamicin sulfate (GS) and/or BMP-2 were sequentially immobilized to the heparinized-Ti (HE-Ti) surface.

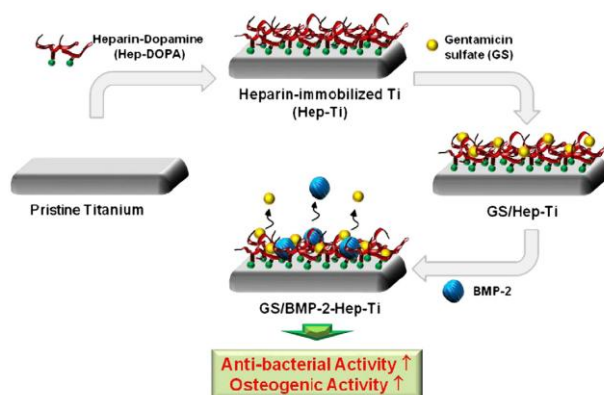


**Fig. 1.15** Schematic diagram for the immobilization of GS and BMP-2 to heparinized-Ti substrate [284].

Antimicrobial activity assay showed that the growth of *S. aureus* on GS/HE-Ti and GS/BMP-2/HE-Ti was significantly lower compared to that on the pristine Ti and BMP-2/HE-Ti. In addition, *in vitro* cell test revealed that BMP-2/HE-Ti and GS/BMP-2/HE-Ti significantly enhanced alkaline phosphatase (ALP) activity and calcium mineral deposition of MG 63 osteoblast cells. Taken together, GS/BMP-2/HE-Ti could achieve the dual functions of excellent antibacterial activity and osteoblast function promotion. Therefore, dual drug (antibiotics and osteoinductive protein)-eluting Ti substrates such as GS/BMP-2/HE-Ti could be a promising material for the enhanced osteointegration and implant longevity in periodontal applications. The same goal has been reached by Saidin et al. [282] through a multistep process of dopamine polymerization, Ag metallization and HAp biomineralisation on stainless steel (SS316L) substrates (Fig. 1.16). The SS316L substrates were first pre-treated and grafted with polydopamine through a self-polymerization technique. The Ag nanoparticles were then metallized on the polydopamine film at different immersion times in AgNO<sub>3</sub> solution, followed by the formation of second polydopamine coating layer. Finally, HAp biomineralisation was performed in 1.5 Simulated Body Fluid (SBF) solution. The presence of Ag conferred antibacterial properties with 97.9% of bactericidal ratio against *E. Coli* after 24 h. Moreover, Ag was ionised up to 7 days which is crucial to prevent bacterial infection during the first stage of implant restoration. The functionalized films were stable with not significant alteration of their chemical composition, surface roughness and wettability properties after incubation in PBS for 7 days.

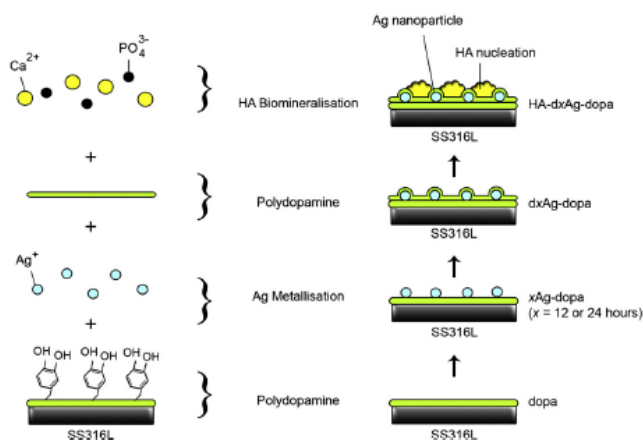


**Fig. 1.16** Schematic illustration of dopamine polymerization, Ag metallization and HAp biominaleralisation on SS316L [282].

Finally, Chen et al. [297] took advantage of polyDOPA coatings ability to graft various biomacromolecules to improve cell response. A novel GBR membrane has been developed through the immobilization of a collagen/chitosan (COL/CH) composite on dopamine modified PLGA, to mimic ECM. The composite membrane retained mechanical properties from PLGA and biological properties from the COL/CH composites. However, diverse ratios of COL/CH displayed different microstructures and effects on cell behavior and proliferation (COL facilitated cell adhesion and spread while CH decreased both). A critical ratio of COL/CH (2:1) above which the addition of CH only slightly impacted cell proliferation was found. The results should be useful for combining versatile materials from different origins to construct GBR membranes and to further optimize the ratio of COL/CHI composites.

Table 1.3 summarized the properties of membranes from literature discussed in previous paragraphs.

**Table 1.3** Resorbable membranes from the State of the Art analysis.

<b>Material</b>	<b>Fabrication Technique</b>	<b>Structure</b>	<b>Properties</b>	<b>Reference</b>
n-HAp/CH	Solvent casting	Compact film	Good biocompatibility $\sigma_{\max} = 29.3\text{-}65.2$ MPa; $\epsilon_{\max} = 6\text{-}18.5\%$	152
PLGC/TCP	Heat-kneading	Compact film	Good regeneration of beagles' mandibular bones Resorption: 24 weeks $\sigma_{\max} = 1\text{-}16$ MPa	12
PLA/Bioglass	Thermally induced phase separation	Foam	High bioactivity	155
Alginate/nBGC	Freeze-drying	Porous scaffold	Good biocompatibility Limited degradation after 4 weeks 100-300 $\mu\text{m}$ pores	156
PLLA/HAp	Electrospinning	Electrospun membrane	Improved cells adhesion and growth Limited degradation after 8 weeks 313 nm fiber diameters $E \sim 118$ MPa; $\sigma_{\max} \sim 3$ MPa; $\epsilon_{\max} \sim 6\%$	157
A187-HAp/PCL	Electrospinning	Electrospun membrane	Good bioactivity Non-toxic to fibroblasts and osteoblasts $E \sim 8$ MPa; $\sigma_{\max} \sim 5$ MPa; $\epsilon_{\max} \sim 70\%$	158
PCL/Bioglass nanofibers	Solvent casting	Compact film	Rapid formation of apatite-like minerals on the surface High osteoblastic activity 260 $\mu\text{m}$ thick	159
PLCL, PLA, G, HAp, MET	Electrospinning	Three-layer membrane	Open porosity, interconnected structures $E \sim 38$ MPa; $\sigma_{\max} \sim 2$ MPa; $\epsilon_{\max} \sim 234\%$	126
PLGA/CaP	Solvent-casting-leaching	Bi-layer membrane	No collapse into the defect Inner side able to retain blood clot throughout the buccal defect	161
nCHAC/PLGA	Solvent casting	Three-layer membrane	Excellent biocompatibility	162

			300-400 $\mu\text{m}$ thick $E \sim 1 \text{ GPa}$ ; $\sigma_{\text{max}} \sim 10 \text{ MPa}$ ; $\epsilon_{\text{max}} \sim 249\%$	
HYA-PLGA/PLGA	Solvent casting	Bi-layer membrane	Limited degradation after 8 weeks Effective bone regeneration	87
PLLA-CH	Electrospinning	Electrospun membrane	Limited degradation after 6 weeks Good biocompatibility Prevent fibroblasts invasion 115 nm fiber diameters 280 nm pores	171
CH-BMP-2	Solvent casting	Compact film	Limited degradation after 3 weeks Osteoblast attachment, proliferation, differentiation $E \sim 50 \text{ MPa}$ ; $\sigma_{\text{max}} \sim 6 \text{ MPa}$	169
PD-PLLA	Electrospinning	Electrospun membrane	Enhanced cells adhesion and proliferation Enhanced osteogenic differentiation and calcium mineral deposition	289
PLGA-COL/CH	Solvent casting	Compact film	COL/CH ratios different effects on cell behaviour $E \sim 8 \text{ GPa}$ ; $\sigma_{\text{max}} \sim 50 \text{ MPa}$	297

## **1.11 Factors influencing the success of GTR/GBR**

Factors that may limit regenerative healing after GTR/GBR surgery can be categorized into [298]:

- barrier-independent factors (i.e. poor plaque control, smoking, occlusal trauma, suboptimal tissue health, mechanical habits that interfere with healing, inadequate overlying keratinized tissue and tissue thickness improper surgical technique, premature plaque colonization and early mechanical insult, loss of wound stability);
- barrier-dependent factors (i.e. inadequate root-barrier seal, non-sterile technique, instability of membrane, premature membrane exposure/loss).

Several studies have demonstrated the importance of patient selection, plaque control, and anti-infective therapy in achieving consistently positive results with GTR procedures. Favorable clinical results have been most often observed in healthy, non-smoking patients demonstrating good plaque control and compliance with recommended oral hygiene measures [298]. The effects of bacterial contamination have been noted in a study of Selvig et al. [299], reporting an inverse relationship between observed plaque contamination of retrieved membranes and clinical attachment gain. Colonization of membranes with black pigmented species [300] and the presence of bacteria in samples treated with regenerative procedures correlates with a diminished healing response [301, 302]. However, a recent report conducted by Machtei et al. [303] indicates that membrane exposure had only a minimal effect on GTR results around natural teeth.

Important defect-specific factors include the number of bony walls and the depth of the intrabony component. Gingival tissue thickness has also been linked to reduce clinical outcomes in GTR, including GTR-based root coverage procedures, with thin tissues achieving significantly less clinical improvements and percentages of root coverage [304, 305].

Identification of the influencing factors should lead to more predictable treatment outcomes following GTR procedures through better patient and defect selection.

## **1.12 Thesis goal**

*The main purpose of this work is the development of biologically active membranes and nanocoatings, with improved osteoconductive and antimicrobial properties, for Guided Tissue/Bone Regeneration applications in periodontal diseases.*

Periodontitis is a chronic inflammatory pathology that can jeopardize the integrity of tooth support and ultimately, lead to tooth loss. To date, flap debridement and/or flap curettage and periodontal regenerative therapy with membranes and bone grafting materials have been employed with distinct levels of clinical success.

Current resorbable and non-resorbable membranes act as a physical barrier to avoid connective and epithelial tissue down-growth into the defect, favoring the regeneration of periodontal tissues. As reported in this chapter, the ePTFE membranes are the “gold standard” for GTR/GBR applications. However, they have different disadvantages such as non-resorbability and the need for a second surgical operation to repair dehiscence. In this work, two different approaches were proposed to improve non-resorbable membranes properties and to avoid a second surgical operation, respectively by using surface-functionalized (i) high-density PTFE membranes and (ii) resorbable membranes, combining synthetic and natural biomaterials. Although membranes based on biodegradable synthetic polymers avoid a second surgical operation, they show drawbacks concerning their capacity of space maintenance, early/late absorption, mechanical properties and bacterial infection during degradation. On the other hand, collagen membranes have additional advantages related to biological properties of collagen itself (cell adhesiveness and biodegradability) but are characterized by low mechanical strength. It is clear that the “ideal” membrane for use in periodontal regenerative therapy has yet to be developed. Based on the State of the Art analysis, research efforts have been addressed to the preparation of (i) composites consisting of osteoconductive calcium phosphate ceramics and biodegradable polymers, (ii) multi-component membranes with specific properties at the interface between the implant and alveolar bone and epithelial tissues, and (iii) surface modification of synthetic polymers to graft bioactive proteins or biomolecules. The introduction of specific cell-adhesion molecules should lead to a specific tissue response on the membrane surfaces, the delivery or incorporation of antimicrobial substances might minimize the influence of bacterial contamination on regenerative outcome and the growth factor release from membranes should stimulate a better bone regeneration.

In this context, the thesis is aimed at the design of advanced products for GTR/GBR applications.

The first part of the thesis follows a more traditional approach, where a commercially available membrane is surface modified by environmentally friendly technique to tailor the surface properties, allowing rapid bone re-growth and exerting antimicrobial action (Fig. 1.17). To this purpose, PTFE film surface is modified by a mussel-inspired coating method, involving the application of a thin film coating of DOPA on a substrate via dip-immersion and oxidative

polymerization. Based on it, the osteoconductive property of PTFE film is improved by the deposition of a HAp film, that may occur by binding of DOPA to the HAp nanoparticles during the DOPA polymerization process. Regarding the antimicrobial activity, the polyDOPA layer on PTFE film allows further deposition of silver nanoparticles, without the addition of reducing agents, surfactants, or energy-consuming steps.

The physicochemical, morphological and biological properties of coated samples are then evaluated through different techniques, such as X-Ray photoelectron spectroscopy, scanning electron microscopy, atomic force microscopy, water contact angle measurements, and cell proliferation and adhesion.

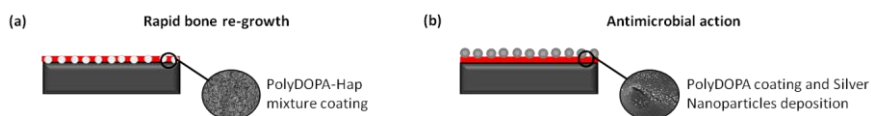


**Fig. 1.17** Not-absorbable PTFE membranes surface modified by mussel-inspired coating methods to (a) allow rapid bone re-growth and (b) exert antimicrobial action.

The second part of the thesis follows a highly innovative approach, where a bi-layered bioabsorbable membrane is developed, by the assembly of a compact and a porous layer (Fig. 1.18). The purpose is to combine the approaches identified in the scientific literature, developing biologically active, osteoconductive and multi-component materials, mimicking native bone and gingival ECM. The multifunctional membranes represent the next generation of GTR/GBR membranes for periodontal tissue engineering.

This work is divided into three parts.

1. Development of the compact layer: poly(DL-lactide-co- $\epsilon$ -caprolactone) and poly(DL-lactide-co-glycolide) are selected as polymers to prepare binary blends. Different compositions are studied to find those with suitable mechanical and biological properties for the application. Then, a nanocoating is deposited on optimized blend film with the aim to tailor surface composition to enhance cell response and antimicrobial activity. To this purpose, a surface priming treatment is performed on substrates to allow the deposition of nanocoating and Layer-by-layer technique is used to obtain nanostructured coating.
2. Development of the porous layer: sponge-like membranes based on TCP as the inorganic phase, stimulating the biomineralisation, and chitosan/gelatin blend as the organic phase, supporting cell adhesion and proliferation, are developed by freeze-drying. A double cross-linking process is introduced with the aim to improve membranes stability in physiological environment. Membranes are then characterized in terms of physicochemical, morphological and mechanical properties.

3. Development of the bi-layered device: a biomedical glue based on polyvinylpyrrolidone and polyethylene glycol blend is employed to assemble the two layers. Physicochemical and adhesion properties of glue are evaluated. Then, preliminary characterizations of the bi-layered membrane are carried out.

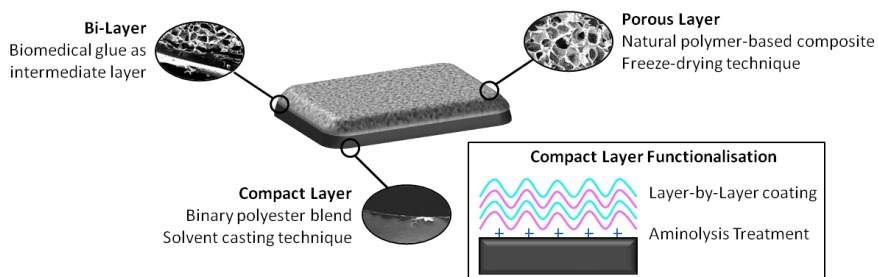


**Fig. 1.18** Functionalized bi-layered bioabsorbable membrane consisting of a compact and a porous layer, assembled with a biomedical glue.

## References

---

1. Pihlstrom BL, et al. *Lancet* 2005;**366**:1809-1820.
2. Nakashima M, et al. *Nature Biotech* 2003;**21**:1025-1032.
3. Jung RE, et al. *Clin Oral Impl Res* 2003;**14**:556-568.
4. Yang F, et al. *Acta Biomater* 2009;**5**:3295-3304.
5. Nyman S, et al. *J Clin Periodontol* 1980;**7**:394-401.
6. Melcher AH. *J Periodontol* 1976;**47**:256-260.
7. Buser D, et al. *Int J Periodont Restor Dent* 1993;**13**:29-45.
8. Taguchi Y, et al. *Biomaterials* 2005;**26**:6158-6166.
9. Fujihara K, et al. *Biomaterials* 2005;**26**:4139-4147.
10. Lindhe J, et al. Anatomy of the periodontium. In: Lindhe J, Karring T, Lang NP, eds. *Clinical Periodontology and Implant Dentistry*. Copenhagen, Denmark: Munksgaard Blackwells, 2003.
11. Bottino MC, et al. *Dental Mater* 2012;**28**:703-721.
12. Nanci A, et al. *Periodontol 2000* 2006;**40**:11-28.
13. Saffar JI, et al. *Periodontol 2000* 1997;**13**:76-90.
14. Albandar JM, et al. *Periodontol 2000* 2002;**29**:7-10.
15. Armitage GC. *Ann Periodontol* 1999;**4**:1-6.
16. Hughes FJ, et al. *Proc I Mech E Part H: J Engin Med* 2010;**224**:1345-1358.
17. Dave S, et al. *Compend Contin Educ Dent* 2005;**25**:26-37.
18. Garcia RI, et al. *Periodontol 2000* 2001;**25**:21-36.
19. Joss A, et al. *J Clin Periodontol* 1994;**21**:402-408.
20. Preshaw PM, et al. *Dent Update* 2004;**31**:570-572,574-578.
21. Listgarten MA. *J Periodontol* 1976;**47**:1-18.
22. Ramberg P, et al. *J Clin Periodontol* 2003;**30**:990-95.
23. Socransky SS, et al. Microbiology of periodontal disease. In: Lindhe J, Karring T, Lang NP, eds. *Clinical Periodontology and Implant Dentistry*. Copenhagen, Denmark: Munksgaard Blackwells, 2003.
24. Socransky SS, et al. *Periodontol 2000* 1994;**5**:7-25.
25. Mandell RL, et al. *J Periodontol* 1981;**52**:593-98.
26. Johnson GK, et al. *J Dent Educ* 2001;**65**:313-21.
27. Bergstrom J. *Odontology* 2004;**92**:1-8.
28. Tezal M, et al. *J Clin Periodontol* 2004;**31**:484-88.
29. Enwonwu CO, et al. *Crit Rev Oral Biol Med* 2000;**11**:159-71.
30. Taylor GW. *Ann Periodontol* 2001;**6**:99-112.
31. Salvi GE, et al. *J Clin Periodontol* 1997;**24**:8-16.
32. Gustke CJ, et al. *J Dent Res* 1998;**77**:1497-503.
33. Kassab MM, et al. *J Am Dent Assoc* 2003;**134**:220-225.
34. Felipe M, et al. *J Periodontol* 2007;**78**:1209-1217.

- 
35. Santos A, et al. *J Periodontol* 2005;**76**:1982-1990.
  36. Sreenivasan P, et al. *J Clin Periodontol* 2002;**29**:965-974.
  37. Loe H, et al. *J Periodontol* 1965;**36**:177-187.
  38. Axelsson P, et al. *J Clin Periodontol* 2004;**31**:749-757.
  39. Sculean A, et al. *J Clin Periodontol* 2008;**35**:106-116.
  40. Wang HL, et al. *J Periodontol* 2005;**76**:1601-1622.
  41. Drisko CH. *Periodontol 2000* 2001;**25**:77-88.
  42. Hanes PJ, et al. *Ann Periodontol* 2003;**8**:79-98.
  43. Polimeni G, et al. *Periodontol 2000* 2006;**41**:30-47.
  44. Leong KF, et al. *J Mech Behav Biomed Mater* 2008;**1**:140-52.
  45. Clark RA. *Dermatol Clin* 1993;**11**:647-666.
  46. Singer AJ, et al. *N Engl J Med* 1999;**341**:738-746.
  47. Clark RAF. Wound repair. Overview and general considerations. In: Clark RAF, editor. *The Molecular and Cellular Biology of Wound Repair*, 2nd ed. New York, NY: Plenum Press, 1996:3-50.
  48. Martin P. *Science* 1997;**276**:75-81.
  49. Oberyszyn TM. *Front Biosci* 2007;**12**:2993-2999.
  50. Aukhil I. *Periodontol 2000* 2000;**22**:44-50.
  51. Häkkinen L, et al. *Periodontol 2000* 2000;**24**:127-152.
  52. Bates P, et al. Bone injury, healing and grafting. In: Ramachandran M, eds. *Basic Orthopaedic Sciences. The Stanmore Guide*, London: Hodder Arnold, 2007:123-134.
  53. Einhorn TA. *Clin Orthop Relat Res* 1998;**355**:S7-S21.
  54. Cho TJ, et al. *J Bone Miner Res* 2002;**17**:513-520.
  55. Hämmerle CHF, et al. *Periodontol 2000* 1998;**17**:151-175.
  56. Bauer TW, et al. *Clin Orthop Relat Res* 2000;**371**:10-27.
  57. Hämmerle CHF, et al. *J Oral Maxillofac Surg* 1995;**53**:167-174.
  58. Kostopoulos L, et al. *Clin Oral Implants Res* 1994;**5**:245-253.
  59. Schenk RK, et al. *Int J Oral Maxillofac Implants* 1994;**9**:13-29.
  60. Hämmerle CHF, et al. *Clin Oral Implants Res* 1996;**7**:38-47.
  61. Cortellini P, et al. *Periodontol 2000* 2000;**22**:104-132.
  62. Ramseier CA, et al. *Periodontol 2000* 2012;**59**:185-202.
  63. McCulloch CA. *Periodontol 2000* 1993;**1**:16-25.
  64. Jung RE, et al. *Clin Oral Implants Res* 2006;**17**:426-433.
  65. Dereka XE, et al. *Growth Factors* 2006;**24**:260-267.
  66. Kaigler D, et al. *Expert Opin Drug Deliv* 2006;**3**:647-662.
  67. Printz MA, et al. *Hum Gene Ther* 2000;**11**:191-204.
  68. Reynolds MA, et al. *Ann Periodontol* 2003;**8**:227-265.
  69. McAllister BS, et al. *J Periodontol* 2007;**78**:377-396.

- 
70. Johansson B, et al. *Dentomaxillofac Radiol* 2001;**30**:157–161.
  71. Young MP, et al. *Clin Oral Implants Res* 2001;**12**:95–103.
  72. Reddi AH, et al. *Orthop Clin North Am* 1987;**18**:207–212.
  73. Richardson CR, et al. *J Clin Periodontol* 1999;**26**:421–428.
  74. Stavropoulos A, et al. *J Periodontol* 2010;**81**:325–334.
  75. Stahl SS, et al. *J Periodontol* 1986;**57**:211–217.
  76. Daly CG. *J Clin Periodontol* 1982;**9**:386–392.
  77. Garrett JS, et al. *J Periodontal Res* 1978;**13**:155–163.
  78. Mariotti A. *Ann Periodontol* 2003;**8**:205–226.
  79. Fuentes P, et al. *J Clin Periodontol* 1993;**20**:425–430.
  80. Blomlof J, et al. *J Clin Periodontol* 1997;**24**:534–537.
  81. Blomlof J, et al. *J Clin Periodontol* 1996;**23**:50–55.
  82. Gestrelus S, et al. *Clin Oral Investig* 2000;**4**:120–125.
  83. Cortellini P, et al. *J Periodontol* 2005;**76**:341–350.
  84. Sculean A, et al. *Med Princ Pract* 2007;**16**:167–180.
  85. Trombelli L, et al. *J Clin Periodontol* 2008;**35**:117–135.
  86. Kikuchi M, et al. *Biomaterials* 2004;**25**:5979–5986.
  87. Park JK, et al. *Acta Biomater* 2009;**5**:3394–3403.
  88. Sculean A, et al. *J Clin Periodontol* 2008;**35**:106–116.
  89. Tonetti MS, et al. *J Clin Periodontol* 1996;**23**:548–556.
  90. Stavropoulos A, et al. *Clin Oral Investig* 2004;**8**:226–232.
  91. Urist MR. *Science* 1965;**150**:893–899.
  92. Ripamonti U, et al. *J Periodontal Res* 1994;**29**:439–445.
  93. King GN, et al. *J Periodontal Res* 1998;**33**:226–236.
  94. Howell TH, et al. *Int J Periodontics Restorative Dent* 1997;**17**:124–139.
  95. Talwar R, et al. *J Clin Periodontol* 2001;**28**:340–347.
  96. Nevins M, et al. *J Periodontol* 2005;**76**:2205–2215.
  97. Herberg S, et al. *J Clin Periodontol* 2008;**35**:976–984.
  98. Baum BJ, et al. *Immunol Lett* 2003;**90**:145–149.
  99. Jin Q, et al. *Mol Ther* 2004;**9**:519–526.
  100. Jin QM, et al. *J Periodontol* 2003;**74**:202–213.
  101. Cirelli JA, et al. *Gene Ther* 2009;**16**:426–436.
  102. Chen YL, et al. *Gene Ther* 2008;**15**:1469–1477.
  103. Tan Z, et al. *Cytotherapy* 2009;**11**:317–325.
  104. Hitti RA, et al. *The Open Pathol J* 2011;**5**:33–45.
  105. Gottlow J, et al. *J Clin Periodontol* 1984;**11**:494–503.
  106. Dahlin C, et al. *Plast Reconstr Surg* 1988;**81**:672–676.

- 
107. Dahlin C, et al. *Int J Oral Maxillofac Implants* 1989;**4**:19-25.
  108. Farzad M, et al. *J Oral Health Oral Epidemiol* 2012;**1**:3-18.
  109. Zhang Y, et al. *Annals Oral Maxillofacial Surg* 2013;**1**:1-10.
  110. Gentile P, et al. *Biotechnol J* 2011;**6**:1187-1197.
  111. Rakhmatia YD, et al. *J Prosthodont Res* 2013;**57**:3-14.
  112. AlGhamdi AS, et al. *J Int Acad Periodont* 2009;**11**:226-231.
  113. Pihlstrom BL, et al. *J Clin Periodontol* 1983;**10**:524-41.
  114. Buser D. Twenty years of guided bone regeneration in implant dentistry. 2nd ed. Chicago, IL: Quintessence; 2009.
  115. Florian A, et al. *Arch Surg* 1976;**111**:267-270.
  116. Simion M, et al. *Clin Oral Implants Res* 1999;**10**:73-84.
  117. Villar CC, et al. *Dent Clin North Am* 2010;**54**:73-92.
  118. Zhao S, et al. *J Craniomaxillofac Surg* 2000;**28**:116-122.
  119. Zwahlen RA, et al. *Clin Oral Implants Res* 2009;**20**:1084-1091.
  120. Tempro PJ, et al. *J Periodontol* 1993;**64**:162-168.
  121. Bartee BK. *Implant Dent* 1995;**4**:21-26.
  122. Marouf HA, et al. *Oral Surg Oral Med Oral Pathol Oral Radiol Endod* 2000;**89**:164-70.
  123. Jovanovic SA, et al. *Int J Periodont Restor Dent* 1995;**15**:56-69.
  124. Lindfors LT, et al. *Oral Surg Oral Med Oral Pathol Oral Radiol Endod* 2010;**109**:825-830.
  125. Watzinger F, et al. *Br J Oral Maxillofac Surg* 2000;**38**:312-315.
  126. Bottino MC, et al. *Acta Biomater* 2011;**7**:216-224.
  127. Zellin G, et al. *Biomaterials* 1995;**16**:601-609.
  128. Miller N, et al. *J Clin Periodontol* 1996;**23**:1051-1059.
  129. Behring J, et al. *Odontology* 2008;**96**:1-11.
  130. Lundgren D, et al. *J Periodontol* 1995;**66**:605-612.
  131. Garg AK. Augmentation and grafting of the maxillary anterior alveolar ridge. In: Garg AK. Ed, Bone biology, harvesting and grafting for dental implants: Rational and clinical application. Quintessence Publishing Co, Inc.; 2004,pp. 213-240.
  132. Ikada Y. Interface and Technology. *Tissue Engineering Fundamentals and Applications*, Academic Press, New York 2006,pp. 189-195.
  133. Pontoriero R, et al. *J Clin Periodontol* 1999;**26**:833-840.
  134. Donos N, et al. *Clin Oral Implants Res* 2002;**13**:203-113.
  135. De Sanctis M, et al. *Int J Periodontics Restorative Dent* 1996;**16**:435-441.
  136. Thoma DS, et al. *Clin Oral Implants Res* 2009;**20**:7-16.
  137. Meek MF, et al. *J Biomed Mater Res* 2004;**68**:43-51.
  138. Hou LT, et al. *J Clin Periodontol* 2004;**31**:68-74.
  139. Camargo PM, et al. *J Periodontal Res* 2002;**37**:300-306.

- 
140. Bilir A, et al. *Clin Oral Implants Res* 2007;**18**:46–52.
  141. Shin H, et al. *Biomaterials* 2003;**24**:4353–4364.
  142. Chen CC, et al. *J Periodontol* 1995;**66**:838–847.
  143. Wang HL, et al. *J Periodontol* 1994;**65**:1029–1036.
  144. Wang HL, et al. *Pract Periodontics Aesthet Dent* 1995;**7**:59–66.
  145. Döri F, et al. *J Clin Periodontol* 2007;**34**:254–261.
  146. Steinberg AD, et al. *J Periodontol* 1986;**57**:516–522.
  147. Postlethwaite AE, et al. *Proc Natl Acad Sci* 1978;**75**:871–875.
  148. Borges GJ, et al. *Clin Oral Implants Res* 2009;**20**:1105–1115.
  149. Oh TJ, et al. *Clin Oral Implants Res* 2003;**14**:80–90.
  150. Kim HW, et al. *J Biomed Mater Res B* 2004;**70B**:240–249.
  151. Yao J, et al. *J Biomed Mater Res A* 2006;**75A**:794–801.
  152. Xianmiao C, et al. *Mater Sci Eng C* 2009;**29**:29–35.
  153. Lu HH, et al. *J Biomed Mater Res A* 2003;**64**:465–474.
  154. Yao J, et al. *Biomaterials* 2005;**26**:1935–1943.
  155. Blaker JJ, et al. *J Biomed Mater Res A* 2003;**67**:1401–1411.
  156. Srinivasan S, et al. *Carb Polym* 2012;**87**:274–283.
  157. Sui G, et al. *J Biomed Mater Res* 2007;**82A**:445–454.
  158. Li L, et al. *J Mater Sci* 2012;**23**:547–554.
  159. Lee HH, et al. *Acta Biomater* 2008;**4**:622–629.
  160. Al-Mubarak SA, et al. *J Int Acad Periodontol* 2000;**2**:64–70.
  161. Reis ECC, et al. *Biomaterials* 2011;**32**:9244–9253.
  162. Liao S, et al. *Biomaterials* 2005;**26**:7564–7571.
  163. Chu PK, et al. *Mater Sc. Eng* 2002;**R36**:143–206.
  164. De Villiers MM, et al. *Advanc Drug Delivery Rev* 2011;**63**:701–715.
  165. Chiono V, et al. 2011. Biomimetic tailoring of the surface properties of polymers at the nanoscale: medical applications. In “Scanning Probe Microscopy in Nanoscience and Nanotechnology”, Part 3 (B. Bhushan, Ed.), Chapter 22, pp. 645–689. Springer-Verlag, Berlin Heidelberg.
  166. Goddard JM, et al. *Prog Polym Sci* 2007;**32**:698–725.
  167. Budiraharjo R, et al. *J Biomater Sci, Polym Ed* 2013;**24**:645–662.
  168. Kang G, et al. *Desalination* 2011;**275**:252–259.
  169. Russo L, et al. *J Mater Sci Mater Med* 2012;**23**:2727–2738.
  170. Zhu YB, et al. *J Biomed Mater Res, Part A* 2004;**69A**:436–443.
  171. Chen S, et al. *J Mater Sci* 2013;**48**:6567–6577.
  172. Lao HK., et al. *Biomacromolecules* 2007;**8**:416–423.
  173. Dos Santos KS, et al. *Int J Pharm* 2006;**310**:37–45.
  174. Guo C, et al. *Eur J Pharm Biopharm* 2008;**70**:597–604.

- 
175. Zhang Y, et al. *Mater Sci Eng C* 2007;**27**:213–219.
  176. Yu DG, et al. *Bioconjugate Chem* 2007;**18**:1521-1529.
  177. Chen G, et al. *J Biomed Mater Res Part A* 2013;**101A**:44–53.
  178. Schmidt TGM, et al. *J Mol Biol* 1995;**255**:753–766.
  179. Klokkevold PR, et al. *Clin Oral Implants Res* 1997;**8**:442–447.
  180. Croll TI, et al. *Biomacromolecules* 2004;**5**:463-473.
  181. Chen JP, et al. *Acta Biomater* 2011;**7**:234–243.
  182. Sartori S, et al. *React Funct Polym* 2008;**68**:809-821.
  183. Wu JD, et al. *Chin Sci Bull* 2009;**54**:3174-3180.
  184. Lin Y, et al. *Acta Biomater* 2006;**2**:155-164.
  185. Kuo JW. Practical aspects of hyaluronan based medical products. Boca Raton, FL: Taylor & Francis 2006:pp. 1–20.
  186. Kotov NA, et al. *Adv Mater* 2006;**18**:3203-3224.
  187. Faure E, et al. *Progr Polym Sci* 2013;**38**:236–270.
  188. Decher G, et al. *Makromol Chem-M Symp* 1991;**46**:321-327.
  189. Decher G, et al. *Ber Bunsen Phys Chem* 1991;**95**:1430-1434.
  190. Ariga K, et al. *Phys Chem Chem Phys* 2007;**21**:2319-2340.
  191. Schlicke H, et al. *Nanotechnology* 2011;**22**:1-9.
  192. Mundra P, et al. *Rev Sci Instrum* 2013;**84**:74-101.
  193. Zhang J, et al. *Biomaterials* 2005;**26**:3353-3361.
  194. Garza JM, et al. *Langmuir* 2005;**21**:12372-12377.
  195. Boulmedais F, et al. *Langmuir* 2003;**19**:440-445.
  196. Saurer EM, et al. *Biomacromolecules* 2010;**11**:3136–3143.
  197. Zhou L, et al. *Appl Mater Interfaces* 2013;**5**:3541–3548.
  198. Ariga K, et al. *J Am Chem Soc* 1997;**119**:2224-2231.
  199. Srivastava S, et al. *Acc Chem Res* 2008;**41**:1831-1841.
  200. Kim YS, et al. *Thin Solid Films* 2014;**550**:184-189.
  201. Teng ZQ, et al. *Adv Mater* 2007;**19**:3687-3691.
  202. Lu YX, et al. *Langmuir* 2010;**26**:17749-17755.
  203. Wang F, et al. *Langmuir* 2007;**23**:9540-9542.
  204. Xu L, et al. *Langmuir* 2011;**27**:409-415.
  205. Welterlich I, et al. *Macromolecules* 2011;**44**:4194-4203.
  206. Ai H, et al. *Cell Biochem Biophys* 2003;**39**:23-43.
  207. Kharlampieva E, et al. *Adv Mater* 2009;**21**:3053-3065.
  208. Decher G. *Science* 1997;**277**:1232-1237.
  209. Kujawa P, et al. *J Am Chem Soc* 2005;**127**:9224-9234.
  210. Lavallo P, et al. *J Phys Chem B* 2004;**108**:635-648.

- 
211. Richert L, et al. *Langmuir* 2004;**20**:448-458.
  212. Laugel N, et al. *J Phys Chem B* 2006;**110**:19443-19449.
  213. Picart C, et al. *Biosens Bioelectron* 2004;**20**:553-561.
  214. Michel M, et al. *Langmuir* 2005;**21**:7854-7859.
  215. Porcel C, et al. *Langmuir* 2006;**22**:4376-4383.
  216. Wazed Ali S, et al. *Polym Comp* 2010;**18**:237-250.
  217. Schoeler B, et al. *Macromolecules* 2002;**35**:889-897.
  218. Warren JC, et al. *Biochemistry* 1966;**5**:1702-1707.
  219. Collins KD, et al. *Q Rev Biophys* 1985;**18**:323-422.
  220. Kolarik L, et al. *Langmuir* 1999;**15**:8265-8275.
  221. Guzmán E, et al. *Soft Matter* 2009;**5**:2130-2142.
  222. Kurt P, et al. *J Mater Chem* 2009;**19**:8920-8927.
  223. Kim YT, et al. *J Electrochem Soc* 1991;**138**:3266-3275.
  224. Erokhina S, et al. *Langmuir* 2008;**24**:12093-12096.
  225. Schwarz B, et al. *Langmuir* 2002;**18**:2964-2966.
  226. Smith RN, et al. *Macromolecules* 2003;**36**:1876-1881.
  227. Yoo D, et al. *Macromolecules* 1998;**31**:4309-4318.
  228. Marx KA. *Biomacromolecules* 2003;**4**:1099-1120.
  229. Lee D, et al. *Langmuir* 2007;**23**:8833-8837.
  230. Wang X, et al. *Biomaterials* 2008;**29**:894-903.
  231. Qifeng Wang HY, et al. *Chem Mater* 2006;**18**:1988-1994.
  232. Stevanović MM, et al. *Polymer* 2012;**53**:2818-2828.
  233. Murata H, et al. *Biomaterials* 2007;**28**:4870-4879.
  234. Nepal D, et al. *Nano Lett* 2008;**8**:1896-1901.
  235. Tedjo C, et al. *J Biomed Mater Res A* 2007;**82**:479-491.
  236. Muszanska AK, et al. *Biomaterials* 2011;**32**:6333-6341.
  237. Malcher M, et al. *Langmuir* 2008;**24**:10209-10215.
  238. Yang SY, et al. *Colloids Surf A* 2008;**313**:526-529.
  239. Shi Z, et al. *J Biomed Mater Res Part A* 2006;**76A**:826-834.
  240. Sanchez-Valdes S, et al. *J Appl Polym Sci* 2009;**111**:953-962.
  241. Marambio-Jones C, et al. *J Nanopart Res* 2010;**12**:1531-1551.
  242. Zan X, et al. *Thin Solid Films* 2010;**518**:5478-5482.
  243. Agarwal A, et al. *Biomaterials* 2010;**31**:680-690.
  244. Podsiadlo P, et al. *Langmuir* 2005;**21**:11915-11921.
  245. Zhou B, et al. *Coll Surf B: Biointer* 2014;**116**:432-438.
  246. Masschalck B, et al. *Crit Rev Microbiol* 2003;**29**:191-214.
  247. Bhattacharya R, et al. *NanoLett* 2004;**4**:2479-2481.

- 
248. Zhao Y, et al. *J Am Chem Soc* 2010;**132**:12349–12356.
  249. Echague C, et al. *Adv Skin Wound Care* 2010;**23**:406–413.
  250. Wu SC, et al. *Int Wound J* 2008;**5**:416–422.
  251. Agarwal A, et al. *Biomaterials* 2012;**33**:6783–6792.
  252. Sax H, et al. *Curr Infect Dis Rep* 1999;**1**:261–266.
  253. Chuang HF, et al. *Biomacromolecules* 2008;**9**:1660–1668.
  254. Ryser HJ. *Nature* 1967;**215**:934–936.
  255. Murata H, et al. *Biomaterials* 2007;**28**:4870–4879.
  256. Lewis K, et al. *Trends Biotechnol* 2005;**23**:343–348.
  257. Koplín SA, et al. *Biotechnol Prog* 2008;**24**:1160–1165.
  258. Milovi NM, et al. *Biotechnol Bioeng* 2005;**90**:715–722.
  259. He T, et al. *J Biomed Mater Res Part A* 2010;**95A**:454–464.
  260. Krebs FC, et al. *Biomed Pharmacother* 2005;**59**:438–445.
  261. Müller G, et al. *J Antimicrob Chemother* 2008;**61**:1281–1287.
  262. Wiegand C, et al. *Wound Repair Regen* 2009;**17**:730–738.
  263. Tang Y, et al. *J Biomed Mater Res Part A* 2012;**100A**:2071–2078.
  264. Rabea EI, et al. *Biomacromolecules* 2003;**4**:1457–1465.
  265. Yu DG, et al. *Bioconjugate Chem* 2007;**18**:1521–1529.
  266. Pinto MS, et al. *Eng Aspects* 2011;**377**:182–186.
  267. Ali L, et al. *Bioresour Technol* 2006;**97**:1887–1893.
  268. Wang B, et al. *Appl Surf Sci* 2012;**258**:7801–7808.
  269. Mei Y, et al. *Biofouling* 2014;**30**:313–322.
  270. Sever MJ, et al. *Angew Chem Int Ed* 2004;**43**:448–450.
  271. Young GA, et al. in *Adhesion 6*, Allen KW, Ed. Appl Sci, London, 1982.
  272. Waite JH, et al. *Biochemistry* 2001;**40**:2887–2893.
  273. Silverman HG, et al. *Marine Biotechnol* 2007;**9**:661–681.
  274. Waite JH, et al. *Science* 1981;**212**:1038–1040.
  275. Ye Q, et al. *Chem Soc Rev* 2011;**40**:4244–4258.
  276. Anderson TH, et al. *Adv Funct Mater* 2010;**20**:4196–4205.
  277. Guvendiren M, et al. *Biomacromolecules* 2008;**9**:122–128.
  278. D’Ischia M, et al. *Angew Chem Int* 2009;**48**:3914 – 3921.
  279. Greco G, et al. *Chem Commun* 2011;**47**:10308–10310.
  280. Black KCL, et al. *Nanomedicine* 2012;**8**:17–28.
  281. Stern DA, et al. *Langmuir* 1988;**4**:711–722.
  282. Saidin S, et al. *Mater Sci Eng C* 2013;**33**:4715–4724.
  283. Shabalovskaya S, et al. *J Biomed Mater Res Part B* 2003;**65B**:193–203.
  284. Lee DW, et al. *Bone* 2012;**50**:974–982.

- 
285. Liu YT, et al. *Coll Surf B: Biointerf* 2013;**106**:37–45.
  286. Wu C, et al. *Acta Biomater* 2014;**10**:428–438.
  287. Cheng C, et al. *J Membr Sci* 2012;**417–418**:228–236.
  288. Zhu LP, et al. *Coll Surf B: Biointerf* 2009;**69**:152–155.
  289. Rim NG, et al. *Coll Surf B: Biointerf* 2012;**91**:189–197.
  290. Kim JH, et al. *J Porous Mater* 2013;**20**:177–182.
  291. Xu H, et al. *Textile Res J* 2013;**83**:321–326.
  292. Ryu J, et al. *Adv Funct Mater* 2010;**20**:2132–2139.
  293. Jiang JH, et al. *J Membr Sci* 2010;**364**:194–202.
  294. Poh CK, et al. *Biomaterials* 2010;**31**:1578–1585.
  295. Zhu LP, et al. *Coll Surf B* 2011;**86**:111–118.
  296. Pop Georgievski O, et al. *Biomacromolecules* 2011;**12**:3232–3242.
  297. Chen G, et al. *J Biomed Mater Res Part A* 2013;**101A**:44–53.
  298. Wang HL, et al. *Dent Clin North Am* 1998;**42**:505–522.
  299. Selvig KA, et al. *J Periodontol* 1992;**63**:974–978.
  300. Nowzari H, et al. *J Clin Periodontol* 1994;**21**:203–210.
  301. Machtei EE, et al. *J Periodontol* 1994;**65**:154–161.
  302. Machtei EE, et al. *J Periodontol* 1993;**64**:968–973.
  303. Machtei EE. *J Periodontol* 2001;**72**:512–516.
  304. Harris RJ. *J Periodontol* 1997;**68**:779–790.
  305. Anderegg CR, et al. *J Periodontol* 1995;**66**:397–402.



# SECTION II



# PolyDOPA mussel-inspired coating as a means for hydroxyapatite entrapment on polytetrafluoroethylene surface for application in Periodontal diseases

---

## Abstract

Periodontal diseases are highly prevalent in population of all ages. They are initiated by bacterial accumulation at the interface of bone and soft tissue leading to the loss of gingival tissue attachment to the root surface. In this context, membranes made from expanded polytetrafluoroethylene (ePTFE) are considered the gold standard for guided tissue and bone regeneration. However these non-resorbable membranes suffer from weak osteoconductive/osteoinductive properties. Therefore, in this chapter a strategy for hydroxyapatite nanoparticles (HAp) coating on PTFE films was developed to improve PTFE osteoconductive properties. Binding ability of 3,4-dihydroxy-DL-phenylalanine (DOPA) to samples of any type, size and shape, was used to firmly coat HAp nanoparticles on PTFE (PTFE-DOPA-HAp). PTFE films and PTFE coated with solely DOPA (PTFE-DOPA) or with HAp (PTFE-HAp) were also characterized. Chemical composition analysis by XPS and FTIR-ATR demonstrated the successful deposition of polyDOPA and HAp on PTFE coated with a combination of DOPA and HAp. Morphological and topographical characterizations further confirmed the total surface coverage of the substrates by the coatings causing an increase in surface roughness and wettability. PTFE-DOPA-HAp films were also immersed in PBS to study coating stability: the HAp coating was still present after 14 days of incubation, with a reduced surface roughness and an unchanged hydrophilicity. MC3T3-E1 pre-osteoblastic cells

cultured on polyDOPA and polyDOPA/HAp coated film showed a pronounced increase of cell proliferation and cellular adhesion. These findings suggest that this environmentally friendly and mussel-inspired coated PTFE membrane could find potential application as scaffold for guided tissue/bone regeneration in periodontal diseases.

## 2.1 Introduction

Periodontitis is a very aggressive pathology that affects the integrity of the periodontal system and lead to damage of the periodontal tissues [1]. Initiated and maintained by bacterial stimulation of a chronic inflammatory and immune response, tissue integrity is compromised with the loss of soft tissue attachment to the root surface and the loss of alveolar bone that results in the formation of a periodontal pocket around the tooth. The pocket acts as a reservoir supporting the growth of anaerobic bacteria, which ultimately may lead to tooth loss [2]. Periodontal disease are highly prevalent; data from the National Institute of Dental and Craniofacial Research (NIDCR, National Institutes of Health, United States) has revealed that nearly 90% of the worldwide adult population present at the least a moderate level of periodontal-related diseases [1, 3].

Since the mid-1980s, several therapeutic approaches have been developed to treat the diseases that affect the periodontium; all have been focused on periodontal tissues regeneration. They include bone replacement grafts, root surface biomodifications, guided tissue and bone regeneration (GTR/GBR), and delivery of growth factors or gene therapies [4]. Among them, GTR/GBR have become the most promising therapies and were widely used in clinical treatment for their convenience and effectiveness [5- 7].

GTR/GBR treatments of periodontitis are surgical procedures that involve the placement of an occlusive barrier membrane between the tooth and the gingival tissue, preventing epithelial and connective tissue down-growth into the defect and allowing the exposed root surface to be repopulated with regenerating cells, such as periodontal ligament cells and osteoblasts [6- 9].

Non-resorbable membranes were the first used in clinical treatments. They are inert and biocompatible, act as a cellular barrier, provide space for tissue regeneration, and allow tissue integration [10]. In this contest, membranes made from expanded polytetrafluoroethylene (ePTFE) are considered the gold standard of GTR/GBR treatments. Effectiveness of ePTFE membranes was investigated in numerous clinical studies, confirming their excellent biocompatibility [11, 12]. However, despite the excellent mechanical properties and the effective biocompatibility, non-resorbable PTFE membranes suffer of weak osteoconductive/osteoinductive properties.

The use of bioactive inorganic compounds is considered an effective way of producing bone regenerative materials with physicochemical properties approaching those of bone and with good tissue compatibility, such as cell affinity, osteoconductivity and enhanced bone formation [13, 14]. Bioactive inorganic components, namely calcium phosphates and bioactive

glasses/glass ceramics, are the most widely used inorganic compounds. Hydroxyapatite (HAp) is a calcium phosphate ceramic with chemical composition similar to the mineral component of bone. Due to its proven osteoconductivity properties, it is extensively used as coating on commercially available metallic implants for orthopedic and dental applications to improve their osteoconductivity [15, 16].

The application of HAp coating on PTFE is very challenging. As known, PTFE is a very inert, hydrophobic and adhesion-resistant material. Various methods used currently, such as UV-induced graft [17], radiation graft copolymerization [18] or plasma-induced surface graft polymerization [19] require expensive equipment and complex process.

Recently, a mussel-inspired coating method has been reported as a versatile surface modification technique that is effective irrespective of material type [20, 21]. The proteins secreted by mussels are found to serve as an adhesive layer in wet condition to introduce further modification on the surface. These proteins contain domains rich in 3,4-dihydroxy-DL-phenylalanine (DOPA) and lysine amino acids as adhesive moieties [22]. Dreyer et al. showed that a thin film of DOPA on a substrate can be achieved via dip-immersion and oxidative polymerization, and the film properties can precisely be controlled by adjusting immersion time, solution concentration and temperature [23]. The dip-coated solid surface could further be modified and functionalized by the adduct formation between thiol- or amine- containing molecules and DOPA coating layer [24, 25].

Guided by these findings, herein, we report on an environmentally friendly technique to apply a HAp-nanoparticles coating on PTFE film through one-step DOPA application process in order to promote the bone re-growth properties of PTFE membranes. In our strategy, HAp coating on polymer films occurs by simultaneous binding of DOPA during its polymerization, to the HAp nanoparticles and to the PTFE substrates. Thus, the immobilization of HAp nanoparticles on PTFE surface could be achieved by their entrapment and/or conjugation with polyDOPA. We fully characterized the surface morphology and surface physicochemical properties of coated films using complementary analytical techniques including scanning electron microscope (SEM), atomic force microscopy (AFM), X-ray photoelectron spectroscopy (XPS), and water contact angle measurements. The stability of the coating was examined in phosphate buffer saline (PBS). We then evaluated the effect of HAp on the adhesion and proliferation of mouse preosteoblast MC3T3-E1 (subclone 14) cells.

## 2.2 Materials and methods

### 2.2.1 Materials

Model PTFE films (10 x 30 mm<sup>2</sup>) were kindly supplied by BIOMICRON s.r.l. Laboratory (Torino, Italy). The surface of the film was cleaned by immersion in ethanol/water (1/1 v/v) solution for 12 h at room temperature. Then, clean PTFE films were rinsed with large amount of demineralised water and dried at room temperature under a vented hood for 24 h.

The monomer DOPA (M<sub>w</sub>: 197.19 Da), the HAp (nanoparticles size < 200 nm; M<sub>w</sub>: 502.31 Da) and Tris (CH<sub>2</sub>OH)<sub>3</sub>CNH<sub>2</sub> (M<sub>w</sub>: 121.14 Da) were purchased from Sigma-Aldrich (Milano, Italy) and used as received.

### 2.2.2 Methods

#### 2.2.2.1 Surface treatment

Clean PTFE films were immersed in three different solutions:

- 1) 2 mg/mL of DOPA in 10 mM Tris buffer
- 2) 10 mg/mL of HAp in 10 mM Tris buffer
- 3) 2 mg/mL DOPA/10 mg/mL HAp in 10 mM Tris buffer.

The pH was adjusted at 8.5 through HCl (1 M) dropwise addition. After 48 h of immersion at room temperature, the films were then rinsed three times with large amount of demineralised water to remove free DOPA and HAp, and dried at room temperature under a vented hood for 24 h. The coated films were coded as follows: PTFE-DOPA, PTFE-HAp and PTFE-DOPA-HAp.

#### 2.2.2.2 Surface analyses

The static water contact angles of the sample surfaces were determined through a sessile drop method, using a 6 µl double distilled water droplet. Static contact angles of films were measured in air at room temperature in a VCA Optima (AST, Massachusetts, USA) instrument equipped with a VCA Optima XE software for data acquisition.

Chemical composition of the functionalized films was investigated by XPS (K-Alpha<sup>TM+</sup> spectrometer, Thermal Scientific, Texas, USA) at a detection angle of 45°. The characterizations were performed in survey and high resolution spectra using standard aluminum (1486.6 eV) and magnesium (1253.6 eV) X-Ray sources, respectively. A surface area of 0.005 cm<sup>2</sup> was analyzed at 150 W without charge compensation. Chemical analysis has been

carried out also in a Perkin Elmer Frontier Optical Spectrometer fitted with an attenuated total reflection sampler (FTIR-ATR, Massachusetts, USA). Spectra were recorded over the 400-4000  $\text{cm}^{-1}$  range at room temperature, using diamond crystal.

The surface morphologies were visualized using scanning electron microscopy (FEI Inspect F-50 FE-SEM, Oregon, USA) and compositional analysis (EDS). Each sample was coated with an ultrathin platinum as a conductive layer for better image quality.

The topographic surfaces were imaged by AFM using the Nanoscope III (Digital Instruments, Veeco, California, USA) system in the tapping mode. Images were acquired in air at room temperature using a silicon probe with a nominal spring constant of 40 N/m and a nominal radius of curvature of 35  $\mu\text{m}$  (model RTESP, Veeco). 10 x 10 and 5 x 5  $\mu\text{m}^2$  areas were scanned at a rate of 1 Hz using the minimum amount of force required to obtain steady images. The root mean square roughness ( $R_{\text{rms}}$ ) was calculated using Nanoscope v5.12r5 software on a 10  $\mu\text{m}$  by 10  $\mu\text{m}$  area.

Finally, the polyDOPA-HAp coating dissolution has been evaluated by immersing surface modified films in PBS (pH 7.4) at 37 °C for 7 and 14 days. The PBS medium was exchanged once every 2 days. At each dissolution time, samples were characterized through XPS, FTIR-ATR, SEM and AFM analyses and water contact angle measurements.

### 2.2.2.3 Cell culture

Mouse preosteoblast MC3T3-E1 (subclone 14) cells were supplied by American Type Culture Collection (ATCC, Virginia, USA). Minimum essential media ( $\alpha$ -MEM; Gibco, Invitrogen Corporation) supplemented with 10% Fetal Bovine Serum (FBS; Gibco, Invitrogen) and 1% penicillin/streptomycin (Invitrogen) was used to culture the osteoblasts. Cells were first expanded, and a concentration of  $5 \times 10^4$  was seeded on the model PTFE films and incubated at 37 °C in a humidified atmosphere of 5%  $\text{CO}_2$  for 1 and 3 days. Cell Crown™ inserts (Scaffdex, Tampere, Finland) were used to fix the films at the bottom of the wells prior to cell seeding.

Cell proliferation was assessed using the colorimetric indicator Alamar Blue assay (Life Technologies, Ontario, Canada). Media was removed, samples were rinsed once in PBS (Sigma-Aldrich), and 300  $\mu\text{L}$  of fresh medium containing a 10% solution of Alamar Blue was added to each well. The culture plates were wrapped in aluminum foil and incubated for 4 h at 37 °C in a humidified atmosphere of 5%  $\text{CO}_2$ . Absorbance of the extracted dye, which is proportional to the number of cells attached to the film, was measured spectrophotometrically with a microplate reader (Molecular Devices, SpectraMax i3 multi-mode detection platform, California, USA) at wavelengths of 570 and 600 nm. A calibration curve, generated from a

known number of osteoblast MC3T3 cells reacting with the Alamar Blue indicator, was used to quantify the number of cells attached on the films.

#### 2.2.2.4 SEM analyses

Cell seeded films were washed two times with PBS, fixed in Paraformaldehyde for 30 min at room temperature, washed again three times with PBS and dehydrated in 30%, 50%, 70%, 80%, 90%, 95%, and 100% ethanol, respectively, for 15 minutes. After dehydration with ethanol, the films were immersed in amyl with a gradient of acetate:ethanol from 25:75; 50:50; 75:25 to 100:0, for 15 min for each composition and then placed in a Critical Point Dryer. The samples were finally air dried under vacuum, coated with platinum, and examined with SEM (FEI Inspect F-50 FE-SEM).

#### 2.2.3 Statistical analysis

All data are expressed as means  $\pm$  standard deviation. Differences between means were analyzed by one-way ANOVA followed by a Tukey's post hoc test. For *in vitro* cell assay, statistical analysis was performed using two-way ANOVA with the Bonferroni's post test. All statistical analyses were performed with Prism, Graph Pad Software.

### 2.3 Results and discussion

#### 2.3.1 Chemical composition

The chemical composition collected from XPS spectra of PTFE, PTFE-DOPA, PTFE-HAp, and PTFE-DOPA-HAp samples (data not shown) are listed in Table 2.1.

**Table 2.1** XPS chemical composition of pristine PTFE film, DOPA powder, PTFE film coated with DOPA (PTFE-DOPA), HAp (PTFE-HAp) and DOPA/HAp mixture (PTFE-DOPA-HAp).

Sample	Atomic percentage (mol%)						C/N
	C1s	O1s	F1s	N1s	Ca2p	P2p	
PTFE	30.8	0.7	68.5	-	-	-	-
DOPA (theoretic value)	64.3	28.6	-	7.1	-	-	9.0
PTFE-DOPA	51.4	15.2	28.7	4.5	-	-	11.4
PTFE-HAp	33.5	9.3	50.9	-	< 1.0	< 0.5	-
PTFE-DOPA-HAp	38.3	23.2	22.9	3.9	12.5	10.2	9.8

XPS spectra of both PTFE and PTFE-DOPA indicated the presence of oxygen (O1s, 534 eV), carbon (C1s, 286 eV), and fluorine (F1s, 689 eV). However, pure PTFE film had no nitrogen

(N1s 400 eV) while on the film surface modified by self-polymerized DOPA (polyDOPA) the N1s could be detected. In addition after the coating of polyDOPA, the contents of carbon and oxygen increased remarkably (reaching values of 51.4mol% and 15.2mol% respectively), while the detected fluorine content decreased from 68.5mol% to 28.7 mol%. As a result, the C/N molar ratio for the PTFE-DOPA film was 11.4, in the same order of the theoretical value for pure DOPA (9.0). In general, the atomic percentages detected on the DOPA-modified PTFE film were in good agreement with theoretic values [22]. These indicated that the PTFE film was fully covered and the thickness of polyDOPA layer surpassed the detection deepness of XPS [26].

The immersion in a DOPA/HAp mixture solution resulted in the appearance of HAp characteristic elements: calcium (Ca2p, 348 eV) and phosphate (P2p, 136 eV). The high atomic percentage of calcium and phosphate indicated that a layer of HAp has been deposited on the PTFE surface. Moreover, surface atomic composition of polyDOPA/HAp coated PTFE was different from PTFE-DOPA film confirming the formation of a HAp layer on PTFE film. The contents of carbon, fluorine and nitrogen decreased to 38.3 mol%, 22.9 mol% and 3.9 mol%, respectively, while the detected oxygen content increased reaching a value of 23.2 mol%.

In order to demonstrate the role of polyDOPA is critical to firmly attach the HAp to the surface, a PTFE film was immersed in a solution containing only HAp and used as control. The XPS spectra of PTFE-HAp film after rinsing the film to remove the excess of HAp showed only a trace of calcium and phosphate (less than 1 mol%).

To further investigate the chemical structure and molecule interaction, spectral deconvolution of C1s and O1s peaks was performed for PTFE, PTFE-DOPA, PTFE-HAp and PTFE-DOPA-HAp samples (Fig. 2.1).

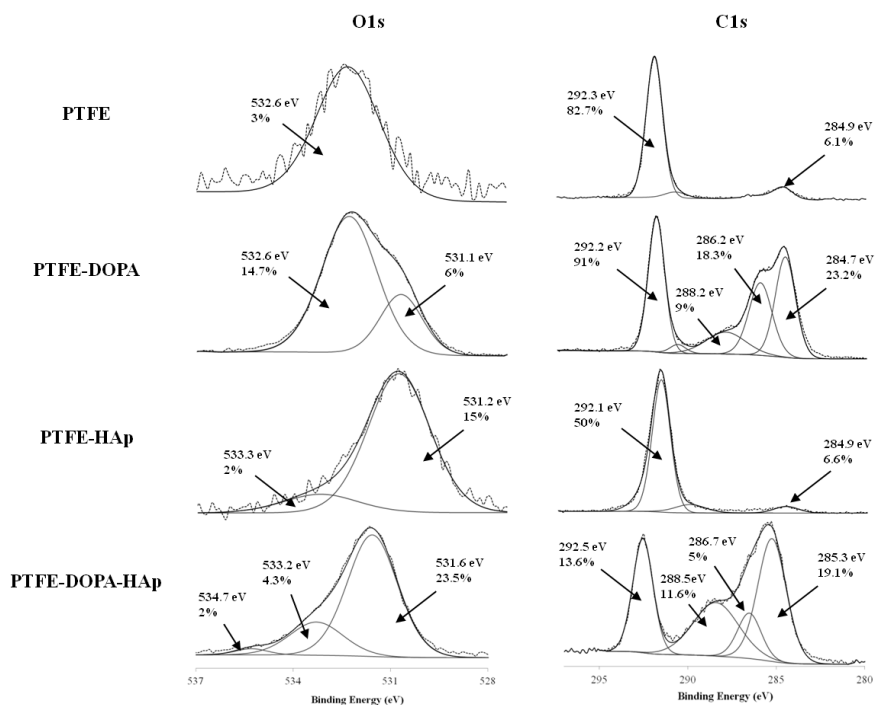


**Fig. 2.1** XPS high resolution spectra of O1s and C1s for PTFE, PTFE-DOPA, PTFE-HAp and PTFE-DOPA-HAp samples.

As shown in Fig. 2.1, the C1s spectrum of unmodified PTFE film exhibited two main bands at 292.3 and 284.9 eV associated to  $\text{CF}_2$  and C-C groups, respectively [27]. Compared to the unmodified PTFE film, some new satellite peaks assigned to C=O/COOH (288.2 eV), C-N/C-OH (286.2 eV), and C-H (284.7 eV) bonds were observed in the deconvolution of the C1s core-level spectrum of PTFE-DOPA samples. The C-C/C-H was attributed to an aromatic carbon chain in the polyDOPA structure, in between amine (C-N) and catechol groups (C-OH). During the polymerization process, the catechol was oxidized into quinone group (C=O) which further participated in the functionalization process. The polymerization process included oxidation, intramolecular cyclisation and rearrangement of the DOPA structure. The reaction with other catechol/quinone and amine functions was then resulted in a cross-linking polymer film [28, 29]. The C-OH (532.6 eV) and C=O/COOH (532.1 eV) bands were also observed in deconvolution spectra of O1s of PTFE-DOPA films. It should be noted that the C-OH peak observed in all pristine PTFE spectra was associated with the interaction of ambient air with the PTFE samples before polyDOPA coating [28].

The relative percentage of C1s and O1s bands were influenced by the introduction of HAp agglomerates on the PTFE surface, which lead also to the generation of new band (1.9%) on O1s deconvolution spectrum at 534.7 eV due to phosphate bonds in HAp structure. Compared

to the literature values (531-531.5 eV) [30, 31], the binding energy observed for PTFE-DOPA-HAp film was very high. This shift which is caused by calcium–phosphate, has been already noticed by Saidin et al. [32].

The deconvolution spectra of C1s for PTFE-HAp sample was almost similar to those of pristine PTFE with the exception of the presence of a small trace of HAp that introduced some changes on O1s spectra of PTFE-HAp.

The successful introduction of polyDOPA and HAp on PTFE model film surface has been confirmed by FTIR-ATR analysis (Fig 2.2).

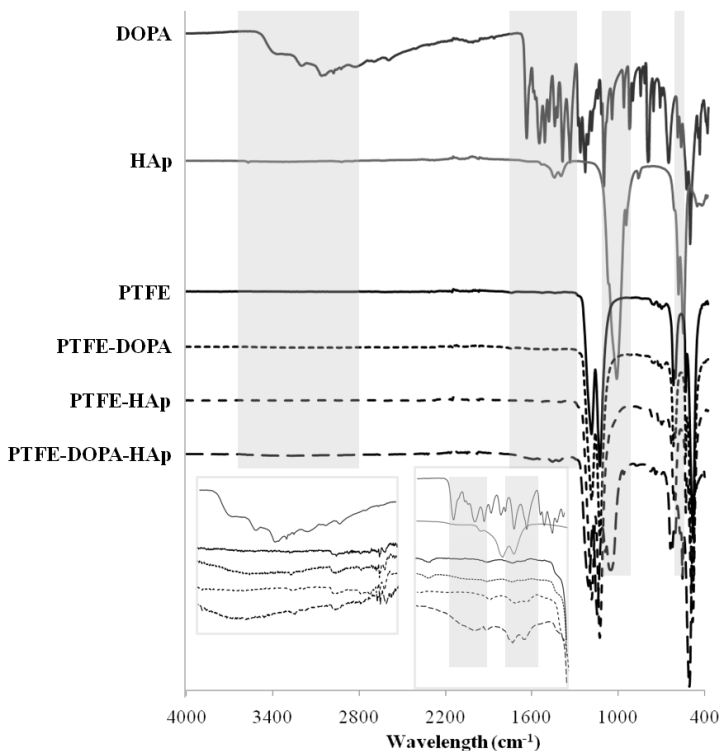


**Fig. 2.2** FTIR-ATR spectra of PTFE, PTFE-DOPA, PTFE-HAp and PTFE-DOPA-HAp films, compared with FTIR-ATR spectra of DOPA HAp powder.

DOPA spectrum showed many narrow peaks, characteristic of small molecules. Although weak, the absorption bands of catechol N-H at 3375 cm<sup>-1</sup> and O-H at 3198 cm<sup>-1</sup> could be observed [33]. The absorption band at 1659 cm<sup>-1</sup> and at 1605 cm<sup>-1</sup> were attributed to the stretching vibration of C=C bond on aromatic rings and N-H bending vibration, respectively [27].

The presence of new broad peaks in PTFE-DOPA spectrum at 3600 cm<sup>-1</sup> and 3200 cm<sup>-1</sup> as compared to unmodified PTFE film was attributed to the stretching vibrations of the N-H/O-H as a result of the surface coating of PTFE film by polyDOPA. The peak at 1600 cm<sup>-1</sup>

overlapping C=C vibrations of the aromatic ring and the N–H bending vibrations along with a peak around 1350  $\text{cm}^{-1}$ , related to the phenolic bending vibration are also indicative of the presence of polyDOPA on the surface of PTFE films.

The immersion of PTFE film in a buffer solution containing DOPA and HAp nanoparticles led to marked changes in PTFE spectra and resulted in three new peaks at nearly 1420  $\text{cm}^{-1}$ , 1030  $\text{cm}^{-1}$  and 603  $\text{cm}^{-1}$  characteristics of  $\nu_3$  vibrational mode carbonate ions, and  $\nu_3$  and  $\nu_4$  phosphate vibrational bands as a result of HAp entrapment in DOPA layer on PTFE films. Similarly to the results obtained by XPS analyses, no peaks related to the presence of HAp could be detected on PTFE-HAp spectra when this inorganic phase deposited without the addition of DOPA confirming that DOPA is critical for introducing this osteoconductive material on PTFE membrane.

### 2.3.2 Morphology

Fig. 2.3 illustrates the surface morphology of coated and uncoated PTFE films as revealed by SEM.

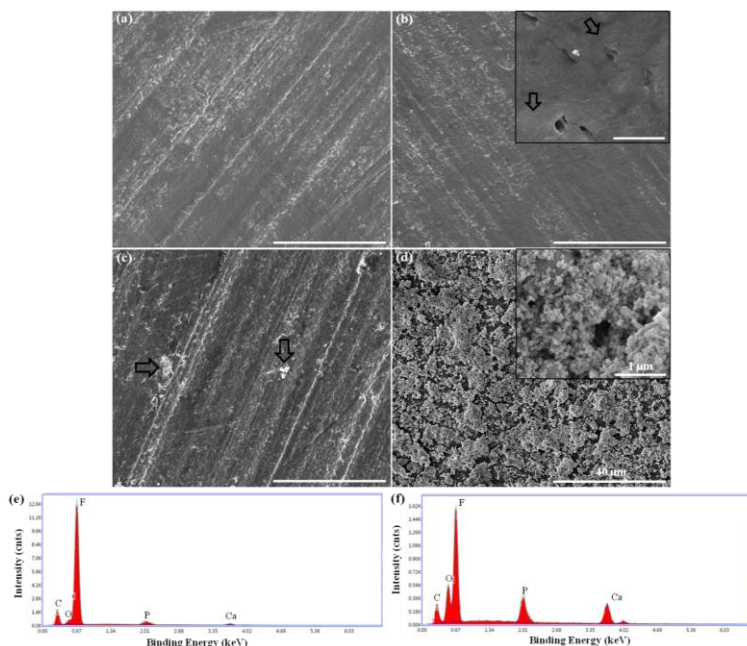


**Fig. 2.3** Morphology of (a) PTFE, (b) PTFE-DOPA, (c) PTFE-HAp, and (d) PTFE-DOPA-HAp films. EDS analyses of (e) PTFE-HAp and (f) PTFE-DOPA-HAp surfaces. The arrows in Fig 3b inset show polyDOPA thin layer on the surface of PTFE-DOPA samples while in Fig 3c they indicate the agglomerates of HAp dispersed on the PTFE surface.

Control PTFE film and those modified by polyDOPA or HAp were characterized by rough surface (Fig. 2.3 a, b and c). After the immersion in DOPA solution, a polyDOPA thin layer

covered the surface of PTFE-DOPA samples, as underlined by the inset in Fig. 2.3b (black arrows). The polyDOPA coating appeared uniformly distributed over the entire substrate surface. On the contrary, only some agglomerates of HAp nanoparticles could be observed on PTFE-HAp film (Fig. 2.3c, black arrows). The PTFE-DOPA-HAp film showed a coating layer of mineral crystal precipitations on the surface of PTFE film. The HAp layer was uniformly covering the entire sample surface, producing a high rough surface. Moreover, the SEM image of PTFE-DOPA-HAp film at a higher magnification (inset in Fig. 2.3d) showed a compact coating with a 3D-structure characterized by the presence of some pores, beneficial for bone integration [34]. Comparing the EDS spectra of PTFE-HAp and PTFE-DOPA-HAp films showing higher amount of Ca and P than PTFE-HAp film confirmed the presence of polyDOPA embedded HAp on the sample surface.

### 2.3.3 Surface roughness and wettability properties

Further characterizations on the film topography and wettability properties confirmed our SEM observations. Indeed, after the immersion of PTFE samples into the DOPA solution for 48 h, the surface roughness increased significantly (\*\*\*)  $P < 0.01$  (Fig. 2.4b). As reported by Xi et al. [22], this phenomenon is attributed to the coverage of polyDOPA layer on film surface. Conversely, the surface roughness slightly increased, but not significantly, in respect to PTFE films when HAp simply deposited on the PTFE. The PTFE immersion in a buffer solution containing DOPA and HAp nanoparticles markedly changed the film surface topography. PTFE-DOPA-HAp samples (Fig. 2.4d) exhibited significantly higher peaks than pristine PTFE, PTFE-HAp and PTFE-DOPA samples and reached over 200 nm after the adsorption of HAp nanoparticles (\*\*\*)  $P < 0.01$ ). The AFM results confirmed again that the use of polyDOPA as embedding layer is essential to deposit an effective amount of HAp on PTFE films.

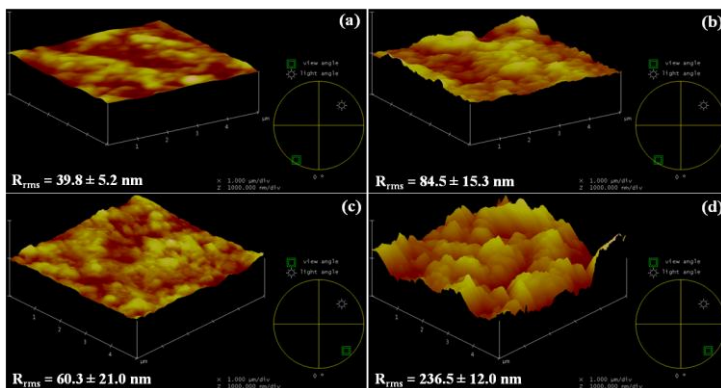


**Fig. 2.4** AFM height mode images and root mean square roughness values ( $R_{rms}$ ) of (a) PTFE, (b) PTFE-DOPA, (c) PTFE-HAp, and (d) PTFE-DOPA-HAp samples.

As expected, polyDOPA or/and HAp coating on PTFE affected also the film wettability, due to both changes in surface roughness and its chemical composition. The presence of hydrophilic functional groups (-NH and -OH) of polyDOPA and HAp coatings significantly increased the wettability properties of PTFE films. As reported in Fig. 2.5, contact angle of PTFE-DOPA samples reached a value of  $69.9^\circ \pm 3.8^\circ$  while the immersion in DOPA/HAp mixture solution decreased the contact angle of PTFE substrate to less than  $50^\circ$ . The surface wettability of PTFE-HAp sample was comparable to that obtained for unmodified PTFE, since the direct HAp deposition do not lead to significant change either in surface chemical composition or roughness (according to previous analyses).

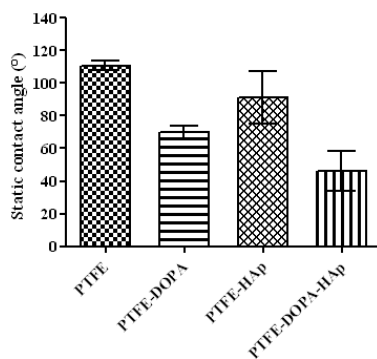


**Fig. 2.5** Static contact angle measurements of PTFE, PTFE-DOPA, PTFE-HAp, and PTFE-DOPA-HAp films. Statistical analysis indicated the presence of statistically significant differences among contact angle values (\*\*\*)  $P < 0.01$ ).

As a result of rougher surface, the surface wettability was significantly increased for PTFE-DOPA-HAp in comparison to all other samples. As known in the literature, a hydrophilic surface is important for protein absorption and proliferation of osteoblast cells [35]. Similarly, a rough surface will provide high surface area for protein absorption, that in turn create more anchoring points for osteoblast adhesion and thereby would accelerate bone growth onto an implant surface [36].

### 2.3.4 Cell proliferation and adhesion

When compared to initial number of seeded cells The improved surface wettability and roughness promoted MC3T3-E1 cells' proliferation on all samples as soon as day one of culture (Fig. 2.6).

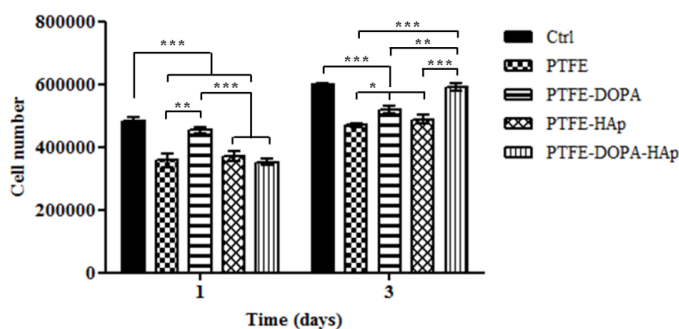


**Fig. 2.6** Alamar Blue assay results for cell proliferation on PTFE, PTFE-DOPA, PTFE-HAP, and PTFE-DOPA-HAP films as a function of time. The initial number of seeded pre-osteoblast MC3T3-E1 was  $1 \times 10^5$  cells in 500  $\mu$ l MEM- $\alpha$ . Petri dish was used as control (Ctrl).

Interestingly, the cells responded more favorably to PTFE-DOPA rather than PTFE-DOPA-HAP. We believed that in addition to improved surface wettability, the presence of bioactive functional groups such as OH- and NH<sub>2</sub>- (from polyDOPA coating) [37] was responsible for such an improvement. However, the overall cell proliferation on PTFE and PTFE modified surfaces was less than the cells on control Petri dishes. This is in alignment with Lincks et al. [38] observation where the authors reported a decreased osteoblast-like cells proliferation on Ti samples with high surface roughness and concluded that high surface roughness was responsible for this decrease at early stage of cell culture (day 1).

After 3 days of culture, cells continue to proliferate on all samples. However, the growth rate was more pronounced, compared to control, on PTFE-DOPA-HAP films compared to others. This result indicates that the polyDOPA and HAP combination strategy allowed to significantly improve the proliferation of MC3T3-E1 cells comparing to PTFE or PTFE modified either by polyDOPA or HAP.

The SEM micrographs of osteoblasts on the PTFE-based films after 1 and 3 days of culture were in good agreement with cell proliferation assay (Fig. 2.7). Higher number of adhered MC3T3-E1 cells were found on PTFE-DOPA and PTFE-DOPA-HAP films than on pure PTFE and PTFE-HAP samples as of day one. The cells were more spread with extended filopodia invading the surface of samples (Fig. 2.7 b1 and d1). At the day 3, the number of MC3T3-E1 cells adhered on the surface markedly increased for PTFE-DOPA-HAP film (Fig. 2.7 d2), where cells stretched out, flattened covered most of the surface of the sample. A good cells adhesion could be observed also for PTFE-DOPA film (Fig. 2.7 b2), while MC3T3-E1 cells cultured on PTFE and PTFE-HAP samples remained rounded, often growing in clusters (Fig. 2.7 a2 and c2).

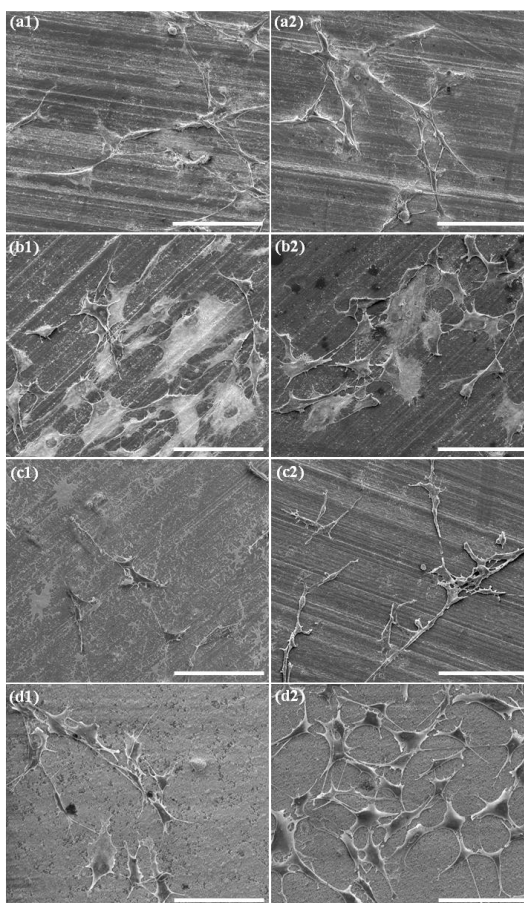


**Fig. 2.7** SEM morphology of preosteoblast cells grown on PTFE (a1, a2), PTFE-DOPA (b1, b2), PTFE-HAp (c1, c2) and PTFE-DOPA-HAp (d1, d2) films after seeding cells for 1 and 3 days, respectively denoted with numbers 1 and 2. Scale bar = 100  $\mu$ m.

The results from proliferation and adhesion tests confirmed that the combined DOPA and HAp coating played an important role in stimulating the proliferation and adhesion of MC3T3-E1 cells and significantly improved the osteoblast response of PTFE.

### 2.3.5 Coating dissolution

As discussed, the polyDOPA/HAp coating was characterized by a high surface roughness. Thus, the polyDOPA/HAp coating would be expected to result in a faster rate of dissolution, as a greater surface area of the coating is exposed to the surrounding environment.

Indeed, XPS results, indicated many changes in the surface composition of PTFE-DOPA-HAp films after incubation over 14 days in PBS (Table 2.2). While an increase in fluorine atomic percentage could be detected, the characteristic peaks of PTFE substrate, mainly carbon and oxygen content, were decreased. Nitrogen content linearly decreased with the increase of

incubation time in PBS, reaching a value of 0.8 mol%. The same happened for the atomic percentage of Ca and P, which markedly decreased to values of 6.9 mol% and 4.8 mol%, respectively, after 7 days of immersion; then, they remained almost constant after this period.

**Table 2.2** XPS chemical composition of PTFE-DOPA-HAp films after incubation in PBS at 37 °C for 0, 7 and 14 days.

Sample	Time (days)	Atomic percentage (mol%)					
		C1s	O1s	F1s	N1s	Ca2p	P2p
PTFE-DOPA-HAp	0	38.3	23.2	22.9	3.9	12.5	10.2
	7	28.6	24.4	29.7	1.4	6.9	4.8
	14	31.9	16.5	40.6	0.8	5.8	4.4

Deconvolution spectra of C1s and O1s were also characterized on PTFE-DOPA-HAp films at each dissolution time (Fig. 2.8). The polyDOPA and HAp release influenced the relative percentage of C1s bands. In fact, it could be observed the atomic percentage reduction of elements associated with the polyDOPA coating. On the contrary, no markedly changes could be detected for O1s bands, except the disappearance of the peak attributed to oxygen from the phosphate bonds in HAp structure.

The results obtained with XPS analysis suggested that dissolution reactions were occurring in two steps: an extremely fast release of HAp during the first week of immersion and a much more gradual release during the next 7 days.

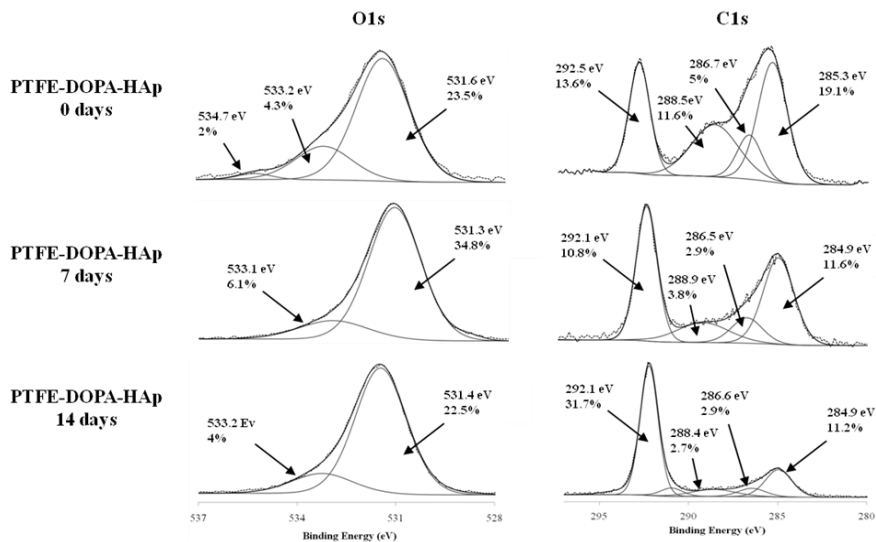


**Fig. 2.8.** XPS deconvolution spectra of O1s and C1s for PTFE-DOPA-HAp samples after incubation in PBS at 37 °C for 0, 7 and 14 days.

The surface chemical composition of PTFE-DOPA-HAp films at each dissolution time has been also evaluated through FTIR-ATR analysis. Peaks associated to the coating were still visible in spectra of samples incubated in PBS and only slight changes in peaks intensity could be observe (data was not shown).

A physical change in the surface morphology of the coating was observed through SEM analysis (Fig. 2.9). After immersion in PBS for 7 days, PTFE-DOPA-HAp films presented a surface morphology which was considerably different from the initial one. The coating was no longer covering the entire surface of the substrate and appeared smoother and thinner than the one before incubation in PBS. The results were the same for samples immersed for 14 days in PBS.

In agreement with SEM analysis, the AFM images showed a gradual decrease of surface roughness as compared to PTFE-DOPA-HAp films at day zero in order to reach a  $R_{rms}$  value of about 111 nm after 14 days of incubation in PBS. However, this value remained higher than the  $R_{rms}$  value of uncoated PTFE. This change in surface roughness was not enough to affect the surface wettability as the PTFE-DOPA-HAp films incubated in PBS for 7 and 14 days have shown contact angle values (respectively  $(51.6 \pm 7.6)^\circ$  and  $(57.4 \pm 11.1)^\circ$ ) comparable to the initial one  $((46.1 \pm 12.4)^\circ)$  coated films. All taken together with XPS analyses support the hypothesis of a two-step dissolution process of polyDOPA/HAp coating.

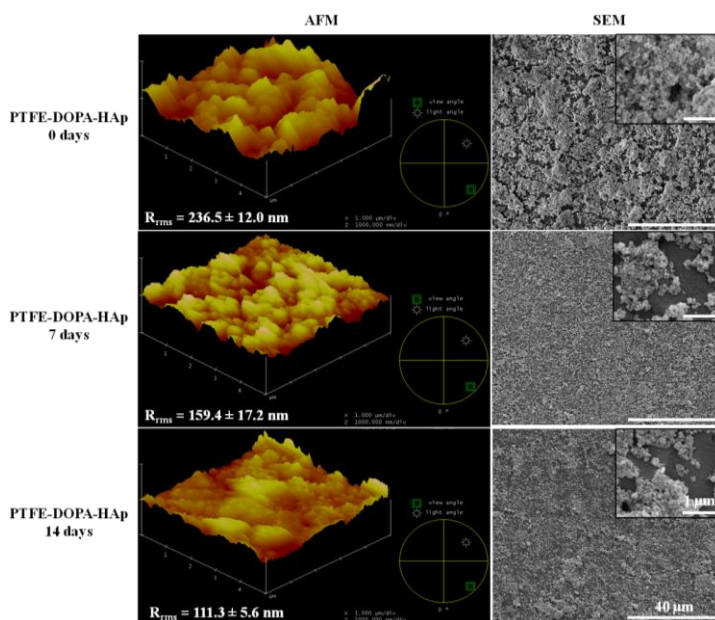


**Fig. 2.9.** AFM height mode images, root mean square roughness values ( $R_{rms}$ ) and SEM micrographs of PTFE-DOPA-HAp samples as a function of the immersion time in PBS at 37 °C. Statistical analysis indicated the presence of statistically significant differences among PTFE-DOPA-HAp 0 days and 7, 14 days (\*\*\*)  $P < 0.01$ ), and PTFE-DOPA-HAp 7 days and 14 days (\*\*  $P < 0.01$ ).

It is widely suggested that the osteoconductive properties of HAp coatings arise as a direct result of their dissolution properties. Dissolution of HAp allows redistribution of Ca and P ions, which may be used by surrounding tissues in the manufacture of new natural bone [39, 40]. Thus, the burst release of HAp observed in this work during the first week of immersion in PBS would provide to osteoblast a high amount of Ca and P that could be useful to speed up the bone mineralization process. The second dissolution step, through the gradual HAp release, would maintain the osteoblast activity and the Ca and P ions in the surrounding environment.

## 2.4 Conclusions

In this chapter, the efficiency of mussel-inspired coating technique has been demonstrated. A HAp coating has been successfully developed on PTFE highly hydrophobic and inert substrates, by entrapment and/or conjugation of HAp nanoparticles with polyDOPA.

The polyDOPA/HAp coating covered the entire surface of the films, producing a very rough surface with improved wettability properties. Moreover, the coating was characterized by a 3D-structure, able to enhance protein absorption and osteoblast proliferation, both very favourable for accelerating osteointegration and bone re-growth. Indeed, *in vitro* cell test with pre-osteoblast MC3T3-E1 cells confirmed these observations. Cells proliferated very well on the PTFE-DOPA-HAp over 3 days. They were extremely well spread and formed long filopodia with firm attachment to the surface of PTFE-DOPA-HAp. There are two potential reasons for the improvement in the cellular activity of MC3T3-E1 on self-assembled polyDOPA/HAp composite coating: (1) the improved surface roughness, hydrophilicity and bioactive chemical cues from both polyDOPA and HAp; (2) the aid in protein adsorption of HAp. An investigation of the coating stability indicated a two-step dissolution process: an initial marked release of HAp in the first week, and a second phase of gradual release in the next 7 days.

Taken together the results of this chapter, we believe that our coating strategy would lead to the development of PTFE substrates with improved osteoconductive properties for their use in tissue engineering. Such an improvement in PTFE is not only very useful for the treatment of periodontal diseases but also for many other pathology requiring the improved osteoconductive properties of PTFE.

## References

---

1. Pihlstrom BL, et al. *Lancet* 2005;**366**:1809-1820.
2. Haffajee AD, et al. *Periodontol 2000* 1994;**5**:78-111.
3. Nakashima M, et al. *Nat Biotechnol* 2003;**21**:1025-1032.
4. Ramseier CA, et al. *Periodontol 2000* 2012;**59**:185-202.
5. Nyman S, et al. *J Periodontal Res* 1987;**22**:252-254.
6. Polimeni G, et al. *Clin Implant Dent Relat Res* 2008;**10**:99-105.
7. Villar CC, et al. *Dent Clin North Am* 2010;**54**:73-92.
8. Gottlow J, et al. *J Clin Periodontol* 1986;**13**:604-616.
9. Piattelli A, et al. *Biomaterials* 1996;**17**:791-796.
10. Polimeni G, et al. *J Clin Periodontol* 2005;**32**:951-954.
11. Zhao S, et al. *J Craniomaxillofac Surg* 2000;**28**:116-122.
12. Zwahlen RA, et al. *Clin Oral Implants Res* 2009;**20**:1084-1091.
13. Kim HW, et al. *J Biomed Mater Res B* 2004;**70B**:240-249.
14. Yao J, et al. *J Biomed Mater Res A* 2006;**75A**:794-801.
15. Roy M, et al. *Surf Coat Technol* 2011;**205**:2785-2792.
16. Yeung WK, et al. *J Biomed Mater Res Part B: Appl Biomater* 2013;**101B**:939-949.
17. Hu MX, et al. *J Membr Sci* 2006;**258**:196-205.
18. Liu F, et al. *Appl Surf Sci* 2006;**253**:2096-2101.
19. Nakata M, et al. *J Appl Polym Sci* 2006;**101**:383-387.
20. Lee H, et al. *Science* 2007;**318**:426-430.
21. Xi ZY, et al. *J Membr Sci* 2009;**327**:244-253.
22. Faure E, et al. *Prog Polym Sci* 2013;**38**:236-270.
23. Dreyer DR, et al. *Langmuir* 2012;**28**:6428-6435.
24. Lee BP, et al. *Biomacromolecules* 2002;**3**:1038-1047.
25. LaVoie MJ, et al. *Nat Med* 2005;**11**:1214-1221.
26. Cheng C, et al. *J Membr Sci* 2012;**417-418**:228-236.
27. Fang Z, et al. *J Phys D: Appl Phys* 2003;**36**:2980-2985.
28. D'Ischia M, et al. *Angew Chem Int* 2009;**48**:3914-3921.
29. Greco G, et al. *Chem Commun* 2011;**47**:10308-10310.
30. Contescu A, et al. *Dig J Nanomater Bios* 2010;**5**:989-1000.
31. Casaletto MP, et al. *Surf Interface Anal* 2002;**34**:45-49.
32. Saidin S, et al. *Mater Sci Eng C* 2013;**33**:4715-4724.
33. Wei M, et al. *Chem Mater* 2008;**20**:5169-5180.
34. Oshida Y. Implant-Related Biological Reactions. In: Oshida Y, editor. *Bioscience and Bioengineering of Titanium Materials*. Oxford: Elsevier; 2007.p 159-214.
35. Nakamura M, et al. *J Ceram Soc Jpn* 2010;**118**:474-478.

- 
36. Padial-Molina M, et al. *Acta Biomater* 2011;**7**:771-778.
  37. Wu C, et al. *J Mater Chem* 2011;**21**:18300–18307.
  38. Lincks J, et al. *Biomaterials* 1998;**19**:2219-2232.
  39. Orly I, et al. *Caclif Tissue Int* 1989;**45**:20-26.
  40. Bagambisa FB, et al. *J Biomed Mater Res* 1993;**27**:1047-1055.

# 3

## Self-polymerizing DOPA as a functional layer for the development of antimicrobial coating on PTFE barrier membranes for GTR procedures

---

### Abstract

Regenerative approaches to treat periodontitis lesions offer exciting possibilities; however, they frequently fail to produce the desired clinical outcome due to infectious complications. Guided tissue regeneration (GTR) procedures, with currently available membranes, exhibit large variability in the surgical outcome due to bacterial infection following placement of the barrier membrane. In this chapter, an antimicrobial coating of polytetrafluoroethylene (PTFE) membrane has been developed in order to eliminate pathogens in the treated site. Silver nanoparticles (AgNPs) have been selected as antimicrobial agents due to their good antimicrobial efficacy against bacteria, viruses and other eukaryotic micro-organisms. The successful deposition of AgNPs on PTFE film surface, through the functional groups of 3,4-dihydroxy-DL-phenylalanine (DOPA), has been demonstrated by physicochemical and morphological analyses. The nanoparticles exhibited a diameter around 68 nm and were homogeneously distributed on the surface, with only some agglomerates. *In vitro* cell tests with fibroblast NIH 3T3 cells showed an inhibition of cells proliferation on PTFE films functionalized with AgNPs after 3 days of culture, while good cells adhesion was observed with cells randomly distributed on sample surface and extensively spread. The antimicrobial efficiency has been demonstrated especially against *Staphylococcus aureus* (*S. aureus*) and Ag release was sustained for at least 14 days.

### 3.1 Introduction

Periodontal diseases, specifically periodontitis, are multifactorial diseases, caused mainly by pathogenic bacterial species located in the subgingival niche. These bacterial species adhere to the tooth surfaces to form in a highly complex and organized structure called dental plaque [1, 2], which displays properties that are typical of biofilms and microbial communities in general [3].

Approximately 500 bacterial species inhabit subgingival niche [4]. The abundance and diversity of microorganisms depend upon several factors, such as effectiveness of oral hygiene measures, degree of gingivitis, pocket depth, and the antimicrobial efficacy of the host immune response. Some microorganisms produce gingivitis and some types of chronic periodontitis, while others produce aggressive forms of periodontitis [5]. Important periodontal pathogens are *Actinobacillus actinomycetemcomitans*, *Porphyromonas gingivalis* (*P. gingivalis*), *Dialister pneumosintes*, *Bacteroides forsythus* and *Treponema denticola* [5].

Regenerative approaches to treat periodontitis lesions offer exciting possibilities; however, they frequently fail to produce the desired clinical outcome due to infectious complications [6]. Long-term evaluation studies indicate that guided tissue regeneration (GTR) procedures, with currently available membranes, exhibit large variability in the surgical outcome due at least in part to bacterial infection following placement of the barrier membrane [7, 8]. *In vitro* data suggest that bacterial species vary in ability to attach to barrier membranes of different materials. For example, Wang et al. [9] demonstrated that *Streptococcus mutans* attached significantly more to the expanded polytetrafluoroethylene (ePTFE) and the collagen (COL) membranes than to the polyglactin 910. Ricci et al. [10] studied varying *in vitro* affinity for *P. gingivalis* to attach to 6 types of bioabsorbable and non-bioabsorbable barrier membranes. Polyglactin and COL membranes demonstrated high bacteria counts, polylactic acid (PLA) and synthetic glycolide and lactide copolymer barrier devices showed lowest bacteria counts, while ePTFE membranes revealed *P. gingivalis* cells mainly in the fibrillar areas of both the internal and external sides of the membrane.

Microbial colonization of barrier membranes may already start at the time of membrane insertion [11]. Most likely, the membrane infecting pathogens are transferred via saliva from infected periodontal lesions or tongue dorsum to the regenerative-treated periodontal site.

To prevent infectious failures with regenerative periodontal therapy, efforts should be directed towards the elimination or marked suppression of pathogens in the treated site as well as in the entire mouth prior to regenerative surgery and throughout the healing phase. Anti-infective

therapy in periodontal regeneration includes: (1) mechanical debridement; (2) local or systemic delivery of antimicrobial agents; (3) antimicrobial coating of barrier membranes; (4) proper oral hygiene measures by the patient [12].

In recent years, the focus of many laboratories has been the design of membranes that have some form of antibacterial properties. Bottino et al. [13] incorporated metronidazole benzoate (MET) to the layer interfacing with the epithelial tissue to reduce the amount of anaerobic Gram-negative bacteria (i.e. *P. gingivalis*) and anaerobic spore-forming Gram-positive bacilli. Chou et al. [14] reported on the antibacterial effects of two commercially available biodegradable membranes after mineralization with zinc phosphate that led to a significant decrease in *Actinobacillus actinomycetemcomitans* activity when compared to non-mineralized membranes. In a less recent work, Harvey et al. [15] have described the potential antibiotic bonding (tetracycline-HCl) to ePTFE by means of the cationic surfactant, tridodecylmethylammonium chloride. *In vitro* studies showed that the coated barrier membranes released biologically active tetracycline for 3-6 weeks, significantly decreasing cultivable pathogens. However, due to the emergence of antibiotic-resistant bacteria and limitations of the use of antibiotics, the researchers are searching for new antibacterial agents. In the present scenario, nanoscale materials have emerged up as novel antimicrobial agents owing to their high surface area to volume ratio and the unique chemical and physical properties [16, 17].

The use of nanoparticles is gaining impetus in the present century as they possess defined chemical, optical and mechanical properties. The metallic nanoparticles are most promising as they show good antibacterial properties due to their large surface area to volume ratio. Different types of nanoparticles (i.e. titanium, gold, silver [18, 19]) have come up but silver nanoparticles (AgNPs) have proved to be most effective as they have good antimicrobial efficacy against bacteria, viruses and other eukaryotic micro-organisms [20]. Due to their low toxicity to human cells, Ag ion or metallic Ag as well as AgNPs can be explored in burn treatment, dental materials, coating, etc. [21]. In recent years, various chemical and physical methods (i.e. plasma sprayed technology [22], sol-gel method [23]) have been employed to prepare AgNPs in different materials. However, poor metal/material adhesion, and incomplete control of the Ag<sup>+</sup> release in the liquid medium are the main drawbacks of these approaches. In addition, the complicated multistep procedures used by the aforementioned methods limited their practical applications. Thus, the development of simple and versatile strategies for surface modification reveal challenging.

Recently, 3,4-dihydroxyphenethylamine (Dopamine), a mussel-inspired catecholamine, has been demonstrated to spontaneously self-polymerize on various inorganic or organic materials surface and form uniformly films (polyDopamine) under mild conditions [24, 25]. The same behavior has been observed for 3,4-dihydroxy-DL-phenylalanine (DOPA), a precursor of Dopamine, leading to the formation of a polyDOPA layer [26]. Because of the self-polymerizing and self-adhesive nature, the surface multifunctional groups on the polyDopamine and polyDOPA ad-layer (catechol and amine functional groups) were reported to be able to spontaneously reduce noble metal nanoparticles, without using a reducing agent, surfactant, or energy-consuming steps [27- 29]. In this chapter, the polyDOPA was applied to produce AgNPs on PTFE compact film surfaces for GTR applications in periodontal diseases.

The functionalized films were characterized by X-Ray photoelectron spectroscopy, scanning electron microscopy, and atomic force microscopy. The coating stability was carried out in phosphate buffer saline (PBS) for 7 and 14 days. In terms of antibacterial efficacy, both Gram-positive and -negative bacteria were tested using inhibition assay; while the toxicity of the functionalized films was evaluated by examining the Mouse embryonic fibroblast NIH 3T3 cells proliferation and morphology.

## **3.2 Materials and methods**

### **3.2.1 Materials**

The PTFE compact films (10 x 30 mm<sup>2</sup>) were kindly provided by BIOMICRON s.r.l. Laboratory (Torino, Italy). The films were pre-treated by immersion in ethanol/water (1/1 v/v) solution for 12 h at room temperature. Then, clean PTFE films were rinsed with large amount of demineralised water and dried at room temperature under a vented hood for 24 h.

The monomer DOPA ( $M_w$ : 197.19 Da), the silver nitrate ( $M_w$ : 169.87 Da) and Tris ((CH<sub>2</sub>OH)<sub>3</sub>CNH<sub>2</sub>;  $M_w$ : 121.14 Da) were purchased from Sigma-Aldrich (Milano, Italy) and used as received.

### **3.2.2 Methods**

#### *3.2.2.1 Surface functionalization*

Clean PTFE films were grafted with poly(DOPA) at room temperature for 48 h (PTFE-DOPA). The DOPA solution was prepared by dissolving DOPA at a concentration of 2 mg/ml in 10 mM Tris buffer. The pH was adjusted at 8.5 through HCl (1 M) dropwise addition into the solution to provide an alkaline medium for spontaneous DOPA polymerisation, as this pH is a typical

seawater pH. PTFE-DOPA films were then rinsed three times with large amount of demineralised water to remove free DOPA and dried at room temperature under a vented hood for 24 h.

The grafted poly(DOPA) films were finally metallised with AgNPs in 50 mM aqueous  $\text{AgNO}_3$  solution, in dark at room temperature (PTFE-DOPA-Ag). After 24 h, films were rinsed three times with large amount of demineralised water and dried at room temperature under a vented hood for 24 h.

As control, pristine PTFE was subjected to the metallization process under the same conditions applied for PTFE-DOPA samples (PTFE-Ag).

#### *3.2.2.2 Water contact angle measurements*

The static contact angles of PTFE-based films were determined through a sessile drop method, using a 6  $\mu\text{l}$  double distilled water droplet. Static contact angles of films were measured at room temperature in a VCA Optima (AST, Massachusetts, USA) instrument equipped with a VCA Optima XE software for data acquisition.

#### *3.2.2.3 Morphological and compositional analysis*

Surface morphology was observed using field emission-scanning electron microscopy (FEI Inspect F-50 FE-SEM, Oregon, USA) and compositional analysis (EDS). Samples were sputter coated with an ultrathin platinum (Pt) as a conductive layer for better quality image.

#### *3.2.2.4 Atomic force microscopy*

The examination of surface topography was imaged by atomic force microscopy (AFM) using the Nanoscope III (Digital Instruments, Veeco, California, USA) system in the tapping mode. Images were acquired in air at ambient temperature using a silicon probe with a nominal spring constant of 40 N/m and a nominal radius of curvature of 35  $\mu\text{m}$  (model RTESP, Veeco). 10 x 10 and 5 x 5  $\mu\text{m}^2$  areas were scanned at a rate of 1 Hz while a 2 Hz frequency was use for 1 x 1  $\mu\text{m}^2$  areas, both using the minimum amount of force required to obtain steady images. Root mean square surface roughness ( $R_{\text{rms}}$ ) was calculated using Nanoscope v5.12r5 software on a 10  $\mu\text{m}$  by 10  $\mu\text{m}$  area.

#### *3.2.2.5 X-ray photoelectron spectroscopy*

Chemical composition of the functionalized films was investigated by X-ray photoelectron spectroscopy (XPS) (K-Alpha<sup>TM+</sup> spectrometer, Thermal Scientific, Texas, USA) at a detection

angle of 45°. The characterizations were performed in survey and high resolution (HR) spectra using standard aluminium (1486.6 eV) and magnesium (1253.6 eV) X-Ray sources, respectively. A surface area of 0.005 cm<sup>2</sup> was analyzed at 150 W without charge compensation.

#### 3.2.2.6 Stability test

For stability studies, only PTFE-DOPA-Ag films were used. Stability test was carried out on 10 x 10 mm<sup>2</sup> film specimens incubated in 3 ml PBS at 37 °C and pH 7.4 for 7 and 14 days. The PBS medium was exchanged once every 2 days.

Morphological and topographical evaluations of the exposed surfaces of film samples at each stability test time were analyzed by FE-SEM and AFM according to the procedures described, respectively, at par. 3.2.2.3 and 3.2.2.4. Surface chemical composition and wettability were evaluated through XPS analysis and water contact angle measurements, according to the previously described methods at par. 3.2.2.5 and 3.2.2.2 respectively.

#### 3.2.2.7 Antibacterial assay

Antibacterial activity of PTFE-DOPA-Ag samples was preliminarily investigated against *Escherichia coli* ATCC 25922 (*E. coli*), a Gram-negative clinical isolate and *Staphylococcus aureus* ATCC 6538 (*S. aureus*), a Gram-positive strain isolated from human lesion. Both strains were supplied from Belgian Coordinated Collections of Microorganisms (BCCM) and play an important role in human infections and biofilm formation on medical devices [30]. *E. coli* and *S. aureus* strains were grown overnight in Luria–Bertani (LB) agar at 37 °C. Then, bacterial suspensions at the concentration of 1.5 × 10<sup>8</sup> Colony Forming Units per milliliter (CFU/mL) were prepared and dispersed uniformly onto the surface of Müller-Hinton agar plates. Disk-shaped samples of PTFE and PTFE-DOPA-Ag (about 1.2 cm diameter) were UV sterilized for 15 min and subsequently laid on the top of the inoculated plates. After 24 h of incubation at 37 °C, the diameter of inhibition against the two bacterial strains was measured.

#### 3.2.2.8 Cell culture

For all cell studies, only PTFE, PTFE-DOPA, and PTFE-DOPA-Ag films were analysed. Mouse embryonic fibroblast NIH 3T3 cells were supplied by American Type Culture Collection (ATCC, Virginia, USA). Dulbecco's modified Eagle's medium (DMEM; ATCC) supplemented with 10% Calf Bovine Serum (CBS; Gibco, Invitrogen) and 1% penicillin/streptomycin (Invitrogen) was used to culture the fibroblasts. Cells were first expanded, and a concentration of 5 × 10<sup>4</sup> was seeded on the blend films and incubated at 37 °C in a humidified atmosphere of

5% CO<sub>2</sub> for 1 and 3 days. Cell Crown™ inserts (Scaffdex, Tampere, Finland) were used to fix the films at the bottom of the wells prior to cell seeding.

Cell proliferation was assessed using the colorimetric indicator Alamar Blue assay (Life Technologies, Ontario, Canada). Media was removed and samples were rinsed once in PBS (Sigma-Aldrich). 300 µL of fresh medium containing a 10% solution of Alamar Blue was added to each well. The culture plates were wrapped in aluminum foil and incubated for 4 h at 37 °C in a humidified atmosphere of 5% CO<sub>2</sub>. Absorbance of the extracted dye, which is proportional to the number of cells attached to the film, was measured spectrophotometrically with a microplate reader (Molecular Devices, SpectraMax i3 multi-mode detection platform, California, USA) at wavelengths of 570 and 600 nm. A calibration curve, generated from a known number of fibroblast NIH 3T3 cells reacting with the Alamar Blue indicator, was used to quantify the number of cells attached on films.

#### 3.2.2.9 Cell adhesion

Morphology and adhesion of the cells cultured on PTFE-based films were examined by FE-SEM. Films were washed two times with PBS and fixed in Paraformaldehyde for 30 min at room temperature. The films were then washed three times with PBS and dehydrated in 30%, 50%, 70%, 80%, 90%, 95%, and 100% ethanol, respectively, for 10 minutes. After dehydration with ethanol, further substitution to amyl acetate was necessary. Thus, films were immersed in amyl acetate:ethanol solutions with composition 25:75; 50:50; 75:25; 100:0, respectively, for 15 min and, then, placed in a Critical Point Dryer room. The samples were finally dried under vacuum, coated with Pt, and examined with FE-SEM.

#### 3.2.3 Statistical analysis

All data are expressed as means ± standard deviation. Differences between means were analyzed by one-way ANOVA followed by a Tukey's post hoc test. For *in vitro* cell assay, statistical analysis was performed using two-way ANOVA with the Bonferroni's post test. All statistical analyses were performed with Prism, Graph Pad Software.

### 3.3 Results and discussion

#### 3.3.1 Chemical composition

Table 3.1 reports on chemical composition of PTFE, PTFE-DOPA, PTFE-Ag, and PTFE-DOPA-Ag samples calculated from XPS spectra (data not reported).

**Table 3.1** XPS chemical composition of pure PTFE film, DOPA powder, PTFE film coated with DOPA (PTFE-DOPA), and films immersed in  $\text{AgNO}_3$  solution (50 mM) for 24 hours (PTFE-Ag and PTFE-DOPA-Ag).

Sample	Atomic percentage (mol%)					C/N
	C1s	O1s	F1s	N1s	Ag(3d)	
PTFE	30.8	0.7	68.5	-	-	-
DOPA (theoretic value)	64.3	28.6	-	7.1	-	9.0
PTFE-DOPA	51.4	15.2	28.7	4.5	-	11.4
PTFE-Ag	34.3	1.1	64.5	-	-	-
PTFE-DOPA-Ag	33.8	7.7	52.5	2.2	3.5	15.4

As previously discussed (Chapter 2 – paragraph 2.3.1), polyDOPA coating induced changes in surface chemical composition (remarkably increased of carbon and oxygen contents and appearance of nitrogen element), indicating the successfully deposition of polyDOPA layer on PTFE film surfaces.

After 24 h of metallization process, Ag element was observed on the surface of PTFE-DOPA-Ag at 369 eV. It could be attributed to Ag(3d). The strong signal of Ag indicated that a layer of Ag has been deposited on the PTFE–DOPA surface. Because no Ag(3d) signal was discernible on the DOPA-modified PTFE film surface before the reaction in  $\text{AgNO}_3$ , the peak in this spectrum was attributable to the silver uptake from the  $\text{AgNO}_3$  solution. The metallization process induced also changes in peak intensities and atomic compositions. Compared with PTFE-DOPA film, the contents of carbon, oxygen and nitrogen were reduced to 33.8 mol%, 7.7 mol% and 2.2 mol%, respectively, while the fluorine percentage significantly increased reaching a value of 52.5 mol%. Thus, PTFE-DOPA-Ag showed atomic percentage similar to the pure PTFE composition, attributable to a partial release of DOPA in the  $\text{AgNO}_3$  solution or to the reaction of  $\text{Ag}^+$  with catechol and N-containing groups of polyDOPA.

As control, pure PTFE was subjected to the metallization process. However, XPS spectra of PTFE-Ag film did not reveal the presence of silver and the atomic composition did not change compared to pristine PTFE.

To further investigate the chemical structure and molecule interaction, high-resolution spectra of C1s and O1s were performed on PTFE, PTFE-DOPA, PTFE-Ag, and PTFE-DOPA-Ag samples as shown in Fig. 3.1.

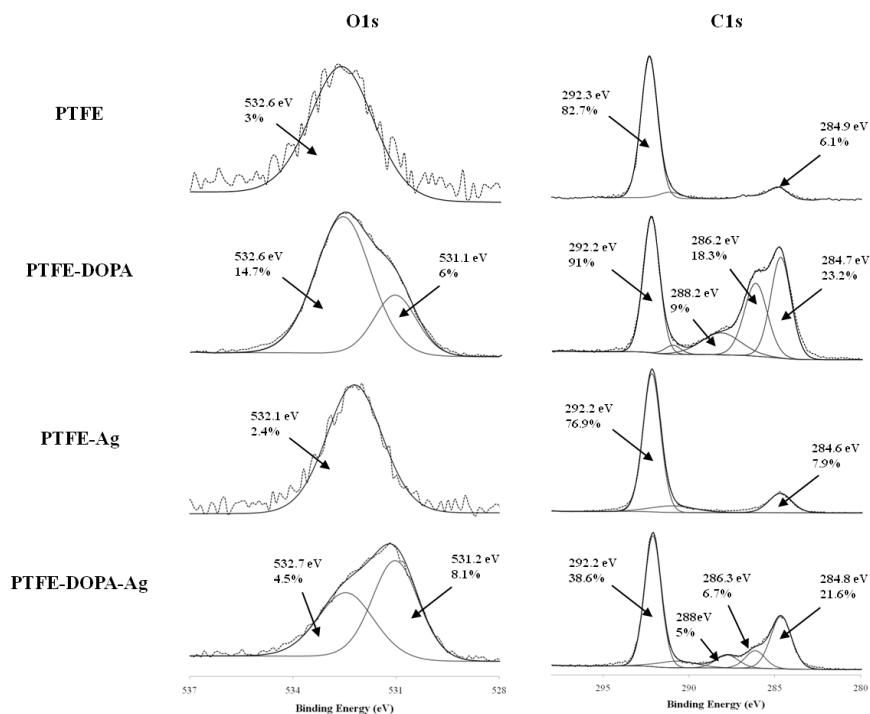


**Fig. 3.1** High resolution XPS spectra of C1s and O1s for PTFE, PTFE-DOPA, PTFE-Ag, and PTFE-DOPA-Ag samples.

As observed in Chapter 2, the results of core-level C1s and O1s spectra of PTFE-DOPA samples proved that the hydrophilic groups, including  $-OH$ ,  $-COOH$ , and  $-NH$ , were introduced onto model films. The relative percentage of O1s band was then influenced by the Ag metallization process. The atomic percentage of quinone (532.7 eV) has markedly reduced due to its involvement in Ag metal binding process (14.7% for PTFE-DOPA vs 4.5% for PTFE-DOPA-Ag). The catechol and quinone groups in polyDOPA were recognized to chelate  $Ag^+$  ions and further induced the reduction of  $Ag^+$  ions into metallic Ag, but no changes could be observed for the C-O band. The metallic Ag was then transformed into AgNPs through atom-by-atom growth mode [28]. As observed before, no marked variations could be detected in the high resolution spectra of pristine PTFE films after 24 h of immersion in  $AgNO_3$  solution. High resolution spectra of Ag(3d) core level were also characterized to determine the chemical state of Ag on the surface of PTFE-DOPA-Ag films (Fig. 3.2). The  $Ag(3d_{5/2})$  and  $Ag(3d_{3/2})$  peaks were found at binding energies of 368 and 374 eV, respectively. The slitting of the 3d doublet of Ag was 6 eV which indicated the formation of metallic Ag on the surface of PTFE-DOPA films [31].

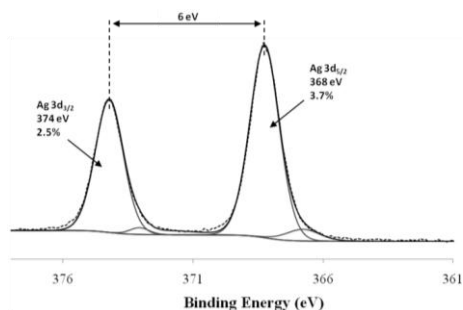


**Fig. 3.2** XPS HR spectra of Ag(3d) for PTFE-DOPA-Ag samples.

### 3.3.2 Morphological analysis

Structure and morphology of PTFE samples before and after the coating process were visualized under SEM as shown in Fig. 3.3.

As observed in Chapter 2 (par. 2.3.2), model PTFE film was not characterized by a smooth surface and some defects could be observed (Fig. 3.3a). The immersion in DOPA solution induced the formation of a polyDOPA thin layer on the surface of PTFE-DOPA samples (Fig. 3.3b, black arrow).

After 24 h of metallization, AgNPs were deposited dispersedly on the surface of DOPA-modified PTFE films with the appearance of some agglomerates. The diameter of AgNPs was  $68.0 \pm 9.5$  nm, as shown in the SEM images. EDS spectra of PTFE-DOPA-Ag film surface confirmed the material that composed the nanoparticles. Moreover, on PTFE-DOPA-Ag film surface it was still visible the polyDOPA layer observed on PTFE-DOPA sample, as underlined by black arrows on Fig. 3.3d.

No morphological changes could be observed on PTFE-Ag film (Fig. 3.3c) which further proof the absence of functionality for AgNPs metallization on the pristine PTFE surface.

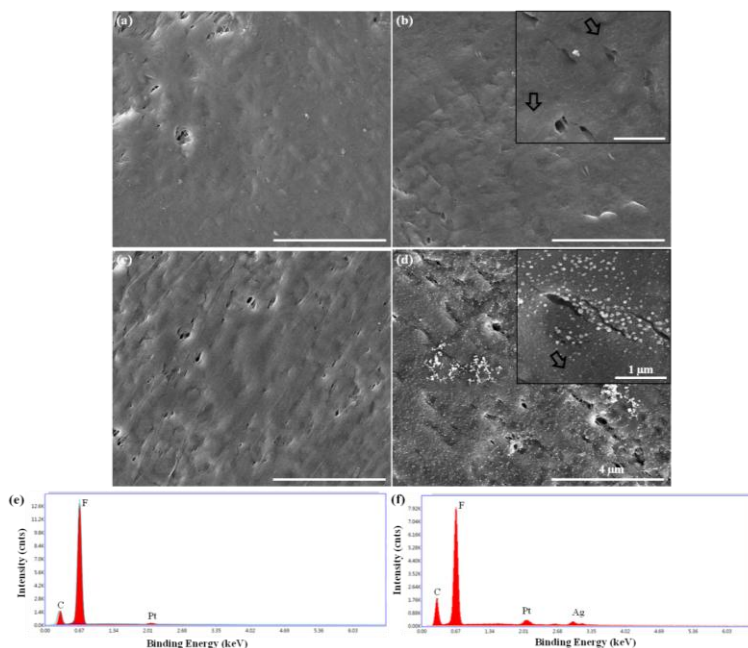


**Fig. 3.3** Morphology of (a) PTFE, (b) PTFE-DOPA, (c) PTFE-Ag, and (d) PTFE-DOPA-Ag films. EDS analyses of (e) PTFE-Ag and (f) PTFE-DOPA-Ag surfaces.

### 3.3.3 Surface roughness and wettability properties

Films topography was evaluated through AFM analysis. AFM images for PTFE, PTFE-DOPA, PTFE-Ag, and PTFE-DOPA-Ag samples along with their surface roughness values are shown in Fig. 3.4.

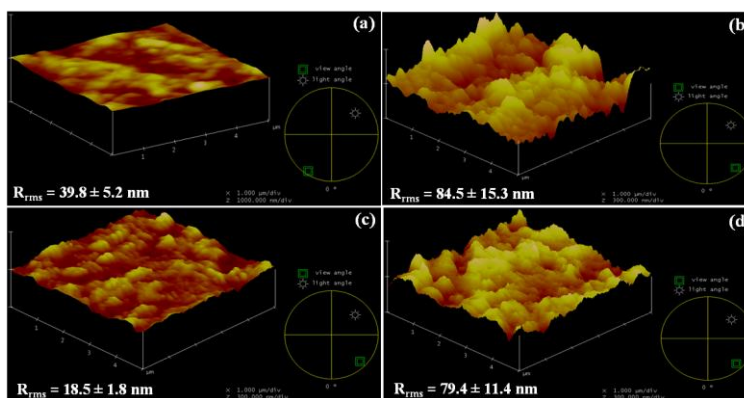


**Fig. 3.4** AFM height mode images and root mean square roughness values ( $R_{rms}$ ) of (a) PTFE, (b) PTFE-DOPA, (c) PTFE-Ag, and (d) PTFE-DOPA-Ag samples.

AFM analysis confirmed the SEM observations. As previously discussed (Chapter 2 – Par. 2.3.3), the immersion in DOPA solution for 48 h markedly changed PTFE surface topography,

leading also to a statistically significant increase of PTFE-DOPA surface roughness compared to pristine PTFE (\*\*\*)  $P < 0.01$ ).

The metallization process in  $\text{AgNO}_3$  solution did not change the surface topography of PTFE-DOPA film. Moreover, no statistically significant changes could be detected in surface roughness values of PTFE-DOPA and PTFE-DOPA-Ag samples. However, as reported in Fig. 3.5, uniform and monodispersed spherical particulates were evidently found by decreasing the scan area, indicating the role of polyDOPA as a reducing agent and template for the formation of AgNPs without requiring additional reducing agent. The particle analysis showed that the size of AgNPs on PTFE-DOPA-24Ag surface was  $68.3 \pm 10.2$  nm, confirming the value obtained with SEM analysis. It is desirable to obtain nano-size nanoparticle instead of micro-size, as it will produce higher antibacterial effect due to larger surface area [32, 33].

Finally, the immersion of pristine PTFE in  $\text{AgNO}_3$  solution resulted in a slightly decrease of  $R_{\text{rms}}$  value (\*  $P < 0.01$ ) but no marked variation in surface topography.

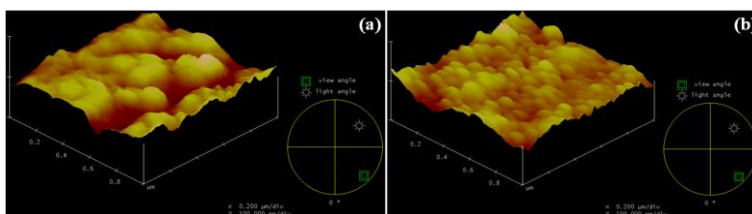


**Fig. 3.5** AFM height mode images of (a) PTFE-DOPA and (b) PTFE-DOPA-Ag samples at  $1 \mu\text{m} \times 1 \mu\text{m}$  scan areas.

To further investigate the effects of functionalization processes on surface properties, water contact angle values have been collected from PTFE, PTFE-DOPA, PTFE-Ag, and PTFE-DOPA-Ag films and reported in Fig. 3.6.

The pristine PTFE showed hydrophobic property with a water contact angle of about  $110^\circ$ . The coating of polyDOPA resulted in a more hydrophilic surface, confirming the successful deposition of polyDOPA nano-layer onto PTFE surface containing hydrophilic groups ( $-\text{OH}$  and  $-\text{NH}-$ ) [34].

The immersion of DOPA modified samples in  $\text{AgNO}_3$  solution led to slightly hydrophobic surfaces with a contact angle around  $87^\circ$  as a result of increased surface roughness due to the formation of AgNPs [35] and a partial release of DOPA in the  $\text{AgNO}_3$  solution. On the contrary, the surface wettability of pristine PTFE was not influenced by the immersion in  $\text{AgNO}_3$  solution; the water contact angle remained constant around  $107^\circ$ . These results corroborate with those obtained by XPS analyses.

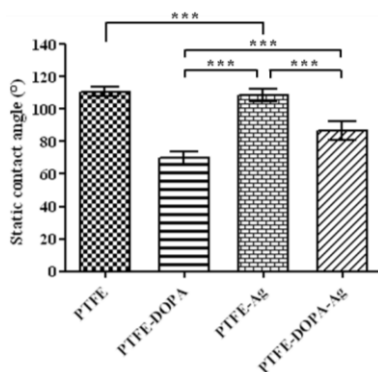


**Fig. 3.6** Water contact angle measurements of PTFE, PTFE-DOPA, PTFE-Ag, and PTFE-DOPA-Ag films.

### 3.3.4 Cell proliferation and adhesion

The toxicity of the prepared samples was evaluated by examining the viability of fibroblast NIH 3T3 cells using Alamar Blue assay, after directly cultivating the cells on the samples for 1 and 3 days. Cells grown on Petri dishes were used as control. Fig. 3.7 shows the number of cells proliferated on PTFE, PTFE-DOPA, and PTFE-DOPA-Ag films after 1 and 3 days of cell culture.

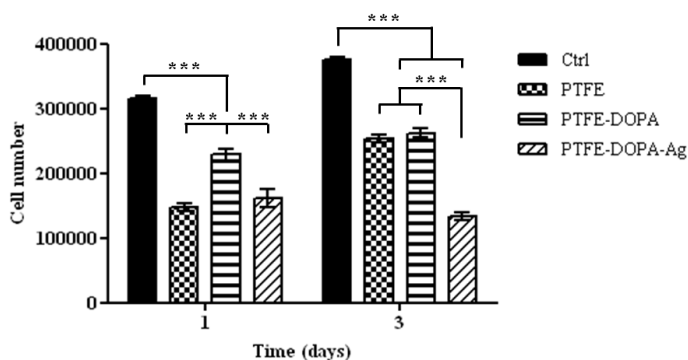


**Fig. 3.7** Cell proliferation on PTFE, PTFE-DOPA, and PTFE-DOPA-Ag films as a function of time. Cell grown on petri dish was used as control (Ctrl).

For all time points, the cell proliferation was lower than Ctrl. However, difference in cell proliferation was observed for various samples. After 1 culture day, the number of cells on PTFE-DOPA samples was significantly higher than those on pristine PTFE, because of the improved surface wettability and the bioactive functional groups (i.e. OH-, NH<sub>2</sub>-) of polyDOPA [36]. Due to the partial release of polyDOPA during the metallization process and the consequent increase of surface hydrophobicity, PTFE-DOPA-Ag samples induced less cell proliferation as compared to PTFE-DOPA. The cell number on PTFE-DOPA-Ag films was

nearly identical to that on PTFE, indicating that no toxicity was involved because of the existence of AgNPs after 1 day of cells immobilization. After 3 days of culture, the number of cells on PTFE and PTFE-DOPA substrates increased reaching values around  $2.5 \times 10^5$  cells. The growth rate was more pronounced for pristine PTFE films. PTFE-DOPA-Ag films showed the same number of cells of day one, thus, for longer culture times, the presence of AgNPs could inhibit proliferation of fibroblasts NIH 3T3 [37].

The cell morphology also assisted to understand cell behavior. Fig. 3.8 shows cells attaching on the surface of PTFE, PTFE-DOPA, and PTFE-DOPA-Ag films.

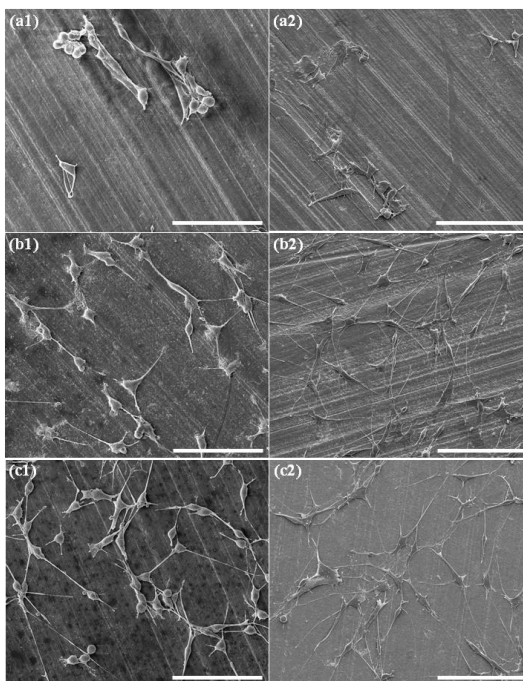


**Fig. 3.8** SEM morphology of fibroblast cells grown on PTFE (a1, a2), PTFE-DOPA (b1, b2) and PTFE-DOPA-Ag (c1, c2) films after seeding cells for 1 and 3 days, respectively denoted with numbers 1 and 2. Scale bar = 100  $\mu$ m.

Fibroblast NIH 3T3 exhibited circular shape on pristine PTFE films at one day of culture (Fig. 3.8 a1), while a more flattened and elongated shape could be observed for cells seeded on PTFE-DOPA and PTFE-DOPA-Ag samples (Fig. 3.8, b1 and c1 respectively). After 3 days of culture, few cells rounded could be noticed on pristine PTFE surface (Fig. 3.8 a2). Contrarily, NIH 3T3 cells grown on PTFE-DOPA and PTFE-DOPA-Ag films (Fig. 3.8, b2 and c2 respectively) were well spread with typical morphology of fibroblasts. Cells were randomly distributed on PTFE-DOPA and PTFE-DOPA-Ag samples surfaces and only some of them remained round in shape and fail to express the typical morphology of spreading fibroblast.

The results from proliferation and adhesion tests proved that the polyDOPA coating allowed to improve cell response of PTFE substrates. The incorporation of AgNPs slightly inhibited fibroblasts proliferation, without compromising cell adhesion and maintaining a good biocompatibility of PTFE-DOPA-Ag films.

### 3.3.5 Antibacterial efficiency

AgNPs were reported as a nonspecific antimicrobial agent against wide range of microorganisms. The exact mechanism of action of silver (Ag) on the microbes is still not known. However, according to the morphological and structural changes found in the bacterial cells, it seems that AgNPs get attached to the cell membrane and also penetrate inside the bacteria. They interact with sulfur-containing proteins of bacterial membrane as well as with the phosphorus-containing compounds like DNA. When AgNPs enter the bacterial cell, it forms a low molecular weight region in the center of the bacteria to which the bacteria conglomerates thus, protecting the DNA from the Ag ions. The nanoparticles preferably attack the respiratory chain, cell division finally leading to cell death. The nanoparticles release also Ag ions in the bacterial cells, which enhance their bactericidal activity [16, 38].

In this chapter, both Gram-positive (*S. aureus*) and Gram-negative (*E. coli*) bacteria were used to evaluate the antibacterial efficacy on PTFE-DOP-Ag films by analysing the zone of inhibition. Fig. 3.9 shows the results of the test, which was conducted on untreated and coated samples.

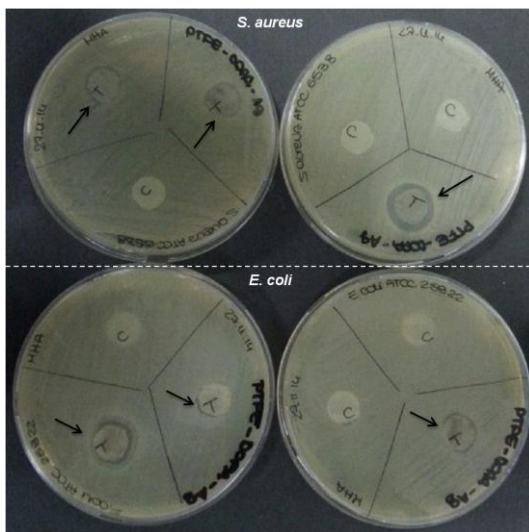


**Fig. 3.9** Antibacterial efficacy on PTFE (C) and PTFE-DOPA-Ag (T) against *S. aureus* and *E. coli* evaluated by zone of inhibition assay.

Preliminary results of antibacterial tests suggested a potential activity of PTFE-DOPA-Ag against bacterial cells. In particular, the biocidal activity on PTFE-DOPA-Ag against *S. aureus* ATCC 6538 was higher when compared with that against *E. coli* ATCC 25922. This could be due to the more vulnerable nature of Gram-positive bacteria in comparison with Gram-negative towards AgNPs [39].

### 3.3.6 Dissolution feature of coating

The dissolution process of DOPA-Ag coating was illustrated across the chemical composition, morphological, topographical and surface wettability changes. XPS results, Table 3.2, showed some changes in surface composition of PTFE-DOPA-Ag films after the immersion in PBS for 7 and 14 days. A markedly decrease of the content of elements associated to the presence of polyDOPA and AgNPs (namely oxygen, nitrogen and silver) could be observed, while the content of the characteristics elements of PTFE substrate (carbon and fluorine) remained almost the same. After 14 days of incubation, nitrogen was no more detectable while the atomic percentage of O1s and Ag(3d) reached values of 0.8 mol% and 0.2 mol% respectively.

**Table 3.2** XPS chemical composition of PTFE film coated with DOPA and AgNPs (PTFE-DOPA-Ag) after incubation in PBS at 37 °C for 0, 7 and 14 days.

Sample	Time (days)	Atomic percentage (mol%)				
		C1s	O1s	F1s	N1s	Ag(3d)
PTFE-DOPA-Ag	0	33.8	7.7	52.5	2.2	3.5
	7	36.4	2.5	58.7	0.2	0.6
	14	37.9	0.8	62.5	-	0.2

Fig. 3.9 shows the high-resolution spectra of C1s and O1s for PTFE-DOPA-Ag at each dissolution time. The polyDOPA release influenced the relative percentage of O1s and C1s bands. In fact, it could be observed that the atomic percentage reduction of species associated to the polyDOPA coating.

As observed for polyDOPA and HAp coating (Chapter 2), the results obtained with XPS analysis suggested that dissolution reactions were occurring in two steps: an extremely fast release of Ag during the first week of immersion and a much more gradual release in the next 7 days.

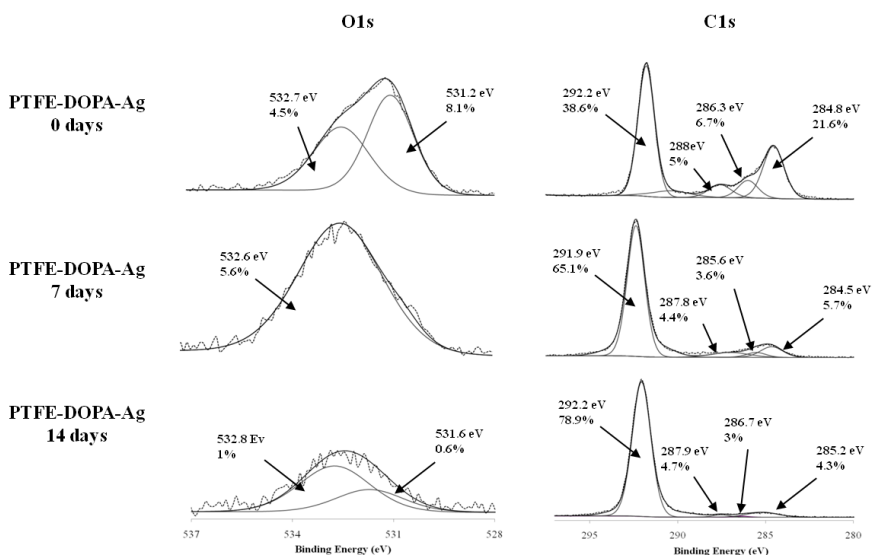


**Fig. 3.10** XPS high-resolution spectra of O1s and C1s for PTFE-DOPA-Ag samples after incubation in PBS at 37 °C for 0, 7 and 14 days. Spectra are compared to those of pristine PTFE film.

Morphological and topographical characterizations are shown in Fig. 3.10. After immersion in PBS for 7 days, AgNPs were still visible but in amounts lower than that of PTFE-DOPA-Ag films before incubation in PBS. The disappearance of AgNPs agglomerates was also observed and, increasing the immersion time at 14 days, no further changes have been detected. The increase in the distance between nanoparticles observed through SEM analysis could explain the XPS results that showed small Ag traces after incubation of PTFE-DOPA-Ag films in PBS. The incubation of samples in PBS for 7 and 14 days slightly reduced surface roughness, leading to values between 60 and 70 nm. However  $R_{\text{rms}}$  values remained higher than value of non-functionalized PTFE and no statistical differences could be observed between films incubated for 7 and 14 days. Regarding the surface topography, the bright high peaks observed on PTFE-DOPA-Ag films were still detectable but characterized by a smoother profile. The polyDOPA and AgNPs release changed also the wettability properties of PTFE-DOPA-Ag films. In fact, the immersion in PBS for 7 and 14 days led to contact angle values of  $(108.1 \pm 2.7)^\circ$  and  $(101.9 \pm 2.6)^\circ$ , respectively, that showed a statistically significant difference with the contact angle value of PTFE-DOPA-Ag film before immersion  $((86.6 \pm 5.8)^\circ)$ .

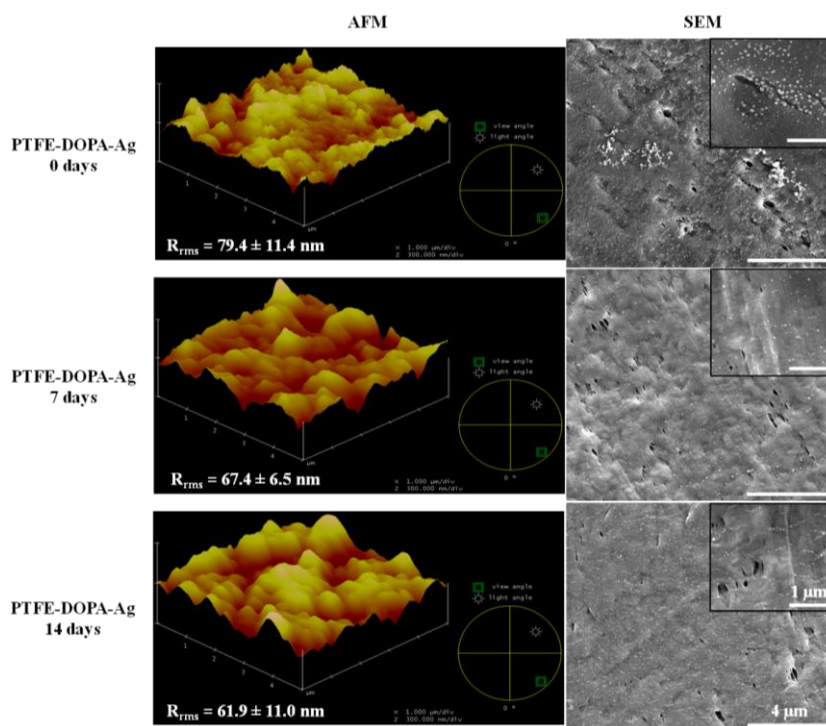


**Fig. 3.11** AFM height mode images, root mean square roughness values ( $R_{rms}$ ) and SEM micrographs of PTFE-DOPA-Ag samples as a function of the immersion time in PBS at 37 °C. Statistical analysis indicated the presence of statistically significant differences among PTFE-DOPA-Ag 0 days and 7, 14 days (\* and \*\*  $P < 0.01$  respectively).

The coating dissolution test demonstrated that polyDOPA and AgNPs coating resulted in a greater early release, which can be of great value in avoiding bacterial infection [40]. Then the Ag release was sustained for at least 14 days, which could be key for inhibition of the bacteria and thereby to aid the regeneration of a new periodontium [41].

### 3.4 Conclusions

Subgingival niche is crowded by pathogenic and opportunistic bacteria that caused periodontal diseases, specifically periodontitis. Without controlling the microbial activity, the regenerative approaches (namely GTR with barrier membranes) generally fail. In this chapter, an environmental-friendly technique has been adopted to anchor AgNPs on the surface of a model PTFE film. A mussel-inspired catecholamine (DOPA) was polymerized on PTFE surface, in mild conditions, to form a uniform film. The surface multifunctional groups on the polyDOPA ad-layer were subsequently used to reduce AgNPs.

Physicochemical and morphological analysis demonstrated that the polyDOPA coating deposited on PTFE surface was an effective functional layer for metallization. The metal-

binding ability of the catechol and N-containing groups presented in the polyDOPA coating could be used to deposit adherent and uniform metal coatings onto the PTFE films.

The AgNPs produced in this work had a diameter around 68 nm and were homogeneously distributed on the surface, with only some agglomerates. The presence of nanoparticles slightly inhibited fibroblasts proliferation, without compromising cell adhesion and maintaining a good biocompatibility of PTFE-DOPA-Ag films. The antimicrobial efficiency has been proved against Gram-negative and Gram-positive bacteria. Moreover, as observed from the coating dissolution test, the AgNPs release and, thus, the antimicrobial effect, seemed to be sustained for at least 14 days.

This work led to the effective development of PTFE substrates with improved antibacterial properties and good biocompatibility that can be used in GTR applications for the treatment of periodontal diseases.

## References

---

1. Listgarten MA. *J Clin Periodontol* 1986;**13**:418–430.
2. Sbordone L, et al. *Clin Oral Invest* 2003;**7**:181–188.
3. March PD. *J Clin Periodontol* 2005;**32**:7-15.
4. Paster BJ, et al. *J Bacteriol* 2001;**183**:3770–3783.
5. Slots J, et al. The oral microflora and human periodontal disease. Tannock GW, editor. Medical Importance of the Normal Microflora. London: Kluwer Academic Publishers;1999:101–127.
6. Nowzari H, et al. *Compendium Contin Educ Dent* 1995;**16**:1042-1058.
7. Karring T, et al. *Periodontol 2000* 1993;**1**:26–35.
8. Temprow PJ, et al. *J Periodontol* 1993;**64**:162–168.
9. Wang H-L, et al. *J Periodontol* 1994;**65**:211-218.
10. Ricci G, et al. *J Periodontol* 1996;**67**:490-496.
11. Nowzari H, et al. *J Periodontol* 1996;**67**:694-702.
12. Slots J, et al. *Periodontol 2000* 1999;**19**:164-172.
13. Bottino MC, et al. *Acta Biomater* 2011;**7**:216–224.
14. Chou AHK, et al. *Implant Dent* 2007;**16**:89-100.
15. Harvey RA, et al. *Surgery* 1982;**92**:504-512.
16. Morones JR, et al. *Nanotechnology* 2005;**16**:2346–2353.
17. Kim JS, et al. *Nanomed Nanotechnol Biol Med* 2007;**3**:95-101.
18. Retchkiman-Schabes PS, et al. *Opt Mater* 2006;**29**:95–99.
19. Gu H, et al. *Nano Lett* 2003;**3**:1261–1263.
20. Gong P, et al. *Nanotechnology* 2007;**18**:604–611.
21. Duran N, et al. *J Biomed Nanotechnol* 2007;**3**:203–208.
22. Li B, et al. *Mater Chem Phys* 2009;**118**:99–104.
23. Akhavan O, et al. *Current Applied Physics* 2009;**9**:1381–1385.
24. Lee H, et al. *Science* 2007;**318**:426-430.
25. Xi ZY, et al. *J Membr Sci* 2009;**327**:244–253.
26. Lee BP, et al. *Biomacromolecules* 2002;**3**:1038–1047.
27. Xu H, et al. *Appl Surf Sci* 2011;**257**:6799–6803.
28. Liao Y, et al. *Mater Chem Phys* 2010;**21**:534–540.
29. Saidin S, et al. *Mater Sci Eng C* 2013;**33**:4715–4724.
30. Lynch AS, et al. *Annu Rev Med* 2008;**59**:415-428.
31. Akhavan O, et al. *J Phys D: Appl Phys* 2009;**42**:135416-135423.
32. Pal S, et al. *Appl Environ Microbiol* 2007;**73**:1712-1720.
33. Sureshkumar M, et al. *J Mater Chem* 2010;**20**:6948-6955.
34. Cheng C, et al. *J Membr Sci* 2012;**417–418**:228–236.
35. Sureshkumar M, et al. *J Polym Sci, Part B: Polym Phys* 2013;**51**:303-310.

- 
36. Hong S, et al. *Nanotechnology* 2011;**22**:494021–494027.
  37. Kreeinthong S, et al. *J Physiol Biomed Sci* 2014;**27**:48-53.
  38. Song HY, et al. *Eur Cells Mater* 2006;**11**:58.
  39. Sondi I, et al. *J Colloid Interface Sci* 2004;**275**:177–182.
  40. He CL, et al. *J Biomed Mater Res Part A* 2009;**89**:80-95.
  41. Zamani M, et al. *Europ J Pharm Biopharm* 2010;**75**:179-185.



# SECTION III



# Investigation of PLCL/PLGA blends physical properties and biocompatibility for Tissue Engineering applications

---

## Abstract

Binary blends of poly(DL-lactide-co- $\epsilon$ -caprolactone) (PLCL) (86 mol.% nominal DL,lactic acid content,  $M_w$ : 28000 Da) and poly(DL-lactide-co-glycolide) (PLGA) (LA:GA = 75:25 mol:mol;  $M_w$ : 66000-107000 Da) with various compositions (100/0, 75/25, 50/50, 25/75, 0/100 wt/wt) were prepared by dissolution in a common solvent, further stirring and final solvent casting. Morphological analysis of fractured sections of PLCL/PLGA blend films did not evidence phase separation between blend components. The behavior of blend glass transition temperatures as a function of composition suggested some degree of blend compatibility. On the other hand, the elastic modulus of PLCL/PLGA blends showed a negative deviation from the additive law of mixture. Mouse embryonic fibroblasts were used to evaluate the biocompatibility of the polymer blends in terms of cell proliferation and adhesion on the surfaces. PLCL/PLGA 25/75 blend promoted cell adhesion and growth. Due to its biocompatibility, its superior mechanical properties and compatibility between the components, PLCL/PLGA 25/75 blend was selected for further characterizations by *in vitro* degradation tests in physiological medium. Results showed PLCL rapid degradation within 4-8 weeks, leading to porous samples.

## 4.1 Introduction

Tissue engineering (TE) is an emerging interdisciplinary and multidisciplinary field, involving biology, medicine, and engineering, aimed at the replacement of damaged, injured or missing body tissues with biologically compatible substitutes [1, 2]. TE research includes many areas, such as biomaterials, cells, biomolecules [3]. In terms of biomaterials, novel biomaterials have been designed to direct the organization, growth, and differentiation of cells in the process of forming functional tissues by providing both physical and chemical cues [4]. Biomaterials for TE should be biocompatible and biodegradable [5], they should promote cell attachment, spreading and proliferation [6], and have suitable mechanical strength and surface characteristics [7, 8]. Resorbable and degradable polymers, such as aliphatic polyesters, including poly(lactic acid) (PLA), poly(glycolic acid) (PGA), poly(caprolactone) (PCL) and their copolymers, have been studied in the last decades for applications such as scaffolds and drug delivery systems [9]. Tailored physicochemical and mechanical properties of polymers to the requirements of the final application can be achieved in a simple and cost-effective way by blending [10]. The final properties of polymer blends depend on the physicochemical properties of the single blend components, blend composition, compatibility between blend components, and the blending method [11].

Polymer industry and academia have developed a wide variety of polymer blends with novel and valuable properties, in order to enlarge the spectrum of available polymers. For example, McDonald et al. [10] tailored the physical properties, degradation rate and drug delivery characteristics of thin films for medical applications by blending PCL with poly(DL-lactic acid) (PDLLA) or with poly(L-lactide-co-glycolide) (PLGA) at a mixing ratio of 95:5; 90:10; 80:20 (wt:wt), respectively. The thermal analysis of the blends indicated that the presence of PDLLA or PLGA increased the degradation rate of PCL amorphous regions. *In vitro* degradation tests showed that PCL/PDLLA blends had a higher weight loss compared to PCL/PLGA blends, as a function of incubation time in phosphate buffered saline (PBS). In the same experiment, the decrease in mechanical properties of both blends was similar. Drug (acetylsalicylic acid) release rate could be modulated by varying blend composition.

Can and co-workers prepared and characterized blends of poly(L-lactide) (PLLA) and PCL with and without paclitaxel [12]. Physical and morphological analysis showed that PLLA/PCL blends (95/5; 90/10; 85/15; 80/20 wt/wt) were phase separated. The *in vitro* degradation rate was close to that of PCL possibly due to the prevention of water diffusion into PLLA as a result of the presence of hydrophobic PCL. However, by increasing PCL content of the blends, PCL

domains increased in size, contact surface between PCL and PLLA phases decreased and water access to PLLA matrix was facilitated resulting in a higher degradation rate of PLLA phase. Degradation-controlled followed by diffusion-controlled paclitaxel release mechanisms were observed. Drug release kinetics depended on blend composition and film thickness.

Recently, poly(DL-lactide-co- $\epsilon$ -caprolactone) (PLCL) copolymer has attracted increasing attention. It is an amorphous biomaterial that combines the higher degradation rate of PLA with the mechanical toughness of PCL. In previous works, PLCL has been used to develop scaffolds for cartilage and nerve regeneration [13, 14] and membranes for periodontal regeneration [15]. However, the exceptional elastic properties of PLCL could be critical for some applications during *in vivo* placement, such as periodontal membranes [16].

One possible approach for enhancing the mechanical properties of PLCL is to blend it with the polymer PLGA in order to improve Young's modulus and tensile strength. Amorphous PLGA copolymer has been extensively investigated and used for various medical applications due to its biodegradability, biocompatibility and good mechanical properties, especially tensile strength [17]. It has been used to prepare scaffolds for cartilage, bone, tendon, and vascular smooth muscle tissue regeneration [18- 21].

The aim of this chapter was the investigation of the physical (morphology, thermal and mechanical properties) and biological (cell adhesion and proliferation) properties of films made of blend between PLCL and PLGA (compositions 100/0, 75/25, 50/50, 25/75, 0/100 wt/wt) with the aim to select an optimal blend composition in terms of compatibility degree between the phases, mechanical properties and cell compatibility, for further testing. The selected composition was further analyzed for its *in vitro* degradation behavior.

Although some compositions of PLCL/PLGA blends have already been developed in a previous work [9], reports on the effect of PLGA content on physicochemical and biological properties of PLCL/PLGA blends are missing. This work provides an extensive characterization of PLCL/PLGA blends which is fundamental for the selection of a suitable blend composition for specific applications in TE.

## **4.2 Materials and methods**

### **4.2.1 Materials**

PLGA (LA:GA = 75:25 mol:mol;  $M_w$ : 66000-107000 Da) and PLCL (nominal 86 mol% of DL,lactic acid,  $M_w$ : 28000 Da) were supplied from Sigma-Aldrich (Milano, Italy). All solvents were of analytical grade and used without further purification (Sigma-Aldrich).

#### 4.2.2.1 Poly(DL-lactide-co-glycolide)

Poly(DL-lactide-co-glycolide) (Fig. 4.1) is synthesized by means of random ring-opening copolymerization of two different monomers, the cyclic dimers (1,4-dioxane-2,5-diones) of glycolic acid and lactic acid. During polymerization, successive monomeric units (of glycolic or lactic acid) are linked together in PLGA by ester linkages, thus yielding a linear, aliphatic polyester as a product.

Depending on the ratio of lactide to glycolide used for the polymerization, different forms of PLGA can be obtained: these are usually identified in regard to the monomers' ratio used (e.g. PLGA 75:25 identifies a copolymer whose composition is 75% lactic acid and 25% glycolic acid). All PLGAs are amorphous rather than crystalline and show a glass transition temperature in the range of 40-60 °C. Unlike the homopolymers of lactic acid and glycolic acids, which show poor solubilities, PLGA can be dissolved by a wide range of common solvents, including chlorinated solvents, tetrahydrofuran, acetone or ethyl acetate.

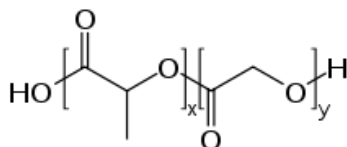


**Fig. 4.1** Poly(DL-lactide-co-glycolide) (PLGA) chemical structure. x= number of units of lactic acid; y= number of units of glycolic.

PLGA has been shown to undergo bulk erosion through hydrolysis of the ester bonds and the rate of degradation depends on a variety of parameters including the LA/GA ratio, molecular weight, and the shape and structure of the matrix. The intermediate co-polymers were found to be much more unstable compared to the homopolymers. Thus, 50/50 poly(DL-lactide-co-glycolide) degrades in approximately 1–2 months, 75/25 in 4–5 months and 85/15 in 5–6 months.

The major popularity of these biocompatible co-polymers can be attributed in part to their approval by the Food and Drug Administration for use in humans, its good processibility which enables fabrication of a variety of structures and forms, controllable degradation rates and their success as biodegradable sutures compared to the earlier suture materials. As such, there has been extensive investigation into its use as an ideal biomaterial for temporary medical applications, such as controlled drug/protein delivery systems and as scaffolds for TE [22].

#### 4.2.2.2 Poly(DL-lactide-co-ε-caprolactone)

Poly(DL-lactide-co-ε-caprolactone) is an amorphous copolymer of DL,lactic acid and ε-caprolactone (Fig. 4.2) with a glass transition temperature of about 16 °C.

By varying the copolymer composition, monomer sequencing and molecular weight, the copolymer properties can be tailored to meet the specific requirements of each particular application. The copolymers have been shown to be both biocompatible and biodegradable. Biodegradation proceeds via simple hydrolysis (random chain scission) leading to progressively lower molecular weight fragments [23].

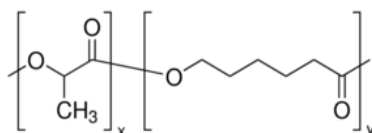


**Fig. 4.2** Poly(DL-lactide-co-ε-caprolactone) (PLCL) chemical structure. x= number of units of lactic acid; y= number of units of caprolactone.

During the past 3 decades, research interest in random copolymers of DL-lactide and ε-caprolactone has increased steadily as their potential in a wide range of biomedical applications has been realized. These applications have so far included biodegradable controlled-release drug delivery systems [24], monofilament surgical sutures [25] and absorbable nerve guides [26].

### 4.2.2 Methods

#### 4.2.2.1 Blend preparation

PLCL/PLGA 100/0; 75/25; 50/50; 25/75; 0/100 (wt/wt) blends were prepared by solution mixing method. The polymers were separately dissolved in chloroform (Sigma-Aldrich) at 6% (wt/v) concentration and each polymer/solvent mixture was stirred using a magnetic stirrer for 4 h, till complete dissolution of polymers. Proper volumes of the polymeric solutions were mixed to prepare blends and stirred for 2 h. Films were obtained by casting a volume of each solution (10 ml) on glass Petri dishes with 55 mm diameter. The solvent was removed via evaporation under a vented hood at room temperature for a period of 48 h. The blends were coded as follows: PLCL/PLGA 100/0; 75/25; 50/50; 25/75; 0/100.

#### 4.2.2.2 Scanning electron microscopy

Scanning electron microscopy (SEM LEO – 1430, Zeiss, Munich, Germany) was performed on cast film surfaces and sections (obtained by fracturing in liquid nitrogen). Samples were sputter coated with Au before SEM analysis.

#### 4.2.2.3 Differential scanning calorimetry

The thermal behavior of cast films based on PLCL/PLGA blends was investigated by differential scanning calorimetry (DSC) using a TA INSTRUMENT DSC Q20. Film specimens (5-10 mg) were inserted into aluminum pans and non-isothermal scans were performed between  $-30\text{ }^{\circ}\text{C}$  and  $200\text{ }^{\circ}\text{C}$  (first heating; cooling; second heating) at a heating rate of  $10\text{ }^{\circ}\text{C}/\text{min}$  under nitrogen atmosphere. The glass transition temperatures ( $T_g$ s) of PLCL and PLGA blend components were measured from the second DSC heating scan.

#### 4.2.2.4 Tensile testing

Tensile mechanical properties of polymer blend films were analyzed to detect any variation respect to the constituent polymers. Tensile tests were performed on dry rectangular specimens ( $10 \times 30\text{ mm}^2$ ) with  $200\text{ }\mu\text{m}$  thickness using MT<sup>®</sup>QTest<sup>™</sup>/10 instrument. The traction force was applied along the length of the samples at a constant cross-head displacement rate of  $2\text{ mm}/\text{min}$ . Young's modulus (E), and maximum tensile strength and strain ( $\sigma_{\text{max}}$  and  $\epsilon_{\text{max}}$ , respectively) were measured from the stress-strain curves. E was calculated from the slope of the initial linear portion of the stress-strain curve, and  $\sigma_{\text{max}}$  and  $\epsilon_{\text{max}}$  were calculated as the maximum stress a material can withstand and the elongation at fracture, respectively [27].

#### 4.2.2.5 In vitro testing

Mouse embryonic fibroblast NIH 3T3 cells were supplied by American Type Culture Collection (ATCC, Virginia, USA). Dulbecco's modified Eagle's medium (DMEM; ATCC) supplemented with 10% Calf Bovine Serum (CBS; Gibco, Invitrogen) and 1% penicillin/streptomycin (Invitrogen) was used to culture the fibroblasts. Cells were first expanded, and a concentration of  $5 \times 10^4$  was seeded on the blend films and incubated at  $37\text{ }^{\circ}\text{C}$  in a humidified atmosphere of 5%  $\text{CO}_2$  for 1 and 3 days. Cell Crown<sup>™</sup> inserts (Scaffdex, Tampere, Finland) were used to fix the films at the bottom of the wells prior to cell seeding.

Cell proliferation was assessed using the colorimetric indicator Alamar Blue assay (Life Technologies, Ontario, Canada). Media was removed, samples were rinsed once in PBS, and

300  $\mu\text{L}$  of fresh medium containing a 10% solution of Alamar Blue was added to each well. The culture plates were wrapped in aluminum foil and incubated for 4 h at 37 °C in a humidified atmosphere of 5%  $\text{CO}_2$ . Absorbance of the extracted dye, which is proportional to the number of cells attached to the film, was measured spectrophotometrically with a microplate reader (Molecular Devices, SpectraMax i3 multi-mode detection platform, California, USA) at wavelengths of 570 and 600 nm. A calibration curve, generated from a known number of fibroblast NIH 3T3 cells reacting with the Alamar Blue indicator, was used to quantify the number of cells attached on films.

Finally, the morphology of the cells cultured on blend films was examined by SEM (FEI Inspect F-50 FE-SEM). For SEM observation, films were washed two times with PBS and fixed in Paraformaldehyde for 30 min at room temperature. The films were then washed three times with PBS and dehydrated in 30%, 50%, 70%, 80%, 90%, 95%, and 100% ethanol, respectively, for 10 minutes. The samples were then dried under vacuum, coated with platinum, and examined with SEM.

#### 4.2.2.6 *In vitro* degradation

For degradation studies, only PLCL/PLGA 100/0, 25/75, 0/100 blend films were used. *In vitro* degradation tests were carried out on 10 x 30 mm<sup>2</sup> cast film specimens incubated in 6 ml PBS at 37 °C and pH 7.4 for 1, 2, 4, 6 and 8 weeks. The PBS medium was exchanged once every 2 weeks.

Changes in sample weight during the *in vitro* degradation tests were monitored. Samples ( $n=5$ ) were accurately weighed before *in vitro* degradation tests ( $W_0$ ). Then, at each time, samples were collected, dried for 1 week under a vented hood at room temperature and then weighed again ( $W_f$ ). The weight loss was calculated as a percentage according to Eq. 1:

$$\Delta W(\%) = \frac{W_0 - W_f}{W_0} \cdot 100 \quad (1)$$

Morphological evaluation of the fractured and exposed surfaces of film samples at each degradation test time was analyzed by SEM according to the procedure described at par. 4.2.2.2. Thermal and chemical properties were evaluated through DSC analysis, according to the previously described method at par. 4.2.2.3 and by infrared analysis in ATR modality (FTIR-ATR). FTIR-ATR analysis was carried out in a Perkin Elmer Frontier Optical Spectrometer fitted with an attenuated total reflection sampler. Spectra were obtained over the 400-4000  $\text{cm}^{-1}$  wavenumber range at room temperature.

Weight average molecular weights ( $M_w$ ), number average molecular weight ( $M_n$ ) and polydispersity indices ( $PI = M_w/M_n$ ) of samples at each degradation test time were measured by gel permeation chromatography (GPC) using an Agilent system equipped with a Water 2414 RI detector. The measurements were performed using four Water columns (range 103–106 Å) at 40 °C; tetrahydrofuran (THF, Sigma-Aldrich) as eluent (1.0 mL/min) and narrow polystyrene standards were used for calibration.

### 4.2.3 Statistical analysis

Results were expressed as mean  $\pm$  standard deviation obtained from three different experiments. Statistical analysis was performed using analysis of variance (two-way ANOVA) by GraphPad Prism 5 software. Differences were considered statistically significant at  $p < 0.05$ .

## 4.3 Results and discussion

### 4.3.1 Morphological analysis

Fractured surfaces of the PLCL/PLGA blends were investigated by SEM analysis. Fig. 4.3 reports the photomicrographs of blend sections.

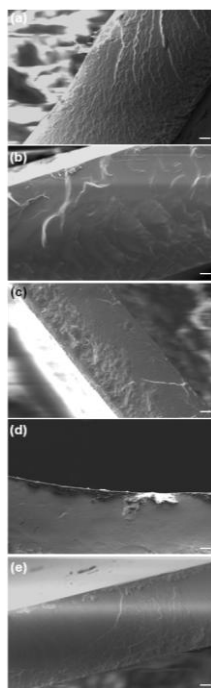


**Fig. 4.3** SEM images of the fractured sections of PLCL/PLGA (a) 100/0; (b) 75/25; (c) 50/50; (d) 25/75; (e) 0/100 blend film samples. *Scale bar* = 20  $\mu\text{m}$ .

Films showed a compact section. No evident phase separation between blend components could be detected for analyzed blend compositions, suggesting physical compatibility of PLCL/PLGA blends.

### 4.3.2 Thermal analysis

Fig. 4.4 collects DSC second heating thermograms for PLCL/PLGA samples (100/0, 75/25, 50/50, 25/75, 0/100 wt/wt) prepared via solvent casting method. Both PLCL and PLGA are amorphous copolymers, therefore their glass transition temperature ( $T_g$ ) is their unique characteristic thermal transition. Pure PLCL and PLGA exhibited a  $T_g$  of around 28 °C and 49 °C, respectively. For each blend, DSC second heating traces showed the presence of two glass transition temperatures for each blend component, which values are collected in Table 4.1.

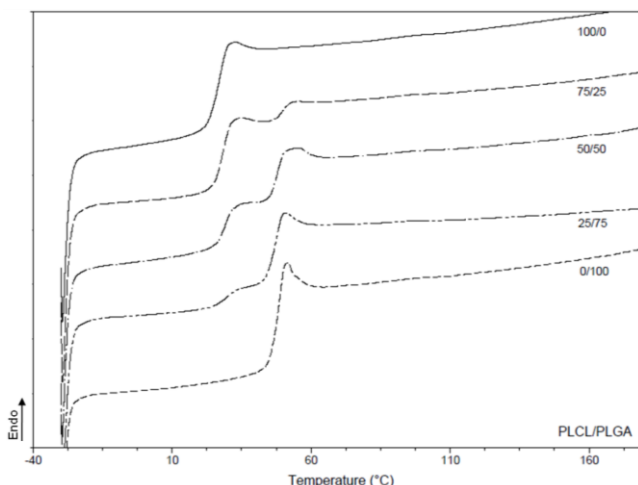


**Fig. 4.4** DSC second heating thermograms for PLCL/PLGA blends.

$T_g$  is a well-known indicator of blend miscibility. If the two components of a binary blend are miscible in the amorphous phase, only one  $T_g$  is expected (Fox equation). If they are immiscible,  $T_g$  values of both components are retained. If the two components are partially miscible, their  $T_g$  in blends shifts towards each other [28]. As shown in Table 4.1,  $T_g$  values of blend components were similar to those of pure polymers; however the difference between PLGA and PLCL  $T_g$ s calculated for each blend was lower compared to pure polymers, suggesting some compatibility degree for PLCL/PLGA 50/50 and PLCL/PLGA 25/75 blend compositions. This result appeared in contrast with SEM analysis, as immiscible (compatible and incompatible) blends generally show a biphasic morphology. However, as reported in

literature [9], the lack of phase separation in SEM analysis may result from close physical properties between blend components, such as shrinkage ratio, absorbance, and refractive index.

**Table 4.1** Glass Transition temperatures measured by DSC analysis (second heating scan at 10 °C/min).

Composition	$T_g^{PLGA}$ (°C)	$T_g^{PLCL}$ (°C)	$\Delta T_g$ (°C)
PLCL/PLGA 100/0	-	27.2 ± 0.6	-
PLCL/PLGA 75/25	49.0 ± 0.2	28.2 ± 0.3	20.7 ± 0.3
PLCL/PLGA 50/50	47.7 ± 0.2	29.0 ± 0.5	19.0 ± 0.1
PLCL/PLGA 25/75	47.7 ± 0.2	29.7 ± 0.1	17.9 ± 0.1
PLCL/PLGA 0/100	48.6 ± 0.2	-	-

$$^1 \Delta T_g = T_g^{PLGA} - T_g^{PLCL}$$

Theoretical  $\Delta T_g$  between PLGA and PLCL phase was 21.4 ± 0.5 °C

### 4.3.3 Mechanical characterization

Fig. 4.5 shows the stress-strain curves measured for PLCL/PLGA blend films by tensile tests. The PLCL/PLGA blend films stress/strain curves showed the typical trend of ductile polymers [27]. They were characterized by an initial linear elastic region, followed by a yielding zone, a subsequent drop in stress with neck formation due to chain orientation along the stress direction and a final increase of stress till final fracture.

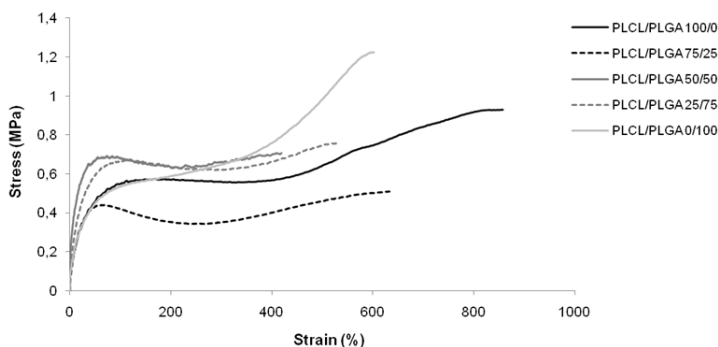


**Fig. 4.5** Tensile stress-strain curves for PLCL/PLGA blend films (cross-head speed = 2 mm/min).

In the elastic region, stress was proportional to strain and the deformation was completely reversible; the slope of this linear portion was calculated as the elastic modulus of the films (E). Yielding is due to plastic deformation leading to a decrease in polymer cross-sectional area. As the stress-strain curves showed, the nominal stress decreased after yielding, before setting at a constant value during necking. The final increase of the stress was due to strain hardening, occurring once the whole sample was necked. The stress increased till fracture which occurred

at maximum tensile stress ( $\sigma_{\max}$ ) and strain ( $\epsilon_{\max}$ ). The values of  $E$ ,  $\sigma_{\max}$ , and  $\epsilon_{\max}$  calculated from the stress-strain curves of PLCL/PLGA blend films are collected in Table 4.2.

Fig. 4.6 and 4.7 show  $E$ ,  $\sigma_{\max}$ , and  $\epsilon_{\max}$  as a function of blend composition compared to the additive law of mixtures. Mechanical behavior of blend samples can be predicted by the additive rule of mixture in case of miscible blends, while it shows a positive or a negative deviation from the additive rule of mixture in the case of compatible and incompatible blends, respectively.

PLCL/PLGA 100/0 and 0/100 exhibited different Young's moduli of around 1.5 MPa and 24 MPa, respectively. Blends showed intermediate values of the Young's modulus respect to the blend components, which increased with increasing PLGA amount.

**Table 4.2** Young's elastic modulus ( $E$ ), maximum tensile strength ( $\sigma_{\max}$ ) and strain ( $\epsilon_{\max}$ ) calculated from stress-strain curves.

Composition	$E$ (MPa)	$\sigma_{\max}$ (MPa)	$\epsilon_{\max}$ (%)
PLCL/PLGA 100/0	$1.5 \pm 0.2$	$0.3 \pm 0.1$	$894.1 \pm 68.5$
PLCL/PLGA 75/25	$1.6 \pm 0.6$	$0.5 \pm 0.0$	$682.7 \pm 84.9$
PLCL/PLGA 50/50	$4.2 \pm 0.5$	$0.7 \pm 0.1$	$481.6 \pm 65.7$
PLCL/PLGA 25/75	$10.2 \pm 0.6$	$0.8 \pm 0.0$	$548.8 \pm 57.9$
PLCL/PLGA 0/100	$23.6 \pm 3.5$	$1.2 \pm 0.1$	$461.4 \pm 131.6$

Fig. 4.6 reports the behavior of  $E$  as a function of composition for PLCL/PLGA blends compared to the additive rule of mixture.  $E$  showed a negative deviation from the additive rule of mixture. Among the tested blend compositions, PLCL/PLGA 25/75 blend composition showed the highest Young's modulus.

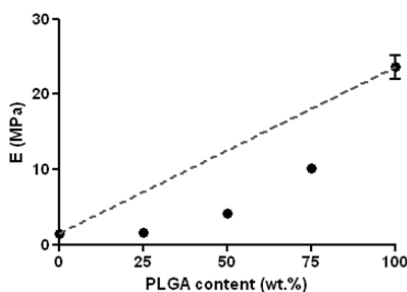


**Fig. 4.6** Elastic modulus of PLCL/PLGA blends against composition. Dotted line indicates prediction by the additive law of mixtures.

The maximum tensile stress (Table 4.2) of PLGA (1.2 MPa) was higher than that of PLCL (0.3 MPa), whereas  $\epsilon_{\max}$  value was higher for PLCL (894% for PLCL vs. 461% for PLGA). Blend maximum tensile stress and strain were intermediate respect to blend components, respectively

increasing and decreasing with increasing PLGA amount (Fig. 4.7). Values of blend  $\sigma_{\max}$  and  $\epsilon_{\max}$  more closely approached those predicted by the additive rule of mixtures (Fig. 4.7).

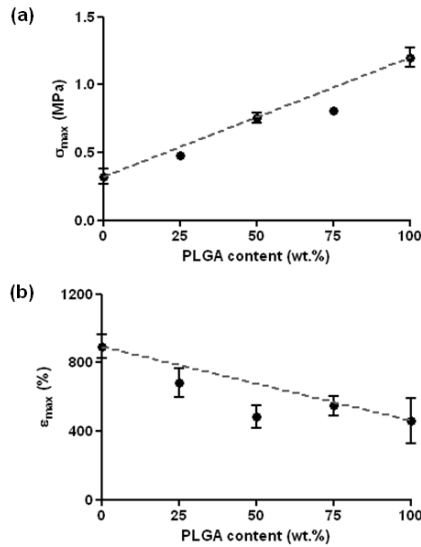


**Fig. 4.7** Maximum tensile strength (a) and strain (b) of PLCL/PLGA blends against composition. Dotted line indicates prediction by the linear additive law.

Therefore, a comparison between tensile mechanical parameters and prediction by the additive rule of mixture suggested that PLCL/PLGA blends displayed limited compatibility. Superior mechanical properties were displayed by PLCL/PLGA 25/75 blend ( $E = 10.2 \pm 0.6$  MPa,  $\sigma_{\max} = 0.8 \pm 0.0$  MPa, and  $\epsilon_{\max} = 548.8 \pm 57.9\%$ ).

#### 4.3.4 Cell proliferation and adhesion

Cell adhesion and proliferation over time on a material are the indication of its cellular compatibility and suitability for TE applications. Different polymeric blends of PLCL/PLGA (100/0, 75/25, 50/50, 25/7, 0/100 wt/wt) prepared via solution casting were seeded with fibroblast NIH 3T3 and tested by Alamar Blue assay in order to determine the cell attachment and proliferation on the films.

Fig. 4.8 shows the number of cells attached to the samples after 1 and 3 days of cell culture. No correlation between blend composition and cell growth could be observed. The number of cells increased on all samples after 1 culture day. The proliferation process was more pronounced for PLCL/PLGA 100/0 and 50/50 films whose cell number almost doubled in the first day, approaching the value of Ctrl ( $3.1 \times 10^5$  cells). At 3 days, a further increase in cells number could be observed for all material tested. The cell number on blends with composition 100/0,

50/50 and 25/75 (wt/wt) was significantly higher than those on PLCL/PLGA 75/25 and 0/100 films after 3 days culture time. Thus, the results indicated that PLCL/PLGA 100/0, 50/50 and 25/75 films were suitable for the support of cell adhesion and proliferation.

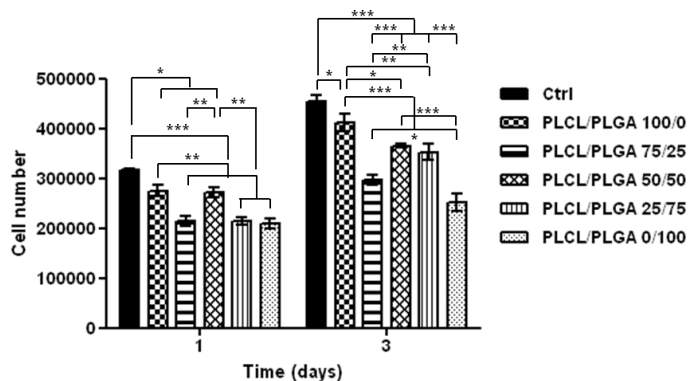


**Fig. 4.8** Cell proliferation on PLCL/PLGA blend films as a function of time. Petri dish was used as control (Ctrl).

The morphologies of adherent cells and cell-polymer interaction were analyzed by SEM. Fig. 4.9 shows the morphology of cells adhered to PLCL/PLGA films with different compositions after 1 and 3 days culture time. After 1 culture day, slightly differences in cell morphology on different samples could be observed. Fibroblasts appeared more elongated and adherent to the films with the increased of PLGA content (Fig. 4.9 c1, d1 and e1).

At 3 days, cell morphology markedly changed on all materials tested except for PLCL/PLGA 0/100 blend: cells appeared more elongated on films with lamellopodia expanded outside. On PLCL/PLGA 25/75 films, showing the highest cell density according to Alamar blue assay (Fig. 4.8), cells spread uniformly and extensively; the development of lamellopodia demonstrated that cell adhesion was high (Fig. 4.9 d2).

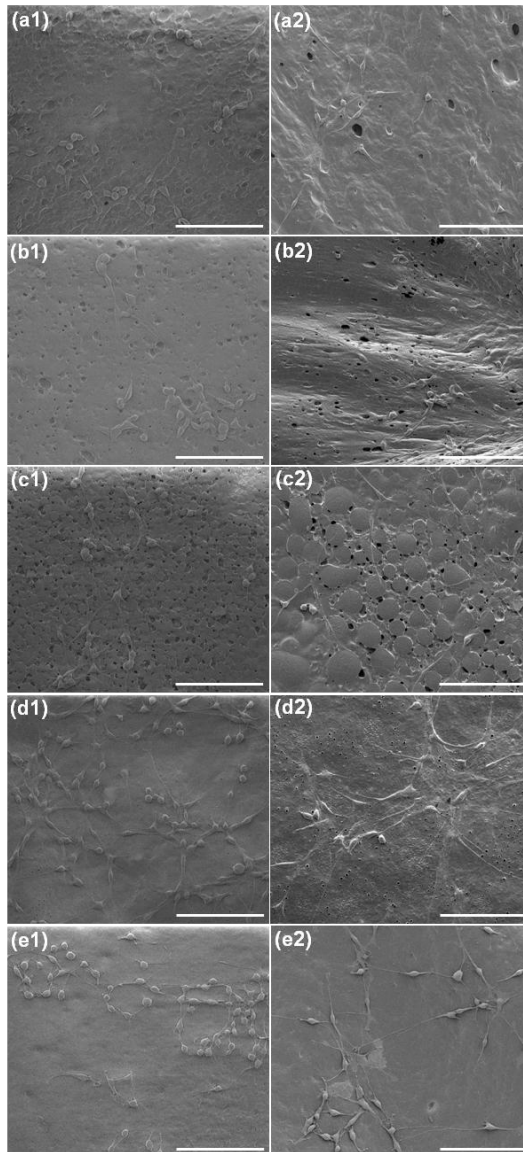


**Fig. 4.9** SEM morphology of fibroblast cells grown on blend PLCL/PLGA 100/0 (a1, a2), 75/25 (b1, b2), 50/50 (c1, c2), 25/75 (d1, d2) and 0/100 (e1, e2) after seeding cells for 1 and 3 days, respectively denoted with numbers 1 and 2. Scale bar = 100  $\mu\text{m}$ .

Based on mechanical characterization and cell proliferation and adhesion tests, the PLCL/PLGA 25/75 blend was found to be a suitable candidate for TE applications.

#### 4.3.5 *In vitro* degradation test

*In vitro* hydrolytic degradation tests were carried out on the selected PLCL/PLGA 25/75 blend films and their control pure components (PLCL, PLGA).

PLGA and PLCL copolymers are known to degrade through bulk hydrolysis of the ester linkages within the polymer backbone to form the constituent monomers (lactic and glycolic acids for PLGA, and lactic acid and caprolactone for PLCL) which can be naturally removed from the body [29, 30]. The hydrolysis reaction is autocatalytic, i.e. the bulk material degrades at a faster rate than the surface due to a build up of carboxylic acid end groups [31].

#### 4.3.5.1 Weight loss and pH variations

The weight percentage reduction of films over the duration of *in vitro* degradation tests was monitored (Fig. 4.10).

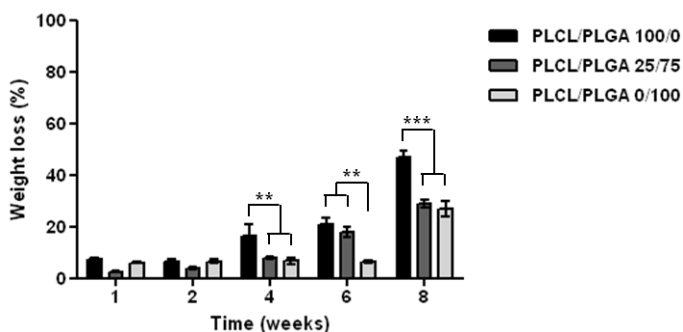


**Fig. 4.10** Weight loss percentage as a function of incubation time in PBS for PLCL/PLGA 100/0, 25/75 and 0/100.

PLCL/PLGA 100/0 showed higher weight loss at each time among the analyzed materials: it lost only  $6.5 \pm 1.7\%$  of the initial weight after 2 weeks of incubation in PBS, and about 46% after 8 weeks. Weight loss for PLCL/PLGA 0/100 specimens remained constant at around 6-6.5% until 6 weeks of incubation in PBS, after which it increased up to  $26.9 \pm 6.8\%$  after 8 weeks. PLCL/PLGA 25/75 blend weight loss progressively increased as a function of time, reaching  $28.8 \pm 3.4\%$  after 8 weeks. Blend weight loss behavior was approximately intermediate between that of the pure polymers.

The pH of the incubation medium was also monitored as a function of time (Fig. 4.11). In the case of PLCL/PLGA 0/100 and 25/75 blend, pH was approximately constant at 7.4 up to 6 and 4 weeks incubation in PBS, respectively. Then, for both samples, pH decreased as a function of incubation time reaching the values of  $5.1 \pm 0.2$  and  $5.2 \pm 0.5$  after 8 weeks.

On the other hand, PLCL/PLGA 100/0 degradation rate was faster than the other materials as suggested by the lower pH at each incubation time. Within the first 4 weeks, pH was approximately 6.9. After 4 weeks incubation in PBS, pH started to become slightly acidic and decreased progressively as a function of incubation time up to about 4 after 8 weeks. Changes in pH were attributed to the release of acidic degradation products.

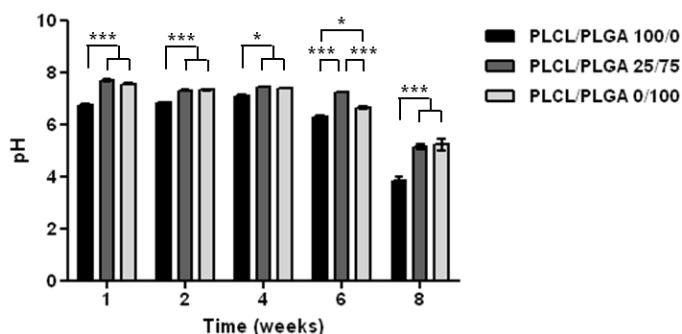


**Fig. 4.11** pH values of the PBS solution as a function of incubation time in PBS for PLCL/PLGA 100/0, 0/100 and 25/75 blend. Data are average values and bars represent standard deviation.

#### 4.3.5.2 Molecular weight measurements

Molecular weight was also monitored as a function of incubation time in PBS. In general, a bulk degradation process occurs for PGA, PLA, PCL, and their copolymers: polymer molecular weight decreases due to the hydrolysis of polymer ester bonds, forming shorter polymer chains [32]. When the size of the polymer fragments becomes small enough so that scaffold mechanical properties are significantly decreased, scaffold collapses and degradation products are released.

Fig. 4.12 shows the  $M_w$  and PI variation of PLCL/PLGA 100/0, 0/100 and 25/75 blend at different incubation time in PBS.

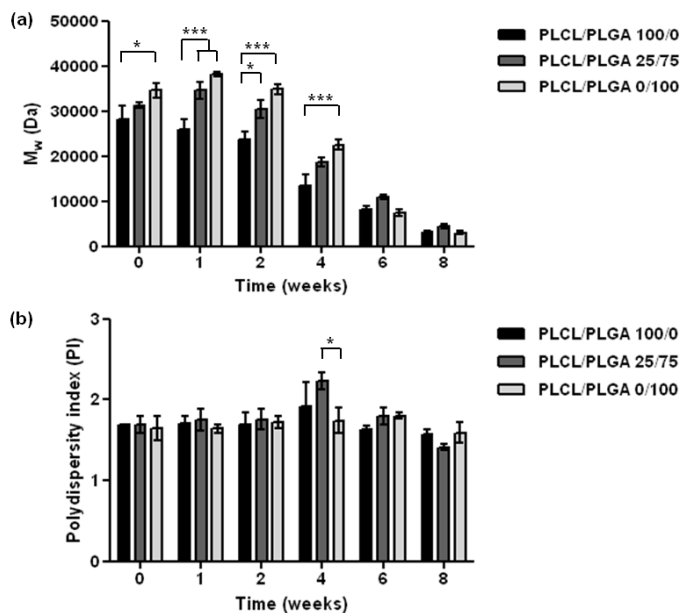


**Fig. 4.12** Variation of (a) weight average molecular weight ( $M_w$ ) and (b) polydispersity indices of PLCL/PLGA 100/0, 25/75 and 0/100 blend films as a function of degradation time.

$M_w$  of PLCL/PLGA 100/0 films decreased progressively as a function of time, from  $28185 \pm 5020$  Da to  $3135 \pm 312$  Da after 8 weeks incubation in PBS. On the other hand, PLCL/PLGA 0/100 and 25/75 blend molecular weights initially slightly increased (1 weeks incubation in PBS), suggesting the degradation and release of low molecular weight fractions. Then, molecular weight of PLCL/PLGA 0/100 and 25/75 blend progressively decreased as a function of time to about 2900 Da and 4300 Da, respectively (8 weeks).

$M_w$  values of PLCL/PLGA 25/75 blend films were intermediate between those of blend components up to 4 weeks, becoming similar to those of pure polymers at 6 and 8 weeks incubation in PBS.

The polydispersity indexes of PLCL/PLGA 100/0 and 25/75 blend samples were approximately constant at 1.7 value up to 2 weeks, then they increased to a maximum of  $1.9 \pm 0.5$  for PLCL and  $2.2 \pm 0.2$  for blend films after 4 weeks. The PLCL/PLGA 100/0 and 25/75 PIs finally decreased to about 1.6 and 1.4 after 8 weeks, respectively. The initial increase in PI was a result of random chain scission during degradation, while the subsequent decrease was due to the decrease in molecular weight and the release of some of the degradation products [33].

No significant variation of PI was measured for PLCL/PLGA 0/100 during degradation tests ( $1.7 \pm 0.3$ ).

#### 4.3.5.3 Thermal properties

Thermal behavior of samples was analyzed as a function of their incubation time in PBS. Polymer glass transition temperature is a function of different parameters among which the polymer molecular weight. It is a reversible step change in molecular mobility, from a rigid glassy state to a mobile rubbery state. This change is linked to the free volume associated to the polymer chain ends. When the molecular weight decreases, more chain ends are present and more free volume is generated. The polymer chains have, therefore, more space to move and the rubbery state is reached earlier, i.e. at a lower temperature [34].

Table 4.3 collects  $T_g$  values (measured from the second DSC heating scan) of PLCL/PLGA 100/0, 0/100 and 25/75 blend as a function of degradation time.

**Table 4.3** Glass transition temperatures of PLCL and PLGA as a function of incubation time in PBS.

<b>Samples degradation time (weeks)</b>	<b><math>T_g^{PLGA}</math> (°C)</b>	<b><math>T_g^{PLCL}</math> (°C)</b>
PLCL/PLGA 100/0		
<b>0</b>	-	$27.2 \pm 0.6$
<b>1</b>	-	$26.2 \pm 0.7$
<b>2</b>	-	$27.7 \pm 0.4$

<b>4</b>	-	21.0 ± 1.1
<b>6</b>	-	20.8 ± 2.5
<b>8</b>	-	12.3 ± 0.2
PLCL/PLGA 25/75		
<b>0</b>	47.7 ± 0.2	29.7 ± 0.0
<b>1</b>	44.3 ± 0.3	30.9 ± 0.2
<b>2</b>	45.5 ± 0.6	30.7 ± 0.2
<b>4</b>	35.6 ± 2.9	-
<b>6</b>	36.7 ± 0.9	-
<b>8</b>	32.7 ± 0.8	-
PLCL/PLGA 0/100		
<b>0</b>	48.6 ± 0.2	-
<b>1</b>	49.2 ± 0.2	-
<b>2</b>	46.4 ± 1.1	-
<b>4</b>	44.8 ± 0.9	-
<b>6</b>	39.2 ± 3.5	-
<b>8</b>	29.8 ± 1.4	-

No significant changes for PLCL/PLGA 100/0 and 0/100  $T_g$ s could be observed up to 2 and 4 weeks of incubation in PBS, respectively. Then, glass transition temperatures progressively decreased reaching 12.3 °C for PLCL/PLGA 100/0 samples and 29.8 °C for PLCL/PLGA 0/100 samples after 8 weeks. This behavior was in agreement with molecular weight data which showed that both PLCL/PLGA 100/0 and 0/100 molecular weights slightly decreased as a function of degradation time. Another factor that may lead to the decrease of material glass transition is the water diffused into the polymer, due to the plasticizing effect of the water molecules [35].

Similarly to the pure polymers, blend thermal properties did not change significantly in the first 2 weeks of the degradation test, in agreement with molecular weight analysis. After 4 weeks, PLCL  $T_g$  was no longer detectable while PLGA  $T_g$  gradually decreased. These changes could be attributed to the molecular weights reduction.

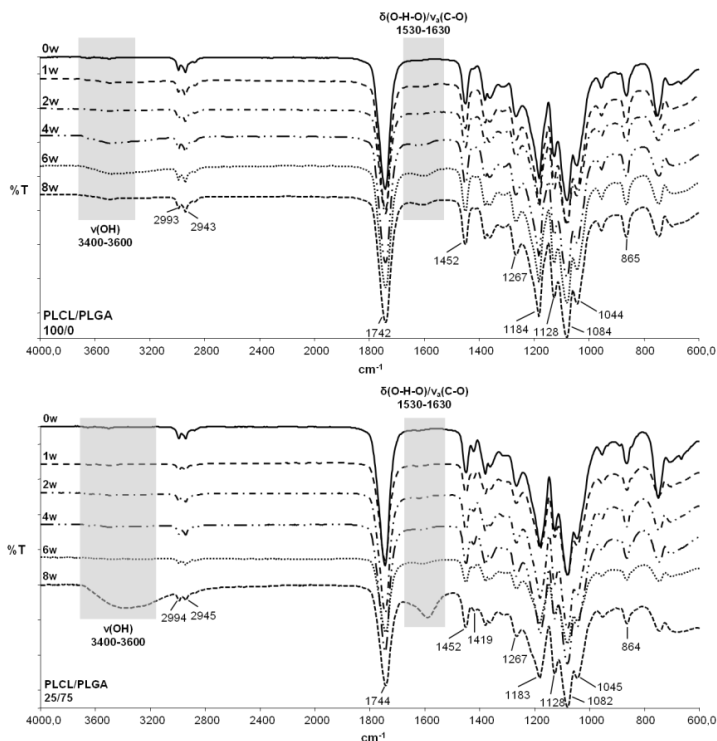
The PLCL  $T_g$  decrease below the physiological temperature (37 °C) was responsible for PLCL softening during incubation of films in PBS, causing PLCL leaching out from the blend membrane structure and progressive pore formation. On the contrary, the glass transition temperature of PLGA, both as blend component and as pure polymer, decreased below 37 °C after 4 and 6 weeks incubation in PBS, respectively. These changes caused film softening and loss of film shape.

#### 4.3.5.4 FTIR-ATR analysis

Changes in surface chemical composition of PLCL/PLGA 100/0, 0/100 and 25/75 blend samples as a function of degradation time were monitored by FTIR-ATR analysis.

The FTIR-ATR spectra of films, as a function of incubation time in PBS, are shown in Fig. 4.13. Spectra showed similar absorption bands: weak absorption bands at around  $3000\text{ cm}^{-1}$  were due to alkyl groups stretching vibration and strong absorption bands at about  $1742\text{ cm}^{-1}$  were attributed to the stretching vibration of C=O bond. The bands at  $1452\text{ cm}^{-1}$  arose from the bending vibration of methyl group  $-\text{CH}_3$  while the absorption peaks of C=O bending vibration appeared at about  $1267\text{ cm}^{-1}$ . The ester bond was confirmed by the presence of absorption bands in the  $1044\text{--}1184\text{ cm}^{-1}$  interval region, assigned to the C–O–C ether group stretching. Finally, the bands at about  $865\text{ cm}^{-1}$  arose from the stretching vibration of C–C bond [36].

PLCL/PLGA 25/75 blend spectra were more similar to PLCL/PLGA 0/100 than to PLCL/PLGA 100/0 spectra, due to the higher quantity of PLGA phase in blend. The main difference between PLCL/PLGA 100/0 and 0/100 was related to the absorption bands around  $1420\text{ cm}^{-1}$  observed for PLGA based films. This peak was attributed to the C–H stretching vibration of methyl groups of PLGA copolymer.



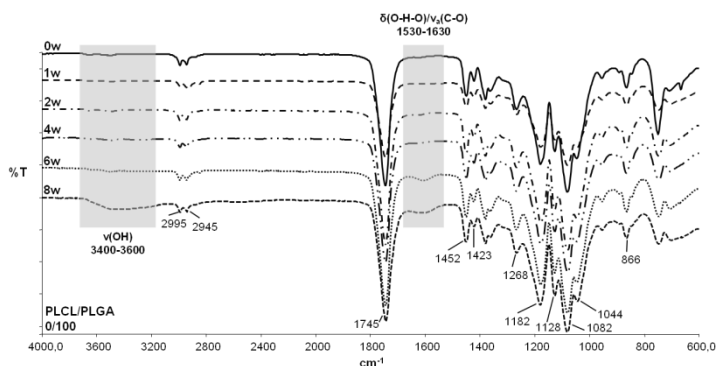


**Fig. 4.13** FTIR-ATR spectra of PLCL/PLGA 100/0, 25/75 and 0/100 samples as a function of incubation time in PBS.

For all analyzed materials, FTIR spectra of films immersed in PBS showed a measurable increase of the absorbance of the peak centered in the 1650-1550  $\text{cm}^{-1}$  interval region with increasing the degradation time. This peak, not present in the spectra of initial samples, is characteristic of the stretching vibrations of carboxylate groups. Indeed, hydrolytic degradation process breaks ester bonds and produces alcohol and carboxylate groups. Moreover, after 8 weeks for PLCL/PLGA 0/100 and 25/75 samples and after 4 weeks for PLCL/PLGA 100/0 samples, a peak between 3400  $\text{cm}^{-1}$  and 3600  $\text{cm}^{-1}$  appeared attributed to the presence of terminal  $-\text{OH}$  groups and to increased amount of absorbed water. In the case of PLCL/PLGA 100/0 samples, its intensity increased with increasing immersion time in PBS [37].

#### 4.3.5.5 Morphological analysis

A non-uniform degradation process, as it is typical in materials that degrade by in bulk autocatalytic hydrolysis, was suggested from visual inspection of the specimens (data not shown).

All the films became softer after incubation in PBS, due to the temperature of the bath, which was close (PLGA) or superior (PLCL) to polymer  $T_g$  and PBS absorption leading to material plasticization. However, PLCL/PLGA 0/100 and 25/75 samples remained intact after 6 weeks while PLCL/PLGA 100/0 films lost their shape and fragmented starting from 4 weeks.

The morphology of the external surface and fractured section of PLCL/PLGA 100/0, 0/100 and 25/75 blend film samples after 0-8 weeks incubation in PBS at 37 °C was observed through SEM analysis. Morphology of both surface and fractured section of PLCL/PLGA 0/100 films did not change significantly as a function of incubation time in PBS while that of PLCL/PLGA 100/0 films could not be monitored after 2 weeks of exposure due to their rapid break up and softening (data not shown).

Fig. 4.14 reports the morphological analysis of PLCL/PLGA 25/75 blend films as a function of incubation time in PBS.

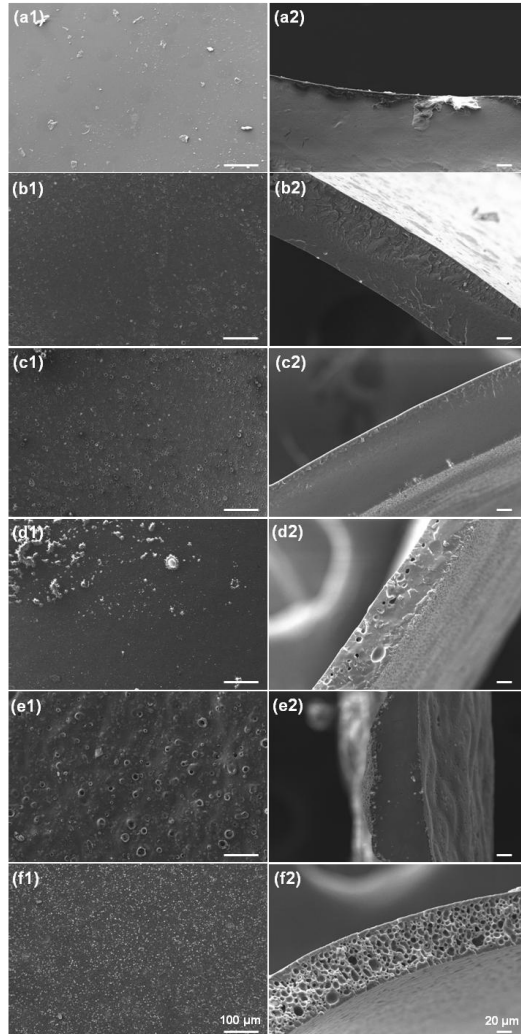


**Fig. 4.14** Morphology of the surface (numbers 1) and fractured sections (numbers 2) of PLCL/PLGA 25/75 samples as a function of their incubation time in PBS: (a) 0 weeks; (b) 1 weeks; (c) 2 weeks; (d) 4 weeks; (e) 6 weeks; (f) 8 weeks. Scale bar = 100 μm (numbers 1) and 20 μm (numbers 2).

PLCL/PLGA 25/75 blend films initially were non-porous, with smooth surfaces; however, extensive micropores developed during degradation. It was possible to observe the appearance of numerous pores on the surface of blend cast films after 1 week incubation in PBS. Moreover, the cross-section of PLCL/PLGA 25/75 blends showed pores with a few micron size after 4 weeks of incubation in PBS, probably caused by PLCL dissolution and degradation.

## 4.4 Conclusions

Blending PLGA and PLCL through a solvent casting process generated suitable materials for TE applications. PLCL/PLGA 25/75, 50/50 and 75/25 did not show evident phase separation, attributed to similar physical properties between blend components. The behavior of blend component  $T_g$ s suggested immiscibility for all the tested compositions; however, some degree of compatibility was found for PLCL/PLGA 25/75 and 50/50 blends. Mechanical properties of blend samples confirmed the limited compatibility for PLCL/PLGA 25/75 and 50/50 blends. Among these two compositions, PLCL/PLGA 25/75 blend showed superior mechanical properties (toughness).

*In vitro* cell tests using mouse embryonic fibroblast NIH 3T3 cells indicated that PLCL/PLGA 100/0, 50/50 and 25/75 films supported cellular attachment and proliferation, especially on PLCL/PLGA 25/75 blend surface, fibroblasts spread uniformly and extensively with the development of lamellopodia. This blend composition was further characterized for its stability in physiological medium, evidencing a degradation behavior intermediate between that of the pure polymers, in term of weight loss and molecular weight changes, becoming similar to those of pure PLGA after 6 weeks incubation in PBS. The cross-section of PLCL/PLGA 25/75 blends showed pores with a few micron size after 4 weeks of incubation in PBS, probably caused by PLCL dissolution and degradation.

In summary, it can be concluded that PLCL/PLGA 25/75 blend polymer film combined the deformability of PLCL with the higher mechanical stiffness, the cell adhesion properties and the slowly degradation rate of PLGA, leading to a tough material with similar degradation rate to PLGA and superior cell adhesion and proliferation.

## References

---

1. Vunjak-Novakovic G, et al. Culture of cells for tissue engineering. 1st ed. New York: Wiley; 2006.
2. Tabata Y. *Drug Discovery Today* 2001;**6**:483–487.
3. Rickne A. Swedish possibilities within tissue engineering and regenerative medicine. VINNOVA—Swedish Governmental Agency for innovation systems/Verket för Innovations system; 2009.
4. Segvich S, et al. Biological interactions on materials surfaces. Understanding and controlling protein, cell, and tissue responses. New York: Springer; 2009.
5. Yan-Peng J, et al. *Biomed Mater* 2007;**2**:R24–R37.
6. Ito Y, et al. *Biomaterials* 1997;**3**:197-202.
7. Mitragotri S, et al. *Nat Mater* 2009;**8**:15-23.
8. Papenburg BJ, et al. *Biomaterials* 2007;**28**:1998-2009.
9. Wang L, et al. *J Polym Res* 2010;**17**:77-82.
10. McDonald PF, et al. *J Mater Sci* 2010;**45**:1284-1292.
11. Lyons JG, et al. *Mater Chem Phys* 2007;**103**:419-426.
12. Can E, et al. *AAPS PharmSciTech* 2011;**12**:1442-1453.
13. Jung Y, et al. *Biomaterials* 2008;**29**:4630–4636.
14. Meek MF, et al. *J Biomed Mater Res* 2004;**68A**:43–51.
15. Bottino MC, et al. *Acta Biomater* 2011;**7**:216–224.
16. Bottino MC, et al. *Dent Mater* 2012;**28**:703-721.
17. Wu XS. Synthesis and properties of biodegradable lactic/glycolic acid polymers. In: Wise DL, Trantolo DJ, Altobelli DE, Yaszemski MJ, Gresser JD, Schwartz ER, editors. Encyclopedic handbook of biomaterials and bioengineering: part A materials. New York: Marcel Dekker; 1995.pp.1015-54.
18. Ma PX, et al. *J Biomed Mater Res* 1995;**29**:1587–1595.
19. Holy CE, et al. *J Biomed Mater Res* 2003;**65A**:447–453.
20. Ouyang HW, et al. *Tissue Eng* 2003;**9**:431–439.
21. Gao J, et al. *J Biomed Mater Res* 1998;**42**:417–424.
22. Astete CE, et al. *J Biomater Sci Polym Ed* 2006;**17**:247–289.
23. Baimark Y, et al. *Science Asia* 2004;**30**:327-334.
24. Ge H, et al. *J Appl Polym Sci* 2000;**75**:874-882.
25. Tomihata K, et al. *Polym Degrad Stab* 1998;**59**:13-18.
26. Den Dunnen WFA, et al. *J Biomed Mater Res* 1995;**29**:757-766.
27. Askeland, Donald R. The Science and Engineering of Materials. 3rd ed. London: Chapman & Hall; 1996.
28. Fox T. *Bull Am Phys Soc* 1956;**1**:123-125.
29. Fukuzaki H. *Biomaterials* 1991;**12**:433-437.
30. Jeong SI, et al. *Biomaterials* 2004;**25**:5939–5946.

- 
31. Bucholz B. Accelerated degradation test on resorbable polymers. In: Plank H, Dauner M, Renardy M, editors. Degradation phenomena on polymeric biomaterials. New York: Springer; 1992.pp.67-76.
  32. Alexis F, et al. *J Appl Polym Sci* 2006;**102**:3111–3117.
  33. Lu L, et al. *J Biomed Mater Res* 1999;**46**:236–244.
  34. Young RJ, et al. Introduction to Polymers. 2nd ed. London: Chapman & Hall; 1991.
  35. Blasi P, et al. *J Control Rel* 2005;**108**:1-9.
  36. Jose MV, et al. *Polymer* 2009;**50**:3778-3785.
  37. Chapanian R, et al. *Eur J Pharm Biopharm* 2010;**74**:172–183.

# 5

## Improving fibroblast response and antimicrobial efficiency via polyelectrolytes multilayer assembly for Tissue Engineering applications

---

### Abstract

In this chapter, the layer-by-layer (LbL) technique was applied for the coating of PLCL/PLGA 25/75 (wt/wt) films with the purpose to enhance fibroblast cell response and confer antibacterial efficacy. A surface priming treatment was applied and optimized before depositing LbL coating. PLCL/PLGA 25/75 (wt/wt) films were pre-functionalized through aminolysis by using 1,6-hexamethylenediamine reagent. The effect of aminolysis treatment on physicochemical and morphological properties was evaluated, leading to the selection of the following parameters:  $C = 0.08$  g/mL,  $t = 8$  min and  $T = 37$  °C. Then, multilayered chondroitin sulfate/chitosan (CHS/CH) coatings were deposited on the aminolysed films. The feasibility of multilayer coating was confirmed by QCM-D analysis. Further confirmations of LbL build up on blend films derived from: water contact angle measurements (the contact angle jumped alternatively between  $45^\circ$  and  $65^\circ$  relying on the outmost layer component), FTIR-ATR analysis (appearance of absorbance peaks characteristics of CHS and CH), and fluorescence microscopy (using FITC-labeled CH). *In vitro* cell tests demonstrated the ability of coated samples to improve fibroblast NIH 3T3 adhesion and proliferation. Biocompatibility properties increased with increasing the layer number and on CH-terminating layers. However, no antibacterial activity was observed for films coated with 16 layers. Finally, the immersion of 16-layers coated samples in physiological medium for 14 days led to almost complete dissolution of the coating.

## 5.1 Introduction

Tissue Engineering (TE) has rapidly developed as a multidisciplinary field in the area of human health care [1]. It combines biology, medicine, materials science and engineering to generate products with suitable biochemical and physical–mechanical performance to repair or replace damaged, injured or missing body tissues [2]. Most of the current research in TE focuses on improving the scaffolds used for tissue culture. Optimal scaffolds are required to be biocompatible, biodegradable and mechanically stable. The scaffold should also provide a physical support for cells and an environment for their proliferation, growth and differentiation. In addition to these basic requirements, it is crucial that the scaffold surface elicits the desired response from cells in contact with it. It is the scaffold surface that determines the initial cellular response to the implant, and therefore its acceptance and durability in the body [3].

The biomaterial chosen to fabricate the scaffolds influences both surface and mechanical properties of the implants. Scaffold surface properties such as chemical composition, wettability, surface charge, and morphology determine the initial interaction of biomaterials with cells [4].

Polyesters, such as poly(lactic acid) (PLA), poly(glycolic acid) (PGA), poly( $\epsilon$ -caprolactone) (PCL) and their copolymers, have been well documented for their excellent biodegradability, biocompatibility, non-toxicity and their biocompatible degradation products [5]. However, the surface properties of polyesters are not ideal for cell growth. They are relatively hydrophobic compared to the natural extracellular matrix, are unable to interact specifically with cells, and do not possess any functional groups for the attachment of biologically active molecules [6]. Surface treatments are thus necessary to optimize the properties of these polymers.

Surface modifications are aimed at increasing biomaterial hydrophilicity through both physical (i.e. plasma treatment [7, 8]) and chemical methods (i.e. hydrolysis, aminolysis [9]), while maintaining their bulk properties. The functional groups introduced can be used as anchors to bind specific biomacromolecules, such as extracellular matrix (ECM) components. Several approaches can be adopted to modify the surface properties of biocompatible polymers with biomacromolecules, such as covalent attachment [10– 12], physical adsorption [13, 14], and affinity bonding [15]. In this chapter, the Layer-by-Layer (LbL) self-assembly technique was investigated to surface engineer polyester films based on poly(DL-lactide-co- $\epsilon$ -caprolactone) (PLCL) and poly(DL-lactide-co-glycolide) (PLGA) blend.

The LbL deposition method consists of the alternate adsorption of oppositely charged polyanions and polycations that self-organize on the material surface, leading to the formation

of polyelectrolyte multilayer (PEM) films [16]. In comparison to conventional coating methods, PEMs are easy to prepare and the procedure is applicable regardless of the shape of solid materials. Varying the nature of the polyelectrolytes selected and the conditions used for the deposition, LbL films with a wide range of physicochemical properties can be produced, thus enabling a diverse array of biomedical applications, including drug delivery, tissue engineering, and bioactive implant coatings [17, 18]. The investigation of LbL multilayers composed of naturally derived polymers, such as proteins, polysaccharides or their fragments, has been of particular interest due to their excellent biocompatibility. In particular, ECM components can promote cell adhesion and proliferation [19].

In this study, chondroitin sulfate/chitosan (CHS/CH) PEM-functionalized PLCL/PLGA blend substrates were developed to enhance fibroblast NIH 3T3 cell adhesion, proliferation and function, and to confer antibacterial efficacy to the membranes. CHS and CH were chosen as PEM layers because they are natural polymers and they are resorbable *in vivo*. CHS is an important ECM polysaccharide of bone, cartilage, and connective tissues; it takes also an important role in maintaining cell functions. Its high negative polarity allows CHS to be used as polyanion in LbL assembly. CH, derived from chitin, has been exploited for wide biomedical applications such as wound dressing, drug delivery, and tissue engineering owing to its non-toxicity, non-immunogenicity, biocompatibility and biodegradability. It is a cationic polysaccharide, which antibacterial activity has received considerable attention in recent years [20, 21].

We investigated the formation, physicochemical properties, cellular response, and antibacterial efficiency of PEMs composed of water-soluble CHS and CH. However, prior to the multilayer build-up, initial charges need to be introduced on the substrate. In this contest, a chemical method was selected: the aminolysis treatment. It was performed, setting different combinations of parameters, in order to find the optimal process conditions on the basis of modified substrate physicochemical properties. The optimal set of aminolysis parameters were then used for the modification of PLCL/PLGA blend films, subsequently coated through LbL technique.

PE film deposition was monitored by dissipative quartz crystal microbalance and fluorescence microscopy, while film morphology, wettability and chemical composition were characterized via SEM, water contact angle measurement and FTIR-ATR, respectively. *In vitro* fibroblast adhesion and proliferation on films were then evaluated.

Once selected the optimal number of layers of LbL coating for our application, the PEM film was further characterized via antibacterial tests, XPS analysis, quantification of surface amino groups, and coating stability in phosphate buffer saline (PBS).

## 5.2 Materials and methods

### 5.2.1 Materials

Poly(DL,lactide-co-glycolide) (PLGA; LA:GA = 75:25 mol:mol;  $M_w$ : 66000-107000 Da) and poly(DL,lactide-co-caprolactone) (PLCL; 86 mol.% nominal DL,lactic acid content;  $M_w$ : 28000 Da) were used to produce the polymeric substrates. Aminolysis was performed by using 1,6-hexamethylenediamine ( $M_w = 116.2$  Da) that is an organic compound with the formula  $H_2N(CH_2)_6NH_2$ . The molecule is a diamine, consisting of a hexamethylene hydrocarbon chain terminated with amine functional groups. Chondroitin sulfate A sodium salt from bovine trachea (CHS) and chitosan highly viscous derived from crab shell with 75-85% deacetylation degree (CH;  $M_w$ : 190-310 kDa) were used as polyelectrolytes for LbL deposition coating. All chemicals and solvents were supplied by Sigma-Aldrich (Milano, Italy) and used as received.

#### 5.2.1.1 Chitosan

Chitosan (Fig. 5.1) is the most important derivative of chitin, a natural polysaccharide first identified in 1884. Chitin is synthesized by an enormous number of living organisms, such as arthropods, fungi and yeast, organisms in the lower plant and animal kingdoms.

CH is obtained by (partial) deacetylation of chitin in the solid state under alkaline conditions (concentrated NaOH) or by enzymatic hydrolysis in the presence of chitin deacetylase. Because of the semicrystalline morphology of chitin, chitosan obtained by solid-state reaction has a heterogeneous distribution of acetyl groups along the chains [22].

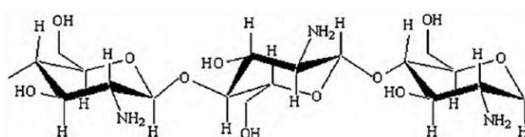


**Fig. 5.1** Chitosan (CH) chemical structure.

CH is biocompatible, biodegradable, non-toxic and non-immunogenic. It is a cationic antibacterial polysaccharide that has been shown to disrupt bacterial cell membrane integrity [22, 23]. These properties find several biomedical applications in TE [24], wound healing [25], drug and gene delivery [26, 27].

### 5.2.1.2 Chondroitin sulfate

Chondroitin sulfate (Fig. 5.2), a natural complex glycosaminoglycan (GAG), is composed of alternate disaccharide sequences of differently sulfated residues of D-glucuronic acid (GlcA) and of N-acetyl-D-galactosamine (GalNAc). Although all natural CHS have an identical carbohydrate backbone, different degrees and positions of sulfate groups give rise to a wide range of composition.

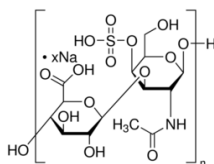


**Fig. 5.2** Chondroitin sulfate (CHS) chemical structure.

Chondroitin sulfate is the most abundant GAG in the body. Although cartilage and intervertebral disc are tissues having the highest content of CHS, these molecules are largely distributed in tissues, and are the main GAG components in blood and urine. Used worldwide in many pharmaceutical and nutraceutical applications, CHS is obtained by extraction from tissues of several animals (i.e. bovine, porcine, avian, cartilagenous fishes).

CHS is quite water soluble, which limits its use alone in the solid state for biomedical applications, being frequently combined with other polymers. In fact, its anionic nature enables efficient interaction with cationic molecules to form interesting structure. Due to its nature, chondroitin sulfate has been mostly used in the development of supports for cartilage tissue engineering applications [28].

## 5.2.2 Sample preparation

### 5.2.2.1 Preparation of PLCL/PLGA 25/75 samples via solvent casting

Substrates were based on PLCL/PLGA 25/75 (wt/wt) blend, prepared by solution mixing technique. The polymers were dissolved in chloroform (Sigma-Aldrich) at 6% (wt/v) concentration, till complete dissolution. Films were obtained by casting 10 ml of solution on glass Petri dishes with 55 mm diameter. The solvent was removed via evaporation under a vented hood at room temperature for a period of 48 h.

### 5.2.2.2 Surface activation through aminolysis treatment

The surface activation of samples is a necessary step to allow the deposition of a multilayered coating by LbL process, as schematizing in Fig. 5.3. PLCL/PLGA 25/75 (wt/wt) blend films were aminolysed by incubation in 1,6-hexamethylenediamine/1-propanol solutions, with different concentrations and treatment times. After the aminolysis treatment, the samples were rinsed with a large quantity of demineralised water to remove free 1,6-hexamethylenediamine and dried at room temperature under a vented hood for 48 h.

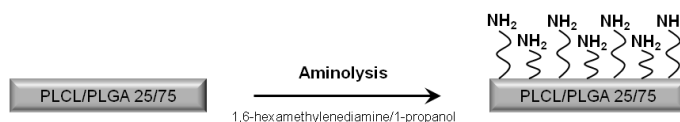


**Fig. 5.3** Schematic representation of aminolysis process by dipping polymeric film in 1-6-hexamethylenediamine/1-propanol solution. The surface exposes primary amino groups.

Aminolysis was performed combining the different conditions listed in Table 5.1. After each aminolysis treatment, samples were subjected to physicochemical characterizations to find the optimal process parameters for the surface modification.

**Table 5.1** Processing parameters analyzed during the optimization of the aminolysis treatment.

Concentration (g/ml)	Time (min)	Temperature (°C)
0.06		
0.08	4, 8, 12, 16, 20	37
0.1		

### 5.2.2.3 Preparation of multilayer coating

Layer-by-Layer process allows the deposition of multilayered coatings on the surface of samples, made of alternately charged polyelectrolytes that electrostatically interact each other stabilizing the coating.

LbL build up was achieved using the pipette approach, wherein 1 ml of each polyelectrolyte was deposited directly onto aminolysed films, beginning with the polyanion (CHS). Polyelectrolyte solutions were prepared at a concentration of 0.2% (wt/v) in 0.2M NaCl buffer (CH was previously dissolved in 1% (v/v) of acetic acid at a concentration of 2% (wt/v)) at pH 4.5. After the polymer was allowed to adsorb for 15 min, substrates were rinsed with 0.2M NaCl buffer (pH 4.5) for 5 min. Then the polycation (CH) was added, allowed to adsorb for 15 min and rinsed for 5 min. These deposition steps were repeated 10 times. Finally, coated

substrates were rinsed with 0.2M NaCl buffer (pH 4.5) for 15 min and dried under vented hood for 48 h.

A total number of 20 layers was deposited on PLCL/PLGA 25/75 (wt/wt) blend film surface through this technique. Pristine and aminolysed films were coded, respectively, as Blend and Blend-NH<sub>2</sub>, while the coated films were coded as Blend-*n*L, where *n* represented the number of deposited layers.

The coating characterization was performed as a function of the deposited layer number.

### 5.2.3 Sample characterization

#### 5.2.3.1 Water contact angle measurement

The static water contact angles of film surfaces were determined through a sessile drop method, using a 6 µl double distilled water droplet. Static contact angles of films were measured in air at room temperature in a VCA Optima (AST, Massachusetts, USA) instrument equipped with a VCA Optima XE software for data acquisition.

#### 5.2.3.2 Infrared analysis in ATR modality

The analysis was carried out in a Perkin Elmer Frontier Optical Spectrometer fitted with an attenuated total reflection sampler (FTIR-ATR, Massachusetts, USA). Spectra were obtained over the 400-4000 cm<sup>-1</sup> range at room temperature, using diamond crystal.

#### 5.2.3.3 Colorimetric method to quantify amino groups

The determination of the density of amino groups on modified (Blend-NH<sub>2</sub> and LbL coated Blend) and control Blend film surfaces was performed by Kaiser Test (Sigma-Aldrich, Milano, Italy), that is based on Ninhydrin reaction with NH<sub>2</sub> terminal groups, that leads to the formation of a purple compound (Fig. 5.4).

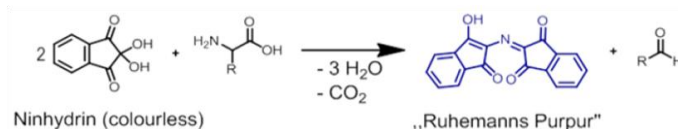


**Fig. 5.4** Reaction of Ninhydrin with amino groups, resulting in a purple compound.

In detail, the Kaiser reagents were added to squared samples (0.5 cm<sup>2</sup>) in the following order and amounts: 75 µl of Phenol, 100 µl of KCN, 75 µl of Ninhydrin. The mixtures were heated at 100 °C for 5 min and then diluted with ethanol/water 60/40 (v/v). The obtained solutions were

filtered by using GHP membrane filters (pores diameter 0.45  $\mu\text{m}$ ) in order to avoid light scattering phenomena, due to the presence of polymer particles inside the solution, that can cause a significant shift of the baseline during the UV test. The optical absorbance of the Kaiser product was recorded at a wavelength interval between 450 and 740 nm, with a spectrophotometer (Perkin Elmer Lambda25 UV/VIS Spectrometer). It is known that the amount of free amino groups in the test sample, after heating with ninhydrin, is proportional to the maximum optical absorbance ( $A$ ) of the solution at 570 nm [29].

The measurements were taken over three replicate samples and then averaged. Starting from the averaged absorbance value ( $A$ ), the molar extinction coefficient  $\epsilon$  ( $15000 \text{ M}^{-1} \text{ cm}^{-1}$ ) and the path length  $b$  (1 cm), the molar concentration of the diluted solution ( $C$ ) was obtained through Lambert-Beer law:

$$A = \epsilon \cdot b \cdot C$$

From this molar concentration and the final volume (after dilution), the number of  $\text{NH}_2$  moles on surface samples was calculated.

#### 5.2.3.4 Morphological analysis

The surface morphologies were visualized using scanning electron microscopy (FEI Inspect F-50 FE-SEM, Oregon, USA). Each sample was coated with an ultrathin platinum (Pt) as a conductive layer for better quality image.

#### 5.2.3.5 Quartz crystal microbalance analyses

LbL film build up for  $(\text{CHS}/\text{CH})_{10}$  films was monitored *in situ* by dissipative quartz crystal microbalance (QCM-D), using a Q-Sense E4 unit (Q-sense, Sweden). Changes in frequency ( $\Delta f$ ) and energy dissipation ( $\Delta D$ ) were measured at the fundamental frequency of the crystal ( $f = 5 \text{ MHz}$ ) as well as at the third, fifth, and seventh overtones (15, 25, and 35 MHz, respectively). The gold coated crystals used in the experiments were used as received, just rinsed several times with demineralised water and ethanol and then dried prior to the experiments. Analysis started with the system primed with a 0.2M NaCl solution (buffer baseline). Then, polyelectrolyte (PE) films were formed by injecting 400  $\mu\text{L}$  of the PE solution (CHS or CH) into the measuring cell, allowing 15 min for adsorption, followed by rinsing with 2000  $\mu\text{L}$  of 0.2M NaCl solution. This procedure continued until 10 bilayers were deposited. The film thickness was calculated from the frequency and energy dissipation data using QTools software and the Voigt-based viscoelastic model proposed by Voinova et al. [30, 31]. For these

calculations, the polyion film density was assumed to be  $1200 \text{ kg/m}^3$  and the 0.2M NaCl buffer fluid density and viscosity were assumed to be  $1000 \text{ kg/m}^3$  and  $1 \text{ mPa}\cdot\text{s}$ , respectively [32].

#### 5.2.3.6 Fluorescence microscopy

To further evaluate the build up of LbL nanocoating, CH was conjugated with fluorescein isothiocyanate (FITC-CH) as described by Huang et al. [33]. Samples coated with CHS and FITC-CH were analyzed under a fluorescence microscope (Nikon ECLIPSE TE2000-U). Photomicrographs were taken using a 100 W mercury arc light source with a standard fluorescein (490 nm excitation/520 nm emission) filter set. Blend, Blend-NH<sub>2</sub> and Blend-*n*L (where *n* = 1, 2, 6, 10, 16, 20 layers) films were analysed. To quantify and compare the differences in fluorescence signal, the images were evaluated with Matlab 2012a. The green channel was extracted and the intensity was calculated as the mean value of the resultant matrix.

#### 5.2.3.7 Cell proliferation and adhesion

Mouse embryonic fibroblast NIH 3T3 cells were supplied by American Type Culture Collection (ATCC, Virginia, USA) and grown in Dulbecco's modified Eagle's medium (DMEM; ATCC) supplemented with 10% Calf Bovine Serum (CBS; Gibco, Invitrogen) and 1% penicillin/streptomycin (Invitrogen). A cells concentration of  $5 \times 10^4$  was seeded on the films and incubated at 37 °C in a humidified atmosphere of 5% CO<sub>2</sub>. Cell Crown™ inserts (Scaffdex, Tampere, Finland) were used to fix the films at the bottom of the wells prior to cell seeding.

Cell proliferation was assessed using the colorimetric indicator Alamar Blue assay (Life Technologies, Ontario, Canada). Media was removed, samples were rinsed once in PBS, and 300 µL of fresh medium containing a 10% solution of Alamar Blue was added to each well. The culture plates were wrapped in aluminum foil and incubated for 4 h at 37 °C in a humidified atmosphere of 5% CO<sub>2</sub>. Absorbance of the extracted dye, which is proportional to the number of cells attached to the film, was measured spectrophotometrically with a microplate reader (Molecular Devices, SpectraMax i3 multi-mode detection platform, California, USA) at wavelengths of 570 and 600 nm. A calibration curve, generated from a known number of fibroblast NIH 3T3 cells reacting with the Alamar Blue indicator, was used to quantify the number of cells attached on films.

The morphology of the cells cultured on Blend-based films was examined by SEM (FEI Inspect F-50 FE-SEM). Films were washed two times with PBS and fixed in Paraformaldehyde for 30 min at room temperature. The films were then washed three times with PBS and dehydrated in

increasing ethanol concentrations for 10 minutes. The samples were then dried under vacuum, coated with Pt, and examined with SEM.

#### 5.2.3.8 X-ray photoelectron spectroscopy

Chemical composition of the modified and control Blend films were investigated by X-ray photoelectron spectroscopy (XPS) (PHI 5000 Versaprobe instrument) at a detection angle of 45°. The characterizations were performed in survey and high resolution (HR) spectra. A surface area of 0.005 cm<sup>2</sup> was analyzed at 25.6 W without charge compensation.

#### 5.2.3.9 Stability test

For stability studies, only LbL coated Blend films with optimized number of layers were used. Stability test was carried out on 10 x 10 mm<sup>2</sup> film specimens incubated in 3 ml PBS at 37 °C and pH 7.4 for 7 and 14 days. The PBS medium was exchanged once every 2 days.

Morphological evaluation of the exposed surfaces of film samples at each stability test time was performed by FE-SEM according to the procedures described at paragraph 5.2.3.4. Surface chemical composition was evaluated through FTIR-ATR and XPS analysis, according to the previously described method at paragraphs 5.2.3.2 and 5.2.3.8, respectively. Finally, surface wettability properties and the density of amino groups were evaluated through the procedures reported on paragraphs 5.2.3.1 and 5.2.3.3, respectively.

#### 5.2.3.10 Antibacterial assay

Antibacterial activities of Blend-16L samples were preliminarily investigated against *Escherichia coli* (*E. coli*) ATCC 25922, a Gram-negative clinical isolate, and *Staphylococcus aureus* (*S. aureus*) ATCC 6538, a Gram-positive strain isolated from human lesion. Both strains were supplied from Belgian Coordinated Collections of Microorganisms (BCCM) and play an important role in human infections and biofilm formation on medical devices [34].

*E. coli* and *S. aureus* strains were grown overnight in Luria–Bertani (LB) agar at 37 °C. Then, bacterial suspensions at the concentration of 1.5 × 10<sup>8</sup> Colony Forming Units per milliliter (CFU/mL) were prepared and dispersed uniformly onto the surface of Müller-Hinton agar plates. Disk-shaped samples of Blend-16L (about 1.2 cm diameter) were UV sterilized for 15 min and subsequently laid on the top of the inoculated plates. After 24 h of incubation at 37 °C, the diameter of inhibition against the two bacterial strains was measured and compared with that of Blend control samples.

## 5.2.4 Statistical analysis

All data are expressed as means  $\pm$  standard deviation. Differences between means were analyzed by one-way ANOVA followed by a Tukey's post hoc test. For *in vitro* cell test, statistical analysis was performed using two-way ANOVA with the Bonferroni's post test. All statistical analysis were performed with Prism, Graph Pad Software.

## 5.3 Results and discussion

### 5.3.1 Characterization of aminolysis treatment

Aminolysis represented the first coating step, activating sample surface for subsequent covering by LbL method. Blend films were incubated in 1,6-hexamethylenediamine/1-propanol solutions in order to form surface  $\text{NH}_2$  amino moieties that, after protonation into  $\text{NH}_3^+$  positively charged groups, allowed the deposition of the first polyanion layer by LbL technique.

The process parameters to be accurately selected in order to optimize the aminolysis procedure were the concentration (C) of aminolysing solution and the time (t) of the treatment, while the temperature of the solution was maintained constant at 37 °C. Different experimental conditions were tested to find the optimal values of aminolysis parameters. Samples aminolysed at each experimental condition were analyzed through contact angle measurement, SEM and FTIR-ATR analyses, and amount of free amino groups introduced on the surface.

The aminolysis treatment has been reported to cause an increase of surface hydrophilicity and, consequently, a decrease of water contact angle values. Moreover, this phenomenon appeared more pronounced with increasing the treatment time and the concentration of aminolysing solution [9]. Fig. 5.5 shows the influence of the different process parameters on Blend- $\text{NH}_2$  surface wettability.

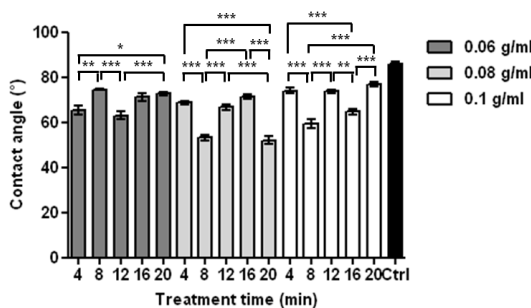


**Fig. 5.5** Average contact angle values measured on untreated Blend samples (Ctrl) and on Blend- $\text{NH}_2$  films aminolysed at 37 °C. using different process conditions.

A statistically significant increase of surface wettability was observed after the aminolysis process, compared to unmodified Blend film (\*\*\*)  $P < 0.01$ ), confirming the successful introduction of amino groups. At the same aminolysis reagent concentration, the water contact angle value did not decrease proportionally with increasing the treatment time. In fact, aminolysis may cause polymer degradation with the formation of cracks and surface roughness, affecting the water contact angle values. At each concentration, the effect of treatment time on surface morphology was thus analysed. The SEM images reported in Fig. 5.6 show the influence of aminolysis time on polymer surface morphology.

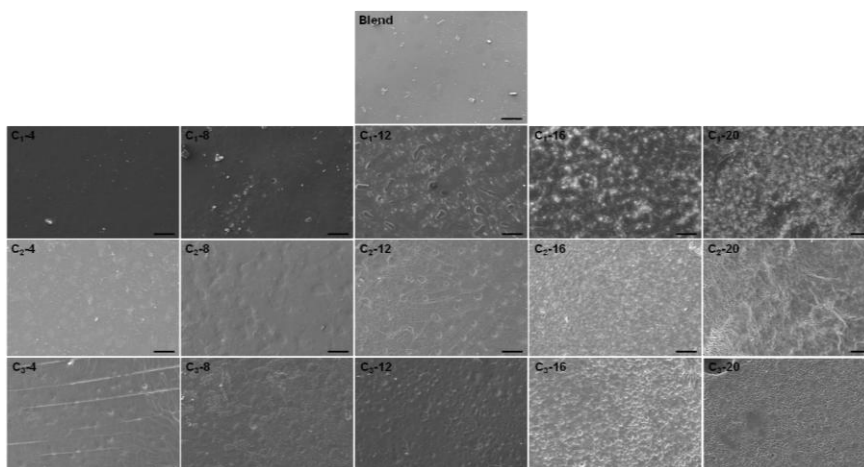


**Fig. 5.6** SEM images of untreated Blend and aminolysed Blend-NH<sub>2</sub> films at 37 °C as a function of solution concentration (where C<sub>1</sub> = 0.06 g/ml, C<sub>2</sub> = 0.08 g/ml, C<sub>3</sub> = 0.1 g/ml) and treatment time (namely 4, 8, 12, 16, 20 min). Scale bar = 100 μm.

Blend films showed pronounced superficial degradation at longer incubation time: after 16 and 20 min of treatment, formation of surface cracks and pores could be observed, independently from solution concentration. These results could explain the lack of a trend in the water contact angle values as a function of treatment time.

By comparing both the surface morphology and the static contact angle, it was possible to select these optimal treatment parameters:

- C = 0.06 g/ml → t = 12 min
- C = 0.08 g/ml → t = 8 min
- C = 0.1 g/ml → t = 8 min.

SEM analysis showed that surface morphology was not significantly different among the 3 selected samples, as compared to control untreated Blend samples. With increasing reagent concentration, the optimal aminolysis time decreased (at fixed temperature). These results showed that it is necessary to adjust aminolysis solution concentration and treatment time to

obtain a significant increase of surface wettability via aminolysis treatment and avoid polymer degradation. In details, using a solution with a lower concentration, a longer exposition time is requested; on the contrary, if the solution concentration is higher, a shorter treatment time is necessary.

Further characterizations have been performed on samples aminolysed with the parameters reported above. A colorimetric assay, based on Ninhydrin reaction with  $\text{NH}_2$  terminal groups, was applied to quantify the amino groups density on aminolysed Blend- $\text{NH}_2$  samples. Fig. 5.7 shows the results obtained from the analysis.

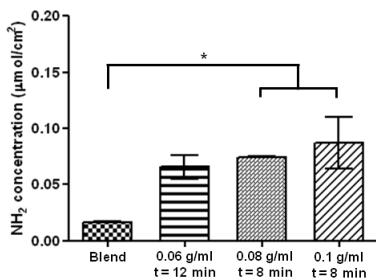


**Fig. 5.7** Amino groups density on not treated Blend samples and aminolysed films using the optimal treatment parameters.

Blend samples physically adsorbed Ninhydrin molecules. After the three aminolysis treatments, the quantity of adsorbed molecules significantly increased as a consequence of the introduction of surface amino groups on Blend film surface. However, no differences could be observed between the three processes, leading to amino groups densities of around  $0.07 \mu\text{mol}/\text{cm}^2$ .

Finally, aminolysed Blend films were characterized by FTIR-ATR analysis to verify the effectiveness of the treatment through the chemical analysis of the surface. Fig. 5.8 compares FTIR-ATR spectra of untreated and aminolysed films.

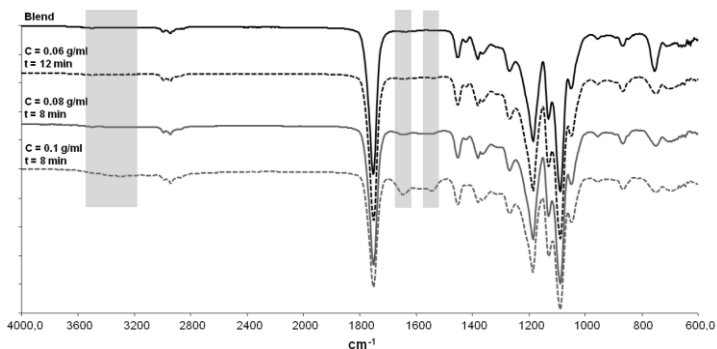


**Fig. 5.8** FTIR-ATR spectra of the surface of untreated Blend film and samples aminolysed with the optimal treatment parameters.

Characteristic peaks of polyesters could be observed in all the analyzed samples, namely, the strong absorption band at about  $1750\text{ cm}^{-1}$  attributed to the stretching vibration of C=O bond and the absorption bands in the  $1000\text{-}1184\text{ cm}^{-1}$  interval region related to the ester bond (C–O–C ether group stretching) [35]. FTIR-ATR spectra of aminolysed films evidenced three additional peaks, suggesting the success of the aminolysis process: the broad peak between  $3600\text{ cm}^{-1}$  and  $3200\text{ cm}^{-1}$  attributed to the stretching vibrations of the N-H/O-H; the wide band in the  $1650\text{-}1600\text{ cm}^{-1}$  region associated to amide I stretching vibration; the peak at around  $1550\text{ cm}^{-1}$  arised from amide II bending vibration [36]. The intensity of these new peaks increased with increasing the aminolysis solution concentration.

Based on the performed characterizations, no significant differences in the surface functionalization with  $\text{NH}_2$  was observed for the three samples. Therefore, the following aminolysis parameters were selected:

$$C = 0.08\text{ g/ml}$$

$$t = 8\text{ min.}$$

as they caused a more significant reduction of static contact angle value (as a consequence of the formation of surface hydrophilic amino groups), without affecting surface morphology of Blend- $\text{NH}_2$  samples.

### 5.3.2 Characterization of multilayer coating

#### 5.3.2.1 CHS/CH film build up

Frequency shifts ( $\Delta F/\nu$ ) and changes in energy dissipation ( $\Delta D$ ) overtime for the build up of  $(\text{CHS-CH})_{10}$  multilayers film, as monitored via QCM-D, are presented in Fig. 5.9.

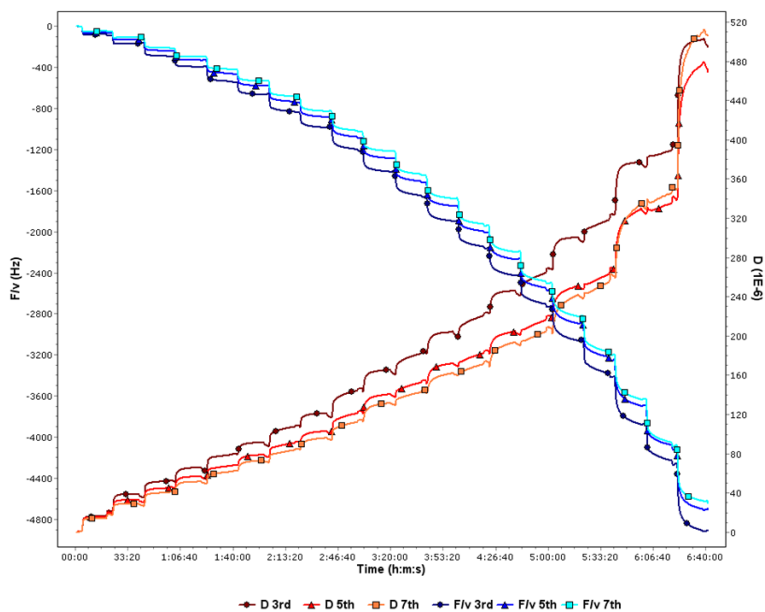


**Fig. 5.9** Plots of change in dissipation ( $\Delta D$ , right axis) and QCM frequency shifts ( $\Delta F/v$ , left axis) over time during the deposition of a (CHS/CH)<sub>10</sub> film. Frequency was monitored at the third (●), fifth (▲), and seventh (■) overtones of the fundamental frequency, corresponding to 15, 25, and 35 MHz, respectively.

Qualitatively identical evolutions could be observed with increasing number of absorption steps for the distinct harmonics. As each polyelectrolyte (PE) was injected into the system, a decrease in frequency was observed corresponding to an increase in film mass, thus indicating LbL deposition. The frequency decay for each CHS/CH deposition step was more pronounced for lower frequencies. Regarding  $\Delta D$ , an increase was detected after each CHS and CH injection due to the non-rigid adsorbed layer structure of the film that was forming onto the crystal surface. When rinsing with NaCl after CHS and CH adsorption, a small upturns in the frequency curve and downturns in the dissipation curve could be identified, suggesting small amounts of polymer desorption.

The normalized frequency shift ( $-\Delta F/v$ ) for each bilayer number (Fig. 5.10 a) showed a non-linear growth regime [37], with higher bilayer numbers (above 5<sup>th</sup>) exhibiting an increased growth rate. Equally, larger dissipation changes were observed at higher bilayer numbers, indicating that CHS/CH films became more viscoelastic as they grew.

The viscoelastic nature of (CHS/CH)<sub>10</sub> films, as indicated by the large dissipation changes, and the differences in the frequency curve decrease for the three overtones revealed that the adsorbed layer did not obey the Sauerbrey equation [38], which directly relates frequency shift data to mass absorbed for rigid films. Indeed, the Voigt-based viscoelastic model [24, 39] was

applied to the frequency and dissipation data measured at the third, fifth, and seventh overtones. Thus, it was possible to estimate the thickness during the building of the film (Fig. 5.10 b).

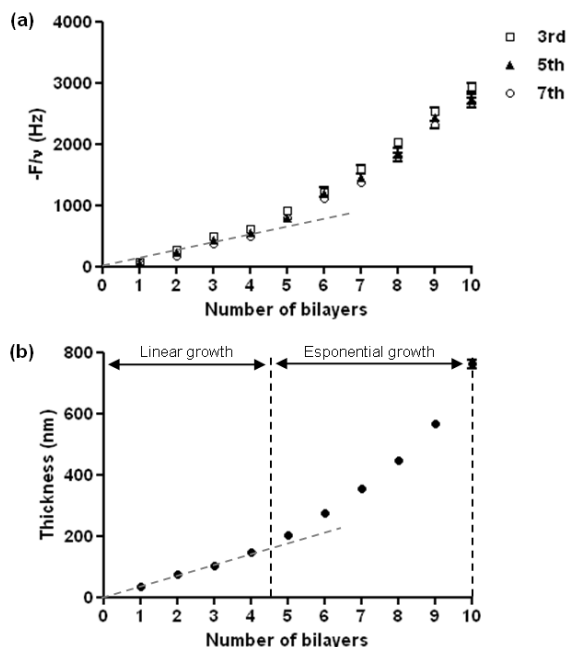


**Fig. 5.10** (a) Normalized frequency shift ( $-\Delta F/v$ ) data for each bilayer number. Frequency was monitored at the third overtone of the fundamental frequency ( $\square$ ), its fifth ( $\blacktriangle$ ) and seventh ( $\circ$ ) overtone. (b) Increase in PE multilayer thickness over time, during the successive polymer layer deposition, calculated with the Voigt model.

It was found that the film thickness increased linearly for the first 5 bi-layers, at a rate of ca. 40 nm per layer. After the deposition of the 5<sup>th</sup> bi-layer, the growth regime changed and an exponential trend was observed, yielding (CHS/CH)<sub>10</sub> multilayers at  $760.7 \pm 21.5$  nm thick (data is the average of three representative experiments).

### 5.3.2.2 Contact angle measurement

Multilayer construction offers many possibilities to change the wettability of substrates since there are a variety of components that can be chosen as polyanion or polycation. The gradual build up of multilayers was expected to modify the wettability of LBL-modified Blend-NH<sub>2</sub> films. This was confirmed by measuring the contact angles with distilled water (Fig. 5.11).

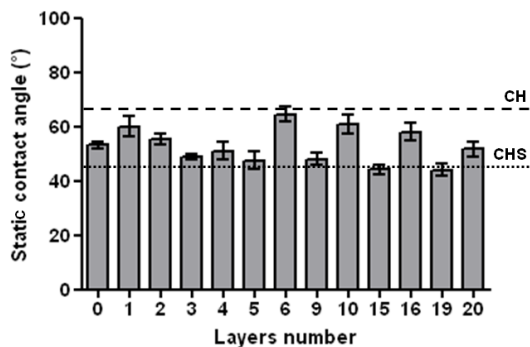


**Fig. 5.11** Water contact angle as a function of the number of coating layers. The even layer numbers correspond to chitosan (CH) as the outermost layer; the odd layer numbers correspond to chondroitin sulfate (CHS) as the outermost layer. The number 0 corresponds to Blend-NH<sub>2</sub> film.

The contact angle initially did not change significantly with increasing layer numbers for the first 4 layers. This phenomenon could be interpreted considering that the substrate surface was not fully covered by the outermost layer component during the initial 4 layer coating steps. Thus, the surface of the first layers is composed of CHS/CH and some uncoated Blend-NH<sub>2</sub> film. These results were consistent with those found in other studies [40]. From the five-layers coating, the contact angle began to jump alternatively between 45° and 65° relying on the outmost layer component. The typical alternate trend of static contact angle suggested the correct deposition of the LbL coatings and at least five layers were necessary to deposit uniform interfaces. This alternate change in contact angle was also reported in other work in the literature [33, 41]; therefore, the wettability of coated Blend-NH<sub>2</sub> films was controlled by the outmost coating component. However, after the deposition of the 16<sup>th</sup> layer, CH outmost layers decreased their contact angle. Liu et al. [42] explained this phenomenon as a layer interpenetration between neighboring CH and CHS layers, where the segments of the underlying layer are able to influence the surface hydrophilicity.

### 5.3.2.3 Fluorescence microscopy

The analysis has been conducted on coated films to further evaluate the build up of LbL nanocoating. FITC-CH was substituted to the normal one during the deposition steps and its distribution on sample surfaces was monitored. Pristine Blend sample was selected as control. Fig. 5.12 shows the images of films intrinsic fluorescence and changes in fluorescence signal with the increase in layer numbers.

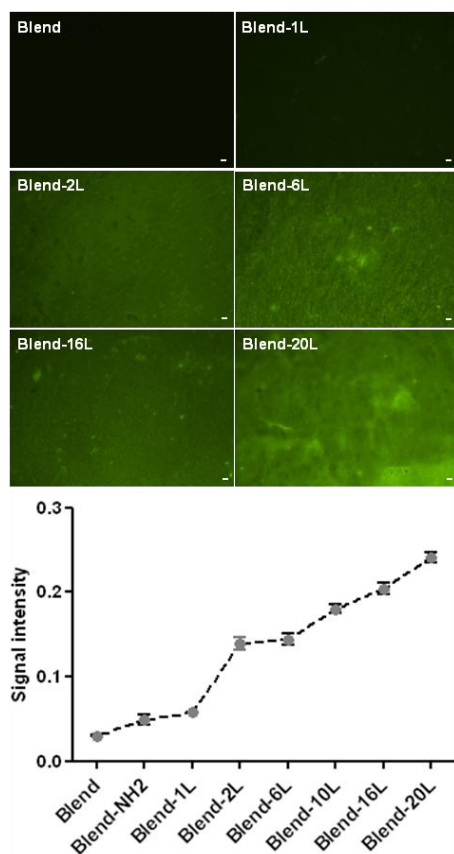


**Fig. 5.12** Images of fluorescence microscopy and changes in fluorescence signal intensity for Blend, Blend-NH<sub>2</sub> and Blend-XL films (where X = 1, 2, 6, 16, and 20 alternate CHS/FITC-CH layers).

Blend and Blend-1L substrates were dark when observed under a fluorescence microscope. After the deposition of the first FITC-CH layer (Blend-2L), a fluorescence phenomenon could be observed, corresponding to a statistically significant increase of fluorescence signal intensity compared to previous values (\*\*\*) P < 0.01). No changes in signal intensity values were detected between Blend-2L and Blend-6L. After the deposition of the 6<sup>th</sup> FITC-CH layer, the fluorescent intensity was found to linearly increase with increasing the FITC-CH layer numbers, demonstrating that the multilayer was built up in a LbL manner. Statistical analysis found significant difference between uncoated and LbL coated samples and between films coated with different number of layers (\*\*\*) P < 0.01). In addition, fluorescence of CHS/FITC-CH-coated substrates was uniformly distributed over the entire film surface with only some bright dots. This suggested a continuous coating of sample surface at the micrometer scale, while the bright areas could be attributed to a higher local concentration of FITC-CH.

### 5.3.2.4 Morphological analysis

SEM images were used to verify if the acid pH (4.5) employed for the deposition of the layers could cause any change of the sample surface, such as increased roughness and formation of cracks. Fig. 5.13 shows the surface morphology of Blend, Blend-NH<sub>2</sub>, and Blend-*n*L films (where *n* = 5, 6, 9, 10, 15, 16, 19, and 20 layers).

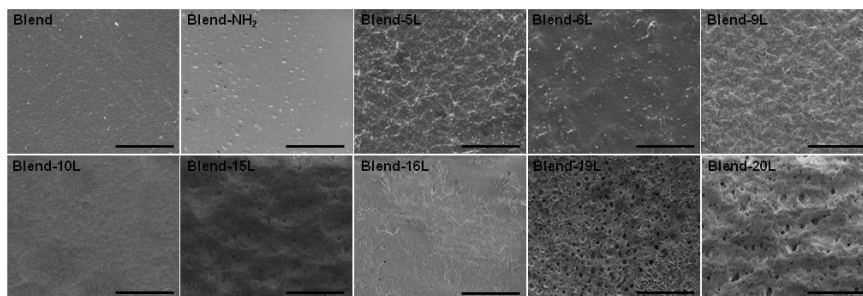


**Fig. 5.13** SEM images of Blend, Blend-NH<sub>2</sub>, and Blend-NH<sub>2</sub> samples coated with 5, 6, 9, 10, 15, 16, 19 and 20 alternate CHS/CH layers. Scale bar = 50 μm.

Blend was characterized by a relatively smooth surface. After aminolysis and deposition of LbL nanocoating, surface roughness increased.

Surface integrity was preserved up to the deposition of the 16<sup>th</sup> layer while sample treatment in polyelectrolyte and washing solutions at pH 4.5 caused surface degradation phenomena and the formation of pores. Shown by water contact angle analysis, the same outmost layer did not present the same contact angle when increase the layer number. This result could be due both to layer interpenetration and to the presence of pores on sample surface.

Based on morphological results, the maximum number of layers deposited on Blend-NH<sub>2</sub> films was 16, to avoid sample surface morphological alteration.

### 5.3.2.5 FTIR-ATR analysis

Chemical composition of Blend films coated with alternate layers of CHS and CH through LbL technique, was investigated by FTIR-ATR analysis. Fig. 5.14 compares FTIR-ATR spectra of untreated, aminolyzed and *n*-layers coated Blend films, where *n* = 5, 6, 9, 10, 15, 16.

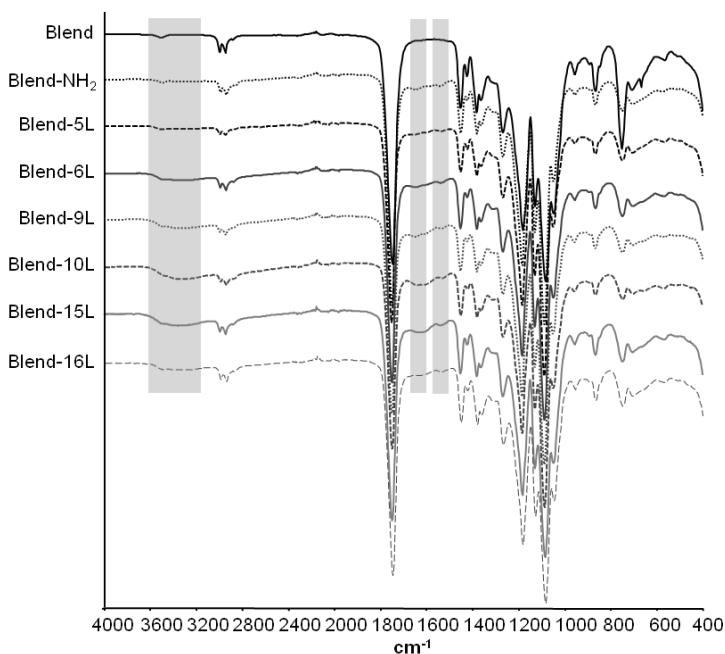


**Fig. 5.14** FTIR-ATR spectra of Blend, Blend-NH<sub>2</sub> and Blend-nL films (where n = 5, 6, 9, 10, 15, 16 layers).

Characteristic peaks of polyesters, already described in paragraph 5.3.1, could be observed in all the analyzed samples. FTIR-ATR spectra of LbL coated and Blend-NH<sub>2</sub> films evidenced three additional bands, attributed to aminolysis modification and the presence of CHS and CH: the broad peak between 3600 cm<sup>-1</sup> and 3200 cm<sup>-1</sup> attributed to the stretching vibrations of the N-H/O-H; the wide band in the 1650-1600 cm<sup>-1</sup> region associated to amide I stretching vibration; the peak at around 1550 cm<sup>-1</sup> arised from amide II bending vibration. The intensity of these new peaks increased with increasing the number of deposited layer. However, the typical absorption band of CHS sulfonate groups (S=O stretching at around 1230 cm<sup>-1</sup>) was not detected in FTIR-ATR spectra of LbL coated Blend samples, as it was masked by the intense C=O bending and C-O-C stretching bands of polymers, in the 1300-1000 cm<sup>-1</sup> wavenumber region [43, 44]. FTIR-ATR results suggested that multilayer deposition of CHS and CH polyelectrolytes on aminolyzed samples was successful.

### 5.3.2.6 Cell proliferation and adhesion

Fibroblast proliferation at 1 and 3 days was evaluated with Alamar Blue assay and results are shown in Fig. 5.15. Cells grown on Petri dishes were used as control.

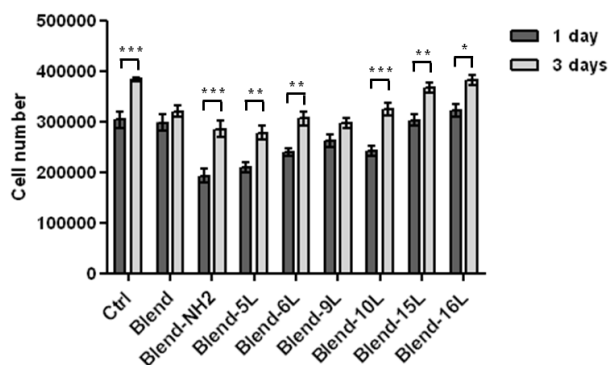


**Fig. 5.15** Cell proliferation on Blend, Blend-NH<sub>2</sub>, and Blend-*n*L films (where *n* = 5, 6, 9, 10, 15, 16 layers) as a function of time. Cells grown on petri dish were used as control (Ctrl).

The number of cells increased on all samples after 1 culture day compared to the initial seeded amount. Moreover, all samples displayed an increase in cell number from 1 to 3 days of culture and no marked differences could be observed on anionic- and cationic-terminating layers.

In detail, a significantly lower cell number was observed on aminolysed Blend films at day 1 compared to unmodified Blend samples, while no marked differences in the number of cells adhered to Blend and Blend-NH<sub>2</sub> films could be detected after 3 days in culture. A similar cell response was found also by Zhu et al. [45] with aminolysed PCL films. Compared to Blend-NH<sub>2</sub>, the deposition of 5 layers did not affect cell response at day 1, which could be due to incomplete coverage of the substrate as already suggested by water contact angle analysis. On the contrary, a slight increase in cell number after 1 day could be observed for a higher layer number than 6, reaching values comparable to Blend and Ctrl for Blend-15L and Blend-16L films. After 3 days of culture, the number of cells proliferated on coated samples with 5-10L was comparable to that on unmodified Blend substrates and lower than for the Ctrl. The number of cells was higher after the deposition of 15 and 16 layers, showing comparable results to Ctrl. The morphology of the fibroblasts seeded on Blend-based substrates after 3 days of culture was compared (Fig. 5.16).

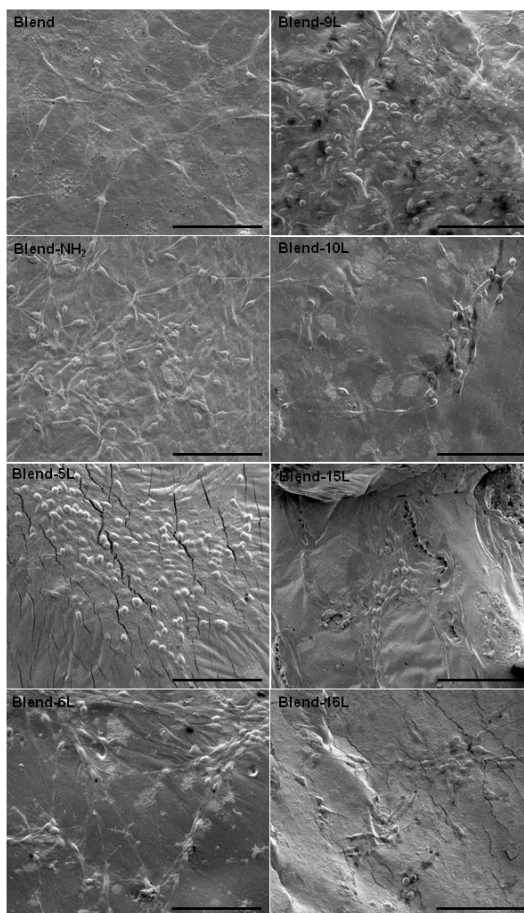


**Fig. 5.16** SEM morphology of fibroblast cells grown on Blend, Blend-NH<sub>2</sub> and Blend-*n*L films (*n* = 5, 6, 9, 10, 15, 16) after seeding cells for 3 days. Scale bar = 100 μm.

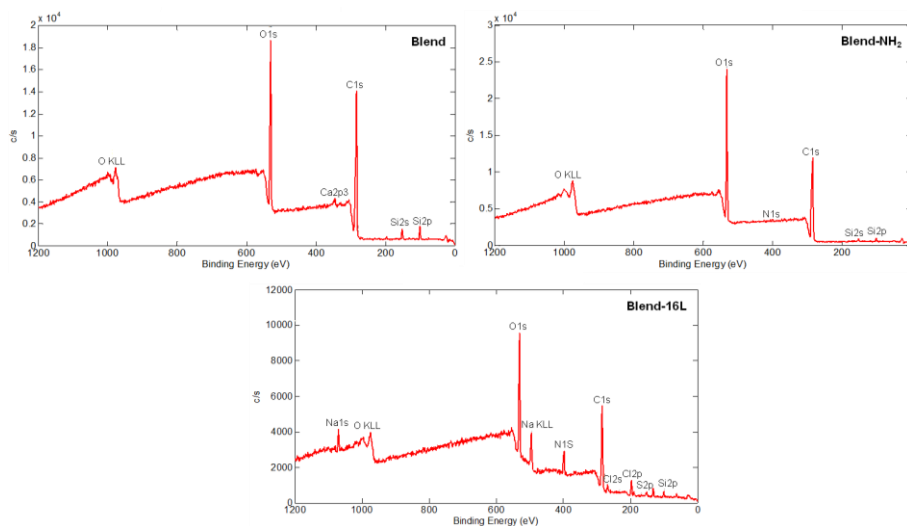
Cells randomly adhered on both control Blend and modified Blend films, without preferred directions. However, fibroblasts attached on Blend and Blend-NH<sub>2</sub> films, and on samples with cationic-terminating layers were more stretched and showed the typical star-like morphology of spreading fibroblast. Cells developed numerous cellular processes (lamellipodia and filopodia) to facilitate cell-substrate and cell-cell interactions. On the contrary, cell morphology on substrates coated with 5, 9 and 15 layers showed that NIH 3T3 cells did not spread but remained rounded.

Considering cell proliferation as the basis of forming tissue, the results suggested that CHS/CH coating was helpful for improving cell growth and in turn tissue formation. In particular, the CH-terminating polyelectrolyte layer markedly improved fibroblast adhesion. Generally, the factors that affect the cell adhesion are considered to be the hydrophobic/hydrophilic property, electric charge, surface morphology, and the surface functional groups of a biomaterial. Cell

adhesion may be mediated by interactions of the positively charged materials with cell membranes or by cellular uptake and subsequent activation of intracellular signal transduction pathways [46]. Thus, the improved cell adhesion for samples coated with CH-terminating layers was due to the electrostatic interactions with the negatively charged surface of the cell membrane. On the contrary, the negative charge on the CHS-terminating layer slightly inhibited the formation of initial cell contact due to the electrostatic repulsion interactions. Due to the results obtained from the proliferation and the adhesion tests, 16 layers were selected as optimal number of layers for our application.

### 5.3.2.7 XPS analysis and CH quantification

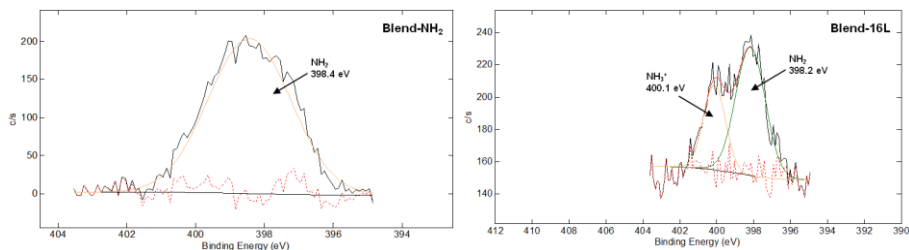
Once Blend samples were aminolysed under the selected optimal process parameters ( $C = 0.08$  g/ml;  $t = 8$  min;  $T = 37$  °C) and subsequently coated via LbL technique with the optimized number of layers (namely, 16 layers), they were characterized by XPS analysis to verify the effectiveness of the aminolysis treatment and the presence of the two deposited polyelectrolytes (CHS and CH) in the LbL coating. Fig. 5.17 compares XPS spectra of untreated, aminolysed and LbL functionalized Blend films.



**Fig. 5.17** XPS spectra of Blend, Blend-NH<sub>2</sub>, and Blend-16L films.

In the reported spectra, peaks due to surface activation and functionalization were present. The characteristic compositional peaks of Blend-based films were detected at around 530 eV, associated with the presence of oxygen (O1s), and at around 285 eV, due to the presence of carbon (C1s). The presence of primary amino groups (-NH<sub>2</sub>) on the surface of aminolysed

sample was confirmed by the appearance of N1s peak at around 400 eV. The deposition of 16 alternate layers of CHS and CH caused the appearance of the S2p peak, confirming the successful deposition of CHS layers, and a marked increase of N1s peak intensity compared to aminolysed sample, suggesting the successful deposition of CH layers. Moreover, peaks associated to the buffer employed for the preparation of polyelectrolyte solutions could be observed on Blend-16L spectra, namely Na1s at about 1100 eV and Cl2p around 200 eV. In addition, a double N1s peak was observed after the deposition of 16 layers as compared to Blend-NH<sub>2</sub> film (Fig. 5.18) indicating the presence of both un-protonated amino groups (-NH<sub>2</sub>) and protonated amino groups (NH<sub>3</sub><sup>+</sup>), at about 398 and 400 eV respectively.



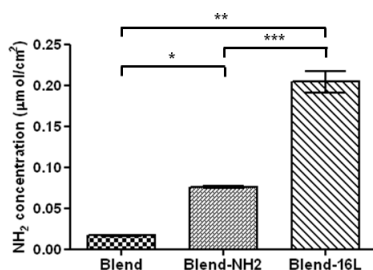
**Fig. 5.18** High resolution XPS spectra of N1s for Blend-NH<sub>2</sub> and Blend-16L films.

Table 5.1 shows the chemical composition of Blend, Blend-NH<sub>2</sub> and Blend-16L films. Aminolysis was effective, in fact the percentage of N on Blend film surface increased from 0 mol% to 0.7 mol% after the treatment. LbL method was effective and the amount of CHS and CH increased. In fact, the percentage of S, which was zero after aminolysis, became 0.1 mol% while the percentage of N increased from 0.7 mol% to 7.7 mol%.

**Table 5.1** XPS chemical composition of untreated, aminolysed and 16-layers coated Blend films.

Sample	Atomic percentage (mol%)					
	C1s	O1s	N1s	S2p	Na1s	Cl2p
Blend	65.9	29.7	-	-	-	-
Blend-NH <sub>2</sub>	63.0	35.4	0.7	-	-	-
Blend-16L	55.8	29.7	7.7	0.1	2.9	2.0

A colorimetric assay (Kaiser test) was applied to quantify NH<sub>2</sub> density on Blend-16L films. The density on untreated, aminolysed and coated samples is shown in Fig. 5.19. The deposition of CH layers caused a marked increase of amino groups concentration that was less than 0.08 μmol/cm<sup>2</sup> for Blend-NH<sub>2</sub> films whereas it was around 0.2 μmol/cm<sup>2</sup> after the LbL deposition. These results further demonstrated the successful deposition of the multilayer nanocoating.



**Fig. 5.19** Amino groups concentration on untreated and aminolysed Blend samples, and coated Blend films with 16 layers.

### 5.3.2.8 Antibacterial efficiency

CH, a naturally occurring, biocompatible, cationic antibacterial polysaccharide has been shown to disrupt bacterial cell membrane integrity [23, 47]. Although many mechanisms of action have been proposed, CH and its derivatives have been shown to bind to the negatively charged bacterial cell membrane and cause leakage, both when used in solution and when immobilized on surfaces [48]. When suitably assembled in a PEM, CH cationic charges are able to interact with bacteria that attempt to adhere to the surface [49].

In this work, both Gram-positive (*S. aureus*) and Gram-negative (*E. coli*) bacteria were used to evaluate the antibacterial efficacy on Blend-16L films by visualizing the zone of inhibition. Fig. 5.20 shows the results of the test, which was conducted on untreated and coated samples.

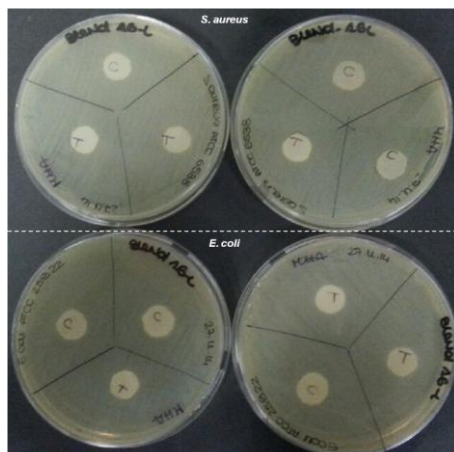


**Fig. 5.20** Antibacterial efficacy on Blend (C) and Blend-16L (T) against *S. aureus* and *E. coli* evaluated by zone of inhibition assay.

No antibacterial activity was observed on all the analysed samples. Two hypothesis could explain the results. First, the amount of CH introduced on Blend surface through the LbL technique was not enough to observe an antibacterial effect. In fact, as reported in literature,

antimicrobial activity of CH was influenced by several factors, including a dose-dependent growth-inhibitory effect [50]. Secondly, the test performed was not enough sensitive for this material. Thus, more extensive tests will be performed (i.e. antimicrobial activity assay in liquid through viable cell counting method) and improvements to the antibacterial activity of the nanocoating will be carried out (i.e. introduction of silver nanoparticles or antimicrobial drugs onto the LbL coating).

### 5.3.2.9 Dissolution feature of coating

The dissolution process of the optimised LbL nanocoating was studied by physicochemical and morphological analyses. Table 5.2 collects data from water contact angle measurements, NH<sub>2</sub> quantification and XPS analysis for Blend-16L films, before and after 7 and 14 days of incubation in PBS at 37 °C.

**Table 5.2** Contact angle values, amount of amino groups and XPS chemical composition of Blend-16L films before and after incubation in PBS at 37 °C for 7 and 14 days.

Sample	Time (days)	Contact angle (°)	NH <sub>2</sub> concentration (μmol/cm <sup>2</sup> )	Atomic percentage (mol%)					
				C1s	O1s	N1s	S2p	Na1s	Cl2p
Blend-16L	0	57.9 ± 6.4	0.20 ± 0.02	55.8	29.7	7.7	0.1	2.9	2.0
	7	52.9 ± 2.7	0.24 ± 0.02	60.5	34.6	4.3	0.1	-	-
	14	62.8 ± 2.7	0.22 ± 0.01	62.7	36.4	< 0.1	0.1	-	-

A marked decrease in the content of nitrogen could be observed: after 14 days of incubation, nitrogen was no more detectable (< 0.1 mol%). On the contrary, the atomic percentage of S2p remained constant.

The incubation of samples in PBS for 7 days did not change the surface wettability properties of Blend-16L. Increasing the immersion time at 14 days, slight variation of surface hydrophilicity could be observed, leading to a contact angle value of about 63° (\* P < 0.01 comparing with Blend-16L incubated for 7 days). Regarding the quantification of amino groups, no significant changes could be observed after the incubation in PBS.

The coating dissolution test demonstrated that the optimised CHS/CH multilayer coating was probably released/degraded in 14 days. The release of CH cationic antibacterial polymer was considered of great value to avoid bacterial infection [51]. Then, the coating dissolution was sustained for at least 14 days, which could be the key for inhibition of the bacteria and thereby to aid tissue regeneration.

## 5.4 Conclusions

LbL self-assembly is a simple and versatile method for the modification of biomaterial surfaces. In this work, CHS and CH were employed to surface engineer polyester blend films by LbL with the aim to improve fibroblast NIH 3T3 cell response and, at the same time, to confer antibacterial efficacy.

Blend sample surface was pre-modified to introduce positively charged groups which are necessary for the stable deposition of the first LbL layer. Aminolysis treatment was performed on Blend films, varying concentration of aminolysing solution and reaction time, in order to find out the optimal aminolysis treatment parameters through a physicochemical analysis.

The film surface characterization allowed to select the optimal parameters of the priming treatment:  $C = 0.08 \text{ g/mL}$ ,  $t = 8 \text{ min}$  and  $T = 37 \text{ }^\circ\text{C}$ . These processing conditions allowed a significant reduction of static contact angle without affecting surface morphology of Blend film, as demonstrated by SEM analysis. The formation of amino groups was verified by XPS and FTIR-ATR analysis.

After aminolysis treatment, LbL coating was performed on activated Blend films. The success of the coating and the change in surface properties were confirmed by combined techniques. The successful deposition of the multilayer coating based on CHS and CH and its nanometric thickness was confirmed by QCM-D analysis. Contact angle analysis suggested an even coating after the deposition of five layers: for that samples, the surface wettability was dominated by the outmost coating layer. Fluorescence microscopy and FTIR-ATR analysis verified the growth of CHS and CH layers on Blend-NH<sub>2</sub> films. Finally, SEM images did not show degradation phenomena for films coated with less than 16 layers.

*In vitro* investigations were also performed. Coated Blend films exhibited stronger ability for fibroblast cells attachment especially for samples coated with 15 and 16 layers and with cationic-terminating polyelectrolyte layers. The optimal number of layers for our application was selected to be 16 and further characterization was performed.

XPS analysis confirmed the presence of the polyelectrolytes on the coated sample and the amount of amino groups significantly increased after the deposition of the coating. The polyelectrolytes release was sustained for at least 14 days but no antibacterial activity was observed on all the analysed samples.

In summary, it can be concluded that both the aminolysis treatment and the LbL coating were carried out with success and optimized. The introduction of CHS and CH onto Blend surface

improved Blend biocompatibility properties but further improvements are needed in terms of antibacterial activity.

## References

---

1. Jiao YP, et al. *Biomed Mater* 2007;**2**:R24-R37.
2. Tabata Y. *Drug Discovery Today* 2001;**6**:483-487.
3. Hench LL. *Science* 1980;**208**:826-831.
4. Mathieu HJ. *Surf Interface Anal* 2001;**32**:3-9.
5. Yaszemski MJ, et al. *Biomaterials* 1996;**17**:175-185.
6. Khang G, et al. *Polym Korea* 2000;**24**:869-876.
7. Chen JP, et al. *Acta Biomater* 2011;**7**:234-243.
8. Sartori S, et al. *React Funct Polym* 2008;**68**:809-821.
9. Croll TI, et al. *Biomacromolecules* 2004;**5**:463-473.
10. Russo L, et al. *J Mater Sci Mater Med* 2012;**23**:2727-2738.
11. Zhu YB, et al. *Biomacromolecules* 2002;**3**:1312-1319.
12. Lao HK, et al. *Biomacromolecules* 2007;**8**:416-423.
13. Guo C, et al. *Eur J Pharm Biopharm* 2008;**70**:597-604.
14. Gong Y, et al. *Acta Biomater* 2007;**3**:677-685.
15. Schmidt TGM, et al. *J Mol Biol* 1995;**255**:753-766.
16. Decher G, et al. *Thin Solid Films* 1992;**210-211**:831-835.
17. Tang Z, et al. *Adv Mater* 2006;**18**:3203-3224.
18. Lichter JA, et al. *Macromolecules* 2009;**42**:8573-8586.
19. Gribova V, et al. *Chem Mater* 2012;**24**:854-869.
20. Rammelt S, et al. *Biomaterials* 2006;**27**:5561-5571.
21. Jing YJ, et al. *Acta Biol Hung* 2007;**58**:75-86.
22. Jayakumar R, et al. *Carb Polym* 2010;**82**:227-232.
23. Chua PH, et al. *Biomaterials* 2008;**29**:1412-1421.
24. Madhumathi K, et al. *Int J Biol Macromol* 2009;**44**:1-5.
25. Madhumathi K, et al. *J Mater Sci: Mater Med* 2010;**21**:807-813.
26. Jayakumar R, et al. *Int J Biol Macromol* 2007;**40**:175-181.
27. Gerrit B. *Adv Drug Deliv Rev* 2001;**2**:145-150.
28. Campo GM, et al. *Med Chem* 2006;**6**:1-10.
29. Zhu J, et al. *Intern J Biol Macromol* 2012;**51**:105-112.
30. Voinova MV, et al. *Phys Scr* 1999;**59**:391-396.
31. Voinova MV, et al. *Biosens Bioelectron* 2002;**17**:835-841.
32. Alves NM, et al. *Macromol Biosci* 2009;**9**:776-785.
33. Huang M, et al. *Pharm Res* 2004;**21**:344-353.
34. Lynch AS, et al. *Annu Rev Med* 2008;**59**:415-428.
35. Jose MV, et al. *Polymer* 2009;**50**:3778-3785.
36. Fu J, et al. *Biomaterials* 2005;**26**:6684-6692.

- 
37. Picart C, et al. *Proc Natl Acad Sci U.S.A.* 2002;**99**:12531-12535.
  38. Sauerbrey G, et al. *Z Phys* 1959;**55**:206-222.
  39. Brandrup J, et al. *Polymer Handbook*; Wiley-Interscience: New York, 1975;Part 5.
  40. Cai K, et al. *J Biomed Mater Res* 2007;**82A**:927-935.
  41. Tan Q, et al. *Biomaterials* 2003;**24**:4699-4705.
  42. Liu YM, et al. *Colloids Surf B* 2005;**46**:117-126.
  43. Sionkowska A, et al. *Biomaterials* 2004;**25**:795-801.
  44. Wang D, et al. *Nat Mater* 2007;**6**:385-392.
  45. Zhu Y, et al. *Biomacromolecules* 2002;**3**:1312-1319.
  46. Fischer D, et al. *Biomaterials* 2003;**24**:1121-1131.
  47. Bratskaya S, et al. *Biomacromolecules* 2007;**8**:2960-2968.
  48. Rabea EI, et al. *Biomacromolecules* 2003;**4**:1457-1465.
  49. Richert L, et al. *Langmuir* 2004;**20**:448-458.
  50. Raafat D, et al. *Appl Environ Microbiol* 2008;**74**:3764-3773.
  51. He CL, et al. *J Biomed Mater Res Part A* 2009;**89**:80-95.

## Composite porous membranes for bone tissue regeneration

---

### Abstract

Guided tissue regeneration (GTR) represents a promising approach for periodontal tissues regeneration in periodontal loss, because it isolates the healing tissue from migration of epithelial and gingival connective tissue cells and allows bone tissue cells to repopulate the bony defect. The aim of the work described in the current chapter was the preparation and characterization of three dimensional sponge-like composite membranes for GTR applications fabricated by freeze-drying, with a similar composition to that of natural bone, and based on  $\beta$ -tricalcium phosphate (TCP) dispersed in a chitosan/gelatin (CH/G) network cross-linked with genipin (GP) and disodium phosphate salt (DSP). Three kind of membranes were developed: CH/G, CH/G+GP-DSP and CH/G/TCP+GP-DSP. They were characterized in terms of their cross-linking degree (Kaiser test), morphology (SEM analysis), chemical structure (EDS and FTIR-ATR analyses), thermal stability (TGA analysis), tensile mechanical behavior, stability in water (water absorption and dissolution tests), and biological response by *in vitro* cell tests using MG-63 human osteoblast-like cells. Successful double cross-linking of CH/G network was confirmed by the performed characterizations. All membranes showed a typical foam-like morphology with interconnected pores having an average diameter of 100-200  $\mu\text{m}$ . Cross-linking and the addition of TCP did not change thermal stability of the membrane. On the contrary, both cross-linking and TCP presence caused a marked increase of membrane stability in water solution, as well as of tensile modulus and maximum tensile strength. In addition, compared to uncross-linked samples, CH/G+GP-DSP and CH/G/TCP+GP-DSP membranes showed improved cell response, in terms of cell viability and morphology.

## 6.1 Introduction

Alveolar bone loss is a common finding associated with periodontal degeneration [1]. Various treatment modalities have been used to regenerate or fill bony defects using a wide variety of surgical approaches, such as barrier membranes, a series of bone grafts and other osteoconductive/inductive materials or protein mixtures, and cell-based technologies. However, guided tissue regeneration (GTR) represents the most well-documented regenerative procedure for obtaining periodontal tissues regeneration in periodontal loss [2]. GTR is effective in halting tissue and bone destruction and promoting new tissue and bone formation [3]. A physical barrier (membrane) is placed to cover the area in which the regenerative process takes place. The membrane prevents migration of unwanted epithelial and gingival connective tissue cells into the healing area and allows bone tissue cells to repopulate the bony defect [4].

Although a number of barrier membranes (non-absorbable and bioabsorbable) are already being used in clinical practice, novel membranes have been developed in an effort to overcome the limitations of the currently used devices, namely the weak mechanical and osteoconductive/osteoinductive properties. The researchers are developing different approaches to meet the demands of degradable GTR membranes in terms of mechanical properties and biocompatibility, like the incorporation of bioactive inorganic fillers.

Devices for bone regeneration should mimic bone morphology, structure and function. Bone is composed of an organic phase (17-20 wt%) made of type I and type III collagen (COL) and glycosaminoglycans (GAGs), and an inorganic phase (69-80 wt%) made up of hydroxyapatite (HAp) [5]. For this reason, composites based on apatite crystals and natural polymers have received increasing attention in bone tissue regeneration due to their ability to preserve the structural and biological functions of the damaged hard tissues in a biomimetic way. Moreover, bone regeneration usually employs three-dimensional (3D) porous materials. The membrane 3D porous structure provides the necessary support for the cells to proliferate and maintain their differential function, and its architecture defines the ultimate shape of new bone [6].

Based on a biomimetic approach, in this chapter, three dimensional sponge-like composite membranes based on  $\beta$ -tricalcium phosphate (TCP) and a double cross-linked network of chitosan/gelatin were obtained and investigated for GTR applications, having a similar composition to that of natural bone.

Calcium phosphate ceramics are excellent candidates for bone repair and regeneration because their chemical compositions are similar to the inorganic component of bone. They were found to bond to bone through a layer of bone-like apatite formed on their surface *in vivo*. In

particular, TCP has been shown to be bioactive and biodegradable. The degradation rate of TCP is 10 times higher than that of HAp [7].

Chitosan (CH) is a partially deacetylated product made from chitin and is structurally similar to GAGs [8]. Chitosan is biocompatible, can be degraded by enzymes in the human body and the degradation products are non-toxic. CH device with various geometries, pore sizes, and pore orientation can be obtained by freezing at a controlled-rate and further lyophilization. CH is widely used in biomedical fields due to its many advantages like hemostasis, accelerating tissue regeneration and antibacterial property [9- 11]. However, for improving its mechanical or biological properties, blending with other polymers (i.e. COL or gelatin) has been widely investigated [12].

Gelatin (G) is a partially degraded product of COL, which has been known to possess antigenicity due to its animal origin. In contrast, G has relatively low antigenicity compared to its precursor, yet it still retains some of the information signals which may promote cell adhesion, differentiation and proliferation, such as the Arg–Gly-Asp (RGD) sequence of COL [13]. For this reason, G has been blended with CH to improve its biological activity.

Chitosan-gelatin devices in both cross-linked and uncross-linked form have been developed and tested for the regeneration of various tissues including skin [14], cartilage [15], nerves [16], and bone [17]. Chemical and physical cross-linking methods have been used to increase CH/G blend stability in aqueous media and mechanical properties. Physical cross-linking methods include microwave energy [18], and UV-irradiation [19]. Their main advantage is that they do not cause potential harm but it is difficult to obtain the desired cross-linking degree. Commonly used chemical cross-linkers include aldehydes (formaldehyde, glutaraldehyde) [20], polyepoxy compounds [21] and carbodiimides [22]. The main limitation in the use of chemical cross-linkers arises from the presence of some unreacted cross-linker inside the CH/G network and from the risk of formation of toxic products by reaction between the substrate and the cross-linking agent during *in vivo* biodegradation. For this reason, much interest has been addressed toward naturally derived cross-linking agents, with a low toxicity.

Genipin (GP) is a natural cross-linking reagent, used for its ability to cross-link CH and proteins containing residues with primary amine groups, particularly G and soy protein isolates [23], producing blue-colored hydrogels. It has been used as a cross-linking agent to prepare cartilage substitutes, drug carriers, or conduits for peripheral nerve regeneration [24- 26]. However, the covalent cross-linking reaction between CH/G blend and GP depends on the pH; values between neutral and weakly basic conditions (pH 7–9) are favorable for the cross-linking reaction [27]. Therefore, in this chapter, CH/G-based solutions were pre-neutralized and

ionically cross-linked by dibasic sodium phosphate (DSP) and subsequently covalently cross-linked by GP to fabricate 3D porous membranes.

The membranes were prepared by freeze-drying process, that is a conventional technique for the fabrication of porous materials which pore structure is controlled by the ice crystal growth. Optimal pore diameters for 3D porous structures for bone repair are in the 100-400  $\mu\text{m}$  range [28]. Pore size may be controlled by the temperature set in the freeze-drying process: pore diameters increase with increasing the temperature due to a higher ice crystal growth rate. Then, the physicochemical, morphological and mechanical properties of double cross-linked porous membranes were investigated.

## 6.2 Materials and methods

### 6.2.1 Materials

Type A gelatin from porcine skin ( $M_w$ : 50-100 kDa), chitosan highly viscous derived from crab shell with 75-85% deacetylation degree ( $M_w$ : 190-310 kDa),  $\beta$ -tri-calcium phosphate ( $M_w = 310.18$  Da), and dibasic sodium phosphate ( $M_w = 141.96$  Da) were supplied from Sigma-Aldrich (Milano, Italy). Genipin was purchased from Challenge Bioproducts (Taiwan). All solvents used were of analytical grade and used without further purification.

#### 6.2.1.1 Gelatin

Gelatin (Fig. 6.1) is a non expensive and commercially available biomaterial that has gained interest in biomedical engineering, mainly because of its biodegradability. It is a protein produced by partial hydrolysis of COL, the most widespread protein in the body occurring in most connective tissues as skin, tendon and bone, that is usually derived from pig-skin with an acidic process (type A) or from bovine origin with a basic (lime cured) process (type B) [29]. G contains: 84-90% proteins, 1-2% mineral salts, and 8-15% water. It is a heterogeneous mixture of single or multi-stranded polypeptides, each with extended left-handed proline helix conformations and containing between 50-1000 amino acids. G does not express antigenicity in physiological conditions, it is completely resorbable *in vivo* and its physicochemical properties can be suitably modulated [30]. Since biodegradable polymers may be rapidly *in vivo* reabsorbed, cross-linking strategies have been applied to prolong G resistance *in vivo* and to improve its mechanical properties [31].

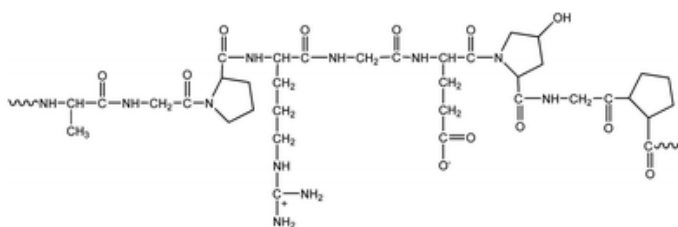


**Fig. 6.1** Gelatin (G) chemical structure.

### 6.2.1.2 $\beta$ -tricalcium phosphate

$\beta$ -tricalcium phosphate (Fig. 6.2) is the beta crystal form of tricalcium phosphate, a calcium salt of phosphoric acid with the chemical formula  $\text{Ca}_3(\text{PO}_4)_2$ , with a Ca/P ratio of 1.5. It is widely used in orthopedic and alveolar reconstruction surgery due to its high bioactivity properties and its biodegradability. TCP and, generally, all calcium phosphate ceramics are absorbed by phagocytosis.

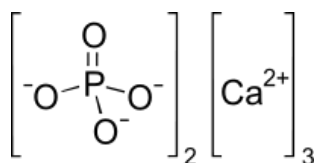


**Fig. 6.2**  $\beta$ -tricalcium phosphate (TCP) chemical structure.

TCP has also the potential to function as a source of calcium and phosphate ions for the local tissue during the degradation process, which possibly results in stimulation of osteoblastic function and promotion of bone formation.

### 6.2.1.3 Genipin

Genipin (Fig. 6.3) is a hydrolytic product of geniposide, an iridoid glucoside isolated from the fruits of *Genipa Americana* and *Gardenia jasminoides Ellis*. Because it is a naturally occurring, biodegradable molecule with low cytotoxicity, GP has found applications in herbal medicine [32], whereas the dark blue pigments obtained by the reaction of GP with primary amines have been used in the fabrication of heat, pH and light resistant food dyes [33]. It has also been investigated as a cross-linking material in many biological applications.

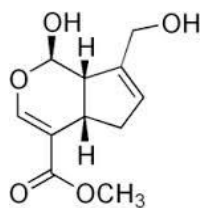


**Fig. 6.3** Genipin (GP) chemical structure.

GP possess cross-linking activity towards amino containing materials [11]. The cross-linking reaction mechanisms between biopolymers containing primary amine groups and GP are different at different pH values as reported in Fig. 6.4. Under acidic and neutral conditions, a nucleophilic attack by the amino groups of biopolymer on the olefinic carbon atom at C-3 occurs, followed by opening of the dihydropyran ring and attack by the secondary amino group on the newly formed aldehyde group. In other words, GP acts as a dialdehyde but its condensation products are much more stable compared to glutaraldehyde [28]. In the product, short chains of condensed GP act as cross-linking bridges. Under basic conditions, the ring-opening reaction of GP occurs via a nucleophilic attack by hydroxyl ions in aqueous solution to form intermediate aldehyde groups, which subsequently undergo aldol condensation. The terminal aldehyde groups on the polymerized GP undergoes a Schiff reaction with the amino groups on biopolymer to form cross-linked networks. Therefore, the pH condition plays an important role in influencing the cross-linking reactions.

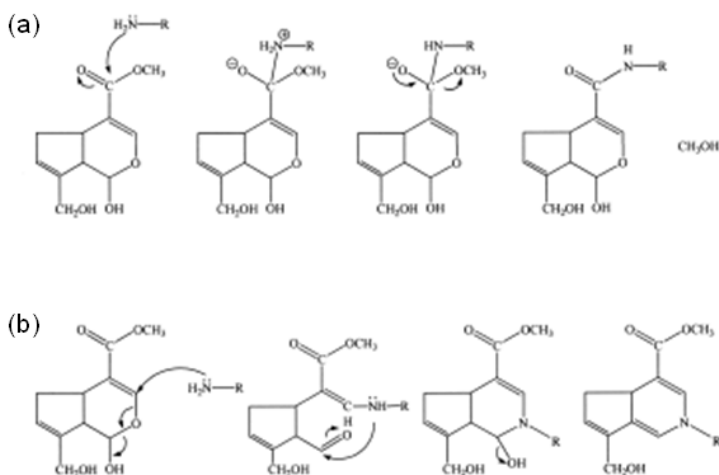


**Fig. 6.4** Cross-linking reactions involving GP, (a) first stage of the reaction (nucleophilic attack) and (b) second stage of reaction (nucleophilic substitution).

Butler et al. [34] found that the fastest reaction is a nucleophilic attack of an amino group of CH to carbon 3 of GP which results in the opening of the dihydropyran ring and the formation of a

tertiary amine, i.e. a GP derivative linked to a glucosamine unit. The subsequent slower reaction is a nucleophilic substitution of the ester group of GP to form an amide. Simultaneously, polymerization can take place between GP molecules already linked to amino groups of CH which could lead to the cross-linking of amino groups by short GP oligomers. The dark-blue coloration of samples is associated with the oxygen radical-induced polymerization of GP as well as its reaction with amino groups.

#### 6.2.1.4 Dibasic sodium phosphate

Dibasic sodium phosphate (Fig. 6.5a) is an inorganic compound with the formula  $\text{Na}_2\text{HPO}_4$ . It is one of several sodium phosphates, it is highly hygroscopic and water soluble. Recently, it has been investigated as a cross-linking material for biomedical applications [35].

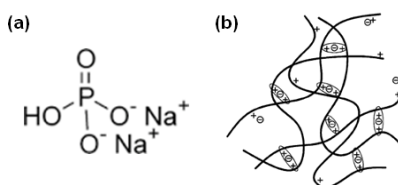


**Fig. 6.5** (a) Dibasic sodium phosphate (DSP) chemical structure, (b) structure of polymer network formed by ionic cross-linking.

DSP possesses cross-linking activity towards positively charged materials. Ionic cross-linking is a simple and mild procedure; no auxiliary molecules such as catalysts are required [36], which is of great interest for medical or pharmaceutical applications. Indeed, ionic cross-linking can be ensured by the classical method of preparing cross-linked network, namely by the addition of the cross-linker, either solubilised [37] or dispersed [38] to the polymeric solution. As reported in Fig. 6.5b, a network is formed in the presence of negatively charged entities, which form bridges between the positively charged polymeric chains.

#### 6.2.2 Sample preparation

Porous CH/G, CH/G+GP-DSP and CH/G/TCP+GP-DSP membranes were prepared by freeze-drying technique. CH was dissolved in 0.5M acetic acid (Sigma-Aldrich, Italy) at a concentration of 2.5% (wt/v). G was dissolved in demineralised water for 1 h at 50 °C, then CH was added under moderate stirring reaching a solution concentration of 3% (wt/v). CH and G were mixed at 1:2 weight ratio and stirred for about 2 h at 50 °C.

For cross-linked samples, DSP was dissolved in demineralised water at a concentration of 1M and added dropwise to CH/G solution at defined volume percentage (7.5% (v/v) respect to the



length  $b$  (1 cm), the molar concentration of the diluted solution ( $C$ ) was obtained through Lambert-Beer law:

$$A = \varepsilon \cdot b \cdot C$$

From this molar concentration and the final volume (after dilution), the number of  $\text{NH}_2$  moles in samples was calculated. Then, the cross-linking degree was calculated by the following equation, using uncross-linked CH/G blend as a control:

$$\text{Cross - linking degree (\%)} = \frac{NH_{\text{control}} - NH_{\text{sample}}}{NH_{\text{control}}} \cdot 100$$

where  $NH_{\text{control}}$  and  $NH_{\text{sample}}$  were the mole fractions of free  $\text{NH}_2$  remaining in uncross-linked (control group) and cross-linked (samples) groups, respectively.

#### 6.2.3.2 Morphological analysis

Scanning electron microscopy (SEM LEO – 1430, Zeiss, Munich, Germany) and compositional analysis (EDS) were performed on membrane surfaces and liquid nitrogen fractured sections. Samples were sputter coated with Au before SEM-EDS analysis.

Both images (sample surface and section) were analysed with ImageJ software (National Institute of Health, USA) to evaluate the average pore size and the pore size distribution. Three images for each samples were analysed at a magnification of 150x.

#### 6.2.3.3 Infrared analysis in ATR modality

The analysis was carried out in a Perkin Elmer Frontier Optical Spectrometer fitted with an attenuated total reflection sampler (FTIR-ATR). Spectra were obtained over the 400-4000  $\text{cm}^{-1}$  wavenumber range at room temperature, using diamond crystal.

#### 6.2.3.4 Thermogravimetric analysis

The thermal stability and degradation profile of porous membranes was evaluated through thermogravimetric (TGA) analysis using a TA INSTRUMENT Q500 system under a nitrogen atmosphere. The experiments were performed with a 10-15 mg sample in aluminum pans at 10  $^{\circ}\text{C}/\text{min}$  heating rate in the 50-800  $^{\circ}\text{C}$  temperature range.

### 6.2.3.5 Tensile test

Porous samples were obtained for tensile test in the form of rectangular samples (10 x 30 mm<sup>2</sup>). Tensile tests were performed on dry and wet specimens using MT<sup>®</sup>QTestTM/10 instrument and a load cell of 500 N was applied. The samples were tested at room temperature. Prior to testing in wet conditions, all samples were immersed in phosphate buffer solution (PBS) at pH 7.4 for 5 min (Sigma-Aldrich, Italy). Then, samples were dried at the surface by gentle contact with a filter paper and immediately tested. The traction force was applied along the length of the samples at a constant cross-head displacement rate of 2 mm/min. Young's modulus (E), maximum tensile strength and strain ( $\sigma_{\max}$  and  $\varepsilon_{\max}$ , respectively) were measured from the stress-strain curves. E was determined as the slope of the linear elastic region, and  $\sigma_{\max}$  and  $\varepsilon_{\max}$  were calculated as the maximum stress a material can withstand before failing and the total elongation just before fracture, respectively [40].

### 6.2.3.6 Water absorption and dissolution tests

The membranes for the water absorption tests were weighed and then put in 6 ml of PBS (pH 7.4) at 37 °C. These membranes had a rectangular shape of 10 x 30 mm<sup>2</sup>. The swollen membranes were drawn at various time points (1, 3, 6, 9, 24 h) dried superficially by gentle contact with a filter paper and weighed again. The water absorption (WA) percentage was calculated using the following equation:

$$WA(\%) = \frac{W_A - W_i}{W_i} \cdot 100$$

where  $W_i$  and  $W_A$  were the sample weight before and after water absorption, respectively.

The membranes for the dissolution tests were weighed and then put in PBS (pH 7.4) at 37 °C. The membranes were drawn at various time points (1, 3, 7, 14, 28, 42, 56 d). After each time point, samples were freeze-dried at -55 °C for 24 h, then they were weighed again and the dissolution percentage ( $\Delta W$ ) was calculated as:

$$\Delta W(\%) = \frac{W_o - W_f}{W_o} \cdot 100$$

where  $W_o$  and  $W_f$  were the sample weight before and after the degradation test.

### 6.2.3.7 Cell viability and adhesion

MG-63 human osteoblast-like cells (ATCC, Rockville, MD) were grown in a controlled atmosphere (5% CO<sub>2</sub>; T = 37 °C) in Dulbecco's Modified Eagle's Medium (DMEM, Sigma-Aldrich, Italy) supplemented with 10% fetal bovine serum (FBS), 1% non-essential aminoacids, 2.0 mM L-glutamine, and 1% penicillin-streptomycin (all from GIBCO, Invitrogen, Italy). After thawing, cells were routinely split 1:10 every 3-4 days and used between the 3<sup>rd</sup> and 4<sup>th</sup> passages.

Before seeding, membranes were sterilized in 70% ethyl alcohol solution (Sigma-Aldrich, Italy) for 2 h and washed two times in PBS (GIBCO) for 1 h. In order to improve cell adhesion, samples were then conditioned overnight in 10% serum added DMEM at 5% CO<sub>2</sub>, 37 °C. The media was then discarded and membranes considered ready for seeding. Cells were detached using 0.25% trypsin in 1 mM ethylenediaminetetraacetic acid (EDTA, Sigma-Aldrich, Italy) and seeded at a density of  $1 \times 10^4$  cell/cm<sup>3</sup> by applying 50 µl of cell suspension on the samples placed in multi-well plates with 24 wells and on control wells at 37 °C for 30 min in a humidified chamber, in order to avoid the slip down of cells. Then 1.5 ml of DMEM was added to cover the samples placed in Corning<sup>®</sup> ultra-low attachment multi-well plates. Cells were cultured for 1 and 3 days.

MG-63 cell viability was evaluated through 3-dimethylthiazol-2,5-diphenyltetrazolium bromide (MTT) colorimetric assay. After incubation (1 and 3 days), the medium was removed and 200 µl of MTT (Sigma, Italy) solution (5 mg/ml in DMEM without phenol red) and 1.8 ml of DMEM were added to the cell monolayer. The multi-well plates were incubated at 37 °C for further 4 h. After discarding the supernatants, the dark blue Formazan crystals were dissolved by adding 2 ml of solvent (10% HCl 1N in isopropanol; Sigma, Italy) and quantified spectrophotometrically (Secomam, Anthelie light, version 3.8, Contardi, Italy) at 570 nm. Results are reported as a percentage viability of polystyrene culture plates (TCP), where the cells were placed directly into adherent TCP at the same culture density as placed onto the samples.

SEM analysis was finally performed to evaluate cell adhesion. Samples from cell culture tests were fixed in 2% glutaraldehyde (Sigma-Aldrich) in 0.1M cacodylate buffer (pH 7.4; Sigma-Aldrich) and post-fixed in 1% osmium tetroxide (Sigma, Milan, Italy). Specimens were then dehydrated in increasing ethanol concentrations, CPD-dried (Crytical Point Drying), mounted on aluminium stubs, gold-sputtered by the Edwards Sputter Coater B150S equipment and observed with a Philips XL 20 SEM (FEI Italia SRL, Milan, Italy) microscope.

### 6.2.4 Statistical analysis

All data are expressed as means  $\pm$  standard deviation. Differences between means were analyzed by two-way ANOVA with the Bonferroni's post test. For mechanical characterization, statistical analysis was performed using one-way ANOVA followed by a Tukey's post hoc test. All statistical analyses were performed by Prism, Graph Pad Software.

## 6.3 Results and discussion

The theoretical double cross-linked structure of CH/G blend is represented in the following diagram (Fig. 6.7).

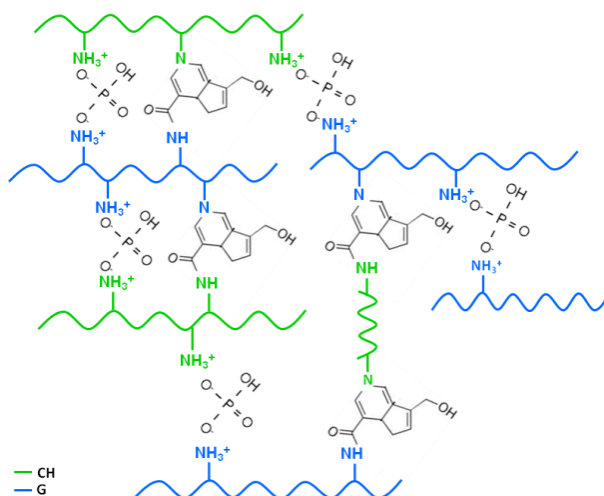


Fig. 6.7 Proposed structure of cross-linked CS/G blend.

### 6.3.1 Cross-linking degree

The cross-linking degree of GP-cross-linked membranes was determined by the ninhydrin assay, and was defined as the percentage of free amino groups in the test membranes reacted with GP subsequent to cross-linking [40]. Table 6.1 collects the results obtained from the UV spectra analysis for CH/G, CH/G+GP-DSP, and CH/G/TCP+GP-DSP porous membranes.

**Table 6.1** Absorbance values at 570 nm and cross-linking degree obtained for CH/G, CH/G+GP-DSP, and CH/G/TCP+GP-DSP porous membranes.

Sample	Absorbance at 570 nm	Cross-linking degree (%)
CH/G	0.84 $\pm$ 0.17	-
CH/G+GP-DSP	0.53 $\pm$ 0.09	35.3 $\pm$ 9.3
CH/G/TCP+GP-DSP	0.54 $\pm$ 0.11	40.6 $\pm$ 4.4

Uncross-linked CH/G samples showed the highest absorbance value at 570 nm ( $0.84 \pm 0.17$ ) due to the high quantity of free amino groups. On the contrary, absorbance values of GP cross-linked membranes significantly decreased, meaning that samples were highly cross-linked. Moreover, the addition of DSP and TCP in CH/G blends did not seem to interfere with the cross-linking process as the ninhydrin assay did not detect the ionically cross-linked amino groups

The cross-linking degree was expressed as a percentage of free amino groups involved in GP-cross-linking mechanism. Cross-linking degree of CH/G/TCP+GP-DSP membranes was similar to that of CH/G+GP-DSP membranes. This result suggested that TCP did not interfere with the GP cross-linking process of the CH/G blend.

### **6.3.2 Porosity and morphological analysis**

The physical characteristics of a scaffold can be described by the average pore size, pore size distribution, pore volume, pore interconnectivity and pore shape. Pores are necessary for bone tissue formation because they allow migration and proliferation of osteoblasts and mesenchymal stem cells, as well as the proper vascularization of the implant [41]. In addition, a porous surface improves the mechanical interlocking between the implant biomaterial and the surrounding natural bone, providing greater mechanical stability at this critical interface [42]. Optimal pore diameters for porous structures for bone repair are in the 100-400  $\mu\text{m}$  range [29] which are suitable for human osteoblast cell penetration and a minimum pore size is required for tissue in-growth [43]. Pore interconnectivity is required for access to nutrients and transport of waste products while pore shape and roughness are necessary for better cell spreading [44]. SEM analysis was performed on surfaces and sections of CH/G, CH/G+GP-DSP and CH/G/TCP+GP-DSP porous membranes to evaluate the effect of composition and cross-linking on sample morphology. SEM photomicrographs and EDS spectra are shown in Fig. 6.8.

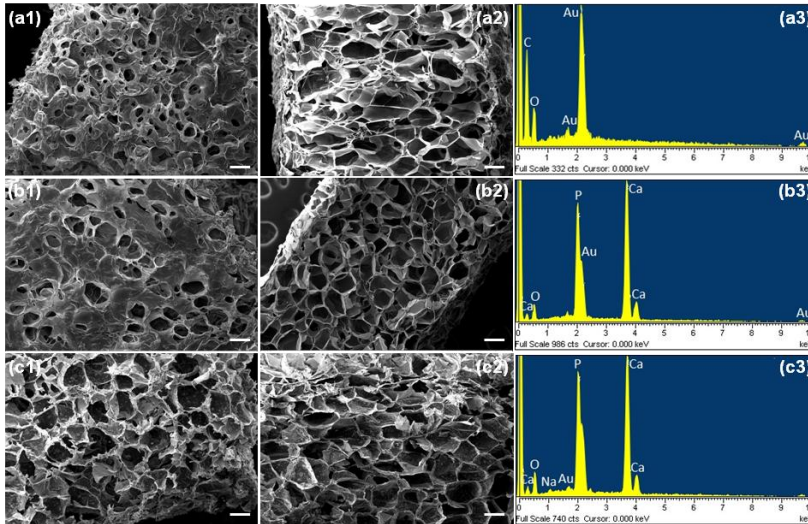


**Fig. 6.8** SEM micrographs of (1) Surface and (2) fractured section, and (3) EDS spectra of (a) CH/G, (b) CH/G+GP-DSP, and (c) CH/G/TCP+GP-DSP porous membranes. Scale bar = 200 µm.

A lower surface pore density was observed for CH/G and CH/G+GP-DSP samples (Fig. 6.9 a1 and b1, respectively) compared to CH/G/TCP+GP-DSP (Fig. 6.9c1). The introduction of TCP increased surface pore density and produced pores with rougher walls (Fig. 6.9c1).

The sections of porous membranes showed a typical foam-like morphology with interconnected pores, characterised by a wide distribution of pore sizes. Pore density was high for all samples and pores showed thin walls. The cross-linking process and the presence of TCP did not cause marked morphological changes.

EDS spectra of fractured sections of CH/G membranes (Fig. 6.9a3) showed the characteristic elements of gelatin and chitosan: carbon (C) and oxygen (O). DSP characteristic elements could be detected for CH/G+GP-DSP and CH/G/TCP+GP-DSP porous membranes (Fig. 6.9 b3 and c3, respectively), namely sodium (Na) and phosphorus (P). Finally, EDS spectra of the composites membrane also showed the characteristic elements of TCP: calcium (Ca) and phosphorus (P).

Pore analysis within membrane surface and section was determined by SEM photomicrographs analysis using ImageJ software. Pore distribution are shown in Fig. 6.8 and Table 6.2.

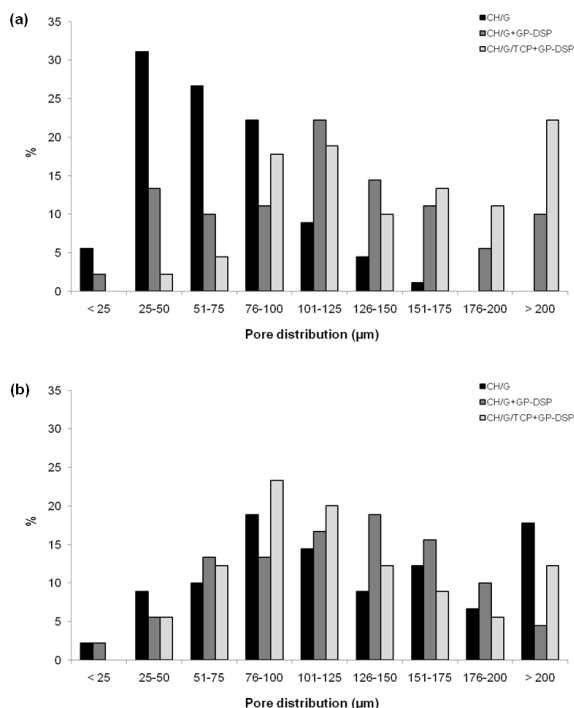


**Fig. 6.9** (a) Surface and (b) section pore distribution of CH/G, CH/G+GP-DSP, and CH/G/TCP+GP-DSP membranes.

**Table 6.2** Mean pore size of CH/G, CH/G+GP-DSP, and CH/G/TCP+GP-DSP samples.

Sample	Section (μm)	Surface (μm)
CH/G	66.8 ± 4.6	129.6 ± 45.2
CH/G+GP-DSP	130.2 ± 60.9	121.5 ± 4.3
CH/G/TCP+GP-DSP	151.7 ± 11.5	123.8 ± 18.1

Results from morphological analysis of surfaces (Fig. 6.9a) demonstrated that a high percentage of pores on CH/G membranes showed sizes in the 25-100 μm range: probably, the additional freeze-drying step induced the formation of small-sized pores. The cross-linking process caused the formation of pores with wider size range (1-300 μm) compared to uncross-linked membranes, which are crucial for protein adsorption and cell adhesion. Finally, the addition of TCP increased the percentage of pores with 75-300 μm size. The mean pore size was found to vary from 66.8 ± 4.6 μm for CH/G membranes to about 130 μm and 150 μm for CH/G+GP-DSP and CH/G/TCP+GP-DSP samples, respectively.

SEM analysis of the fractured sections (Fig. 6.9b) showed a porous morphology with a different pore size distribution compared to sample surface. In detail, SEM analysis indicated that 75-80% of pores within the membranes had a size in the 75-300 μm range. A mean pore size of around 125 μm was found for all the analysed membranes.

### 6.3.3 FTIR-ATR analysis

Chemical composition of membranes has been evaluated through FTIR-ATR analysis. Fig. 6.10 compares FTIR-ATR spectra of CH/G, CH/G+GP-DSP and CH/G/TCP+GP-DSP samples. All spectra showed the typical adsorption bands of gelatin and chitosan. Bands due to N-H and O-H stretching vibrations overlapped in the absorption peak at  $3288\text{ cm}^{-1}$  while the peak at  $2879\text{ cm}^{-1}$  represented the symmetric stretching vibration of aliphatic group ( $-\text{CH}_3$ ). The characteristic bands of amide I ( $\text{C}=\text{O}$ ) axial stretching vibration and amide II ( $\text{N-H}$ ) bending vibration appeared, respectively, at  $1639\text{ cm}^{-1}$  and  $1544\text{ cm}^{-1}$ , and that of amide III at  $1236\text{ cm}^{-1}$ , caused by C-N stretching vibrations, amide N-H in-plane bending vibrations and  $\text{CH}_2$  wagging vibrations [45]. Finally, bands at  $1414\text{ cm}^{-1}$ ,  $1150\text{ cm}^{-1}$  and  $1070\text{ cm}^{-1}$  represented, respectively, the O-H bending vibration, the C-O-C asymmetric stretching and the C-O stretching vibrations. The first peak originated from CH deacetylation, while the last two bands were typical of CH saccharide structure [46].

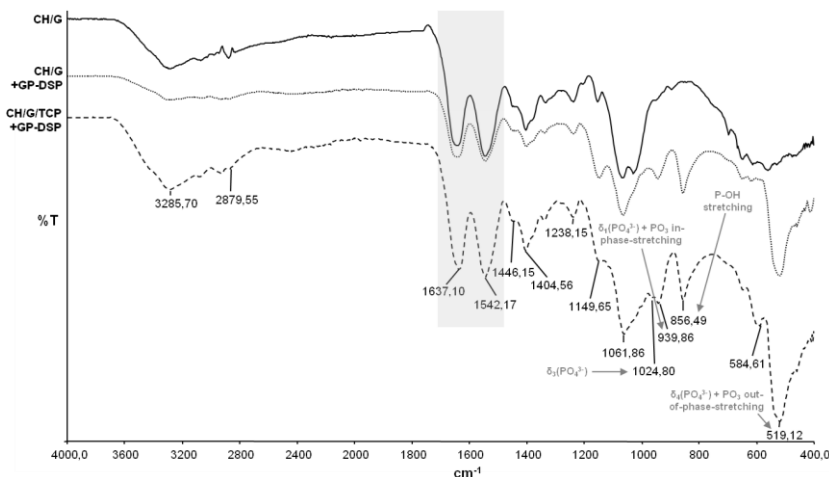


Fig. 6.10 FTIR-ATR spectra of CH/G, CH/G+GP-DSP, and CH/G/TCP+GP-DSP porous membranes.

As reported in literature [47], FTIR-ATR spectra of GP-cross-linked samples should display a slight increase of the ratio between the intensities of amide I ( $1630\text{--}1640\text{ cm}^{-1}$ ) and amide II ( $1540\text{--}1550\text{ cm}^{-1}$ ) bands, attributed to the formation of amide and tertiary amine linkages between CH and G macromolecules through the reaction of primary amine moieties with the cross-linker. In this chapter, CH/G+GP-DSP and CH/G/TCP+GP-DSP samples only showed slight variations respect to those of uncross-linked sample due to (1) the absorption band of GP-cross-linked amide groups at around  $1600\text{ cm}^{-1}$  which merged with the strong absorption band of amide I in CH and G, and (2) the formation of a reduced number of cross-links between CH

macromolecules in the form of GP oligomers [48, 49]. On the contrary, it was possible to observe the characteristic peaks of DSP cross-linker. Bands at  $943\text{ cm}^{-1}$ ,  $853\text{ cm}^{-1}$  and  $517\text{ cm}^{-1}$  were attributed to  $\text{PO}_3$  in-phase-stretching, P-OH stretching and  $\text{PO}_3$  out-of-plane-bending, respectively [50]. Moreover, characteristic bands of the inorganic phase were detected in the composite membrane: peak at  $1025\text{ cm}^{-1}$  was due to  $\delta_3$  of phosphate mode, peak at  $940\text{ cm}^{-1}$  corresponded to  $\delta_1$  of phosphate and band at  $853\text{ cm}^{-1}$  was attributed to P-OH stretching vibration [51]. These peaks were partially overlapped with DSP typical absorption bands.

### 6.3.4 TGA analysis

The thermal stability and degradation profile of CH/G, CH/G+GP-DSP, and CH/G/TCP+GP-DSP porous membranes were evaluated through thermogravimetric (TGA) analysis. The derivative of TGA (DTG) curves is shown in Fig. 6.11.

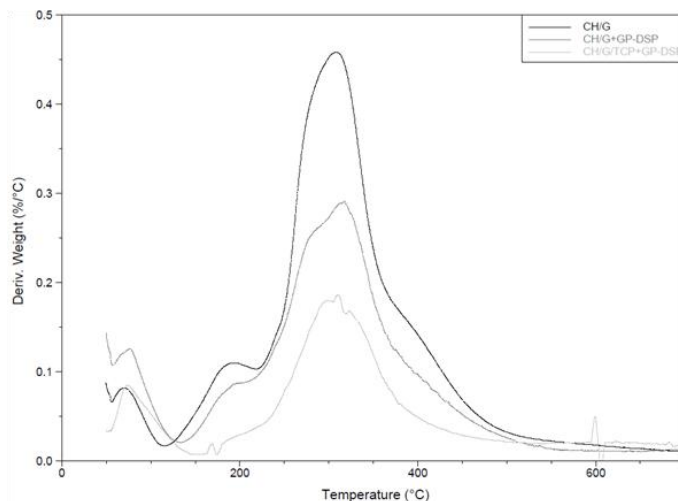


**Fig. 6.11** Derivative of TGA curves for CH/G, CH/G+GP-DSP, and CH/G/TCP+GP-DSP porous membranes.

DTG curves revealed three weight loss steps [9]: the first was related to water evaporation while the other two were due to CH and G pyrolysis, that occurred separately. As reported in literature, during heating, the initially ordered structure of G was gradually destroyed. This may be possible after the break-up of inter- and intra-molecular hydrogen bonds which were responsible for maintenance of G chains in the form of a triple helix. After that, breaking up of C-C, C-H, C-NH, C-C=O, and C-COOH bonds increased the state of disorder in the G structure [52]. According to the literature [53], pyrolysis of polysaccharides, such as CH, started by a random split of the glycosidic bonds, followed by a further decomposition forming acetic and butyric acids and a series of lower fatty acids, where C2, C3 and C6 were predominant.

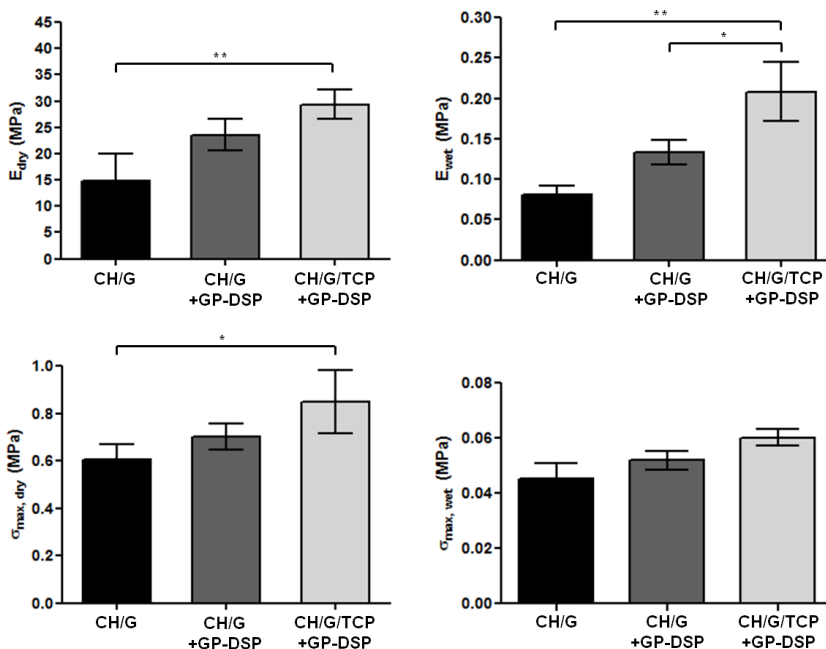
Table 6.3 collects values of degradation temperature ( $T_d$ ) and weight loss calculated from the DTG curves. Values of  $T_d$  did not change significantly upon cross-linking and addition of TCP. On the contrary, it could be possible to observe a slight decrease in weight loss for CH/G/TCP+GP-DSP composite membranes.

**Table 6.3** Maximum degradation rate temperatures ( $T_d$ ) and weight loss for CH/G, CH/G+GP-DSP, and CH/G/TCP+GP-DSP porous membranes.

Sample	I STEP		II STEP		III STEP	
	$T_d$ (°C)	Weight loss (%)	$T_d$ (°C)	Weight loss (%)	$T_d$ (°C)	Weight loss (%)
CH/G	70.4	5.7	194.9	12.9	308.3	40.9
CH/G+GP-DSP	78.2	8.8	181.1	14.2	318.1	37.6
CH/G/TCP+GP-DSP	74.6	3	182.7	6.4	310.3	17.6

### 6.3.5 Mechanical characterizations

Tensile tests were performed on dry and wet samples. Fig 6.12 shows the behavior of the elastic modulus (E), maximum tensile strength and strain ( $\sigma_{max}$  and  $\epsilon_{max}$ , respectively) of CH/G, CH/G+GP-DSP, and CH/G/TCP+GP-DSP porous samples.



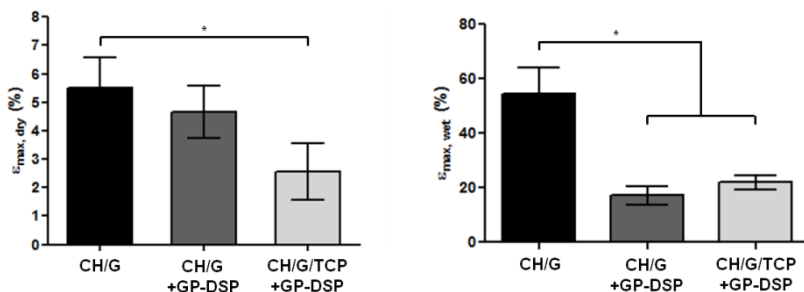


**Fig. 6.12** Young's modulus ( $E$ ), maximum tensile strength ( $\sigma_{\max}$ ) and strain ( $\epsilon_{\max}$ ) of CH/G, CH/G+GP-DSP, and CH/G/TCP+GP-DSP porous membranes in dry (on the left) and wet (on the right) conditions.

Both in dry and wet conditions, GP-DSP cross-linking slightly improved the mechanical properties of CH/G membrane in terms of Young's modulus and maximum tensile strength. For dry samples, Young's modulus and maximum tensile strength were, respectively,  $14.9 \pm 5.1$  MPa and  $0.6 \pm 0.0$  MPa for CH/G, and  $23.6 \pm 3.0$  MPa and  $0.7 \pm 0.0$  MPa for CH/G+GP-DSP. For wet samples, they reached values of  $0.08 \pm 0.01$  MPa and  $0.04 \pm 0.01$  MPa for CH/G, and  $0.13 \pm 0.01$  MPa and  $0.05 \pm 0.01$  MPa for CH/G+GP-DSP. In dry condition, a statistically significant increase of  $E$  and  $\sigma_{\max}$  was obtained by adding inorganic phase into CH/G matrix, due to the superior mechanical behavior of TCP compared to the polymeric phase. In detail, the tensile Young's modulus increased to about 30 MPa, while the maximum tensile strength reached a value around 0.9 MPa. On the other hand, no significant differences could be observed between CH/G+GP-DSP and CH/G/TCP+GP-DSP samples. The elastic modulus of wet composite membranes markedly increased compared to uncross-linked and GP-DSP cross-linked polymeric samples, reaching a value of 0.2 MPa, while no statistically significant difference could be detected for  $\sigma_{\max}$ . However, all tested materials displayed a marked decrease of  $E$  and  $\sigma_{\max}$  after immersion in PBS for 5 min, due to their plasticization.

On the other hand, the cross-linking mechanism and the addition of TCP caused a decrease in the deformability of CH/G membranes both in dry and wet conditions. Significant changes could be observed between CH/G and CH/G/TCP+GP-DSP dry membranes, with maximum tensile strain values of  $5.5 \pm 1.1\%$  and  $2.6 \pm 1.0\%$ , respectively. In wet condition, cross-linked samples displayed identical  $\epsilon_{\max}$  values of about 20%, which were statistically lower than for CH/G membranes ( $54.5 \pm 16.6\%$ ).

It is widely accepted that tensile strength for inorganic–organic hybrid materials can be viewed as an indication of the interfacial bonding strength between the mineral and organic components [54]. In addition, the proper stress transfer occurring between the mineral phase and the organic matrix has a major effect on the mechanical properties of the composite materials [55].

Regarding the present contest, the chemical interaction and the intimate adhesion between inorganic powders and the organic matrix, as well as the superior stiffness of the organic phase were the reasons for the enhanced tensile strength of composites as compared to CH/G samples. As suggested by Bigi et al. [56], the presence of inorganic phase in the composite films induced an increase of its stiffness.

### 6.3.6 Water absorption and dissolution tests

One of the main factors affecting biocompatibility of biomaterials is their water content: a polymer matrix imbibing an adequate amount of water shows similar properties to living tissue in terms of physiological stability, low interfacial tension, and permeability [57]. Water absorption increases the pore size and total porosity, maximizing the surface area/volume ratio and allowing the porous matrices to have probability of cell inclusion as well as cell growth into the scaffold. The increase in water uptake influences also nutrients/waste exchange from culture media. However, while the water absorption behavior promotes cell adhesion, it could lower scaffold mechanical properties [58].

The water uptake of any polymer network depends on the nature of the polymer, polymer-solvent compatibility and degree of cross-linking [59]. The influence of chemical composition of CH/G, CH/G+GP-DSP, and CH/G/TCP+GP-DSP porous membranes on their water absorption has been investigated; Fig. 6.13 reports the water absorption (WA) degree as a function of time for porous matrices.

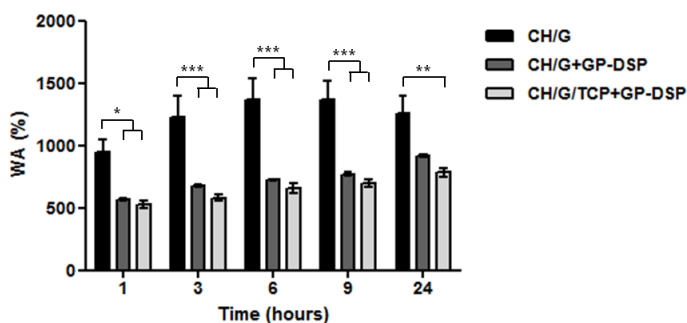


**Fig. 6.13** Water absorption (WA) behavior of CH/G, CH/G+GP-DSP, and CH/G/TCP+GP-DSP porous membranes as a function of immersion time in PBS.

Uncross-linked samples showed a higher water absorption behavior. Their WA degree increased in the first 6 h, reaching a plateau of about 1300%; then, a slightly decrease was observed, probably due to the beginning of dissolution process. The stability of CH/G samples in aqueous media increased with the addition of cross-linking agents and inorganic phase.

CH/G+GP-DSP and CH/G/TCP+GP-DSP porous membranes showed the same behavior: the WA degree slowly increased in a linear way, reaching values of around 850% after 24 h of immersion in PBS.

CH and G contain primary amine and hydroxyl groups that increased their affinity to water and could form hydrogen bonds with water [60]. In cross-linked form, the ability of CH/G membranes to form hydrogen bonds with water molecules decreased [61]. Moreover, the higher the cross-linking density, the lower the swelling ability of CH/G samples due to the slower relaxation time of the polymeric chains [62].

The presence of TCP slightly decreased the water absorption as compared to cross-linked membranes. This was attributed to the lower hydrophilicity of the inorganic phase as compared to the polymer matrix. Moreover, TCP formed cross-links between the chains and decreased gelatin hydrophilicity by binding Ca and P to  $-COOH$  or  $NH_2$  groups. Since some of the  $NH_2$  were bound to Ca groups, the  $-OH$  groups could not form hydrogen bonds, hence the decrease in water absorption behavior [58].

The weight loss of CH/G, CH/G+GP-DSP, and CH/G/TCP+GP-DSP membranes after predetermined times of immersion in PBS is represented in Fig. 6.14. Previous literature indicated that the degradability of CH/G porous scaffold proceeds through chitosan degradation and gelatin dissolution [63].

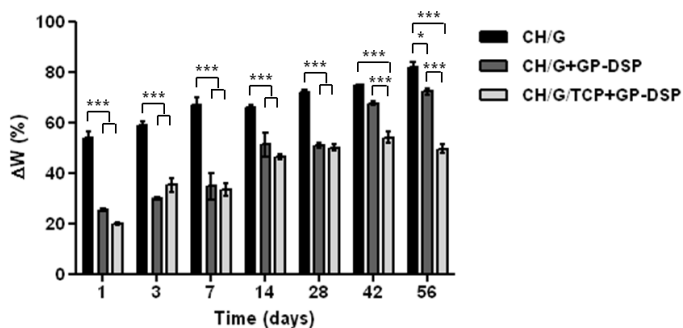


**Fig. 6.14** Weight loss percentage as a function of incubation time in PBS for CH/G, CH/G+GP-DSP, and CH/G/TCP+GP-DSP porous membranes.

All the different kinds of samples were not completely dissolved at the end of the dissolution test. In detail, at each observation time, uncross-linked membranes showed the highest weight loss with statistically significant different values compared to cross-linked samples. CH/G weight loss increased with time: at 14 days it was  $(66.0 \pm 2.5)\%$ , while, after 56 incubation days in PBS, it reached a value of  $(81.8 \pm 5.8)\%$ .

The two types of GP-DSP cross-linked membranes showed the same dissolution rate during the first 28 days of immersion in PBS: their weight loss increased with time, reaching values of about 50%. In the literature, the addition of TCP has been found to significantly decrease the dissolution rate of the composite membranes, as reported by Peter et al. [64]. After 28 incubation days in PBS, CH/G+GP-DSP weight loss rapidly increased with time reaching a value of  $(72.2 \pm 3.3)\%$  after 56 days. On the contrary, CH/G/TCP+GP-DSP weight loss remained approximately constant up to the end of the dissolution test.

### 6.3.7 *In vitro* cell tests

MTT assay involves a reduction reaction which reduces MTT reagent to a blue formazan product when incubated with viable cells. Thus, the absorbance of formazan indirectly reflected the level of cell metabolism and this process is taken as a measure of the viability of cells in culture. Fig. 6.15 shows cell viability at 1 and 3 days evaluated by MTT test.

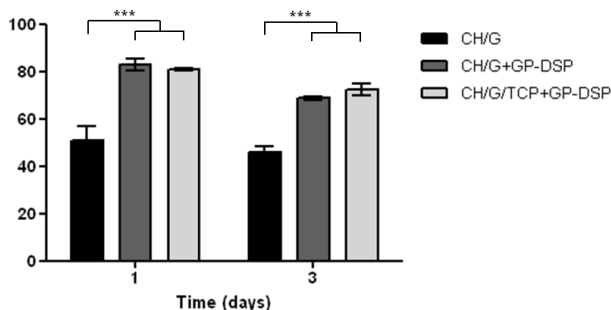


**Fig. 6.15** MTT Test in MG63 cells on CH/G, CH/G+GP-DSP, and CH/G/TCP+GP-DSP porous membranes.

Both after 1 and 3 days of culture, CH/G membranes were the less performing materials as compared to CH/G+GP-DSP and CH/G/TCP+GP-DSP samples, showing MTT values around 50%. Probably, the high solubility of these membranes impaired the test.

After 1 day of culture, MTT values detected in cells seeded onto the CH/G/TCP+GP-DSP membranes were slightly lower than those observed for CH/G+GP-DSP samples ( $(81 \pm 1)\%$  and  $(83 \pm 3)\%$ , respectively), while they slightly increased after 3 days of culture (about 72% for CH/G/TCP+GP-DSP and 69% for CH/G+GP-DSP). However, viability of MG-63 human osteoblast-like cells was no significantly different between the two cross-linked membranes.

Figure 6.16 depicts the morphology of MG-63 cells adhering to CH/G, CH/G+GP-DSP and CH/G/TCP+GP-DSP membranes.

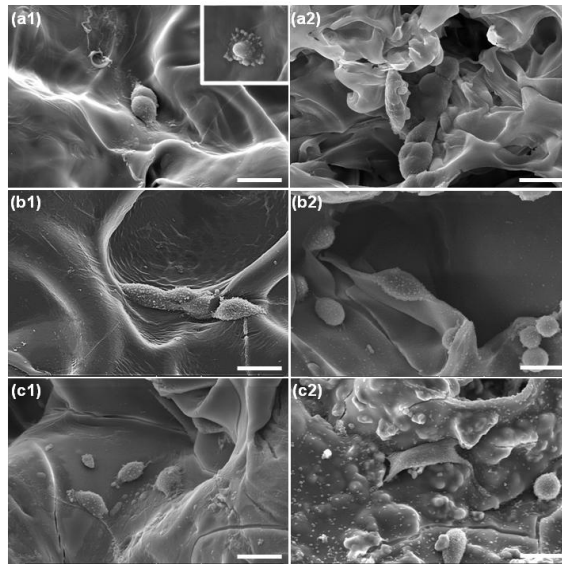


**Fig. 6.16** SEM micrographs of MG-63 human osteoblast-like cells seeded onto (a) CH/G, (b) CH/G+GP-DSP, and (c) CH/G/TCP+GP-DSP porous membranes, for (1) 1 day and (2) 3 days. *Scale bar = 20  $\mu$ m.*

SEM observations confirmed the MTT results. Cells seeded onto CH/G membranes were characterized by a round shape both at 1 and 3 days of culture. In detail, after 1 day (Fig. 6.16 a1), cells were poorly adherent to the substrate with apoptosis signs (as underlined by the arrow) while, after 3 days (Fig. 6.16 a2), no increase in the number of cells could be observed and the few cells formed clusters.

No differences in cells morphology could be observed between 1 and 3 days for CH/G+GP-DSP membranes (Fig. 6.16 b1 and b2, respectively). Some cells had a round shape while others have spread out and possessed long filopodia attachment.

The addition of TCP did not change cells adhesion at 1 day of culture compared to CH/G+GP-DSP samples. On the contrary, SEM micrographs after 3 days showed that MG-63 cells had a high affinity for CH/G/TCP+GP-DSP samples, displaying the typical spindle-like shape, with a stretched elongated shape and a spread morphology.

## 6.4 Conclusions

This chapter was focused on the development and characterization of porous membranes by freeze-drying method, having a similar composition to that of natural bone. A double cross-linking method was studied, based on a covalent and ionic cross-linker (GP and DSP, respectively), and three different type of membranes were prepared. GP-cross-linking mechanism was confirmed by the ninhydrin assay, while the introduction of DSP was proved

by FTIR-ATR analysis. The double cross-linking process did not significantly influence sample morphology and thermal stability. An optimal interconnected porous networks for bone repair, with pores size within 100–200  $\mu\text{m}$  range, were obtained for all membranes, as shown by SEM analysis. Lower sized pores were also present able to favor protein adsorption and thus cells attachment on the membrane, and to allow the flow of nutrients to cells within the substrate. Regarding the thermal stability, it did not change significantly upon cross-linking and addition of TCP. On the contrary, the cross-linking process and the addition of TCP increased the mechanical properties (both in dry and wet conditions), the membrane stability in contact with water media, and the cell response of CH/G network. In fact, Young's modulus and maximum tensile strength increased, while deformability of CH/G membranes decreased by cross-linking, as a consequence of a stiffening effect by the cross-linkers and TCP. The water absorption degree and the dissolution rate were markedly reduced in cross-linked samples. Finally, viability of MG-63 human osteoblast-like cells seeded onto CH/G+GP-DSP and CH/G/TCP+GP-DSP membranes (measured by MTT assay) was significantly higher than for CH/G samples. SEM micrographs after 3 days showed that MG-63 cells had a high affinity for CH/G/TCP+GP-DSP samples, displaying the typical spindle-like shape, with a stretched elongated shape and a spread morphology.

As a conclusion, CH/G/TCP+GP-DSP membranes were demonstrated to be suitable candidate as osteoconductive layer of GTR membranes.

## References

---

1. Armitage GC. *Periodontology* 2004;**34**:9-21.
2. Karring T, et al. Regenerative periodontal therapy. In: Lindhe J, Thorkild K, Niklaus PL, editors. *Clinical periodontology and implant dentistry*. Copenhagen: Blackwell Publishing Company;2003:669-694.
3. Baskbutski JD, et al. *J Endod* 2009;**35**:321-328.
4. Xu C, et al. *J Biomed Mater Res Part B: Appl Biomater* 2012;**100B**:1435-1443.
5. Rodrigues CVM, et al. *Biomaterials* 2003;**24**:4987-4997.
6. Wang Y, et al. *Macromol Mater Eng* 2006;**291**:254-262.
7. Yaszemski MJ, et al. *Biomaterials* 1996;**17**:175-185.
8. Muzzarelli R, et al. *Biomaterials* 1988;**9**:247-252.
9. Jayakumar R, et al. *Int J Biol Macromol* 2007;**40**:175-181.
10. Muzzarelli RAA. *Carb Polym* 2009;**76**:167-182.
11. Muzzarelli RAA, et al. *Antimicrob Agents Chemother* 1990;**34**:2019-2023.
12. Mao JS, et al. *Biomaterials* 2003;**24**:1067-1074.
13. Lien SM, et al. *Acta Biomater* 2009;**5**:670-679.
14. Dhandayuthapani B, et al. *J Biomed Mater Res Part B: Appl Biomater* 2010;**94B**:264-272.
15. Xia W, et al. *J Biomed Mater Res* 2004;**71B**: 373-380.
16. Nie X, et al. *Cell Biochem Biophys* 2014;**68**:163-172.
17. Miranda S, et al. *Arch Oral Biol* 2011;**56**:1-15.
18. Vandelli MA, et al. *J Control Release* 2004;**96**:67-84.
19. Ma L, et al. *J Biomater Sci Polym Ed* 2003;**14**:861-874.
20. Diogenis GA, et al. *J Pharm Sci* 1994;**83**:915-921.
21. Miyada T, et al. *Clin Mater* 1992;**9**:139-148.
22. Kuijpers AJ, et al. *J Biomater Sci Polym Ed* 2000;**11**:225-243.
23. Bigi A, et al. *Biomaterials* 2002;**23**:4827-4832.
24. Yan LP, et al. *J Biomed Mater Res* 2010;**95A**:465-475.
25. Campos MGN, et al. *J Mater Sci Mater Med* 2009;**20**:537-542.
26. Yang Y, et al. *European J Pharm Biopharm* 2011;**79**:519-525.
27. Mi FL, et al. *J Polym Sci Part A: Polym Chem* 2005;**43**:1985-2000.
28. Burg KJL, et al. *Biomaterials* 2000;**21**:2347-2359.
29. Rose PJ, et al. 1987. In: *Encyclopedia of polymer science and engineering*, 2nd ed., Wiley Interscience, Vol. 7, pp 251-278.
30. Huang Y, et al. *Biomaterials* 2005;**36**:7616-7627.
31. Esposito E, et al. *Biomaterials* 1996;**20**:2009-2020.
32. Akao T, et al. *Biol Pharm Bull* 1994;**17**:1573-1576.
33. Paik YS, et al. *J Agric Food Chem* 2001;**49**:430-432.

- 
34. Butler MF, et al. *J Polym Sci. Part A: Polym Chem* 2003;**41**:3941-3953.
  35. Zhu J, et al. *Intern J Biol Macromol* 2012;**51**:105–112.
  36. Shu XZ, et al. *Int J Pharm* 2001;**212**:19-28.
  37. Ruel-Gariepy E, et al. *Int J Pharm* 2000;**203**:89-98.
  38. Brack HP, et al. *Polymer* 1997;**38**:2351-2362.
  39. Mi FL, et al. *J Biomater Sci Polymer Edn* 2001;**12**:835–850.
  40. Askeland, Donald R. *The Science and Engineering of Materials*. 3rd ed. London: Chapman & Hall; 1996.
  41. Kuboki Y, et al. *J Biomed Mater Res* 1998;**9**:190-193.
  42. Story BJ, et al. *Int J Oral Maxillofac Implants* 1998;**13**:749-757.
  43. Zeltinger J, et al. *Tissue Eng* 2001;**7**:557-572.
  44. Ranucci C, et al. *Tissue Eng* 1999;**5**:407-420.
  45. Sionkowska A, et al. *Biomaterials* 2004;**25**:795-801.
  46. Peniche C, et al. *Polymer* 1998;**39**:6549–6554.
  47. Chiono V, et al. *J Mater Sci Mater Med* 2008;**19**:889-898.
  48. Sarema M, et al. *Carb Polym* 2013;**93**:635–643.
  49. Mi FL, et al. *Polymer* 2003;**44**:6521-6530.
  50. Larkin PJ. *Infrared and raman spectroscopy principles and spectral interpenetration*. Elsevier 2011.
  51. Peña J, et al. *J Europ Ceram Soc* 2003;**23**:1687–1696.
  52. Kamińska A, et al. *Polym Degrad Stab* 1996;**51**:15-18.
  53. Nieto J, et al. *Thermochimica Acta* 1991;**176**:63-68.
  54. Evans GP, et al. *J Mater Sci: Mater Med* 1998;**1**:38-43.
  55. Wang L, et al. *Carb Polym* 2007;**68**:740-745.
  56. Best SM, et al. *J Eur Ceram Soc* 2008;**28**:1319-1327.
  57. Janaki K, et al. *Trends Biomater Artif Organs* 2008;**22**:169–178.
  58. Peter M, et al. *Carb Polym* 2010;**80**:687–694.
  59. Frank S, et al. *Nature* 1993;**363**:334–336.
  60. Nettles DL, et al. *Tissue Engineering* 2002;**8**:1009–1016.
  61. Aly AS. *Angew Macromol Chem* 1998;**259**:13–18.
  62. Mi FL, et al. *Carb Polym* 2000;**41**:389–396.
  63. Mao JS, et al. *Biomaterials* 2003;**24**:1067–1074.
  64. Peter M, et al. *Chem Eng J* 2010;**158**:353–361.

## Bi-layered absorbable membrane for Guided Tissue Regeneration

---

### Abstract

Periodontitis is an infectious disease that causes destruction of the tooth-attachment apparatus. When left untreated, periodontitis can result in progressive attachment loss that may eventually lead to tooth loss. Periodontal treatment can arrest further disease progression and promote the periodontal tissue to be reconstructed in some extent. Guided tissue/bone regeneration strategies (GTR/GBR) represent the most well-documented regenerative procedures for obtaining periodontal regeneration in periodontal loss. GTR/GBR membranes can be considered an interface-implant between gingival connective tissue/epithelium and alveolar bone tissue. Thus, developing a membrane with differentiated-structure, i.e. with compositional and structural properties that meet the functional requirements of the local tissue interface, could represent a challenge. In this chapter, a novel multicomponent membrane has been developed by the assembly of a compact layer, based on poly(DL-lactide-co- $\epsilon$ -caprolactone)/poly(lactic-co-glycolic acid) (PLCL/PLGA) 25/75 (wt/wt) blend, and a porous layer, based on chitosan/gelatin/ $\beta$ -tricalcium phosphate network cross-linked with genipin and dibasic sodium phosphate. The assembly process was based on the insertion of an intermediate adhesive layer composed by a polyvinylpyrrolidone/polyethylene glycol (PVP/PEG) 70/30 (wt/wt) blend, which was selected based on different analysis (namely, water contact angle measurements, thermogravimetric analysis, differential scanning calorimetry, and lap shear strength test). Preliminary characterizations were then carried out on the bi-layered membrane. Morphological analysis did not show changes in compact and porous layer structure due to PVP/PEG 70/30 insertion. The final device was characterized by an elastic modulus of about 61 MPa in dry

condition that markedly decrease in wet state (about 5 MPa). Finally, qualitative analysis of membrane manageability revealed its ability to adapt to mandible conformation after immersion in physiological solution. Despite the need for additional tests, it was possible to state the usability of the membrane in GTR/GBR applications.

## 7.1 Introduction

Periodontal apparatus is the complex multi-tissue system, anchoring the teeth in the maxillar/mandibular bone. It includes dental root cementum, periodontal ligament (PDL), dento-gingival junction and alveolar bone. Periodontitis is the inflammatory disease of this system that can lead to its destruction, which may eventually result in tooth loss. Periodontitis is a very aggressive pathology and represents one of the major global health problem [1].

During the past few decades, several therapeutic approaches have been developed. Among them, two surgical regenerative approaches, namely guided tissue/bone regeneration (GTR/GBR), have been increasingly used for the repair and regeneration of both the structure and function of damaged periodontal tissues. In both techniques, a membrane is used as a physical barrier to create an excluded space around the defect by preventing the invasion of the fibrous connective and epithelial tissues into the defect space, thus allowing the missing periodontal tissues to regenerate [2-4]. Thus, GTR/GBR membranes for periodontal regeneration can be considered an interface-implant, having interfaces with gingival connective tissue/epithelium and PDL/alveolar bone tissue. An interface-implant should possess biomimetic composition and structure respect to the different interfaces. In the specific case, membranes should promote the regeneration of periodontium by enhancing bone growth while preventing the gingival tissue down-growth [5].

In this chapter, a novel functionally bi-layered membrane with a spatially designed structure was fabricated via assembly of the previously developed compact and porous layers. The rationale of a periodontal membrane with a bi-layered structure relies on the idea that the properties of the different layers should be optimized to design a membrane with compositional and structural properties as well as suitable dimensional properties and time-dependent mechanical integrity to allow periodontal regeneration.

The bi-layered absorbable membrane developed in this chapter was composed by a compact synthetic film, based on poly(DL-lactide-co- $\epsilon$ -caprolactone)/poly(lactic-co-glycolic acid) (PLCL/PLGA) 25/75 (wt/wt) blend, and a porous membrane, based on chitosan/gelatin network enriched with  $\beta$ -tricalcium phosphate and cross-linked with genipin and dibasic sodium phosphate (CH/G/TCP+GP-DSP).

For the assembly of the two layers, different techniques could be used. One approach could be based on a thermal treatment applied to the compact membrane at a temperature higher than the glass transition temperatures of PLCL/PLGA 25/75 blend films (T<sub>gs</sub> in the range 30-50 °C). CH/G/TCP+GP-DSP membrane could be placed (and pressed) on the compact film, previously

softened by the thermal treatment, in order to link the layers after cooling. In alternative, the bi-layered membrane could be fabricated by freeze-drying the porous layer directly on the compact film. As described by Franco et al. [6], PLCL/PLGA 25/75 film could be prepared in a petri dish; then, a suitable amount of CH/G/TCP+GP-DSP solution, at a temperature of 50 °C, could be poured on the Petri dish (coating the compact film base). The resulting samples could be then frozen and lyophilised to obtain the final device. However, both temperature and pressure employed in these process may change the structural-mechanical and morphological properties of the layers. Therefore, the use of an intermediate adhesive layer could represent an alternative, preserving the properties of the membrane layers.

Different adhesive biomaterials could be employed, such as fibrin glues, cyanoacrylate or gelatin. For example, Shi et al. [7] developed a bi-layered dermal equivalent by combining a collagen/chitosan porous scaffold with a silicone membrane through a gelatin intermediate layer. In detail, at 50 °C, the 10% (wt/v) gelatin solution was smoothly spread on the silicone membrane (10  $\mu\text{l}/\text{cm}^2$ ). After cooling to room temperature, at which the gelatin adhesive was transferred to a semi-gelation state, the scaffold was put onto the silicone membrane surface slightly to obtain the bi-layered device. However, the use of gelatin involves again the use of temperatures above compact film  $T_g$ , whereas cyanoacrylate degradation products may be cytotoxic and fibrin glue may results in infection transmission.

In this chapter, blends between polyvinylpyrrolidone (PVP) and polyethylene glycol (PEG) (compositions 100/0, 80/20, 70/30, 60/40 wt/wt) were investigated with the aim to select an optimal blend composition in terms of compatibility degree between the phases and adhesive properties. PVP/PEG blends are examples of pressure-sensitive adhesives (PSAs), which are commonly used in a variety of applications because of their ease of application, low toxicity, and versatility [8]. In particular, a resorbable adhesive based on PVP/PEG blend is currently employed in a self-adhering hernia mesh (Cousin Biotech® Adhesix™).

To function properly, PSAs must combine a liquid-like character to form good molecular contact under a light applied pressure and a solid-like character to resist an applied stress once the bond has been formed. This combination of properties usually requires a high molecular weight polymer, forming the backbone of the adhesive, and a low molecular weight fraction, favoring flow and deformation. The miscibility between the two components in PVP/PEG blends is provided by hydrogen bonding between PEG terminal hydroxyl groups and carbonyl groups of PVP monomeric units [9, 10], and it has been studied in detail in a series of articles [11-13]. PVP and PEG are fully miscible over the entire composition range [14], but they

display interesting PSA properties only in a fairly narrow window of compositions (between 30 and 40 wt% PEG) [15].

We characterized PVP/PEG blends physicochemical and adhesive properties using water contact angle measurements, infrared spectroscopy, thermogravimetric analysis (TGA), differential scanning calorimetry (DSC) and lap shear strength test. The selected composition was then employed for the development of a bi-layered absorbable membrane, which was preliminarily characterized via scanning electron microscopy (SEM) and tensile test.

## 7.2 Materials and methods

### 7.2.1 Materials

PLGA (LA:GA = 75:25 mol:mol;  $M_w$ : 66000-107000 Da), PLCL (nominal 86 mol% of DL,lactic acid,  $M_w$ : 28000 Da), Type A gelatin from porcine skin ( $M_w$ : 50-100 kDa), chitosan highly viscous derived from crab shell with 75-85% deacetylation degree ( $M_w$ : 190-310 kDa),  $\beta$ -tri-calcium phosphate ( $M_w = 310.18$  Da), and dibasic sodium phosphate ( $M_w = 141.96$  Da) were supplied from Sigma-Aldrich (Milano, Italy). Genipin was purchased from Challenge Bioproducts (Taiwan). Polyvinylpyrrolidone (PVP;  $M_w$ :  $10^6$  Da) and polyethylene glycol (PEG;  $M_w$ : 400 Da) were supplied by BASF (Italy). All solvents were of analytical grade and used without further purification.

#### 7.2.1.1 Polyvinylpyrrolidone

Polyvinylpyrrolidone (Fig. 7.1), also called polyvidone, is a white, hygroscopic powder with a weak characteristic odor. In contrast to most polymers, it is readily soluble in water and a large number of organic solvents, such as alcohols, amines, acids, chlorinated hydrocarbons, amides and lactams. On the other hand, the polymer is insoluble in the common esters, ethers, hydrocarbons and ketones.

PVP is synthesized by free-radical polymerization of *N*-vinylpyrrolidone in water or alcohols with a suitable initiator. By selecting suitable polymerization conditions, a wide range of molecular weights can be obtained, extending from low values of a few thousand Daltons to approximately 2.2 million Daltons [16].

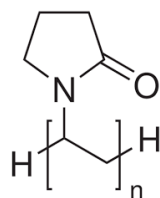


**Fig. 7.1** Polyvinylpyrrolidone (PVP) chemical structure.

PVP is markedly hygroscopic and able to absorb up to 40% of its weight in atmospheric water. This property combined with outstanding film formation, initial tack and adhesion to different materials, high capacity for complex formation, good stabilizing and solubilizing capacity, insensitivity to pH changes, ready radiation-induced cross-linkability as well as good biological compatibility have made PVP one of the most frequently used specialty polymers [1].

The U.S. Food and Drug Administration has approved this chemical for many uses and it is generally considered safe. In biomedical field, PVP is used as a binder in many pharmaceutical tablets; it simply passes through the body when taken orally [17]. PVP added to iodine forms a complex, called povidone-iodine, that possesses disinfectant properties. This complex is used in various products like solutions, liquid soaps and surgical scrubs. It is known under the trade names Betadine and Pyodine among a plethora of others.

#### 7.2.1.2 Polyethylene glycol

Polyethylene glycol (Fig. 7.2) is a polyether compound with many applications from industrial manufacturing to medicine. PEG is also known as polyethylene oxide (PEO) or polyoxyethylene (POE), depending on its molecular weight. PEG, PEO, or POE refers to an oligomer or polymer of ethylene oxide. PEG and PEO are liquids or low-melting solids, depending on their molecular weights. PEG is prepared by polymerization of ethylene oxide and is commercially available over a wide range of molecular weights, from 300 g/mol to 10000000 g/mol [18].

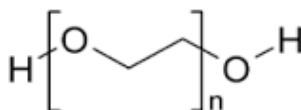


**Fig. 7.2** Polyethylene glycol (PEG) chemical structure.

PEG has several chemical properties that make it especially useful in various biological, chemical and pharmaceutical settings. It is non-toxic and non-immunogenic, thus it can be added to media and attached to surfaces and conjugated to molecules without interfering with

cellular functions or target immunogenicities. It is hydrophilic (aqueous-soluble) and its attachment to proteins and other biomolecules decreases aggregation and increases solubility. Finally, it has high flexibility, thus it provides for surface treatment or bioconjugation without steric hindrance [3].

## 7.2.2 Sample preparation

### 7.2.2.1 Preparation of blend PVP/PEG

PVP/PEG 100/0; 80/20; 70/30; 60/40 (wt/wt) blends were prepared by solution mixing method. The polymers were separately dissolved in MilliQ water at 4% (wt/v) concentration and each polymer/solvent mixture was stirred using a magnetic stirrer for 1 h, till complete dissolution of polymers. Proper volumes of the polymeric solutions were mixed to prepare blends and stirred for 2 h. Films were obtained by casting a volume of each solution (15 ml) on Teflon Petri dishes with 50 mm diameter. The solvent was removed via evaporation under a vented hood at room temperature for a period of 7 days and in vacuum oven at 65 °C for other 6 h. The blends were coded as follows: PVP/PEG 100/0; 80/20; 70/30; 60/40. PEG films could not be prepared as the polymer was in molten state at room temperature.

### 7.2.2.2 Preparation of bi-layered absorbable membrane

Compact (PLCL/PLGA 25/75) and porous (CH/G/TCP+GP-DSP) layers were combined with optimized PVP/PEG blend composition, namely 70/30 (wt/wt), as schematically reported in Fig. 7.3. Each layer was produced as reported in Chapter 4, 5 and 6. Then, a 20% (wt/v) PVP/PEG 70/30 blend solution was smoothly spread on the PLCL/PLGA 25/75 film (20  $\mu\text{l}/\text{cm}^2$ ). After 30 min, CH/G/TCP+GP-DSP membrane was put onto the compact film to obtain the bi-layered absorbable device and left under a vented hood at room temperature for 1 day.

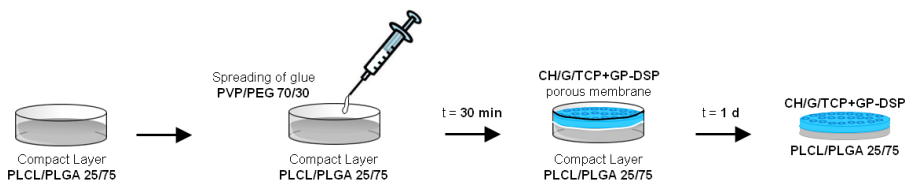


Fig. 7.3 Schematic representation of the assembly process for the bi-layered absorbable membrane.

### 7.2.3 Sample characterization

#### 7.2.3.1 Water contact angle measurements

The static contact angles of PVP/PEG blend films were determined through a sessile drop method, using a 5  $\mu\text{l}$  double distilled water droplet. Static contact angles of films were measured in air at room temperature in a CAM 200 KSV Instrument equipped with an Attention Theta software for data acquisition.

#### 7.2.3.2 Infrared analysis in ATR modality

The analysis was carried out in a Perkin Elmer Frontier Optical Spectrometer fitted with an attenuated total reflection sampler (FTIR-ATR). Spectra of PVP/PEG blend films were obtained over the 400-4000  $\text{cm}^{-1}$  range at room temperature, using diamond crystal.

#### 7.2.3.3 Thermogravimetric analysis

The thermal stability and degradation profile of PVP/PEG blend films was evaluated through thermogravimetric (TGA) analysis using a TA INSTRUMENT Q500 system under a nitrogen atmosphere. The experiments were performed with a 10-15 mg sample in aluminum pans at 10  $^{\circ}\text{C}/\text{min}$  heating rate in the 35-700  $^{\circ}\text{C}$  temperature range. Results were then analysed through a TA Universal Analysis 2000 software.

#### 7.2.3.4 Differential scanning calorimetry

The thermal behavior of cast films based on PVP/PEG blends was investigated by differential scanning calorimetry (DSC) using a TA INSTRUMENT DSC Q20. Each film specimens (5-10 mg) were precisely weighed in aluminum pans and non-isothermal scans were performed between  $-65$   $^{\circ}\text{C}$  and 100  $^{\circ}\text{C}$  for pristine PEG and between  $-65$   $^{\circ}\text{C}$  and 220  $^{\circ}\text{C}$  for the other materials (first heating; cooling; second heating) at a heating rate of 10  $^{\circ}\text{C}/\text{min}$  under nitrogen atmosphere. The characteristic temperatures of PVP and PEG blend components were measured from the DSC heating scan through a TA Universal Analysis 2000 software.

#### 7.2.3.5 Lap shear strength test

The test was performed according to ASTM D3163 which is commonly performed to measure the shear strength of adhesives that bond plastic substrates. It uses a single lap joint (lap shear) specimen to determine the shear strength of adhesives.

Two plates were bonded together with adhesive as shown in Fig. 7.4. The test specimens were placed in the grips of MT<sup>®</sup>QTestTM/10 instrument and pulled at 1.3 mm/min until rupture occurs. The grips used to secure the ends of the assembly must align so that the applied force is applied through the centerline of the specimen.

Two different adhesion conditions have been investigated:

1. the plates were bonded as soon as the adhesive was spread on the surface, with or without the application of a pressure for 1 day;
2. the plates were bonded one day after the spreading of the adhesive, with or without the application of a pressure for 1 day.

Pressure was applied by pouring a becker with 25 ml of water on the superimposed plates.

The maximum force and maximum shear stress (divide the maximum force by the shear area and report in units of kilogram/square centimeter) were measured. The type of failure was also determined; it can be either adhesive (the adhesive separates from one of the substrates) or cohesive (the adhesive ruptures within itself).

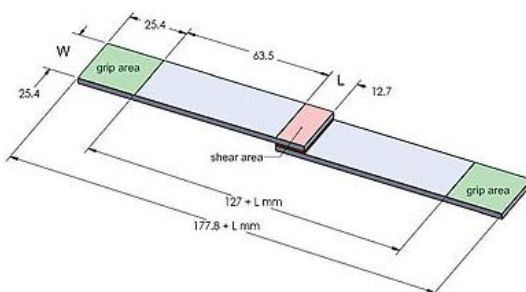


**Fig. 7.4** Adhesive lap joint shear strength test specimen.

#### 7.2.3.6 Morphological analysis

Scanning electron microscopy (SEM LEO – 1430, Zeiss, Munich, Germany) was performed on bi-layered membrane sections (obtained by fracturing in liquid nitrogen). Samples were sputter coated with Au before SEM analysis.

#### 7.2.3.7 Tensile test

Tensile mechanical properties of bi-layered membranes were analyzed in dry and wet conditions. Tensile tests were performed on rectangular specimens (10 x 30 mm<sup>2</sup>) using MT<sup>®</sup>QTestTM/10 instrument. The traction force was applied along the length of the samples at a constant cross-head displacement rate of 2 mm/min. Young's modulus (E) and maximum tensile strength and strain ( $\sigma_{\max}$  and  $\epsilon_{\max}$ , respectively) were measured from the stress-strain

curves.  $E$  was calculated from the slope of the initial linear portion of the stress-strain curve, and  $\sigma_{\max}$  and  $\varepsilon_{\max}$  were calculated as the maximum stress a material can withstand before failing and the total elongation just before fracture, respectively [19].

#### 7.2.3.8 *Bi-layered membrane manageability*

Mandible anatomical model with periodontal defects were employed to evaluate membrane manageability. The device was immersed in PBS for 5 min, then it was properly cut to fit the defect site and finally inserted. Digital pictures were taken.

#### 7.2.4 Statistical analysis

All data are expressed as means  $\pm$  standard deviation. Differences between means were analyzed by one-way ANOVA followed by a Tukey's post hoc test. For lap shear strength test, statistical analysis was performed using two-way ANOVA with the Bonferroni's post test. All statistical analysis were performed with Prism, Graph Pad Software.

### 7.3 Results and discussion

#### 7.3.1 Characterization of PVP/PEG blend

The surface wettability of PVP/PEG films (Fig. 7.5) changed based on blend composition. The static contact angle significantly decreased with the addition of PEG content, reaching a value of  $(44.4 \pm 0.9)^\circ$  for PVP/PEG 60/40.

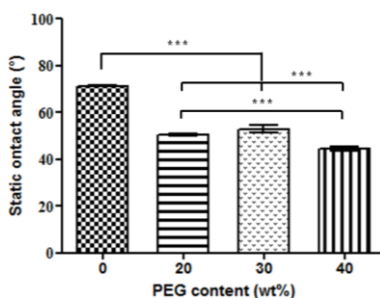
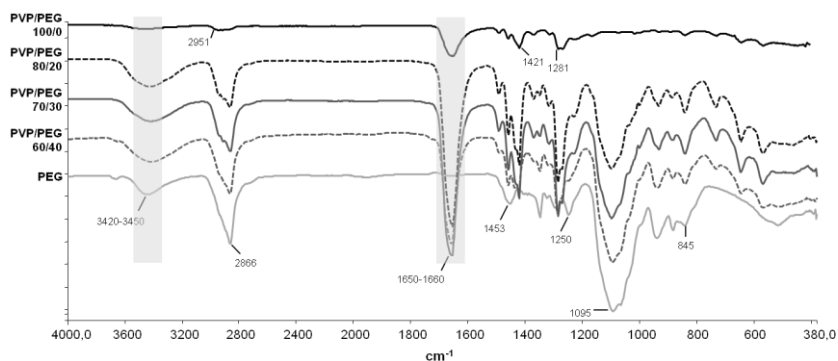


Fig. 7.5 Static contact angle measurements of PVP/PEG cast blend films as a function of PEG content.

Changes in chemical composition of PVP/PEG blends were evaluated through FTIR-ATR analysis. In fact, the results obtained from FTIR-ATR spectroscopy gave a unique identification of the functional interacting groups [20]. Fig. 7.6 compares the FTIR-ATR spectra of cast blend films and pure polymers.



**Fig. 7.6** FTIR-ATR spectra of PVP/PEG 100/0, 80/20, 70/30, 60/40 and PEG.

PVP/PEG 100/0 spectra showed characteristic bands at  $1652\text{ cm}^{-1}$  and  $1281\text{ cm}^{-1}$  related, respectively, to the stretching vibrations of C=O and C-N bonds. The peak at  $1421\text{ cm}^{-1}$  arose from the stretching vibration of  $-\text{CH}_2$  group while the peak at  $2951\text{ cm}^{-1}$  was attributed to the stretching vibration of C-H bond. Finally, the wide band at  $3445\text{ cm}^{-1}$  could be due to the presence of water into the polymer [21, 22]. The characteristic adsorption bands of PEG were associated to the stretching vibration of the  $-\text{OH}$  functional group ( $3449\text{ cm}^{-1}$ ) and to the symmetric stretching vibration of C-O bond ( $1095\text{ cm}^{-1}$ ). Other peaks related to the stretching and bending vibrations of  $-\text{CH}_2$  group at  $2866\text{ cm}^{-1}$  and  $844.7\text{ cm}^{-1}$ , respectively. Finally, the adsorption bands in the region  $1249\text{--}1295\text{ cm}^{-1}$  arose from the asymmetric stretching vibration of C-O-C group [23].

The adsorption bands of PVP and PEG described above could be observed also in the spectra of blend samples; the intensity of these bands changed based on blend composition.

At room temperature, PVP is easily soluble in liquid PEGs with a low molecular weight (100–600 g/mol). PVP solubility is related to the formation of hydrogen bonds between hydroxyl terminal groups of PEG short chains (proton donators) and the complementary carbonyl groups of long PVP macromolecules (electron donators). The simultaneous formation of two hydrogen bonds through the two  $-\text{OH}$  terminal groups of PEG makes this polymer a reversible cross-linker for PVP [5].

The hydrogen bond formation is generally associated to a shift of wavenumbers in FTIR-ATR spectra. As it is possible to observe in Table 7.1, the wavenumbers of  $-\text{OH}$  and C=O groups slightly changed in blend spectra compared to the values observed for the pure polymers. This was probably caused by the formation of hydrogen bonds between PVP and PEG.

**Table 7.1** Wavenumbers of -OH and C=O groups obtained from the FTIR-ATR spectra of PVP/PEG 100/0, 80/20, 70/30, 60/40 and PEG.

Composition	-OH (cm <sup>-1</sup> )	C=O (cm <sup>-1</sup> )
PVP/PEG 100/0	-	1652.0
PVP/PEG 80/20	3428.2	1655.2
PVP/PEG 70/30	3419.9	1657.8
PVP/PEG 60/40	3421.8	1658.7
PEG	3445.4	-

Thermal properties of PVP/PEG blend films were evaluated through TGA and DSC analyses. Fig. 7.7 compares the mass loss derivative curves (DGA) of cast blend films. PVP/PEG blends were characterized by a two step thermal degradation, one for each blend component. The first degradation step could be attributed to PEG pyrolysis while the second one could be associated to PVP degradation. The mass loss during the two steps changed based on blend composition (Table 7.2): PVP/PEG 60/40 samples showed the maximum mass loss value in the first step (about 33%) while in the second step, the maximum value was reached by PVP/PEG 80/20 sample (around 68%).

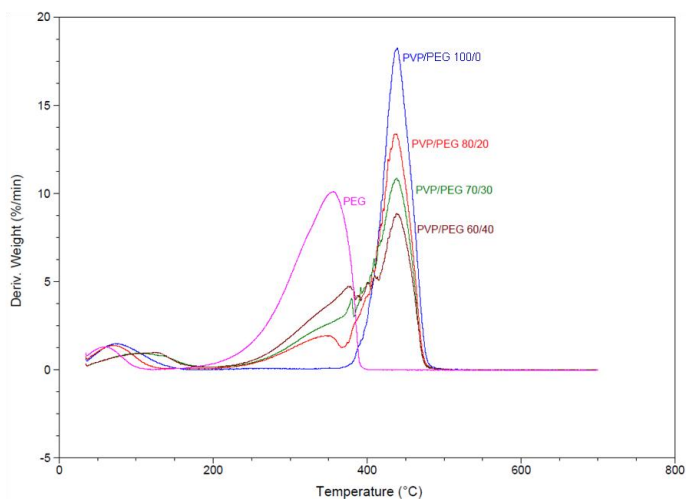


**Fig. 7.7** DGA curves of PVP/PEG blend films and PEG.

**Table 7.2** Characteristic temperatures obtained from DGA curves analysis for PVP/PEG blend films and PEG.  $T_i$  and  $T_f$  represent, respectively, the temperature of beginning and end of the thermal degradation process while  $T_{degr}$  represents the degradation temperature.

Composition	1 <sup>st</sup> STEP				2 <sup>nd</sup> STEP			
	$T_i$ (°C)	$T_f$ (°C)	Weight loss (%)	$T_{degr}$ (°C)	$T_i$ (°C)	$T_f$ (°C)	Weight loss (%)	$T_{degr}$ (°C)
PVP/PEG 100/0	-	-	-	-	376.2	481.1	81.4	439.6
PVP/PEG 80/20	221.6	372.1	15.8	345.7	378.1	479.3	67.7	438.7
PVP/PEG 70/30	223.9	387.7	26.7	331.8	393.3	479.9	55.6	438.3
PVP/PEG 60/40	220.1	378.9	32.9	375.2	385.7	474.6	49.5	440.7
PEG	187.6	390.6	88.6	356.3	-	-	-	-

Fig. 7.8 collects DSC first heating thermograms for PVP/PEG samples. The heating thermogram of PVP/PEG 100/0 revealed a broad symmetric endotherm of water thermodesorption at  $(100.2 \pm 8.4)$  °C related to water evaporation. In fact, PVP is a highly hygroscopic polymer able to absorb high quantity of water from the surrounding environment, absorbed in vapour state or residual from material processing [13]. Thermograms of PVP/PEG blends showed the same endothermic peak of PVP/PEG 100/0 sample, with similar temperature and with progressively decreasing intensity as a function of PEG content.

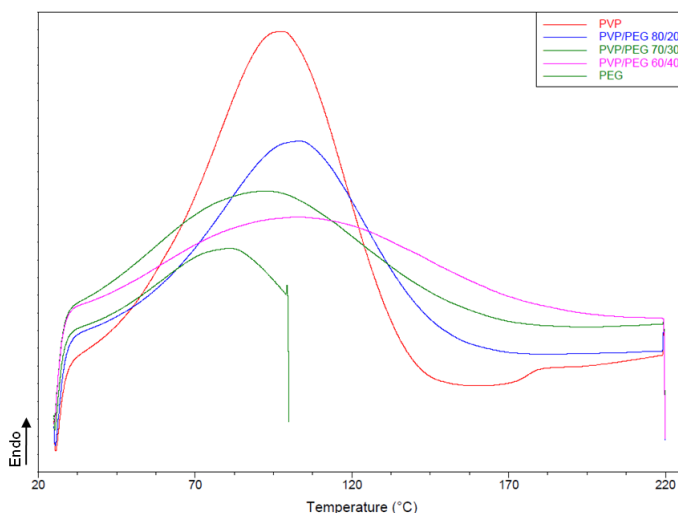


**Fig. 7.8** DSC first heating thermograms for PVP/PEG blend films and PEG.

As reported in literature, the DSC technique provides an alternative tool to determine the amount of water absorbed by hydrophilic polymers [24]. To this purpose, the heat of water thermodesorption must match that of bulk water evaporation. Polymer hydration may then be measured through the enthalpy change associated with water desorption, dividing the obtained dehydration enthalpy ( $\Delta H_d$ ) by the reference value of water vaporization ( $\Delta H = 2255$  J/g) [25].

Table 7.3 collects the hydration values for PVP/PEG blend samples and PEG, obtained from DSC first heating thermograms. The amount of water absorbed by PVP/PEG 100/0 films was about 10 times higher than the quantity absorbed by PEG ( $10.2 \pm 1.2$  % and  $0.6 \pm 0.1$  %, respectively). PVP–PEG hydrogen bonding resulted in the formation of a hydrogel containing 2–5% of water at room temperature.

**Table 7.3** Dehydration enthalpies ( $\Delta H_d$ ) and hydration values measured by DSC analysis (first heating scan at 10 °C/min).

<b>Composition</b>	<b><math>\Delta H_d</math> (J/g)</b>	<b>Polymer hydration (%)<sup>1</sup></b>
PVP/PEG 100/0	$230.5 \pm 28.2$	$10.2 \pm 1.2$
PVP/PEG 80/20	$112.1 \pm 27.3$	$4.9 \pm 1.2$
PVP/PEG 70/30	$64.9 \pm 1.3$	$2.9 \pm 0.6$
PVP/PEG 60/40	$46.9 \pm 15.3$	$2.0 \pm 0.7$
PEG	$12.9 \pm 2.0$	$0.6 \pm 0.1$

$$^1 \text{ Polymer hydration (\%)} = \frac{\Delta H_d}{\Delta H} \cdot 100$$

Results obtained from the analysis of the first heating thermograms showed that (i) PVP is an amorphous polymer with a high affinity for water while PEG is a comparatively less hygroscopic polymer, (ii) both polymers are easily soluble in water but short-chain liquid PEG can be also a good solvent for PVP. Consequently, the PVP–PEG hydrogels may be treated either as ternary compatible blends or PVP solutions in the PEG–water cosolvent [26].

DSC second heating traces for PVP/PEG blend and PEG are shown in Fig. 7.9. The heating DSC trace of PVP/PEG 100/0 showed a heat capacity jump at the glass transition temperature ( $T_g = (177.5 \pm 1.6)$  °C) while it was not possible to measure PEG  $T_g$  because it was localized near the low temperature limit detected by the instrument ( $-65$  °C). Thus, the value reported in literature was considered ( $-70$  °C) [27]. The DSC heating trace of unblended PEG displayed a melting endotherm at  $(7.7 \pm 0.1)$  °C.

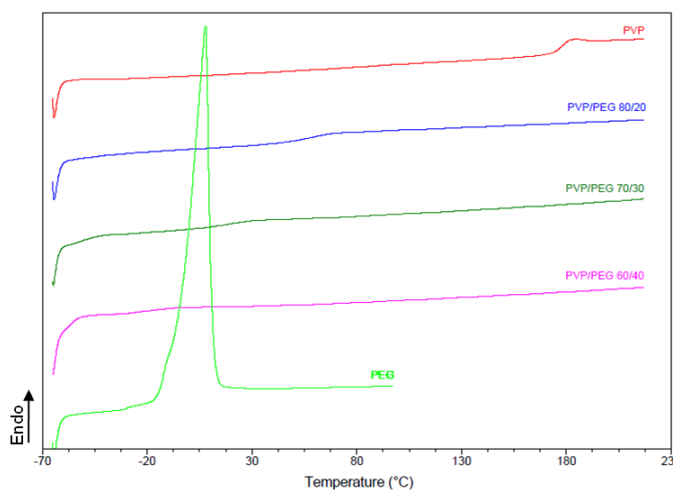


**Fig. 7.9** DSC second heating thermograms for PVP/PEG blend films and PEG.

Adding PEG to the glassy PVP resulted in the appearance of two  $T_g$ s. Their values were close each other and they were called  $T_g^{\text{UPPER}}$  and  $T_g^{\text{LOWER}}$ . As reported in Chapter 4 – Paragraph 4.2, experimental evidence of polymer miscibility is associated with a single glass transition temperature, which is intermediate between the two  $T_g$ s of the blend components [28]. On the contrary, blends of immiscible polymers that segregate into distinct phases exhibit two separate glass transitions with a similar value to that of the unblended components. In the intermediate case of partial blend miscibility, the  $T_g$ s of individual components are closer as compared to the values of pure polymers [29].

The PVP and PEG glass transition temperatures differed by a value of  $(247.5 \pm 1.6)^\circ\text{C}$ . The temperature difference between the two  $T_g$ s in blend samples markedly decreased with increasing PEG content, reaching a value of about  $50^\circ\text{C}$  for blends containing 40 %wt of PEG (Table 7.4). This result was a consequence of a decrease of both  $T_g$ s with increasing PEG content.

**Table 7.4** Glass Transition temperatures measured by DSC analysis (second heating scan at  $10^\circ\text{C}/\text{min}$ ).

Composition	$T_g^{\text{UPPER}}$ ( $^\circ\text{C}$ )	$T_g^{\text{LOWER}}$ ( $^\circ\text{C}$ )	$\Delta T_g$ ( $^\circ\text{C}$ ) <sup>1</sup>
PVP/PEG 100/0	$177.5 \pm 1.6$	-	-
PVP/PEG 80/20	$62.1 \pm 3.4$	$-39.8 \pm 1.2$	$132.1 \pm 3.4$
PVP/PEG 70/30	$15.2 \pm 3.4$	$-50.9 \pm 1.3$	$85.2 \pm 3.5$
PVP/PEG 60/40	$-19.3 \pm 3.2$	$-53.9 \pm 2.8$	$50.6 \pm 3.2$
PEG	-	-70	-

<sup>1</sup>  $\Delta T_g = T_g^{\text{PLGA}} - T_g^{\text{PLCL}}$

The two  $T_g$ s in PVP/PEG blend thermograms are due to:

1. PVP–PEG hydrogen bonds, leading to the appearance of  $T_g^{\text{LOWER}}$ ,
2. the presence of a non-balanced phase composed by plasticised PVP with small quantities of PEG and water, which caused the appearance of  $T_g^{\text{UPPER}}$  [10].

Both  $T_g$ s were composition dependent. The plasticizing effect of PEG affected the  $T_g^{\text{UPPER}}$  value which strongly decreased with the addition of PEG. The composition dependence of the  $T_g^{\text{UPPER}}$  was fitted through a simple weight-average rule of mixing, the Fox equation, which describes the theoretic behavior of  $T_g$  in polymeric blends with specific interactions. The equation applied is reported below:

$$\frac{1}{T_g} = \frac{w_{PVP}}{T_g^{PVP}} + \frac{w_{H_2O}}{T_g^{H_2O}} + \frac{w_{PL}}{T_g^{PL}}$$

where  $T_g$  refers to the glass transition temperatures of blend and  $T_g^x$  and  $w_x$  refers, respectively, to the  $T_g$  and the weight fractions of PVP, water and plasticizing agent ( $PL = \text{PEG}$ ).

Fig. 7.10 plots both  $T_g$ s evaluated by the DSC technique and theoretic  $T_g$ s evaluated by Fox equation, against the composition of PVP/PEG blends. The theoretical curves were obtained setting  $w_{H_2O}$  equal to 0 for the upper curve and  $w_{H_2O} = 0.05$  for the lower one (selected from the PVP/PEG hydration results described before). When PEG concentration was around 20-40 %wt, the  $T_g^{\text{UPPER}}$  dropped below the temperature of water evaporation and obeyed to some extent to the Fox rule for the blends of 5% hydration. On the contrary, as reported in literature [27], at low PEG content in blends (0–10 wt%), the  $T_g$  was preceded by a water evaporation endotherm and the composition dependence of the  $T_g^{\text{UPPER}}$  followed the pattern predicted by the Fox rule of mixing for dry PVP/PEG blends.

The success of the Fox equation in describing the composition dependence of the  $T_g^{\text{UPPER}}$ -phase suggested the miscibility of PVP with PEG. Moreover, the negative deviation from Fox equation, observed for plasticizing agents with more than one hydroxyl group, underlined the formation of specific interactions between PVP and PEG.

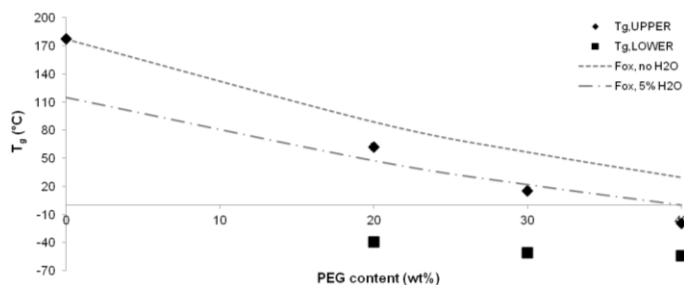


**Fig. 7.10** Glass transition temperatures of PVP/PEG blends against composition and predictions by Fox equation.

The value of  $T_g^{\text{LOWER}}$  in PVP/PEG blends matched closely that found in literature for unblended PEG. Nevertheless, the  $T_g^{\text{LOWER}}$  could not be attributed to the occurrence of unblended PEG phase within the blends due to following reasons.

1. If the  $T_g^{\text{LOWER}}$  belonged to the unblended PEG phase, the composition dependence of the upper  $T_g$  would display positive deviations from the values predicted by the Fox equation.
2. PEG is a crystalline polymer, however its blends with amorphous PVP developed no crystallinity. Apparently PEG was strongly involved into formation of specific interactions (hydrogen bonding) with PVP and did not form a separate crystalline phase.

In conclusion, the  $T_g^{\text{LOWER}}$  related unambiguously to some amorphous PVP-PEG interaction product that nucleated and grew within the upper  $T_g$ -phase. The  $T_g^{\text{UPPER}}$  corresponded to a homogeneous PVP/PEG mixture, or PVP solution in PEG, where in average each PEG molecule formed only a single H-bond with the PVP carbonyl, leaving the second OH group, at the opposite chain end, free. The phase with  $T_g^{\text{LOWER}}$  was due to the PVP-PEG complex formation, where the PVP units were cross-linked by H-bonding through both terminal groups of PEG short chains. The phase with lower  $T_g$  component was not spatially separated from the phase with higher  $T_g$  value, representing a homogeneous mixture on a molecular scale.

It is well known from the literature that polymer cross-linking usually causes an increase in  $T_g$  [30]. Nevertheless, in PVP/PEG systems the PVP cross-linking through PEG chains resulted in appreciable  $T_g$  reduction compared with uncross-linked PVP in the upper  $T_g$ -phase at equivalent PEG concentrations. Apparent anomalous behavior of the PVP/PEG blends was due to the appreciable length and the flexibility of PEG chains, which represented both a H-bonded cross-linker and spacer. Creating a space between longer PVP macromolecules, the PEG chains increased the free volume and, eventually, the molecular mobility of PVP chain segments between close H-bond network junctions [31]. Cross-linking PVP units by H-bonding to PEG terminal hydroxyls, the PEG chains behaved also as a cohesive toughness enhancer [32]. As

PEG short chains were responsible for cohesive strength among PVP molecules and also enhanced the free volume, a pressure sensitive adhesive formed.

The results discussed above led to the selection of blends with PVP/PEG 70/30 and PVP/PEG 60/40 composition as suitable adhesives for the bi-layered device. Both blends were further characterized through Lap shear strength test in order to evaluate their adhesive strength and results are reported in Fig. 7.11. The maximum shear stress ( $\sigma_{\max}$ ) was calculated from the stress-strain curves, dividing the maximum force by the shear area.

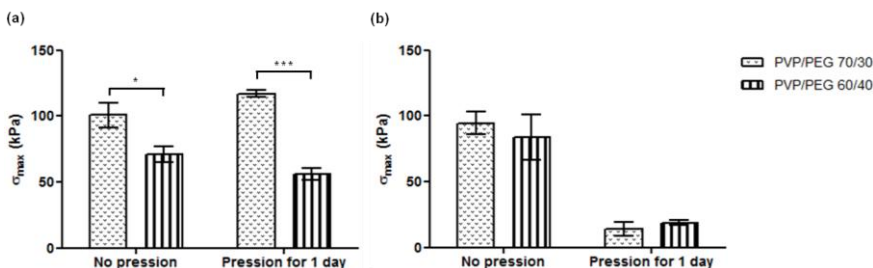


**Fig. 7.11** Maximum shear stress ( $\sigma_{\max}$ ) for PVP/PEG 70/30 and PVP/PEG 60/40 adhesives (a) immediately bonded and (b) bonded after 1 day.

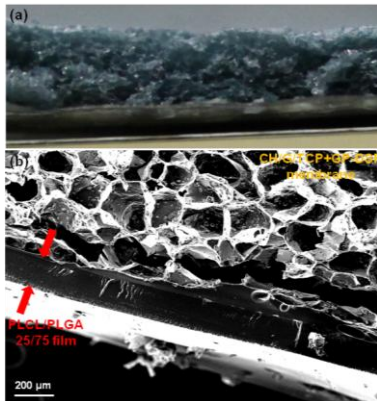
Statistically significant differences could be observed between PVP/PEG 70/30 and PVP/PEG 60/40 adhesives when the plates were immediately bonded (Fig. 7.11a). In detail,  $\sigma_{\max}$  decreased with increasing PEG content. For both blends, no appreciable changes in adhesive ability derived from the application of a pressure.

Fig. 7.11b reports results adhesive effectiveness for samples bonded one day after the spreading of the adhesive on the sample surface. No differences were detected between PVP/PEG blends with different composition, bonded by the same method (no pression, pression for 1 day). On the contrary, a marked decrease in maximum shear stress appeared when pressure was applied. The adhesive selected for the assembly of the bi-layered membrane was PVP/PEG 70/30 due to its superior maximum shear stress. Moreover, we decided to link the two layers as soon as the adhesive was spread over the compact layer and without the application of a pression.

### 7.3.2 Preliminary characterization of absorbable bi-layered membrane

The macroscopic shape and the SEM photomicrographs of bi-layered device are displayed in Fig. 7.12. The device can be obtained after CH/G/TCP+GP-DSP porous membrane was combined with a PLCL/PLGA 25/75 compact film. The bi-layer structure was clearly identified by the SEM cross-section image (Fig. 7.12b). Moreover, photomicrographs showed that the assembly process did not alter the morphology of compact and porous layers. In particular, the

use of PVP/PEG 70/30 glue did not change CH/G/TCP+GP-DSP membrane porosity, preserving the initial porous and interconnected structure.



**Fig. 7.12** (a) Macroscopic view of the section and (b) SEM images of the fractured section of bi-layered membrane.

Fig. 7.13 shows the stress-strain curves measured for the bi-layered membrane by tensile tests in dry and wet conditions. The curves could be divided in two distinct regions:

1. initial linear elastic region characterized by the mechanical behavior of both compact and porous layer;
2. region characterized by the mechanical properties of compact layer.

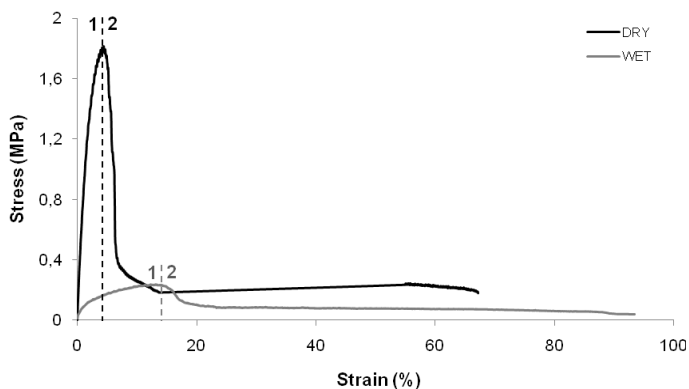


**Fig. 7.13** Tensile stress-strain curves for bi-layered membrane in dry and wet conditions (cross-head speed = 2 mm/min).

The values of  $E$ ,  $\sigma_{\max}$ , and  $\epsilon_{\max}$  calculated from the stress-strain curves of bi-layered membranes, both in wet and dry conditions, are collected in Table 7.5. Statistically significant differences could be observed between the elastic modulus, which decreased from about 61 MPa in dry condition to about 5 MPa in wet state. Similarly,  $\sigma_{\max}$  decreased from 1.7 MPa in

dry conditions to 0.2 MPa in wet conditions. On the contrary, no marked differences were detected for the maximum tensile strain.

**Table 7.5** Young’s elastic modulus (E), maximum tensile strength ( $\sigma_{max}$ ) and strain ( $\epsilon_{max}$ ) calculated from stress-strain curves.

Composition	DRY	WET
E (MPa)	61.2 ± 11.1	5.1 ± 0.8
$\sigma_{max}$ (MPa)	1.7 ± 0.6	0.2 ± 0.0
$\epsilon_{max}$ (%)	73.9 ± 27.3	81.4 ± 5.3

Finally, membrane manageability was qualitatively evaluated on a mandible anatomical model with simulated periodontal defect in alveolar bone (Fig. 7.14b). Before the insertion, membrane was immersed in PBS for 5 min in order to improve its flexibility (Fig. 7.14a) and properly cut to fit the defect site. Then, the bi-layered device was placed between gingival tissue and bone defect (Fig. 7.14 c and d). Through this experiment, it was possible to verify the ability of the membrane to adapt to the anatomical conformation of mandible. Finally, the device was covered with gum flaps that were fixed with sutures (Fig. 7.14 e and f). Due to the presence of an antimicrobial coating on the membrane side in contact with gingival tissue, it was not necessary to close with first intention gum flaps.

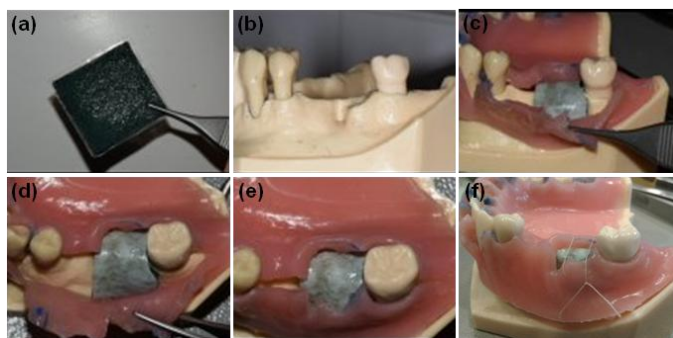


**Fig. 7.14** Manageability of the bi-layered absorbable membrane evaluated in mandible anatomical model with periodontal defect.

## 7.4 Conclusions

In this chapter, a process for bi-layered membrane preparation based on the assembly of previously prepared compact and porous layers was developed, and preliminary characterizations of the bi-layered absorbable membrane were carried out. The assembly

process was based on the insertion of an intermediate adhesive layer composed of a PVP/PEG blend.

Blending PVP and PEG through a solvent casting process generated a PAS system already employed in biomedical field. Results from physico-chemical characterizations showed an increase in surface hydrophilicity with increasing PEG content. The miscibility between the two components in PVP/PEG blends was verified through DSC analysis. In detail, the temperature difference between the  $T_g$ s of the blend components markedly decreased with increasing PEG content. The analysis of the behaviour of blend component  $T_g$ s suggested the formation of hydrogen bonds between PEG terminal hydroxyl groups and carbonyl groups of PVP repeating units.

The Lap shear strength test allowed the evaluation of PVP/PEG blend adhesive properties. Superior adhesiveness was found for PVP/PEG 70/30 blend that was thus selected for the assembly of the bi-layered device. The assembly process developed in this chapter did not change the morphology of both compact and porous layer and led to a device with good manageability. Further characterizations need to be carried out in order to evaluate membrane stability in physiological conditions and biocompatibility. However, the preliminary results obtained in this work are promising for a future use of the bi-layered membrane in GTR/GBR applications.

## References

---

1. Haffajee AD, et al. *Periodontol 2000* 1994;**5**:78-111.
2. Nyman S, et al. *J Periodontal Res* 1987;**22**:252-254.
3. Karring T. *J Int Acad Periodontol* 2000;**2**:101-109.
4. Villar CC, et al. *Dent Clin North Am* 2010;**54**:73-92.
5. Bottino MC, et al. *Acta Biomater* 2011;**7**:216-224.
6. Franco RA, et al. *J Mater Sci: Mater Med* 2011;**22**:2207-2218.
7. Shi Y, et al. *Polym Adv Technol* 2005;**16**:789-794.
8. Roos A, et al. *J Polym Sci Part B: Polym Phys* 2002;**40**:2395-2409.
9. Feldstein MM, et al. *Polym Sci Ser A* 1999;**41**:854-866.
10. Feldstein MM, et al. *Polym Sci* 1999;**41**:867-875.
11. Feldstein MM, et al. *Polymer* 2000;**41**:5339-5348.
12. Feldstein MM. *Polymer* 2001;**42**:7719-7726.
13. Feldstein MM, et al. *Polymer* 2001;**42**:971-979.
14. Baraimov DF, et al. *J Appl Polym Sci* 2002;**85**:1128-1136.
15. Chalykh AA, et al. *J Adhes* 2002;**78**:667-694.
16. Haaf F, et al. *Polym J* 1985;**17**:143-152.
17. Bühler, et al. Polyvinylpyrrolidone excipients for pharmaceuticals: povidone, crospovidone and copovidone. 2005. Berlin, Heidelberg, New York: Springer. pp.1-254.
18. Online catalog of Thermo Scientific. Polyethylene Glycol (PEG) and Pegylation of Proteins.
19. Askeland, Donald R. "The Science and Engineering of Materials: Third Edition", Chapman & Hall, London, 1996.
20. Kireeva PE, et al. *J Appl Polym Sci* 2007;**105**:3017-3036.
21. Li X, et al. *J Nanosci Nanotechnol* 2008;**8**:1-5.
22. Van den Mooter G, et al. *Int J Pharm* 1998;**164**:67-80.
23. Li H, et al. *Chem Eng Technol* 2010;**33**:1650-1654.
24. Zang YH, et al. *Polymer* 1991;**32**:489-92.
25. Feldstein MM, et al. *Polymer* 2000;**41**:5327-5338.
26. Feldstein MM, et al. *Polymer* 2000;**41**:5349-5359.
27. Feldstein MM, et al. *Polymer* 2003;**44**:1819-1834.
28. Paul DR, et al. Polymer blends. New York: Academic Press;1978:2.
29. Zhang G, et al. *J Appl Polym Sci* 2003;**88**:973-979.
30. Maes C, et al. *Polymer* 1995;**36**:3159-3164.
31. Vartapetian RS, et al. *Macromol Chem Phys* 2001;**202**:2648-2652.
32. Feldstein MM, et al. *Proc 25th Annu Meeting Adhesion Soc* 2002;292-294.

# SECTION IV



## Final discussion and conclusions

---

### 8.1 General discussion

Periodontal diseases are highly prevalent and can affect up to 90% of the worldwide population. These diseases may be of developmental, inflammatory, traumatic, neoplastic, genetic, or metabolic origin [1, 2]. However, the term periodontal disease usually refers to the common inflammatory disorders of gingivitis and periodontitis that are caused by pathogenic microflora in the biofilm or dental plaque that forms adjacent to the teeth on a daily basis [3].

Gingivitis, the mildest form of periodontal disease, is highly prevalent and readily reversible by simple, effective oral hygiene. It affects 50-90% of adults worldwide [3]. Inflammation that extends deep into the tissues and causes loss of supporting connective tissue and alveolar bone is known as periodontitis. It results in the formation of soft tissue pockets or deepened crevices between the gingival and tooth root. Severe periodontitis can result in loosening of teeth, occasional pain and discomfort, and impaired mastication [4].

Treatments of gingivitis and periodontitis include various non-surgical and surgical therapies, depending on the specific treatment objective [4]. The different strategies of periodontal therapy aim to (1) reduce and/or eliminate inflamed tissues caused by bacterial plaque, (2) correct defects or anatomical problems due to the disease, and (3) regenerate new periodontal tissues [5, 6]. A number of different treatments have been developed to promote periodontal regeneration since the mid-1980s; they include bone replacement grafts, root surface biomodifications, guided tissue/bone regeneration (GTR/GBR), and delivery of growth factors or gene therapies [7]. Among them, GTR and GBR have become the most promising therapies and were widely used in clinical treatment for their convenience and effectiveness [8, 9].

GTR/GBR treatments of periodontitis are surgical procedures to implant a regeneration membrane that specifically aims to restore the periodontal tissues supporting the teeth. It is commonly found that the epithelial and gingival connective tissues migrate rapidly into the wound, preventing periodontal regeneration [9]. In these therapies, the ideal regeneration membrane plays a key role to work both as a barrier to prevent epithelial and gingival connective cells growing into periodontal defects and as a favorable niche to maximize the migration and proliferation of periodontal ligament cells and osteoblasts within the periodontal defects to promote the reconstruction of the supporting tissue [10]. In order to achieve better clinical outcomes in dental implantology, barrier membranes should fulfill some fundamental requirements, such as good biocompatibility and biodegradability, suitable adhesiveness between the membrane and surrounding bone tissues to prevent the movement of the membrane, high flexibility to provide surgical facility, and sufficient mechanical strength to maintain their barrier function long enough for bone regeneration [11, 12]. In addition, a further improvement in the GTR/GBR techniques can be achieved by using a bioactive membrane capable of accelerating bone formation while minimizing the influence of bacterial contamination on regenerative outcome [4, 13].

Different non-resorbable and resorbable membranes have been developed and are currently available on the market. The so-called “gold standard” non-resorbable membranes for GTR/GBR procedures are currently based on polytetrafluoroethylene (PTFE). However, they have different disadvantages such as non-resorbability and the need for a second surgical operation to repair dehiscence [10]. Although membranes based on biodegradable synthetic polymers, such as polylactic acid (PLA), poly(D,L-lactide-co-glycolide) (PLGA) and poly(DL-lactide-co- $\epsilon$ -caprolactone) (PLCL), avoid a second surgical operation, they show drawbacks concerning their capacity of space maintenance, early/late absorption, mechanical properties and bacterial infection during degradation. On the other hand, collagen membranes have additional advantages related to biological properties of collagen itself but are characterized by low mechanical strength [14, 15].

The “ideal” membrane for use in periodontal regenerative therapy has yet to be developed. Based on the State of the Art analysis, research efforts were addressed to the preparation of (i) composites consisting of osteoconductive calcium phosphate ceramics and biodegradable polymers, (ii) multi-component membranes with specific properties at the interface between the implant and alveolar bone and epithelial tissues, and (iii) surface modification of synthetic polymers to graft bioactive proteins or biomolecules. The introduction of specific cell-adhesion molecules should lead to a specific tissue response on the membrane surfaces, the delivery or

incorporation of antimicrobial substances might minimize the influence of bacterial contamination on regenerative outcome and the growth factor release from membranes should stimulate a better bone regeneration.

In this contest, the thesis was aimed at the development of biologically active products for GTR/GBR procedures, with improved osteoconductive and antimicrobial properties. In the first part of the work, a commercially available membrane based on PTFE was surface modified to tailor the surface properties, allowing rapid bone re-growth (Chapter 2) and exerting antimicrobial action (Chapter 3). In the second part, an innovative bi-layered bioabsorbable membrane was developed (Chapter 7), by the assembly of a compact (Chapter 4 and 5) and a porous layer (Chapter 6).

A mussel-inspired coating method, involving the application of a thin film coating of 3,4-dihydroxy-DL-phenylalanine (DOPA) on a substrate via dip-immersion and oxidative polymerization, was employed to surface modify PTFE films. This versatile method was first proposed by Lee et al. [16]. The thickness of the adherent polymer film (polyDOPA) is a function of the immersion time and the polymerization temperature. Moreover, to avoid non-specific microparticle formation on surfaces, stirring and/or vertical sample orientation is necessary. The polyDOPA coating is able to form on virtually all types of material surfaces. Then, it can further support a variety of secondary reactions, leading to tailoring of the coating for diverse functional uses.

Guided by these findings, we applied a hydroxyapatite nanoparticles (HAp) coating on PTFE film through one-step DOPA/HAp application process in order to promote the bone re-growth properties of PTFE membranes. In our strategy, HAp coating on polymer films occurred by simultaneous binding of DOPA during its polymerization, to the HAp nanoparticles and to the PTFE substrates. Thus, the immobilization of HAp nanoparticles on PTFE surface was achieved by their entrapment and/or conjugation with polyDOPA. It was found that the polyDOPA/HAp coating covered the entire surface of the films, producing a very rough surface with improved wettability properties. The coating was characterized by a 3D-structure, able to enhance protein absorption and osteoblast proliferation. Indeed, *in vitro* cell tests with pre-osteoblast MC3T3-E1 cells confirmed these observations. Cells proliferated on the modified PTFE substrate over 3 days. They were extremely well spread and formed long filopodia with firm attachment to the surface.

The surface multifunctional groups on the polyDOPA layer (catechol and amine functional groups) were also reported to be able to spontaneously reduce noble metal nanoparticles, without using a reducing agent, surfactants, or energy-consuming steps [17, 18]. In this contest,

the polyDOPA was applied to produce silver nanoparticles (AgNPs) on PTFE film surfaces in order to exert antimicrobial action against pathogens in the periodontal treated site. Physicochemical and morphological analyses demonstrated that the polyDOPA coating deposited on PTFE surface was an effective functional layer for metallization. The AgNPs showed a diameter around 68 nm and were homogeneously distributed on the surface. Nanoparticles slightly inhibited fibroblasts NIH 3T3 proliferation, without compromising cell adhesion and maintaining a good biocompatibility of modified PTFE films. Moreover, the antimicrobial efficiency was proved against Gram-negative and Gram-positive bacteria.

The second part of the thesis followed a highly innovative approach, leading to the development of a bi-layered bioabsorbable membrane. The purpose was to combine the approaches identified in the scientific literature, developing biologically active, osteoconductive and multi-component materials, mimicking native bone and gingival extracellular matrix (ECM). The work was divided into three parts: the development of the compact (1) and porous (2) layers and their combination onto a bi-layered membrane (3).

#### 1. Compact layer development

Physical (morphology, thermal and mechanical properties) and biological (cell adhesion and proliferation) properties of films made of blend between PLCL and PLGA (compositions 100/0, 75/25, 50/50, 25/75, 0/100 wt/wt) were investigated with the aim to select an optimal blend composition in terms of compatibility degree between the phases, mechanical properties and cell compatibility for our application. PLCL/PLGA 25/75, 50/50 and 75/25 did not show evident phase separation, attributed to similar physical properties between blend components. The behavior of blend component  $T_g$ s suggested some degree of compatibility for PLCL/PLGA 25/75 and 50/50 blends. Mechanical properties confirmed the limited compatibility for PLCL/PLGA 25/75 and 50/50 blends, with superior mechanical properties for PLCL/PLGA 25/75 blend. *In vitro* cell tests using mouse embryonic fibroblast NIH 3T3 cells indicated that PLCL/PLGA 100/0, 50/50 and 25/75 films supported cellular attachment and proliferation, especially on PLCL/PLGA 25/75 blend surface; fibroblasts spread uniformly and extensively with the development of lamellopodia. This blend composition was further characterized for its stability in physiological medium, evidencing a degradation behavior intermediate between that of the pure polymers, in terms of weight loss and molecular weight changes, becoming similar to those of pure PLGA after 6 weeks incubation in PBS. The cross-section of PLCL/PLGA 25/75 blends showed pores with a few micron size after 4 weeks of incubation in PBS, probably caused by PLCL dissolution and degradation.

Layer-by-Layer (LbL) self-assembly technique was investigated to surface engineer PLCL/PLGA 25/75 blend films. A chondroitin sulfate/chitosan (CHS/CH) polyelectrolyte multilayer coating was deposited on blend films to enhance fibroblast NIH 3T3 cell adhesion, proliferation and function, while at the same time conferring antibacterial efficacy. Blend sample surface was pre-modified to introduce positively charged groups which are necessary for the stable deposition of the first LbL layer. Aminolysis treatment was performed on blend films and optimized to finally select the following parameters: C = 0.08 g/mL, t = 8 min and T = 37 °C. Then, LbL coating was performed on activated blend films. The success of coating as well as the great improvement in surface properties were confirmed by combined techniques. QCM-D confirmed the nanometric thickness of the coatings. Contact angle measurements suggested a full coverage of the coating after the deposition of at least five layers and, for those fully coated surfaces, the surface wettability was dominated by the outmost coating layer. Fluorescence microscopy and FTIR-ATR analysis were performed to follow the growth of CHS and CH layers on aminolysed blend films. *In vitro* investigations with fibroblast NIH 3T3 cells showed that films incorporated with biomacromolecules exhibited stronger ability to support fibroblast cells adhesion and to maintain fibroblast function, in particular for those assembled with high number of CHS/CH layers and having a cationic polyelectrolyte layer on top. A number of 16 layers was thus selected as optimal number of layers for our application. However, no antibacterial activity was observed by the optimized nanocoating.

## 2. Porous layer development

Based on a biomimetic approach, three dimensional sponge-like composite membranes based on  $\beta$ -tricalcium phosphate (TCP) and a double cross-linked network of chitosan/gelatin (CH/G) were obtained and investigated, having a similar composition to that of natural bone. The double cross-linking method was based on a covalent and ionic cross-linker, genipin (GP) and dibasic sodium phosphate salt (DSP) respectively. The cross-linking process did not significantly influence sample morphology and thermal stability. An optimal interconnected porous network for bone repair, with pores size within 100–200  $\mu\text{m}$  range, was obtained for all membranes. Lower sized pores were also present in order to favor protein adhesion and thus cells attachment on the membrane, and to allow the flow of nutrients to cells within the substrate. On the contrary, the double cross-linking process and the addition of TCP increased the mechanical properties (both in dry and wet conditions), the membrane stability in contact with water media, and the cell response of CH/G network. In fact, Young's modulus and maximum tensile strength increased, while deformability of CH/G membranes decreased by cross-linking, as a consequence of a stiffening effect by the cross-linkers and TCP. The water

absorption degree and the dissolution rate were markedly reduced in cross-linked samples. Finally, viability of MG-63 cells seeded onto CH/G+GP-DSP and CH/G/TCP+GP-DSP membranes was significantly higher than for CH/G samples. SEM micrographs after 72 h showed that MG-63 cells had a high affinity for CH/G/TCP+GP-DSP samples, displaying the typical spindle-like shape, with a stretched elongated shape and a spread morphology.

### 3. Bi-layered membrane development

The assembly process was based on the insertion of an intermediate adhesive layer composed of a polyvinylpyrrolidone (PVP)/polyethylene glycol (PEG) blend. PVP/PEG blends are pressure-sensitive adhesives (PSAs), which are commonly used in a variety of applications because of their ease of application, low toxicity, and versatility [19]. PSAs combine a liquid-like character, which allows a good molecular contact under a light applied pressure, and a solid-like character, that resists an applied stress once the bond has been formed. In particular, PVP/PEG blends display interesting PSA properties only in a fairly narrow window of compositions (between 30 and 40 wt% PEG) [20]. The Lap shear strength test allowed the evaluation of PVP/PEG blends adhesive properties. Better results were found for blend with PVP/PEG 70/30 composition that was selected for the assembly of the final device. Preliminary characterization of the bi-layered membrane showed that the assembly process did not change the morphology of both compact and porous layer and led to a device with good manageability and mechanical properties.

## 8.2 Conclusions and future developments

In this thesis work, synthetic and natural polymeric materials and nanostructured coatings were designed for the fabrication and coating of membranes for GTR/GBR applications in periodontal diseases.

The coating strategies adopted to surface modified non-resorbable PTFE membranes led to the development of PTFE substrates with improved osteoconductive and antibacterial properties. Such an improvement in PTFE is not only promising for the treatment of periodontal diseases but also for many other pathologies requiring improved surface properties of PTFE.

In the future, the ability of substrates coated with HAp nanoparticles to support Mouse preosteoblast MC3T3-E1 cells differentiation will be evaluated, while more extensive antibacterial tests will be performed (i.e. antimicrobial activity assay in liquid through viable cell counting method) on PTFE films enriched with AgNPs, using also periodontal pathogens (i.e. *Porphyromonas gingivalis*, *Actinobacillus actinomycetemcomitans*).

Regarding the development of the bi-layered bioabsorbable membrane, the selected materials for compact and porous layers introduced improvements in the biomaterial field for Tissue Engineering (TE) applications.

In detail, blend for the compact layer (PLCL/PLGA 25/75) combined the deformability of PLCL with the higher mechanical stiffness, the cell adhesion properties and the slowly degradation rate of PLGA, leading to a tough material with similar degradation rate to PLGA and superior cell adhesion and proliferation. The surface modifications of PLCL/PLGA 25/75 blend films (aminolysis treatment and LbL coating) were carried out with success and optimized. The introduction of CHS and CH onto blend surface improved biocompatibility properties. However, in the future, further improvements will be introduced in the optimized CHS/CH multilayer nanocoatings in terms of antimicrobial activity. In this context, different strategies can be compared. Firstly, extensive antibacterial tests can be performed (i.e. antimicrobial activity assay in liquid through viable cell counting method) using also periodontal pathogens, to verify if the absence of antibacterial activity is related to the amount of CH into the nanocoating. Secondly, AgNPs, antimicrobial drugs (e.g. metronidazole) or both agents can be introduced onto the LbL nanocoating and membranes will be further characterized.

The composite material for the porous layer (CH/G/TCP+GP-DSP) was demonstrated to be suitable candidate as osteoconductive layer. In the future, its bioactivity and its ability to support osteoblast cells differentiation needs to be evaluated. Moreover, to better mimic bone ECM matrix, the freeze-drying process adopted in this thesis can be replaced by electrospinning in order to obtain biomimetic nanofibrous mats.

Finally, the assembly process based on the application of an adhesive layer (PVP/PEG 70/30) between compact and porous component led to the development of membranes with preserved morphology of the two components, good mechanical properties and manageability. These preliminary results were promising for a future application of the bi-layered membrane in GTR/GBR applications. In the future, further characterizations are required in order to evaluate membrane stability in physiological conditions (water uptake and dissolution tests) and biocompatibility (in vitro cell tests using both osteoblast and fibroblast cells).

## References

---

1. Armitage GC. *Periodontol 2000* 2004;**34**:9-21.
2. Jordan RC. *Periodontol 2000* 2004;**34**:217-229.
3. Albandar JM, et al. *Periodontol 2000* 2002;**29**:7-10.
4. Pihlstrom BL, et al. *Lancet* 2005;**366**:1809-1820.
5. Sculean A, et al. *J Clin Periodontol* 2008;**35**:106-116.
6. Wang HL, et al. *J Periodontol* 2005;**76**:1601-1622.
7. Ramseier CA, et al. *Periodontol 2000* 2012;**59**:185-202.
8. Villar CC, et al. *Dent Clin North Am* 2010;**54**:73-92.
9. Nyman S, et al. *J Clin Periodontol* 1982;**9**:257-265.
10. Bottino MC, et al. *Dent Mater* 2012;**28**:703-721.
11. Huang JQ, et al. *J Oral Maxillofac Surg* 2002;**60**:1449-1454.
12. Oh SH, et al. *J Biomat Sci Polym Ed* 2006;**17**:1375-1387.
13. Jeon O, et al. *Biomaterials* 2007;**28**:2763-2771.
14. Bottino MC, et al. *Acta Biomater* 2011;**7**:216-224.
15. Miller N, et al. *J Clin Periodontol* 1996;**23**:1051-1059.
16. Guvendiren M, et al. *Biomacromolecules* 2008;**9**:122-128.
17. Xu H, et al. *Appl Surf Sci* 2011;**257**:6799-6803.
18. Saidin S, et al. *Mater Sci Eng C* 2013;**33**:4715-4724.
19. Roos A, et al. *J Polym Sci Part B: Polym Phys* 2002;**40**:2395-2409.
20. Chalykh AA, et al. *J Adhes* 2002;**78**:667-694.